A Nanoscale Investigation of Microbial Adhesion to Biomedical Implant Devices

By

Ray Jenkins Emerson IV

A Dissertation

Submitted to the Faculty of

Worcester Polytechnic Institute

In Partial Fulfillment of the Requirements for the

Degree of Doctor of Philosophy

in

Chemical Engineering

5th April, 2006

Terri Camesano, Ph.D.
Primary Advisor
Assistant Professor
Department of
Chemical Engineering

Nancy Burnham, Ph.D.
Committee Member
Associate Professor
Department of
Physics

George Pins, Ph.D.
Committee Member
Assistant Professor
Department of
Biomedical Engineering

Robert Thompson, Ph.D.
Committee Member
Professor
Department of
Chemical Engineering

David DiBiasio, Ph.D.
Head of Department
Associate Professor
Department of
Chemical Engineering

Document Information

Research Motivation

Microbial infections of medical implants often provide significant difficulties for the medical community. These microbes, including various species of bacteria and fungi, are able to adhere to implants, to grow and replicate, to release toxic chemicals, and to disseminate throughout the hosts body, spreading the infection. In 1995, over 10% of all implanted devices, from simple intravenous catheters to the total artificial heart, became infected, leading to increases in the morbidity and mortality of more than 2 million patients. Medical treatment of these infections generated over $11 billion in additional patient costs. As the aggregate age of the population and the frequency and invasiveness of required and voluntary surgeries increase each year, the risk of acquiring an implant infection, as well as the values of the statistics presented above, increase proportionately.

Available treatments exist to combat these infections, but the predominant mode of microbial growth (the biofilm) provides protection to the cells, making infectious biofilm-based microbes up to 500 times more resistant to antimicrobial therapies as compared to their free-swimming counterparts. Systemic antibiotics generally target a broad spectrum of microbes, require additional patient cost, and may eradicate beneficial microbes, such as those that reside in the digestive tract and aid digestion. Local antibiotic treatments, including implants coated or impregnated with antimicrobial chemicals, are effective over short time periods (4-6 weeks), but lose their efficacy as physiological molecules

attach to the implants, providing a physical transport barrier for the antibiotic and a suitably conditioned surface for microbial adhesion. Further, these implants are often several times more expensive than their conventional equivalents. Currently, the only guaranteed method of removing an established microbial implant infection is to physically excise the implant and all surrounding infected tissue. This technique is not without fault, however, as the additional surgeries leave the patient vulnerable to subsequent infections, and also incur additional patient costs. Clearly, this is a problem requiring swift and thorough investigation.

The research described in this document is based on the *a priori* principle that a medical implant infection cannot occur unless a microbial cell is capable of adhering to the implant surface. Following that assumption, the subsequent sections will focus primarily on identifying the necessary and sufficient factors influencing microbial adhesion, discretising those factors into measurable quantities, and developing methods by which those factors may be mitigated or eliminated. Following is a brief summary of each major topic treated within this research period.

Research Summary

Chapter 1 Comprising a rigorous review of the open literature, treating the major themes investigated during each of the subsequent sections, including relevant discussion taken from the open literature. The topic of microbial adhesion in biomedical implant systems is discussed, including information regarding specific organisms and materials, currently available medical treatments, and their drawbacks. The fundamental operating principles of the atomic force microscope (AFM), which is the primary tool used in this research, are detailed, as well as methods of interpreting topographical and force data obtained from the instrument. Finally, the various mathematical models to be used as analytical tools for AFM data are introduced.

Chapter 2 This section is based upon both the Master's Thesis submitted to Worcester Polytechnic Institute in February 2004 by Ray J. Emerson [3], and upon a peer-reviewed publication which summarised this work [4]. We characterise the interactions

between *Pseudomonas aeruginosa* ATCC 10145 and *Candida parapsilosis* ATCC 90018 using a novel method of cellular immobilisation, which emphasises minimal chemical modification of the cell surface. The paper describes the very different force-separation interactions seen between *C. parapsilosis* and both a common medical implant material (*viz.*, silicone rubber) and a nascent *P. aeruginosa* biofilm grown on the same material. This study was the first step in developing an *ab initio* technique which may be used to determine the relative affinity of a microbial cell for an implant material surface.

Chapter 3 Including a peer-reviewed publication developed in collaboration with a research group at Albert Einstein College of Medicine, Bronx, NY, USA [2]. The experimentation examines the structure of a melanin capsule formed by *Cryptococcus neoformans* in response to harsh environmental conditions. In the paper, we characterise the surface morphology of the melanin capsules by AFM and SEM, as well as the pore size distribution in the capsule by NMR cryoporometry. The paper proposes a supermolecular structure for the melanin capsule, which has heretofore been poorly understood, as well as a rationale for capsule formation in response to environmental stimuli.

Chapter 4 Consisting of a peer-reviewed publication describing the application of established calibration techniques to the Digital Instruments Dimension 3100 atomic force microscope equipped with a Nanoscope IIIa controller [5]. We specifically investigate the effects of piezoactuator travel distance and cantilever spring constant on force-separation curves by comparing manufacturer-reported values for these two quantities to those actually measured *in situ*. We also explore the effects of the magnitude of the probe radius of curvature as it relates to mathematical models (*e.g.,* the classical DLVO theory of colloid stability). Initial results describing the dynamic behaviour of these three quantities is also reported. Final recommendations are made regarding adaptation of these calibration techniques to a variety of microscopes, as well as towards a fulsome and rigorous calibration of the instrument beyond the manufacturer's recommendation.

Chapter 5 This section is based upon a research project performed in collaboration with a group at the University of Connectict, Storrs, CT, USA, and in the doctoral disserta-

tion of one of the group's students [6]. The experimentation develops a methodology for creating oriented fibronectin layers via controlled deposition of biotin, streptavidin, and regioselective (either N-terminal or C-terminal) monoclonal antibodies. ELISA and AFM were used in parallel to verify the composition and topography of the surfaces at each stage of the method. Specific adhesion of *Staphylococcus epidermidis* RP62A to the surfaces was quantified under static conditions for the two different fibronectin surfaces. Results indicate that C-terminus-bound fibronectin (N-terminus presenting into solution) enhances the adhesion of *S. epidermidis*. Conversely, fibronectin presenting the C-terminus displayed a significant preferential specific adhesion of *S. epidermidis* to fibronectin anchored by the C-terminus. Fibronectin tethered in the reverse manner significantly inhibited *S. epidermidis* adhesion.

Chapter 6 Describing an ongoing research study coupling the topographic and force acquisition features of the AFM with the microbial probe developed in 2. The project has included collaborations with the Department of Chemistry and Biochemistry and the Department of Mechanical Engineering at Worcester Polytechnic Institute. High-resolution images of several putative anti-adhesive surfaces were captured using an unmodified probe, and mapped according to Mandelbrot fractal theory, generating a scale-independent representation of the original surface. Using a probe modified with a clinical isolate of *Staphylococcus epidermidis*, retraction curves were captured using an AFM, describing the relative affinity of the microbe for each surface, and quantifying the magnitude of the tensile strength of each pull-off event. According to a novel mathematical model, described as a Discrete Bonding Model [1,7], the fractal map and tensile strength data may be combined to characterise the influence of the substrate on the bonding event. Fundamentally, this model identifies the necessary surface area and/or texture required for a single bonding event to occur, and provides qualitative information describing the importance of this texture on the strength of the adhesive event as a whole.

Chapter 7 This ongoing project extends upon an existing mathematical model, developed to describe the changes in osmotic pressure and systemic entropy within a polymer

brush oriented normal to a substrate material (*e.g.,* a microbial exopolymer brush). Research is carried out in collaboration with the Department of Physics at Worcester Polytechnic Institute. Historically, AFM force-separation curves demonstrating only repulsive behaviour on extension of the piezoactuator have been largely ignored, in terms of quantitative modeling of the interactions. In bacterial systems, such behaviour describes the majority of the force profiles recorded by the instrument. As a result of the former lack of study, the latter data sets have remained unanalysed and unanalysable. Available models describing steric interactions between a bare AFM tip and a microbial polymer brush have heretofore been used after the points of zero force and zero separation have been defined, providing results which may not accurately characterise the systems under study, and include non-physical assumptions regarding the energy held within the polymer brush. This model has been reformulated to overcome the weaknesses inherent in the original formulation, and is now useful as a tool for identifying the point of zero separation between a bare AFM tip and a surface coated with two polymer brushes having distinct thicknesses and densities.

Chapter 8 This section describes research topics currently under exploration, but which have not yet reached sufficient maturity to warrant individual sections. Further, this section introduces topics for potential future projects which make use of the research presented herein.

Chapter 9 This section provides an overall research summary, and includes conclusions regarding the contribution of these projects to the underlying problem of microbial infections of biomedical implant devices.

Document Information

 Much of the work presented has been compiled from previous publications by the same.

This document was written in `VIM` version 6.3.86 by Bram Moolenaar *et al.* The document was typeset using the editors Kile v. 1.8.1 and `VIM` v. 6.3, and was compiled using LaTeXv.

3.14159-2.1. Data were analysed using Nanoscope® version 4.43 r8 by Veeco Metrology Group/Digital Instruments (Santa Barbara, CA, USA), Matlab® R14 Service Pack 1 (v. 7.0.1.24704) by The Mathworks (Natick, MA, USA), SPSS SigmaScan® v. 5.0.0, SPSS SigmaStat® v. 2.03, and Microsoft® Excel 2003. All charts were generated using SPSS® SigmaPlot 8.02, Microsoft® Excel 2003, and Matlab® R14 Service Pack 1 (v. 7.0.1.24704), and optimised using GNU ImageMagick™ version 6.2.0. Images were edited using Adobe Photoshop® 7.0 and `The GIMP` version 2.2.0. This document makes extensive use of software made available under the GNU Public License (The Free Software Foundation, Boston, MA, USA), and many thanks go out to the Open Source Community for their tireless work in non-proprietary software development.

Bibliography

[1] C. A. Brown and S. Siegmann. Fundamental scales of adhesion and area-scale fractal analysis. International Journal of Machine Tools and Manufacture, 41:1927–1933, 2001.

[2] H. C. Eisenman, J. D. Nosanchuk, J. B. W. Webber, R. J. Emerson, T. A. Camesano, and A. Casadevall. Microstructure of the cell wall-associated melanin in the human pathogenic fungus *Cryptococus neoformans*. Biochemistry, 44(10):3683–3693, 2005.

[3] R. J. Emerson. Microbial Adhesion to Medical Implant Materials: An Atomic Force Microscopy Study. Master's Thesis, Biological Interaction Forces Lab, Department of Chemical Engineering, Worcester Polytechnic Institute, 2004.

[4] R. J. Emerson and T. A. Camesano. A nanoscale investigation of pathogenic microbial adhesion to a biomaterial. Applied and Environmental Microbiology, 70(10):6012–6022, 2004.

[5] R. J. Emerson and T. A. Camesano. On the importance of precise calibration techniques for an atomic force microscope. Ultramicroscopy, 106(4-5):413–422, 2006.

[6] R. A. Jarvis. Quantification of *Staphylococcus epidermidis* Specific Adhesion to Ligand-Modified Substrata Controlling Fibronectin Orientation Using Immoblized

Antibodies. Doctoral Dissertation, Center for Biomaterials, University of Connecticut, 2005.

[7] S. Siegmann and C. A. Brown. Surface texture correlations with tensile adhesive strength of thermally sprayed coatings using area-scale fractal analysis. In E. Lugschneider and P.A. Kammer, editors, United Thermal Spray Conference - Proceedings DVS Verlag, Düsseldorf, Germany, 1999.

Acknowledgments

It has been nearly a quarter of a century since the beginning of my formal education, and almost ten years since I first came to Worcester Polytechnic Institute. This document is both the final product of that time period, and a testament towards what passion and resolve can accomplish. It represents the end of one phase of my life, and the beginning of another. The former has shown me wonderful things about the world; I trust the latter will do the same. In the next few pages, I gratefully recognize many (certainly not all) of the people who have made all of this a reality.

First and foremost, my thanks go to Professor Terri Camesano, who has been my advisor, colleague, and friend through the past several years. You have provided me with innumerable opportunities to hone my abilities, and I can never aptly express my gratitude for all you have enabled me to accomplish. I can only hope the mark I leave behind with you is comparable to the one I carry with me into the world.

To Professor Nancy Burnham, certainly the most active member of my advisory committee, and a welcome colleague and friend. Thank you for making my favourite parts of science become reality ... proving me wrong, but teaching me how to make it right. It has been my pleasure to work with you.

To Professor George Pins, a knowledgeable scientist, and a relentless questioner. I often let my head wander too high in the clouds, but you always pulled me back to the ground. Thank you for helping me keep my goals realistic.

To Professor Robert Thompson, who was always available for discussion and free with praise for even the smallest victories over nanoscale adversity. Your experience and candor kept me honest, and I can't thank you enough.

Further, I acknowledge Worcester Polytechnic Institute, the Department of Chemical Engineering, its faculty, staff, and students for maintaining a wonderful place for the execution and study of science.

To the agencies who have generously funded my work, I give my sincere thanks. The National Science Foundation (Grants DGE-9355019 and BES-0238627) and the donators of the American Chemical Society Petroleum Research Fund (Grant 38988-G2) have helped immeasurably in the completion of this research.

To my lab mates over the last five years: Laila Abu-Lail, Dr. Nehal Abu-Lail, Bhupinder Arora, Arzu Atabek, Dr. Torbjorn Bergstrom[1], Matthew Black, Dr. Yatao Liu, Paola Pinzon-Arango, Paula Restrepo and Joshua Strauss. All have my sincere gratitude for their ideas and discussions. Further, my thanks to Giacomo Ferraro and Douglas White, for their endless assistance and practical knowledge in equipment design and maintenance, as well as to Elaine Brady, Joseph Kaupu and Sandra Natale for keeping the department running on a daily basis.

To the teachers who have inspired and encouraged me since I first walked into a classroom in 1985[2]: Prof. Jose Argüello (WPI), Prof. Herbert Beall (WPI), Mr. David Bergman (NQHS), Mr. Steven Brenner (NQHS), Ms. Ann Carrol (NQHS), Prof. Louis Curran (WPI), Prof. Ravindra Datta (WPI), Prof. David DiBiasio (WPI), Prof. Anthony Dixon (WPI), Prof. Chrysanthe Demetry (WPI), Mr. Thomas Donnelly (NQHS), Ms. Patricia Drew (CMS), Mr. Mark Flaherty (CMS), Mr. Ernest Gizzarelli (NQHS), Ms. Mary Gralton (NQHS), Mrs. Jean Healy (CMS), Mr. Michael Jorgenson (NQHS), Mr. J. Steven Joyce (NQHS), Mr. Richard Kenneally (CMS/NQHS), Prof. Yi Hua Ma (WPI), Prof. W. Grant McGimpsey (WPI), Mr. William McWeeny (CMS), Mr. Frank Moffett

[1]At the time of this writing, many of the people noted as "Dr." have not yet received their degrees. I know they will soon!

[2]WPI – Worcester Polytechnic Institute; NQHS – North Quincy High School; CMS – Central Middle School; WES – Wollaston Elementary School

(NQHS), Dr. Laurence Osbourne (CMS), Mr. Kenneth Panaro (CMS), Ms. Ann Pegg (WES), Mrs. Margaret Spencer (CMS), Mr. Edward Steele (CMS), Mr. Arthur Svensen (CMS), Prof. Kristin Wobbe (WPI), and Prof. Barbara Wyslouzil (WPI).

To my friends and colleagues, thank you for your discussion and support through all of these years. Special thanks go to Hussain and Omar Abu-Lail (أهلًا، إبن اختي!), Dr. Nada Al-Ananzeh, Melissa Alexander, Dr. Ana Avalos, Dr. M. Engin Ayturk and M. Didem Avcioglu-Ayturk, Nichole Bisceglia, Laura Brady, Prof. Christopher Brown (WPI), Kelli Bukofser, Dr. Caitlin Callaghan, Brittany Campbell, Melissa Cusano, Prof. Erwin Danneels (WPI), Melissa Deschler, Brett Downing, Dr. Erik Engwall, Pascal Eyriés, Prof. Domenico Grasso (Smith College), Dr. Federico Guazzone, Sarah Haney, Carina Hart, Prof. Frederick Hart (WPI), Dr. Stephen Heard (University of Massachusetts Medical School), Dr. Nikhil Jalani, Dr. Rebecca Jarvis, Officer Jeffrey Laramee, Pat McPhail (Veeco Metrology Group), Dr. Amparo Gallardo-Moreno (Universidad de Extremadura, Spain), Dr. Jayne Morrow (NIST), Sally Nobrega, Paolo Paci, Fabien Ramat, Christopher Rehm, Dr. Ernesto Soto-Villatoro, Justin Surpless, Dr. Erik Thoreson, and Prof. Jennifer Wilcox (WPI). The diverse contributions of these and many other people made much of this work a reality.

To my Brothers in Sigma Pi Fraternity, thank you for the last nine years[3]. Douglas Alexander, Jose Bañez, Michael Bartley, Jeremy Boylan (HT), Michael Brady, Robert Bukofser, Eugene Campbell, Robert Craig, Kurt Deschler, John DiGiacomo, Dr. Benjamin Falk, David Gray, David Grondin, Eric Hart, Fr. Michael Hobson, Peter Launie, Edward Levesque (HH), Scott Lucarelli, Vincent-Matthew Malfa, James Michaud, Daniel Morin, Christopher Pacitto, Justin Pelkowski, Andrew Piner, William Price, Vincent Salemi, Brady Schulman, Glen Sergeant, Justin Sherman, Joel Smith, Dr. Robert Tuttle, Justin Wahlstrom, Ryan Zarkesh, and Michael Zarozinski. I Believe

To my family, who have supported me throughout my entire life, thank you so much. Kathryn Emerson and Keith Eisenhauer, Ray J. Emerson II†, George and Meredith Fitzmaurice, William and Ada Keefe, William Keefe Jr., Thomas† and Sadie† Mangan,

[3]Unless otherwise noted, all listed are members of the ΓΙ chapter of the fraternity.
†Deceased

Melody Stanton, Joseph and Sharon Swindells, Joey and Jackie Swindells, Darrell and Helen White, Julie White, Kathryn F. White†, Wendy White, the majority of the population of Prince Edward Island, Canada, and all the rest.

To the many and varied authors who reminded me that, while science and reason are inexorably intertwined with all things in life, it is not necessarily a bad thing to put them by the wayside for a bit. These include, but are most certainly not limited to: D. Adams, M. Z. Bradley, J. Burke, A. Carter, C. Dickens, S. Donaldson, Sir A. C. Doyle, D. Eddings, Rev. R. W. Emerson, E. Ensler, N. Gaiman, W. Goldman, Prof. S. Hawking, R. Jordan, S. King, U. K. Le Guin, C. S. Lewis, H. P. Lovecraft, Sir T. Malory, E. A. Poe, A. Rice, J. K. Rowling, W. Shakespeare, H. D. Thoreau, J. R. R. Tolkien, K. Vonnegut and T. H. White.

These people are all responsible, for better or worse, for the man I am and the work I have done.

"While Man, being finite, cannot comprehend the Highest, still he can and should dedicate the best that he has to the Highest that he knows"

Pythagoras

"If we shadows have offended,
Think but this, and all is mended,–
That you have but slumber'd here,
While these visions did appear.
And this weak and idle theme,
No more yielding but a dream,
Gentles, do not reprehend:
If you pardon, we will mend.
And, as I am an honest Puck,
If we have unearnéd luck
Now to 'scape the serpent's tongue,
We will make amends ere long;
Else the Puck a liar call:
So, good night unto you all.
Give me your hands, if we be friends,
And Robin shall restore amends."

A Midsummer Night's Dream, Act V, Scene I.

Contents

List of Figures

List of Tables

CHAPTER 1

Literature Review

The various species of microorganisms, including bacteria, fungi and yeasts, are ubiquitous entities that both benefit and confound humankind's efforts to enrich their own lives. The adhesive interactions of these creatures to different surfaces, including soil particles [28, 74], industrial bioreactors and heat exchangers [81, 104], foodstuffs [44, 73], medical implants [49, 52, 58] and human cells [31, 76], has spawned an entire field of research through which humanity seeks to exploit, and in many cases overcome, the activities of creatures one one-millionth their size. The studies described in subsequent chapters of this document describe research topics by which these adhesive events may be better understood and understood for the benefit of humanity.

The following review explores, in depth, currently-available information regarding surface adhesion, with specific focus on biomedical implant device infections. Topics discussed include the definition of infection, available treatments, and their ubiquitous drawbacks and failures. Characteristics of common clinically isolated microorganisms and implant materials are presented, with additional discussion regarding the bacteria and fungi chosen for subsequent experimentation. Atomic force microscopy, the principle experimental technique, is described, including its history, applications, operation and interpretation of collected data.

Finally, several classical and novel mathematical models are presented which, in some cases, have been successfully applied to similar systems, and, in others, show promise as potential tools to be used in deeper understanding of the initial mechanisms of microbial infections of medical implants.

1.1 Microbial Adhesion in Biomedical Systems

Every year, in the United States alone, over 20 million surgical procedures are performed [58]. Each procedure requires temporary and/or permanent implantation of a medical device. The materials chosen for implantation, predominantly hydrophobic polymers, are noted for their biocompatibility and biostability *in vivo* [53]. For all these benefits, however, the materials prove to be adequate sites for microbial adsorption and growth, often leading to infection. Ultimately, of those 20 million procedures, 10 % result in implant infections; in specific devices, such as the total artificial heart (*e.g.,* polyurethane), this value can reach 30 % [49]. As a specific example, we may look at the central venous catheter, infections of which are recorded at a rate of 200,000 per year in the United States alone [52].From a financial point of view, these infections generate over $11 billion annually for additional patient treatment [90]. These values increase each year as the total number of medical procedures performed increases.

On implantation, a medical device is immediately coated with physiological molecules (fluids, peptides, etc.), forming a conditioning film [14,85]. Regardless of the material's surface chemistry at implantation, a gradual buildup of these molecules changes the surface to one easily colonised by microbes. Microbes, either actively or passively transporting to the implant surface, can reversibly adsorb to the biomaterial. Over time, this sorption becomes irreversible, and is often followed by the secretion of exopolysaccharide (EPS) material, surface growth, and biofilm formation. It is after the formation of a biofilm, when the microbes in the film are least susceptible to the host's immune response and external antimicrobial treatments, that the cascade of biochemical events associated with an infection begins within the microbial cells. This may include the secretion of a variety of toxic substances, of additional protective EPS, or of quorum-sensing autoinducer molecules, which signal nearby cells to initiate similar activity [49].

1.1.1 Available Treatments for Biomedical Implant Infections

Once an infection is established, a variety of treatments are available. Each, however, has disadvantages. Global antimicrobial treatment, either by oral or intravenous antibiotic, is

capable of eradicating a wide range of microbial species. The technique is, however, rate-limited in transporting the antibiotic through infection-associated biofilms [90]. These microbial colonies, discussed below in 1.1.2, confer significant antimicrobial resistance on their component organisms. Further, systemic treatment may also eradicate beneficial microbes, such as those that reside in the gut and aid digestion [94]. This alteration in the normal physiological flora can have significant negative side-effects on the host, and can, in fact, promote growth of antimicrobial-resistant strains by eliminating competition for nutrients [5, 64].

Local treatment is accomplished by coating or impregnating an implant with antimicrobial compounds. This method also has drawbacks, most importantly in its capability of generating a bulk antimicrobial concentration which is lethal to pathogenic microbes [52]. Small variations in bulk environmental conditions (pH, bulk chemical concentration, etc...) may prevent the antimicrobial from reaching an effective dosage. Further, upon implantation, the device is immediately coated with physiological fluids and molecules, which can block transport of the antimicrobial into the bulk phase.

One preventative treatment recommends the careful integration of the host's own tissue around the implant at the time of surgery, giving somatic cells a spatial advantage in the so-called "race for the surface" [49]. However, the extent of tissue integration is evaluated by the surgical team and is highly subjective. Currently, the only sure way to eradicate an implant infection once it has established itself is to excise the implant and all surrounding infected tissue. This increases patient cost and recovery time, a well as risk of subsequent infections due to additional surgeries.

To summarise, it is evident that none of the common treatments for eradicating microbial infections of implant devices is guaranteed to do so. Many of the failures arise from the ability of microbes to create a structure known as a biofilm on the implant surface, which protects the cells dwelling within it from many environmental factors. The following section describes the biofilm, its importance to the successful establishment of a device infection, and the mechanisms by which it is created.

1.1.2 Biofilms

While bacteria are commonly thought to be free-swimming organisms, the majority of their life cycle is spent in a sessile state [33]. After initial adhesion occurs, the sessile microbes form a structure known as a biofilm. A biofilm is a poly-laminar, often polymicrobial, arrangement of microbial cells and EPS which affords many metabolic and protective benefits for the cells [9, 107]. Once a biofilm has successfully formed, specific metabolic processes begin. These may include the degradation of substrata, uptake of environmental pollutants, secretion of protective EPS matrix, and production of toxins which are transported into the bulk phase.

Biofilms were first identified by Anton van Leeuwenhoek, who examined oral gingival plaque under one of the first light microscopes in the late 1600's, and identified the "wee beasties" therein [40]. Three hundred years later, ZöBell and Anderson [109] identified biofilms in marine environments. Since that time, biofilms have been identified as the predominant stage of microbial life, and have been shown to be extremely important in environmental, industrial and medical concerns [34, 35].

A simplified mechanistic view of biofilm formation is shown in Figure 1.1.1, which details the processes of initial adhesion, due to specific and non-specific physicochemical interactions, growth and diversification to include multiple microbial species [14].

The biofilm is a homeostatic structure, capable of self-regulation of physiological processes (*e.g.,* metabolism, transport) in response to fluctuations in environmental conditions [107]. This is accomplished by the formation of channels, which act as a primitive circulatory system and allow for rudimentary transport of water and nutrients to the lower layers of the structure. Further, the biofilm provides significant protection against environmental factors (*e.g.,* temperature, chemical composition, antimicrobial compounds). The inherent thickness of the film allows cells nearer the substratum to survive and reestablish the colony, while cells nearer the external surface perish. Further, the decreased concentration of oxygen in the lower regions of the film decrease microbial metabolic activity, slowing cellular response to external stimuli. This protection is of particular importance in pathogenic microbial strains, as it allows the microbes to secrete toxins into the host without vulnerability to host antigenic responses.

Figure 1.1.1: Diagram describing the formation and growth of a microbial biofilm over time. Cells initially bind and secrete EPS. Other cells adhere, causing the biofilm to thicken. Once the film has grown to a sufficient maturity, virulence factors produced by the cells may be secreted into the bulk phase. Adapted from [14].

In many cases, the biochemical processes leading to toxin production do not commence until a biofilm has formed, shielding the microbes from host antigenic responses. As a result of this added protection, any host immune activity or medical treatment seeking to eliminate the microbial infection will be less effective on a biofilm than on planktonic organisms. In clinical tests, microbes growing in biofilms were shown to be as much as 500 times more resistant to antimicrobial therapies than their planktonic counterparts [33]. This arises from the fact that most antimicrobials are developed using planktonic microbial populations, which grow more rapidly and require less capital investment than biofilm systems. As a result, the medical community is provided with tools that are capable of killing microorganisms quickly and efficiently, but which do not adequately affect the dominant infrastructure of an infection.

Diversification of the film also aids in biofilm resistance to antimicrobial therapy, in that the chemical agents that effectively eliminate some microbes may not necessarily work on other species, or even on strains of the same species. Also, even if all microbes within the film are killed by medical or industrial treatment, the superstructure of the film may still remain, providing a suitable binding domain for other microbes, along with a high concentration of useable nutrients. Such a situation creates extreme difficulties for engineers and medical professionals seeking to sanitise surfaces which have been colonised.

1.1.3 Relevant Microbes

A large number of microbes may be responsible for infections of medical devices [49,58,90], a representative list of which may be seen in Table 1.1.1. These are often classified according to specific physicochemical properties of the bacterial cell wall and gross cell morphology. Such assays are, in general, faster and less costly than culture-based identification techniques. While completely qualitative in nature, these assays are often the *prima facie* diagnostic tools, particularly when patient symptoms suggest a rapidly-progressing illness. Further, these analyses give the clinician clearer insight into the relative *in vivo* distribution of species in a polymicrobial population, where *in vitro* culture conditions may limit or prevent the growth of one or more species.

"Gram-positive" and "Gram-negative" refer to the results of a chemical assay, devel-

oped by Hans Christian Gram in 1844, used to characterise relative peptidoglycan and lipid content of the cell wall [59]. Gram-positive cells are able to retain the dye Crystal Violet, and have a higher concentration of peptidoglycan and lipid in the cell wall. Conversely, Gram-negative cells cannot retain this stain and have a lower relative peptidoglycan and lipid content. "Cocci" and "bacilli" are morphological terms referring to either ball-shaped (coccus) or rod-shaped (bacillus) cells. Fungi, being eukaryotic organisms, where bacteria are prokaryotic, are not classified according to these terms, and are therefore presented separately.

Each of the strains shown above, as well as many other pathogenic species not referenced, are widely different in their affinities for different substrata, methods of infection, and susceptibility to antimicrobial therapies *in vivo* [52, 72]. This leads to difficulties in creating materials which do not prevent microbial colonisation, and in formulating medications that effectively treat established infections. Since, in many cases, the microbes do not secrete toxic substances until they have formed a biofilm, which protects the cells from host antigenic activity, these difficulties are significantly increased.

For this study, four model microbes were chosen based on their frequency of clinical isolation, pathogenicity, and ease of acquisition and handling. Qualitative descriptions of these microbes and their relevance to medical implant infections are provided in the following sections.

Table 1.1.1: A list of clinically relevant microbes (Adapted from [52])

Gram-Positive Cocci	**Gram-Negative Bacilli**	**Fungi**
Staphylococcus aureus	*Escherichia coli*	*Candida* spp.
Staphylococcus	*Escherichia fæcalis*	*Saccharomyces*
epidermidis	*Escherichia fæcium*	*cerevisiae*
Staphylococcus	*P. aeruginosa*	
marcescens	*Klebsiella* spp.	
Staphylococcus	*Enterobacter* spp.	
maltophilia	*Actinobacter* spp.	
Coagulase-negative		
Staphylococci		

Staphylococcus aureus and *Staphylococcus epidermidis*

Staphylococcus aureus and *Staphylococcus epidermidis* are both Gram-positive, spherical bacteria. The two species are among the most frequently isolated strains associated with nosocomial and biomedical implant infections [7,82], with *S. aureus* being only slightly more common than *S. epidermidis*. An AFM image of *S. epidermidis* may be seen in Figure 1.1.2.

Especially prevalent in infections associated with blood-contacting devices (*e.g.,* central venous and intravenous catheters), these two species have become increasingly common as etiologic isolates within the last twenty-five years [62]. The primary cause of this increase may be linked to the increased use of both temporary and semi-permanent medical implants in surgical procedures, and more widespread use of antimicrobial prophylactics, such as penicillin, to treat a variety of different infections. Both *S. aureus* and *S. epidermidis* are able to adapt rapidly to medical treatments, both in terms of biofilm formation and production of enzymes which catalyse digestion of the antimicrobial. Increasing the number of potential binding surfaces, as well as eliminating non-resistant strains through widespread use of one antimicrobial treatment, has promoted the dissemination of a large number of subspecies which are partially, if not completely, resistant to most antibiotic treatments [82].

Pseudomonas aeruginosa

Pseudomonas aeruginosa is a Gram-negative bacterium that is omnipresent in both environmental and hospital settings [47, 69, 70]. While not a threat to healthy individuals, this microbe is categorised as an "opportunistic pathogen," *viz.*, an organism that can cause additional illness in patients who are previously immune-compromised. *P. aeruginosa* is isolated in almost 99% of all cases of bacteræmia, most commonly from keratitis of the ocular cornea, and from infections associated with burn wounds. It is also commonly found in sputum secreted from cystic fibrosis patients [69]. An image of a single *P. aeruginosa* cell may be seen in Figure 1.1.3.

P. aeruginosa is one of the most widely studied pathogens on record, owing to its ubiquity in the environment, as well as its versatility in adapting to a number of different surroundings [47,88]. *P. aeruginosa* possesses one of the largest microbial genomes, with a genetic sequence that is highly conserved (>90%) between strains [93,108]. This conservation includes genetic

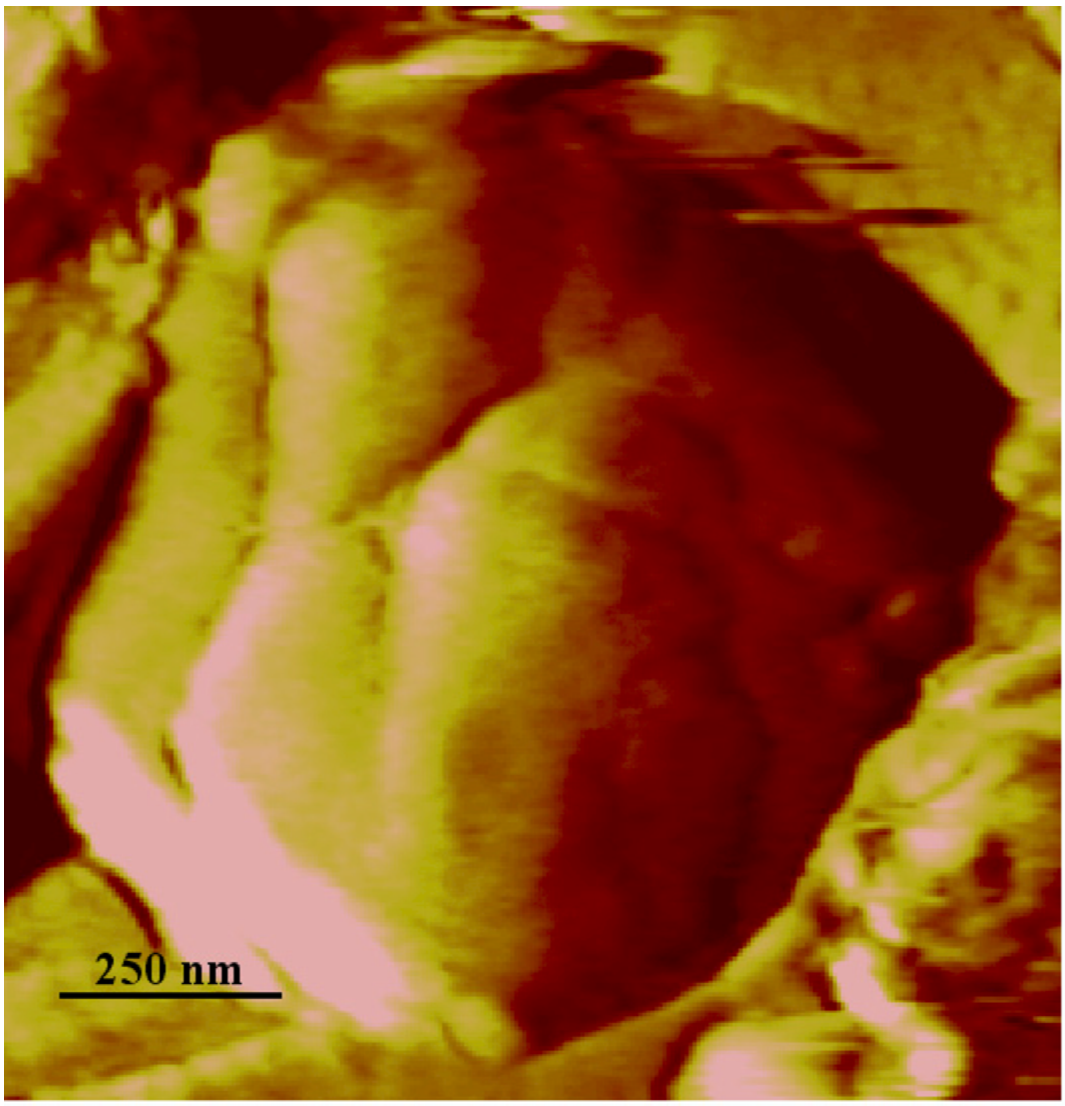

Figure 1.1.2: TappingMode^{TM} AFM image of *S. epidermidis* Clinical Isolate under 100 mM MES buffer (pH = 7.1). The vertical scale of the image is 1000 nm.

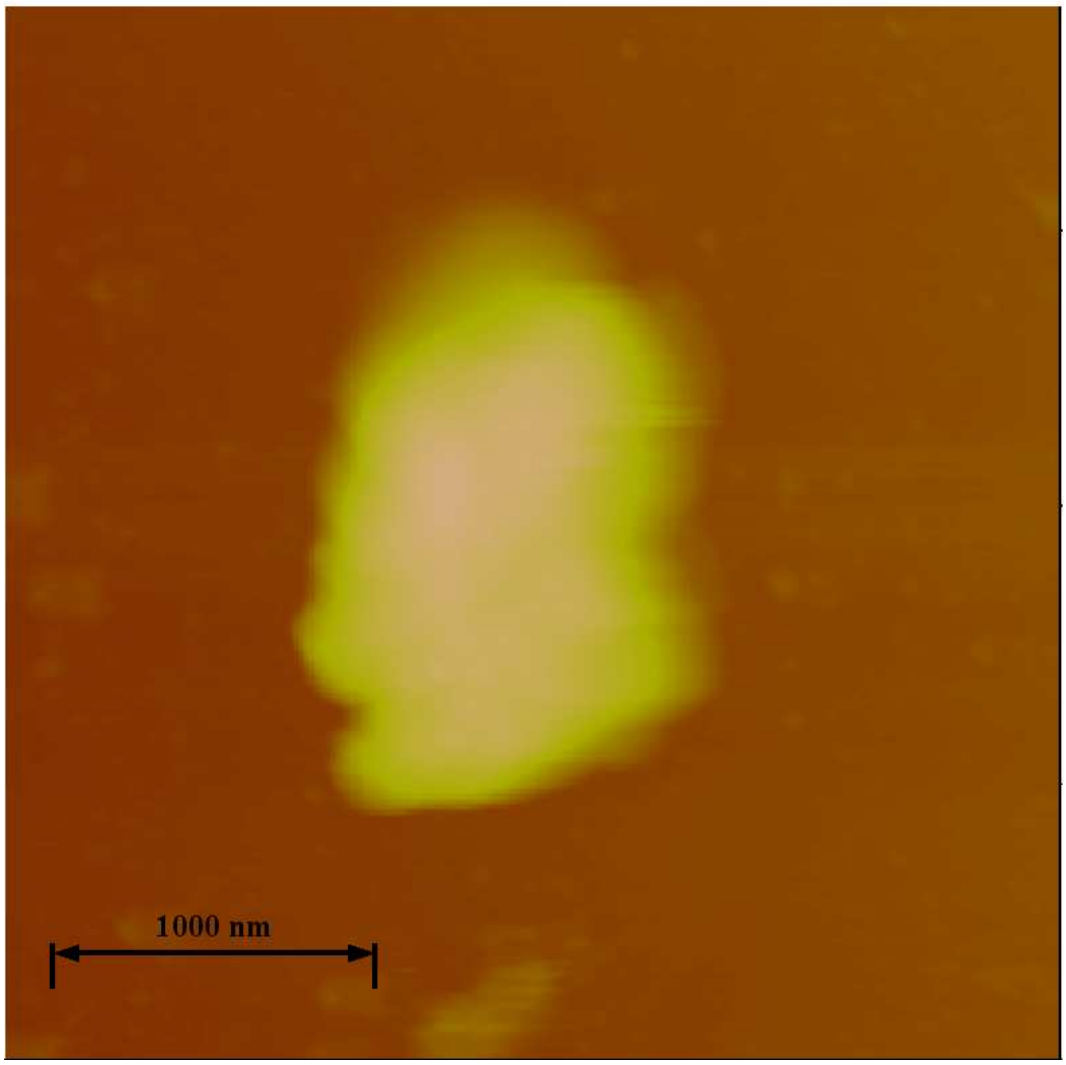

Figure 1.1.3: TappingMode^{TM} AFM image of *P. aeruginosa* ATCC 10145 under distilled, deionized water. The vertical scale of the image is 1000 nm.

information controlling production of a number of different virulence factors and regulatory systems (*e.g.,* antimicrobial pumps, which transport antigenic compounds out of the cell). Further, the genome contains large islands capable of integrating new genetic data through horizontal transfer. While horizontal gene transfer is common in many bacterial strains, *P. aeruginosa* shows a distinct talent for this difficult process, frequently obtaining genetic information from its own and widely different microbial species.

P. aeruginosa's versatility and adaptability extend into its abilities to cause infection [69]. Virulence factors include pili, flagella, lipopolysaccharides (LPS), exotoxins, exoenzymes, and a number of other mechanisms by which this organism inflicts injury upon medical patients. These factors are all related to genes expressed solely during the sessile biofilm-phase [69]. Understanding the adhesion mechanisms of this microbe at the scale these mechanisms occur would greatly benefit many thousands of medical patients each year.

Candida parapsilosis

For many years, *Candida parapsilosis* has been a relatively rare isolate from nosocomial infections [75, 87]. Recent studies, however, show and increased frequency of *C. parapsilosis* infections, and the microbe is exceeded in isolation frequency only by *C. albicans* in hospital-acquired fungal infections. An image of *C. parapsilosis* may be seen in Figure 1.1.4.

C. parapsilosis is also an opportunistic pathogen, and has a remarkable ability for horizontal transmission [68,105]. This refers to the ease with which the cells may be transmitted between host organisms. In the case of *C. parapsilosis*, horizontal transmission is a very common and very rapid mode of cellular dissemination from patient to patient. This microbe is commonly found in infections of medical implants, most especially those of implantable central venous catheters and bronchoscopes [63, 80].

The increasing isolation of *C. parapsilosis* among medical fungæmiæ, its ease of transmission, and extreme virulence in medical infections dictate that this microbe must be understood. Information regarding its affinity for different biomaterial surfaces will increase the body of knowledge available for this organism, and will aid in finding methods to circumvent its adhesive and infective capabilities.

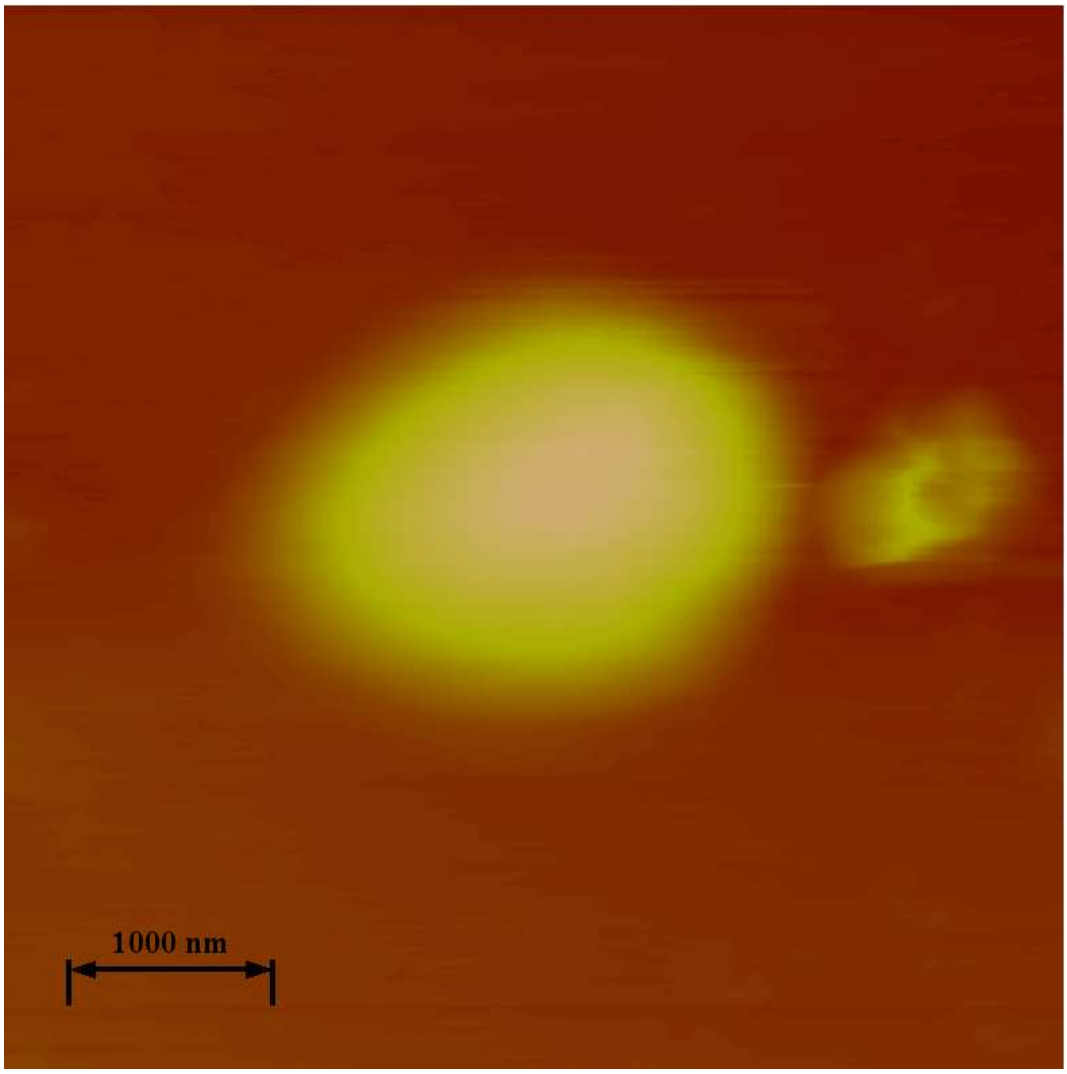

Figure 1.1.4: TappingMode^{TM} AFM image of *C. parapsilosis* ATCC 90018 under distilled, deionized water. The vertical scale of the image is 1500 nm.

1.1.4 Relevant Materials

Many of the devices implanted into medical patients contain polymeric materials [53]. From a thermodynamic standpoint, most of these are hydrophobic in nature, since hydrophobic materials tend to be more biocompatible and biostable. Many hydrophilic materials, including oxidized plastics and metals, show sufficient biostability, but do not possess mechanical properties conducive to soft-tissue implantation, and often degrade into toxic substances during protracted implantation. A list of several common biomaterials, and their uses, may be seen in Table 1.1.4. Each of these materials is susceptible to microbial infection. The exact probability that an implant will become infected, however, is dependent upon a number of factors, including the number and type(s) of microbes present, the exact chemical composition of the surrounding media (*e.g.,* inside a blood vessel or the urinary tract), and the patient's overall health. As such, no quantitative data may be given at this point as to how likely, in a broad sense, each material is to be infected.

While excellent materials, in that they perform their designed task *in vivo*, and do not themselves cause additional harm to the patient, they are adequate sites to which microbes may bind, form biofilms, and release virulence factors [14]. This is predominantly due to similarities (*viz.*, hydrophobicity) between molecules in the environment, the microbial colonisers and the biomaterial substrate. Biological molecules (*e.g.,* proteins) physisorbed to the materials provide a conditioning film which makes the surface even more welcoming to microbes [90, 94].

As a solution to this problem, designers have introduced implant devices which are coated or impregnated with antimicrobial agents [52]. This provides a high implant surface concentration of the antimicrobial, and a chemical gradient as the agent diffuses into the surroundings. Given the heterogeneity of the implantation environment (*e.g.,* blood and other fluids contacting the devices, differences in patient chemistry), however, it is not likely that all patients will receive a sufficient systemic dose of the agent to kill all cells present [36, 64]. And, if this dose is achieved, it is very likely that beneficial microbes will be killed as well [64].

Table 1.1.2: A list of commonly used medical device materials and their applications (Adapted from [47]).

Poly(dimethyl siloxane)		(PDMS)
Pacemakers	Arteriovenous shunts	Intravascular devices
Mammary prostheses	Voice prostheses	Urological catheters
Cerebrospinal fluid shunts	Peritoneal dialysis catheters	
Polyethylene		(PET)
Cerebrospinal fluid shunts	Intravascular devices	Orthopedic implants
Poly(ethylene terephthalate)		(PETE)
Vascular grafts	Arteriovenous shunts	Intravascular devices
Left ventricular assist devices	Prosthetic heart valves	Peritoneal dialysis catheters
Total artificial heart	Mammary prostheses	
Poly(methyl methacrylate)		(PMMA)
Bone cement	Cranioplastic implants	Intraocular artificial lens
Polypropylene		(PP)
Abdominal wall prostheses	Intravascular devices	
Poly(tetrafluoro ethylene)		(PTFE)
Vascular grafts	Arteriovenous shunts	Intravascular devices
Abdominal wall prostheses		
Polyurethane		(PU)
Left ventricular assist devices	Total artifical heart	Intravascular devices
Mammary prostheses	Pacemakers	

1.2 Atomic Force Microscopy

1.2.1 The Origins of Atomic Force Microscopy

In 1986, the Nobel Prize for Physics was divided amongst three scientists. The first, Dr. Ernst Ruska of the Technical University of Berlin, was recognised for his invention of the first electron microscope. The other two scientists, Drs. Gerd Binnig and Heinrich Rohrer of IBM's Zurich Research Laboratories, received their awards for the invention of the scanning tunneling microscope (STM). This device, described in [11, 12], relies upon a very sharp tip made of a conducting material. The tip is brought very close to the sample surface, and a tunneling voltage is applied to the tip. As the tip is raster-scanned across the sample, variations in the tunneling current at constant voltage appear as the tip-sample separation distance changes. These variations are used as the error signal in a feedback loop, which controls a piezoactuator tube. Since the tunneling current is strongly dependent upon the tip-sample separation, deviations from the setpoint current instruct the piezoactuator tube to move the tip vertically up or down, maintaining a constant tunneling current, and, therefore, a constant tip-sample separation. The error signal is also used to create topographical images of the samples at extremely small lateral resolutions (≈ 2 Å in 1982).

While both of the above devices were revolutionary, they did have shortcomings. The STM, which relies upon the error signal from the tunneling current, requires that both tip and sample be able to conduct electricity. With the increasing importance of the semiconductor industry in the early 1980s, a device capable of achieving similar resolutions on semiconducting and insulating materials was essential to the progress of microchip fabrication.

So, in the same year he received a Nobel Prize for developing the STM, Dr. Binnig, along with Dr. Christophe Gerber (IBM Zurich) and Dr. Calvin Quate (Stanford University), reported the invention of the Atomic Force Microscope (AFM) [10]. The principle function of the AFM was to achieve the lateral resolutions comparable to those seen using the STM, while allowing for the examination of nonconductive surfaces in a nondestructive manner [10]. Further development of the AFM has allowed for nanometer lateral resolution in topographical imaging of samples [25]. And, under high-vacuum conditions, resolutions at

the atomic scale are possible [91].

While the topographical imaging functionality of the instrument is valuable, the AFM has another functionality which is of much greater importance. Namely, the AFM is able to measure the strength of an interaction between its probe and the substrate material. Similarly to the STM, the AFM utilizes a proportional-integral feedback loop to control the motion of the piezoactuator tube in three dimensions. The exact methodology applicable to the AFM control loop is described in detail below (1.2.2), but a brief, qualitative description will follow here. As described above, the error signal for the STM feedback loop is provided by variations in tunneling current as the probe is raster-scanned across the same surface. In the case of AFM, where we do not necessarily have a difference in electrical potential, the error signal arises from the deflection of the probe assembly as it moves in response to features on the sample surface. This deflection is captured by reflecting a laser beam from the back of the probe into a detector, which measures the voltage change as the laser moves across its surface.

If the horizontal raster motion is stopped, then the error signal arising from cantilever deflection represents motion in the vertical direction only. Applying a voltage ramp to the piezoactuator then displaces the probe downwards, into contact with the sample, and then pulls the probe back to its initial position. By recording the deflection of the cantilever across this ramp, a 1-D profile of the tip's interaction as it approaches to, contacts with, and retracts from the sample surface is generated. Applying equilbrium relationships between deflection and force (*e.g.,* Hooke's Law), the deflection profile may then be translated into a map of the force of an interaction across some distance associated with the voltage ramp. These data may be used to determine physicochemical and physicomechanical properties of the samples [22–24, 60, 98], including hardness, stiffness and adhesive/tensile strength. In conjunction with appropriate mathematical models, so-called force cycles may be used to determine the relative importance of electrostatic, dispersion, London-van der Waals and electromagnetic forces in producing the interaction profile [25].

AFM in Biological Systems

While specifically designed for applications to the semiconductor and electronics industries, the AFM has been applied to a variety of fields, including biology and microbiology. Several examples of these applications include: the measurement of atomic bond rupture-forces between organosilane monolayers [106]; the study of the physicochemical properties of microbial surface topographies [43]; characterisation of lectin-carbohydrate interactions at the nanometer scale [99]; measurement of interaction forces between complementary DNA strands [61]; and characterisation of bacterial-biomaterial interactions via mechanically or chemically modified probes [78, 83, 84].

In situ Probe Modifications

Design and fabrication of AFM probes is a very precise process, but is performed using a very small variety of materials. Probes are usually fabricated from silicon or silicon nitride, which are relatively inert materials with predictable mechanical properties. In many cases, however, the relevance of the interaction forces between a substrate and silicon or silicon nitride is of only academic interest. To facilitate the study of a wider range of systems, it is therefore necessary to purchase or fabricate modified probes. As-received probes have been coated with a variety of soil minerals [66, 67], biomaterials [46, 84] and relevant single molecules, including fibronectin [56], DNA [61] and lectins [99]. Further Bowen *et al.* were the first to functionalize the AFM tip with a whole microbial spore [16,17]. Tipless cantilevers may be fitted with silica [97] or polystyrene [65] beads, and similar beads have been used as a binding platform for microbial lawns [78, 83]. Each of these very different applications of the base AFM system show the versatility of the instrument, as well as its applicability to a wide variety of industrial, environmental and biomedical applications.

1.2.2 Basic Theory of Atomic Force Microscopy

The AFM is, most simply, a hybrid of IBM's STM and a stylus profilometer. The latter uses a sharp cantilever-mounted probe affixed with a mirror to magnify surface features onto photographic paper. A light source is shined into the mirror, which reflects onto the

paper. As the cantilever scans across the surface, it deflects as it interacts with various surface features. Deflections are then translated to the photographic paper by changes in the intensity of the light from the mirror. Depending on the placement of the photographic paper in relation to the sample and the sharpness and compliance of the cantilever, the stylus profilometer is capable of resolutions up to 1000X [10]. Combining this principle with the STM, however, allowed for resolutions at the atomic scale.

A generalised schematic of the AFM is shown in Figure 1.2.1. A solid-state laser diode generates a beam, which passes through the scanner head. The beam reflects from the back of the cantilever, into a split photodiode sensor. A sharp probe is affixed to the underside of the cantilever, which tracks height/interaction force differences in the sample surface, causing the cantilever to deflect and changing the incident angle of the laser on the photodiode. Data recorded by the photodiode is then translated into deflection voltage and piezoactuator displacement, allowing the computer software to maintain a feedback loop based on constant cantilever deflection/interaction force (Contact mode) or constant cantilever oscillation amplitude (Intermittent contact mode[1]), in which cantilever is displaced laterally at the peak of the oscillation. Intermittent contact affords several benefits over contact mode, in that it allows for increased lateral resolution of soft and/or hydrated samples, and decreased damage to the sample surface. It has been shown, however, that use of intermittent contact with compliant samples may introduce artifacts into the collected data [20], as the amplitude signal is likely to be damped as it rapidly indents into the sample. While both common operational modes afford different benefits, it is left to the judgment of the researcher as to which is more appropriate to the system under analysis.

During operation, the head raster-scans the sample surface. Features on the surface, such as microbial cells, cause changes in the cantilever deflection, altering the input signal to the feedback loop. Depending on the AFM operational mode (contact or intermittent contact), the feedback loop is adjusted back to the setpoint by means of a series of gains.

The data collected from the cantilever deflection may also be used to generate plots of deflection voltage versus separation distance. As an example, Figure 1.2.2 shows a force

[1] "TappingMode^{TM}," a specific implmentation of intermittent contact mode, is a trademark of Digital Instruments/Veeco Metrology Group, Santa Barbara, CA, USA, and is used only in conjunction with DI/VMG AFM systems

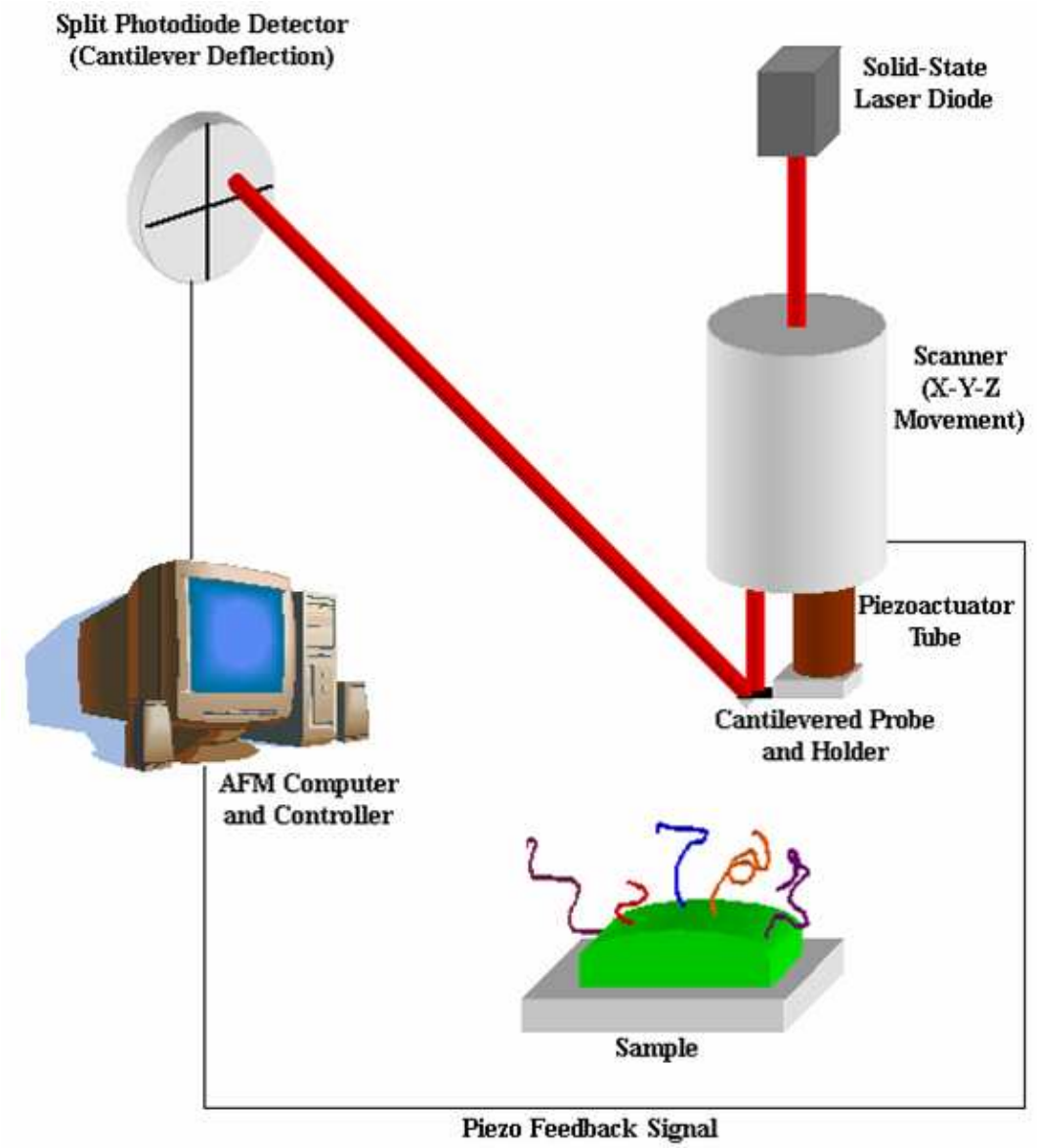

Figure 1.2.1: Schematic diagram of AFM analysis of a bacterial surface. The laser reflects from the metal-coated cantilever, into the photodiode detector. In TappingMode^{TM}, the cantilever oscillation is maintained at a constant amplitude by the movement of a piezoactuator tube. Changes in the angle of the incident light on the detector register as potential changes, which enter the controller feedback loop (essentially a PI controller), and adjust the position of the piezoactuator. In Force Mode, these data may be used to obtain a plot of detector voltage versus piezoactuator position, which may be converted into a plot of force versus separation. Adapted from [57]

cycle for a cantilever interacting with a "cell". Relative cantilever position is noted in both the curve and the inset of the figure.

At position A, the probe is far from the cell surface, as is indicated by the schematic, and by the lack of any change in force with separation distance in the curve. As the probe comes closer to the cell, however, it begins to interact with the microbial polymer brush and cell wall (Position B). A positive value of force indicates a repulsive interaction, meaning the cantilever is deflected upwards by the physical (cell wall elasticity, polymer rigidity) and/or chemical (electrostatic or steric interactions) properties of the cell. Position C represents the region of rigid contact, where the probe deflects linearly with piezoactuator displacement. As the cantilever is pulled back from the cell surface, it is possible that surface structures have sorbed to the probe during contact. These structures extend from the surface and, at some point in the retraction, desorb from the probe. These pull-off events are represented by negative forces (adhesions) in the force cycle.

1.2.3 Calibration of the Atomic Force Microscope

The AFM is a highly sensitive tool, capable of analysing a wide variety of substrates under as wide a variety of experimental conditions. Regardless of its capabilities, however, the AFM must still be operated with a degree of expertise to produce credible and reproducible results. Of primary importance to this reproducibility is knowledge of the state of the machine as it operates, which is obtained through careful calibration of the instrument. Specifically, the investigator must measure three quantities (*e.g.,* the AFM laser wavelength, the ratio between actual and software-reported piezoactuator displacement, and the spring constant of the cantilevered probe) before measurements of height, force and separation may be reported and compared to other experiments with any sense of precision. Additionally, the probe radius of curvature has a profound effect on processing and interpretation of AFM data, in terms of the degree of dilation present in topographical images, the available contact area in a force-separation interaction, and the error propagated when using the radius as a parameter in mathematical models.

The following sections briefly describe each parameter to be measured during instrument calibration. Chapter 4 provides a broader description of the techniques involved in calibrat-

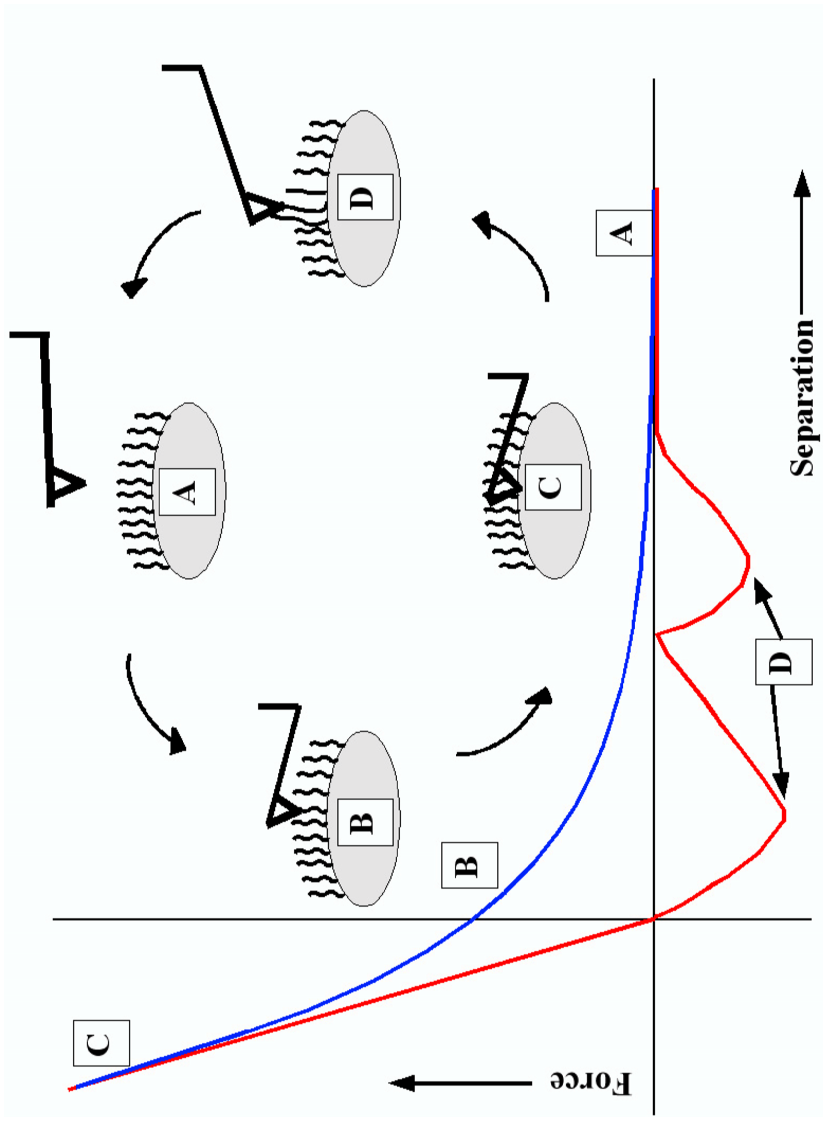

Figure 1.2.2: Schematic of relative cantilever position during force-separation measurements. The blue curve represents the approach or decreasing-separation portion of the cycle, while the red indicates the retracting portion. At position (A), the probe is far from the sample surface, and remains in its equilibrium position. At (B), the cantilever begins to detect the brush, and deflects upwards as a result of electrostatic and steric hindrance, shown as repulsive force in the recorded data. (C) shows the tip in contact with a surface as stiff as the cantilever, demonstrated by a linear response between force and separation. As the cantilever is retracted from the surface, as in (D), exopolymers sorb to the tip. These cause the cantilever to deflect downwards, indicating adhesive interactions. Local minima arise in the retraction curve as these exopolymers desorb from the tip.

ing an AFM, and displays some of the ramifications of doing so. The techniques may also be seen in more detail in [21, 45, 96, 97].

Measurement of the AFM Laser Wavelength

The nominal wavelength of the Dimension 3100 laser is 670 nm, as read from the side of the scanner head. However, the actual wavelength may vary from the manufacturer's specification, and may also change over time as the material (in this case, the solid-state laser diode) ages. Determination of the actual wavelength is accomplished using a diffraction grating, shown schematically in Figure 1.2.3. The laser is activated with the holder removed and the scanner locked in the AFM mounting bracket. A 90° prism is placed directly below the scanner, deflecting the laser beam through a confocal lens. This serves to focus the beam before it passes through a diffraction grating of known slit spacing. A screen is placed after the diffraction grating, which is moved backwards and forwards until the laser diffraction pattern appears and is well-focused.

After measuring the distance between the primary (brightest) laser spot and those adjacent to it, the distance between the diffraction grating and the screen is also recorded. According to the geometry of the system, we define the wavelength of the laser, λ_L, as:

$$\lambda_L = \frac{yd}{mH} \tag{1.1}$$

where H is the distance between the grating and the screen, y the distance between the two spots in the diffraction pattern, d the spacing coefficient of the diffraction grating, and m an integer multiplying the wavelength of the laser. A schematic of the system and the relevant geometric parameters involved in the calculation may be seen in Figure 1.2.4[2].

Calculation of the AFM Piezoactuator Stepheight

With the laser diode wavelength known, it is now possible to define the correction factor between the software-measured values of separation and the actual piezoactuator stepheight.

[2]The recent installation of an optical network on the Worcester Polytechnic Institute campus has allowed the measurement of the laser wavelength with much greater accuracy than the geometric method described. By focusing the laser on one end of a fiberoptic cable and connecting the opposite end of the cable to an optical network port, the laser light may be passed through the network to a spectrum analyser and processed.

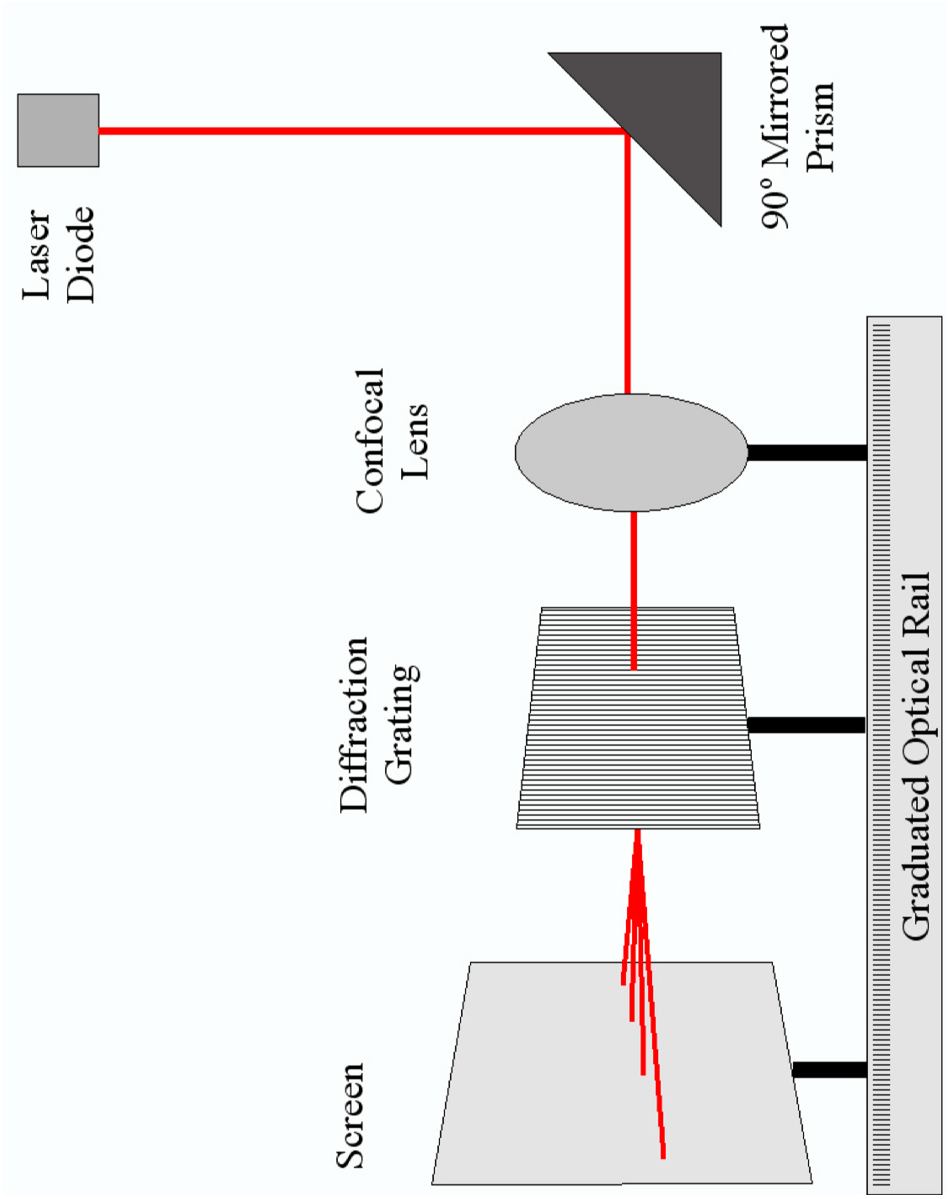

Figure 1.2.3: Schematic of the equipment used to determine the wavelength of the AFM laser diode.

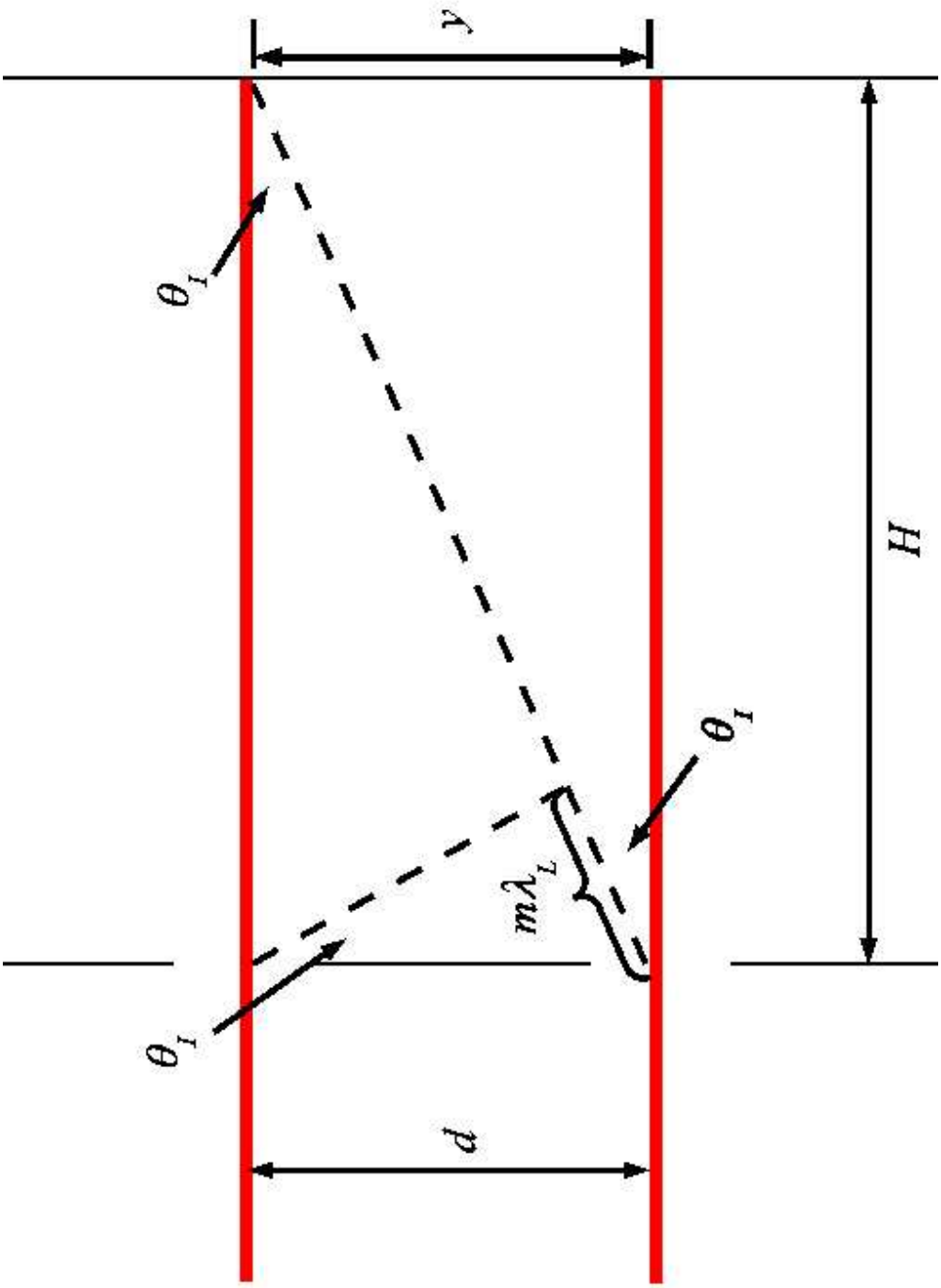

Figure 1.2.4: Schematic describing the geometric problem to be solved when calculating the AFM laser diode wavelength.

This is accomplished by a basic interferometric technique described by Burnham *et al.* [21], and adapted to the Dimension 3100 as described in [45] and Chapter 4 of this document.

Calculation of the AFM Probe Radius of Curvature

The probe radius of curvature can have significant effects upon topographical and force-separation data collected from the AFM. In terms of the former, a tip having a larger radius reduces the effective resolution of the instrument, as the probe is not able to track the surface as accurately, were it sharper. For the latter, a tip having a small radius contacts the surface with a smaller projected area, allowing for more accurate characterisation of the force-separation interactions in that area. Additionally, the probe radius of curvature is a common parameter in many mathematical models applicable to AFM systems. Variation of the actual value from that used in the model by even a small amount may have significant effects on the ability of the researcher to compare their data to model predictions. The technique of determining the probe radius was adapted from [97] and modified to account for a paraboloid, rather than spherical, tip profile. The methodology is described in detail in [45] and Chapter 4 of this document.

Measurement of the AFM Cantilever Spring Constant

In the microfabrication of the AFM cantilevers, regardless of their geometry, the least controllable parameter is the thickness of the cantilever. This may vary significantly, even from one end of a row to another in the same wafer. The spring constant, which relates the deflection of the cantilever to the force of an interaction, scales with the cube of the cantilever thickness. Therefore, to accurately characterise the magnitude of an interaction force, the value of the spring constant must be accurately measured. Several methods, based on the geometry [32, 86] or the thermal properties [26, 55] of the cantilever, have been developed to determine the cantilever spring constant. Geometric methods, however, do not accurately account for heterogeneities in the silicon or silicon nitride making up the cantilever, nor do they measure the effect of the metal backing layer, which is normally applied to increase the reflectivity of the beam, and therefore amplify the signal reaching the photodiode detector. Therefore, thermal methods are preferable, as they are geometry- and material-independent,

and rely on fundamental physical properties of the cantilever.

The thermal method chosen to quantify the spring constant is described in [21] and adapted to the Dimension 3100 according to [45]. This technique is described in detail in Chapter 4.

1.2.4 Force Curve Analysis

One of the most important capabilities of the AFM is the ability to quantify the interaction forces between the probe and sample. The so-called "force curve" is commonly discretised into the extending or approaching portion, in which the tip-sample distance is decreased as the piezoactuator tube displaces downwards, and the retracting portion, where the tip-sample distance increases.

The term "force curve," however, is a misnomer, as the AFM is not actually capable of measuring and reporting either force or tip-sample separation. The following sections describe the methodology used to convert from the raw AFM data to the force-separation curve. Discussion also follows regarding methods by which these data may be interpreted.

The Raw Data

"Raw" AFM data are recorded as the change in potential across a photodiode detector as the cantilever deflects, relative to its rest position. This change is further correlated to the ramp size, which is a voltage applied to the piezoactuator tube within a fixed scan rate. The ramp size is equivalent to the vertical piezoactuator displacement, and defines the horizontal coordinate of the Cartesian plane. By plotting cantilever deflection against piezoactuator displacement in Cartesian coordinates, we have a graphical representation of the extension-contact-retraction profile. This profile may be seen in Figure 1.2.5.

Conversion of Deflection-Displacement to Force-Separation

While representative of the probe-sample interaction, several processing steps are still necessary to generate the final force curve. Namely, these data do not have a specific coordinate system which describes the magnitude of the interaction in physical space. Also, the data

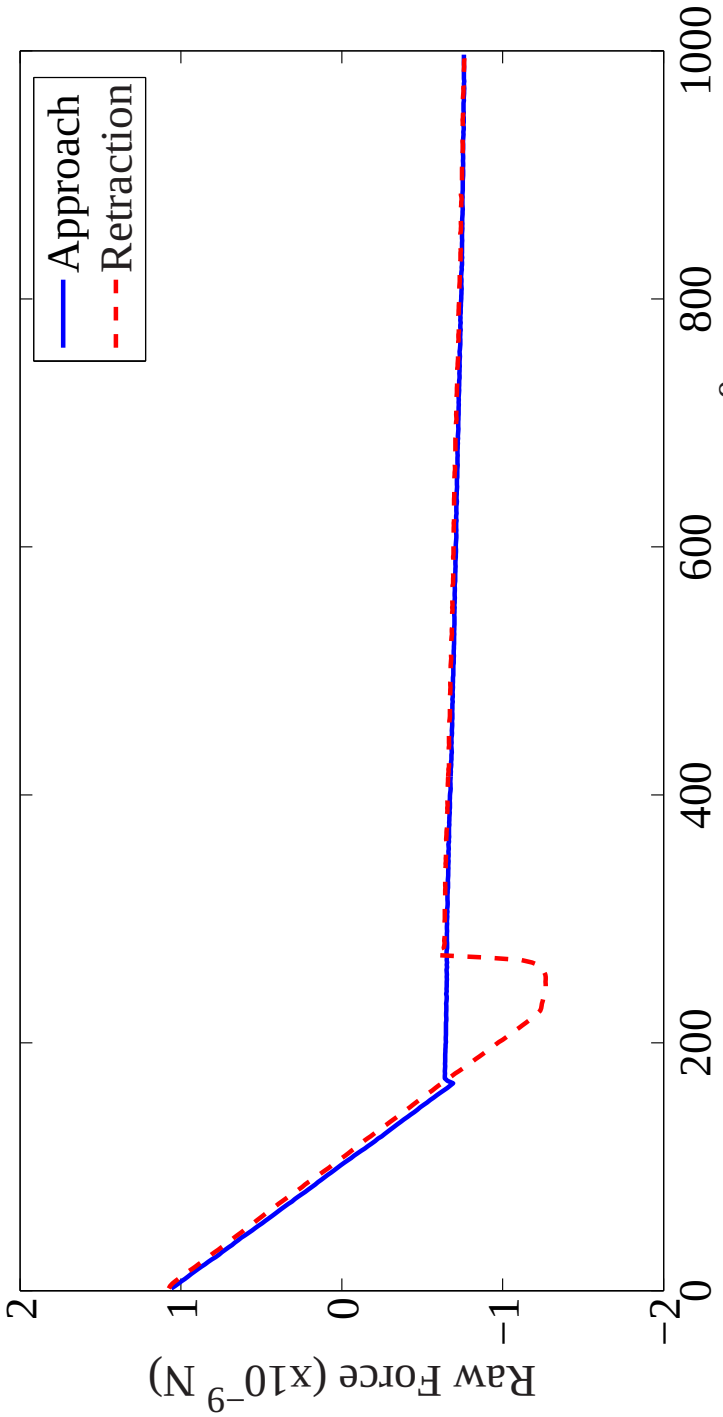

Figure 1.2.5: Raw force-displacement data as collected from the AFM.

at high loading forces are a convolution of the cantilever deflection resulting from the interaction, and from the piezoactuator pressing down on the fixed end of the cantilever. To define a point of zero separation, it is necessary to assume that the substrate is stiffer than the cantilever, and that the relationship between cantilever deflection and piezoactuator displacement is linear, within this high-load region. To satisfy these two assumptions, the high-load or constant compliance region must be linear and vertical, which is accomplished by subtracting the deflection of the cantilever while in rigid contact with the surface from the data set. The algebraic difference between the raw data and deflection while in firm contact are subtracted mathematically from all points in the data set, but show the most significant influence in the constant compliance region. This is demonstrated in Figure 1.2.6.

It should be noted that very compliant substrates, *i.e.*, those having very small values for the Young's modulus, may prevent the user from reaching the constant compliance region within the capabilities of the instrument. These provide additional complications in analysing the collected data, but are not treated explicitly within this research.

Now that the data include only the probe-sample interaction across the voltage ramp, and superfluous data from the constant compliance region have been removed, it is possible to convert from the deflection of the cantilever to the force of the interaction according to Hooke's Law [1]. This corollary defines the force (F) necessary to displace a linear spring at stresses below the spring's yield strength as being proportional to the displacement of the spring (h) and a constant (k_c). Mathematically, this is formulated as

$$F = -k_c h \tag{1.2}$$

By multiplying the corrected deflection from our data set above by the spring constant of the cantilever, we calculate the force necessary to restore the spring to its original position, or, by reversing the sign of Equation 1.2, the force exerted upon the cantilever by the surface as the lever deforms. After this step, it is possible to define a coordinate system for the data, in terms of reference points describing zero force and zero separation.

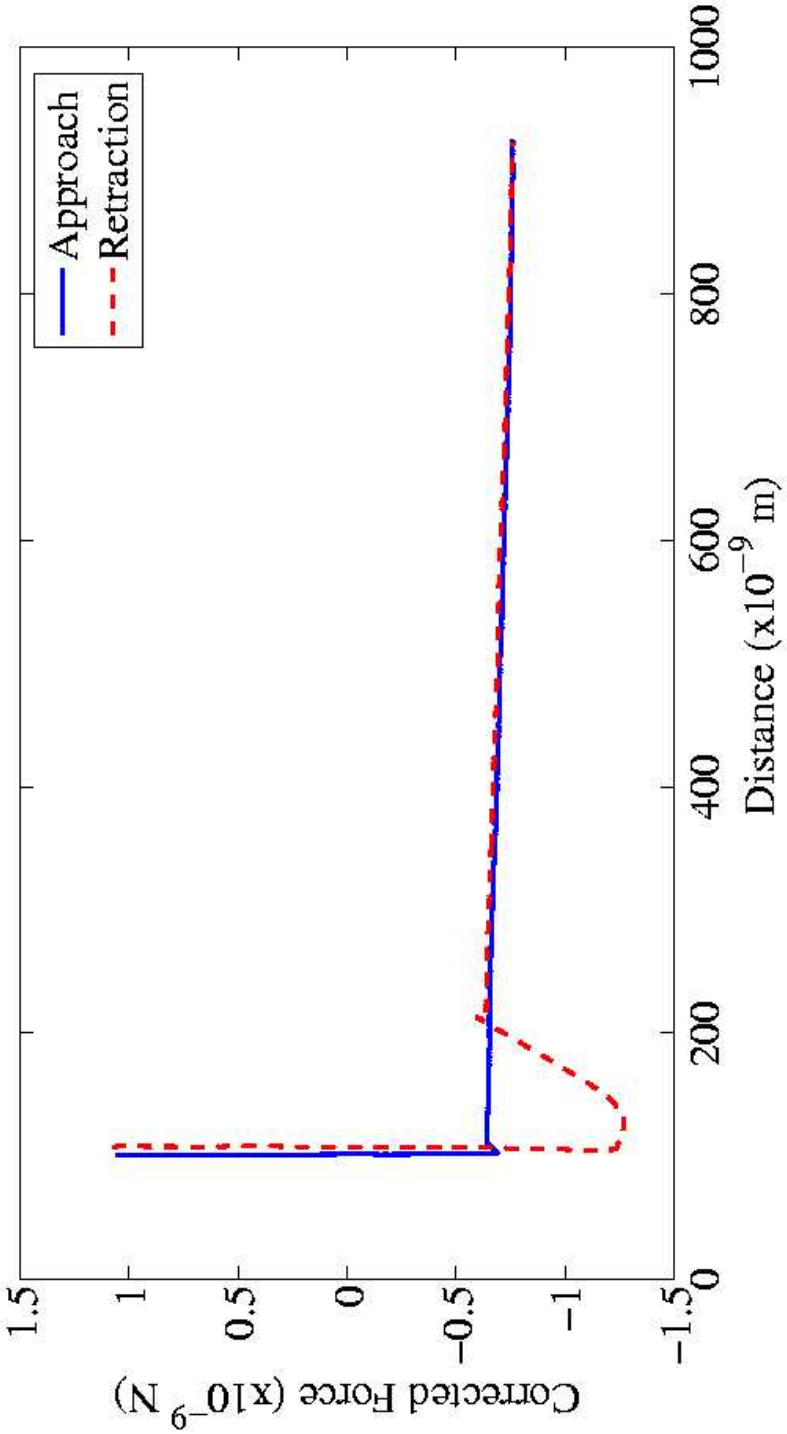

Figure 1.2.6: Force-distance curve which has been corrected by subtracting deflection while in stiff contact with the substrate from all data points. At small separations, where this deflection is large, the constant compliance region is vertical. At larger separation values, this deflection is negligible, and does not significantly affect the values of the recorded data.

Assigning a Coordinate System - The Zero of Force

The zero of force is the more easily definable of the two. At large separations, beyond the range of the tip-sample interactions, the force curve is essentially flat. This horizontal region is then defined as the zero of force, around which all attractive and repulsive interactions occur. Values of the force are changed such that the horizontal portion of the curve rests upon the horizontal axis. This is shown in Figure 1.2.7.

Assigning a Coordinate System - The Zero of Separation

More complicated in its definition is the zero of separation, or, in other words, the location of the sample surface. The complications in this definition arise from the different interactions which occur in the approach portion of the force cycles. To generalise, we expect to see either purely attractive (negative forces) or purely repulsive (positive forces) behaviour as separation distance decreases. In general, to satisfy the fundamental assumption that a force measurement is a closed thermodynamic cycle, which is inherent in using Hooke's Law to convert between deflection and force, it is agreed that the constant compliance regions of both the approach and the retraction curves must overlap. Therefore, the zero of separation is commonly defined according to the features of the approach curve, and the retraction curve is subsequently translated horizontally to satisfy the requirements of the equilibrium assumption.

Zero Separation - Attraction in the Approach Curve Attractive interactions on approach are common amongst stiff, clean sample surfaces, such as gold, glass or mica. They may also occur as the result of opposite-charge interactions between the tip and structures on the sample surface, or as two complementary molecules interact. In the case of attractive interactions, zero separation is defined as the minimum of the approach interaction, according to [25]. Other definitions may also be applied, as in [41], where the constant compliance region is aligned to the force axis, or [23], where the inflection point in the advancing section of the attractive interaction (*viz.*, where the first spatial derivative of the data changes sign from positive to negative) is defined as zero separation. All cases use a specific reference point/region from the data set in their definitions, although those presented in [23] and [25]

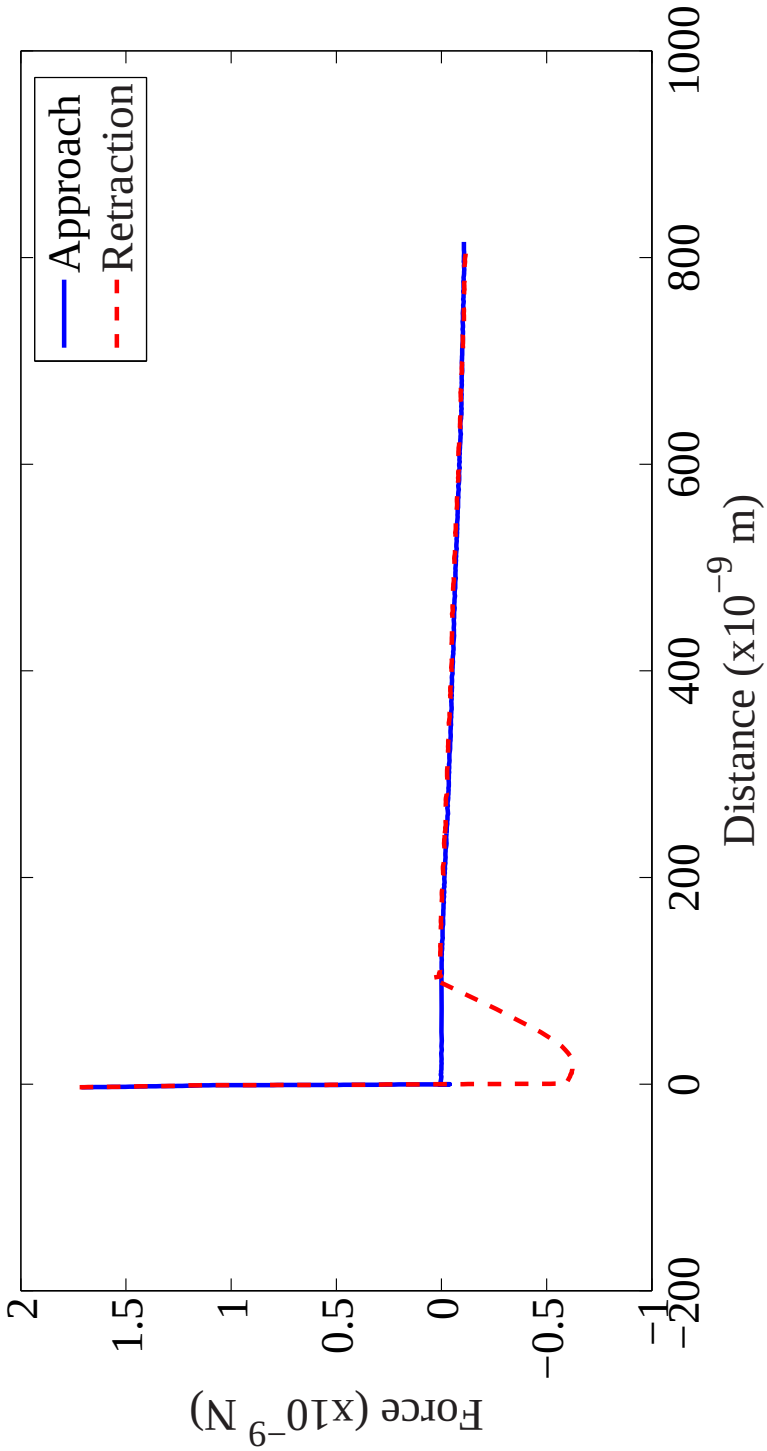

Figure 1.2.7: Corrected force-distance curve where the zero of force has been defined according to the horizontal, large-separation portions of the curves.

have rigorous mathematical backgrounds. The case presented in [41], under the specific circumstances of soft samples, can result in repulsive forces in the retraction curves. This behaviour is physically unlikely, as it requires the sample surface move vertically at a velocity greater than that of the piezoactuator's displacement away from the surface. As such, the methods from [23, 25] tend to be more accurate.

Zero Separation - Repulsion in the Approach Curve In the cases of like-charge interactions and interactions with microbial polymer brushes, there is usually no attractive interaction on approach [3,4]. As such, the definition of zero separation is much less straightforward. In fact, several researchers would argue that the definition of zero separation for a surface coated with a polymer brush does not exist. This is due to the fact that it is impossible to actually reach the surface, since the polymer brush may not be compressed to zero thickness. Commonly, researchers will define zero separation according to the linear constant compliance region, as this is the only reference point available at small values of separation. However, as in the case of [41], positive retraction forces may arise, leading to a physical impossibility of a vertically mobile sample. While a useful definition for zero separation in the cases of brushed surfaces is not widely available, a new model is put forward in Chapter 7, in which mathematical methods are used to define the point of zero separation.

Data Interpretation - The Approach Curve

Approach curves allow the researcher to examine the interaction profile as the probe-sample distance decreases. Several mathematical models (*e.g.,* the DLVO theory of colloid stability [39, 103] and the polymer-brush steric model [6, 27]) have been formulated for this physical situation, and many have been applied to the approach interactions recorded by the AFM. Specifically, the DLVO theory allows the researcher to characterise the relative importance of London-van der Waals and electrostatic forces at short separation distances. The steric model provides information on the length and density of polymers grafted to a sample surface. Qualitatively, the curves reveal the gross characteristics of a probe-sample interaction, *viz.*, whether the probe is attracted to or repelled from the sample surface.

Data Interpretation - The Retraction Curve

Retraction curves describe the adhesive strength of one or more interactions as the tip is pulled away from the area of contact. Adhesive events appear as minima in the data set, as in 1.2.7. Specifically for polymeric/microbial systems, it is possible to record the distribution of the minima in terms of the pull-off distance and pull-off force, which are related to the strength of polymers sorbed to the probe. Pull-off points indicate the coordinates at which desorption occurs, and provide information on the length, strength and flexibility of the sorbed molecules.

Retraction curves tend to be more variable than approach curves, as the interactions are dependent on the number and location of sorbed molecules [3,4]. The distribution of pull-off distances and forces may be recorded for a representative population of interactions, and statistical analysis performed to quantify the characteristics of the distribution. For example, mathematical models such as the Freely-Jointed Chain and Wormlike Chain theories (discussed in [2]) provide information on polymer elasticity and equilibrium-state conformation (*e.g.,* polymer contour length) based on the distribution of pull-off events in the retraction curves.

1.3 Mathematical Modeling of AFM Data

The data contained in force-distance curves are the product of multiple discrete forces acting simultaneously as the AFM probe and sample interact. Individual contributions of these forces may be modeled mathematically, assuming that these forces are superposable. Figure 1.3.1 demonstrates this phenomenon of superposed forces (van der Waals, electrostatic and steric interactions) adding to a single observed force-distance interaction.

Each of these separate forces creates some aspect of the interactions recorded with AFM, and must be separately identified and described before the total interaction is fully understood. In the following sections, the problem of quantifying and predicting microbial adhesion to substrata are described. Initially, the "classical" approaches of colloid stability theories are discussed, which are followed by more novel applications of statistical mechanical and fractal mapping models to explaining AFM topographical and force-separation data.

1.3.1 Colloidal Stability of Small Particles (The DLVO Theory)

In suspension, microorganisms are often considered to be colloidal particles, as they are small and do not easily settle out once dispersed. Following this rationale, mathematical models normally applied to colloidal suspensions of particles have been utilised to describe the interactions between microbes and surfaces as their relative separation distance decreases [3, 29]. The most common model used to support this rationale has been the Derjaguin-Landau-Verwey-Overbeek (DLVO) theory of colloid stability.

As an approximation of the long-range interactions between colloidal particles and flat surfaces, Derjaguin and Landau [39] and Verwey and Overbeek [103] formulated a linearisation of the Poisson-Boltzmann equation using the Debye-Hückel approximation (*viz.*, that ions in solution contribute equally within the electrostatic double-layer around two spherical particles). Their separate work led to solvable equations that describe the London-van der Waals and electrostatic interactions between colloidal particles at ranges of tens of nanometers from a particle surface. The linear superposition of these two equations together is known as the "classical" DLVO theory of colloid stability. Additional components describing other forces (*e.g.,* hydration forces, acid-base interactions, etc. . .) have been formulated

Figure 1.3.1: Example of three different energy contributions (London-van der Waals, electrostatic double-layer and steric) towards a total interaction energy profile. Adapted from [29]. Curves shown were generated using the classical DLVO theory [39, 103] and steric scaling [27] models using sphere-sphere geometry. Theoretically, the arithmetic sum of the three energy contributions at each value of position will replicate the total energy profile of an interaction. Generally, they do not, indicating that most interaction forces are the result of additional components (*viz.*, acid-base interactions, hydration forces, etc. . .)

as extensions to the classical theory [101].

Assuming a sphere-sphere systemic geometry, and that electrostatic repulsions (E_E) and London-van der Waals attractions (E_V) may be linearly superposed, the generalised expression for the total interaction energy, E_T, is described by Hogg *et al.* [54] as:

$$E_T = E_E + E_V \tag{1.3}$$

where E_E for the system is given by:

$$\begin{aligned} E_E =& \frac{2\pi a_m a_p N_A}{(a_m + a_p)\kappa^2} \left(\varphi_m^2 + \varphi_p^2\right) \Rightarrow \\ & \Rightarrow \left(\frac{2\varphi_m \varphi_p}{\varphi_m^2 + \varphi_p^2} ln \left[\frac{1 + exp(-\kappa h)}{1 - exp(-\kappa h)} \right] - ln[1 + exp(-2\kappa h)] \right) \end{aligned} \tag{1.4}$$

or, in terms of the force due to electrostatic interactions,

$$\begin{aligned} F_E = \frac{dE_E}{dh} =& \frac{4\pi N_A a_m a_p}{\kappa \left(a_m + a_p\right) \left(e^{-4\kappa h} - 1\right)} \Rightarrow \\ & \Rightarrow \left[2\varphi_m \varphi_p \left(e^{-3\kappa h} + e^{-\kappa h}\right) + \left(\varphi_m^2 + \varphi_p^2\right) \left(e^{-2\kappa h} - e^{-4\kappa h}\right) \right] \end{aligned} \tag{1.5}$$

With a_m and φ_m being the radius and reduced potential of the microbe, respectively, a_p and φ_p the radius of curvature and reduced potential of the cantilever probe, respectively, h the separation distance between the two, and N_A Avogadro's number. The reduced potentials are functions of the microbial and probe surface potentials (ψ_m and ψ_p, respectively), following:

$$\varphi_i = \frac{ze\psi_i}{k_B T} \tag{1.6}$$

where k_B represents the Boltzmann constant, T the absolute temperature, z the bulk valence of ionic species, and e the unit charge of a single electron. κ, the Debye screening length, is

defined as:

$$\kappa = \left(\frac{1}{\varepsilon_0 \varepsilon_R k_B T} \sum_{i=1}^{n} z_i^2 e^2 n_{i,\infty} \right)^{\frac{1}{2}} \tag{1.7}$$

where ε_0 is the dielectric permittivity of a vacuum, ε_R the relative dielectric permittivity of water, and $n_{i,\infty}$ the number concentration of ions in solution. This model is applicable to systems of 1:1 electrolytes with surface potentials less than 60 mV, and assumes that the surface potentials remain constant throughout the approach [54].

The surface potential of the microbe is assumed equal to its zeta potential [89], as calculated from experimental values of electrophoretic mobility and the Smoluchowski Equation, Equation 1.8 [100].

$$\mu_E = \frac{\varepsilon_0 \varepsilon_R \zeta_{Smol}}{\mu_f} \tag{1.8}$$

where μ_E refers to the sample's electrophoretic mobility, ζ_{Smol} the zeta potential and μ_f the fluid viscosity, taken as that of water in many experimental systems.

London-van der Waals interactions between colloidal particles were described by Hamaker [50] in 1937. Further study showed that, at distances greater than a few nanometers, the electromagnetic nature of the interactions had a retarding effect on their magnitude. Gregory [48] described an approximation, based on the work of Overbeek [79] and Casimir and Polder [30], to account for the retarded interactions between a sphere (the AFM probe) and a flat plate (the microbial cell).

$$E_V = -\frac{A a_m a_p}{6h(a_m + a_p)\left(1 + \frac{14h}{\lambda_c}\right)} \tag{1.9}$$

or, in terms of the force due to London-van der Waals interactions,

$$F_V = \frac{dE_V}{dh} = \frac{A\lambda_c a_m a_p \left(28h + \lambda_c\right)}{6h^2 \left(a_m + a_p\right)\left(14h + \lambda_c\right)^2} \tag{1.10}$$

where a_i and h are defined as before, A is the Hamaker constant, describing the dispersion forces between bodies as calculated from the pairwise summation of the polarisability, energy, primary dispersion frequency and number density of atoms in solution according to [101],

and λ_c is the collective decay length of the retarded van der Waals interaction [101], whose value is often taken as 100 nm [48]. The term $1 + 14h/\lambda_c$ is an empirical correction factor, adapted from the work of Schenkel and Kitchener [89], accounting for retardation effects at short distances ($0 < h < (\lambda_c/\pi)$ (31.83 nm) and $h \ll a_p$).

A plot of the total interaction energy and its components against separation distance (*viz.*, Figure 1.3.1 provides a profile describing the approach of one spherical component to another. This is applicable both to modeling a system of a cantilever approaching an immobilised cell, and a planktonic cell approaching a biomaterial or biofilm surface.

Calculation of the Hamaker constant, for use in Equation 1.9 may be related to contact angles on microbial lawns through the van Oss-Chaudhury-Good equation [100–102]:

$$(1 + cos\,[\theta_L])\gamma_L = 2\left(\sqrt{\gamma_M^{LB}\gamma_L^{LW}} + \sqrt{\gamma_M^{+}\gamma_L^{-}} + \sqrt{\gamma_M^{-}\gamma_L^{+}}\right) \tag{1.11}$$

In this equation, θ_L is the contact angle under liquid L, γ_L the total free energy of the liquid, γ_i^{LW} the apolar (Lifshitz-van der Waals) component of the surface free energy, γ_i^{+} the electron-accepting component of the polar (Acid-Base) surface free energy and γ_i^{-} the electron-donating component of the polar surface free energy, where i may be M, denoting the microbe, or L, the liquid. Values of γ_L for a number of liquids have been tabulated [101], and values for water, formamide and diiodomethane were taken for calculation of the microbial free energy components.

van Oss *et al.* have formulated an algebraic method of determining the Hamaker constant based on the apolar component of the microbial surface free energy [101].

$$A = 24\pi l_0^2 \gamma_M^{LW} \tag{1.12}$$

With l_0 being the minimum separation distance between the two contacting bodies. From further work, van Oss determined that the minimum separation distance fell within a range of 1.57 ± 0.09 Å, reducing Equation 1.12 to the Hamaker constant being equal to the product of the constant terms ($1.8585\text{x}10^{-18}$ m^2) and the apolar surface free energy component.

1.3.2 Colloidal Stability of Small, Soft Particles (The Soft-Particle DLVO Theory)

Recent work has shown that the Smoluchowski formulation of electrophoretic mobility overestimates zeta potentials for soft materials, such as bacterial cells [13, 51, 77]. Ohshima *et al.* [13, 77, 95] have formulated a correction to the classical DLVO theory which takes both the ionic strength of the solution and the "softness" of the microbial cells into account when calculating the electrophoretic mobility.

The Ohshima model describes the approximate electrophoretic mobility of soft particles as:

$$\mu_E = \frac{\varepsilon_0 \varepsilon_R}{\mu_f} \frac{\frac{\Psi_0}{K_m} + \frac{\Psi_{Don}}{\lambda}}{\frac{1}{K_m} + \frac{1}{\lambda}} + \frac{eZN}{\mu_f \lambda^2} \tag{1.13}$$

where Ψ_0 represents the surface potential, Ψ_{DON} the Donnan potential of the polymer layer, K_m the Debye-Hückel parameter, Z the valence of ions in the polymers, N the density of charged groups, and λ a softness parameter with units of inverse length. The parameters Ψ_0, Ψ_{DON} and K_m are all functions of ionic strength, shown by [51]:

$$\begin{aligned} \Psi_0 = \frac{k_B T}{ze} \Rightarrow \\ \Rightarrow \left(\ln \left\{ \frac{ZN}{2zn} + \left[\left(\frac{ZN}{2zn} \right)^2 + 1 \right]^{\frac{1}{2}} \right\} + \frac{2zn}{ZN} \left\{ 1 - \left[\left(\frac{ZN}{2zn} \right)^2 + 1 \right]^{\frac{1}{2}} \right\} \right) \end{aligned} \tag{1.14}$$

$$\Psi_{Don} = \frac{k_B T}{ze} \ln \left\{ \frac{ZN}{2zn} + \left[\left(\frac{ZN}{2zn} \right)^2 + 1 \right] \right\}^{\frac{1}{2}} \tag{1.15}$$

$$K_m = \kappa \left[1 + \left(\frac{ZN}{2zn} \right)^2 \right]^{\frac{1}{4}} \tag{1.16}$$

where z_i represents the valence of each ionic species in solution, n the bulk concentration of ions, and $n_{i,\infty}$ the number concentration of ions in solution. The grouped parameter ZN represents the spatial charge density in the polyelectrolyte region.

This system of equations may be solved by the regression of a plot of calculated versus

experimental electrophoretic mobility, with fitting parameters ZN and $1/\lambda$. Parameters were varied such that the regression yielded a straight line with a slope of unity and an intercept passing through the origin.

Limitations of Classical and Soft DLVO Theories In Biological Systems

While often successful in describing the interactions between colloidal particles and surfaces, both classical and soft-particle DLVO theories fail to adequately predict the behaviour of a microbial cell adhering to a substrate surface. Boström *et al.* have shown that DLVO theory, as well as many of its extensions, cannot characterise systems at biological salt concentrations [15]. This is due to the inherent assumption that all interactions may be linearly superposed to a total energy profile, and the fact that electrostatic interactions are highly screened at physiological conditions. Further, de Kerchove and Elimelech [38] have shown that the Ohshima soft-particle correction is not applicable to biological systems, as the model does not provide realistic values of the fixed charge density and the electrophoretic softness. They have additionally hypothesised that the weaknesses of the model stem from its inability to account for physicochemical heterogeneities within the electrolyte brush, *viz.*, that the brush is not uniformly ion-permeable at all points.

So, to summarise, it has been shown the DLVO theory, and its extensions, have been and continue to be regularly applied to biological, particularly microbial, systems. These models, however, fail to accurately describe experimental interaction profiles in all cases. As the microbes examined in subsequent experimentation have not yet been rigorously studied with these tools, it is of interest to determine if either classical or soft-particle DLVO theory is applicable to their adhesion to medical implant materials.

1.3.3 Steric Interactions with the Microbial Exopolymer Brush

In many cases, the DLVO theories insufficiently describe systems of small particles, especially if the particles are coated with polymer brushes. This is because DLVO theory inherently assumes that the particles under examination are perfectly smooth, with no asperities or surface structures. In the case of a particle with a polymer brush extending outward into the bulk phase, the steric force becomes important. This force arises from contact between

the probe and the polymer brush, where, as the probe pushes down on the brush, the polymers are forced into a more compact spatial arrangement. This reduces the conformational freedom of the polymers in contact with the probe, leading to a net negative loss in entropy. This thermodynamic loss manifests as repulsion exerted by the polymer brush as the bonds in each polymer are changed from their equilibrium position. If both the probe and the sample surface are coated with polymers, additional steric interactions may arise from contact between the two brushes. The total steric force is dependent upon the area density of polymers grafted to the substrate and the thickness of that brush at thermodynamic equilibrium. In microbiology, where most cells are coated with thick, dense polymer brushes, the steric force is often the dominant interaction in force-distance curves.

A steric model of the force per unit area experienced by two interacting surfaces, one possessing a grafted polymer brush and the other bare, was developed by Alexander [6] and de Gennes [37], and modified by Butt *et al.* [27] to describe the interactions between an AFM probe and a polymer brush.

$$F_{St} = 50 k_B T a_{p,eff} L_0 \Gamma^{\frac{3}{2}} exp\left(\frac{-2\pi h}{L_0}\right) \tag{1.17}$$

where F_{St} is the total force due to steric interactions integrated across the surface of a hemispherical probe, L_0 the equilibrium polymer brush length, $a_{p,eff}$ the effective tip radius, as described in [29], and Γ the grafted polymer density. L_0 and Γ serve as fitting parameters. This model assumes the total force may be approximated by integrating the force over the entire surface of the probe, which is modeled as a sphere with radius of curvature equal to 250 nm [29]. Using nonlinear regression software, the model may be fitted to the recorded approach curves.

Steric Interaction With Multi-Polymer Brushes

Equation 1.17 is formulated specifically for a surface possessing a brush comprised of polymers having identical length and spacing at their grafting points. Returning to the original scaling expression [6, 37], however, one may derive a similar expression for multiple polymer

brushes acting in series, according to:

$$F_{St} = 50 k_B T a_{p,eff} \sum_{i=1}^{N} L_i \Gamma_i^{\frac{3}{2}} e^{\frac{-2\pi h}{L_i}} \tag{1.18}$$

And, in the case of two polymers of different lengths and grafting densities,

$$F_{St} = 50 k_B T a \left[L_1 \Gamma_1^{\frac{3}{2}} e^{\frac{-2\pi h}{L_1}} + L_2 \Gamma_2^{\frac{3}{2}} e^{\frac{-2\pi h}{L_2}} \right] \tag{1.19}$$

In terms of an AFM force-separation curve, the behaviour described by Equation 1.19 will be evident in a semilog plot of the force against separation, where the transition point at which the longer polymer is no longer solely responsible for the interaction profile is shown by an inflection in the curve. Physically, this may describe polymers of two different lengths, or a transition point in the flexural properties of a single polymer as the brush is compressed and the volume density of polymers increases. This extension may better describe some experimental data, in terms of the quality of the regression, although the physical accuracy of the formulation has not been empirically verified.

1.3.4 Definition of Zero Separation

Several methods exist to describe the point of zero separation for force cycles which include attraction in the approach segment [25, 42, 84]. These, however, are based largely upon model surfaces with no structures existing between the AFM probe and the surface. Further, no reliable correlations have been developed for force cycles exhibiting only repulsive interactions on approach. As this behaviour is very common in interactions with microbial exopolymers, which are dominated by steric repulsion, there is a significant need for such a method.

A variety of procedures have been introduced to evaluate these scenarios, including that of Camesano and Logan [29] and Li and Logan [65]. The former applies a geometrical approach to force cycles, where the point of zero separation is defined by the intersection of two segments extended from the regions of rigid contact and zero interaction. However, this method neglects to subtract the influence of the cantilever's deflection while in contact with the surface. As such, these curves may be interpreted as representing an infinitely-indentable

surface.

Li's method [65] describes a moving-average approach, in which the slope of a segment drawn between four data points is calculated, and plotted against separation. This plot may be discretised into four regimes, namely: non-interaction (far from the surface), non-contact (interacting with, but not touching, the surface; includes electrostatic and steric interactions), contact (touching and indenting the sample surface or probe), and constant compliance (no indentation; deflection is due solely to piezoactuator displacement). We see issues with this model in terms of loss of data resolution on averaging, as well as the justification of choosing four points in all cases. By subtracting the influence of the cantilever while in contact, we are, in effect, changing the spacing between individual data points in the region near the point of zero separation. Using the moving-average approach as described, each point in the average represents a different separation. Additionally, significant noise artifacts exist in the region close to the sample surface, making an accurate determination of the point of zero separation difficult.

Application of the Steric Model to Define Zero Separation

As has been shown in the previous section, repulsive interactions involving polymer brushes fall within the realm of steric interactions. The original model by de Gennes [37] describes two phenomena taking place during interactions, namely: 1) the increase in osmotic pressure, and 2) the decrease in the entropy of the brush as it is compressed by the AFM probe.

Assuming that these are the only factors present in an interaction dominated by steric forces, the model may be useful in quantifying the point of zero separation. By taking the natural logarithm of both sides of Equation 1.17 and separating the product of a logarithm, we see that:

$$ln\left(F_{St}\right) = ln\left[50k_BTa_{p,eff}L\Gamma^{\frac{3}{2}}\right] - \frac{2\pi}{L}z \tag{1.20}$$

Applying Equation 1.20 to AFM force-separation data, it is possible to obtain the equilibrium polymer brush length from the slope of the segment, and the grafting density from the intercept. Several theoretical and physical flaws exist in this formulation, however, and

efforts to overcome them in generating a quantitative and meaningful definition of the point of zero separation for a brushed surface are described in Chapter 7.

1.3.5 Fractal Texture Analysis Of Surface Topographies

In the design of medical implant device materials, two heuristics are commonly employed. The first states, essentially, that "smoother is better," meaning that a material will be more resistant to microbial colonisation if it has little or no surface texture. The second states that materials are more biocompatible (*viz.*, less likely to be rejected by the host's immune system) if they are more hydrophobic. The first of these two may be tested by relating the strength with which a microbial cell adheres to a material (*viz.*, the magnitude of the pull-off interactions recorded in the retracting portion of an AFM force curve) to the texture of the material. Several classical engineering methods of texture characterisation are described in the following section, after which a novel fractal-based approach is discussed. The application of this fractal model, as well as quantification of the validity of increasing hydrophobicity causing a decrease in microbial colonisation, are explored in detail in Chapter 6.

Classical Surface Characterisation

Commonly, the texture of a surface is reported in terms of its average roughness (R_a), defined as the mean of the absolute value of the height of a surface, or the root-mean-square roughness (R_q), defined as the square root of the sum of the squares of the mean and the standard deviation [8]. Many other correlations have been developed to characterise the texture of various surfaces. These are defined and maintained by the International Organization for Standardization (ISO), as well as by the American Society of Mechanical Engineers (ASME). These parameters have been used extensively to relate experimental results, including the strength of adhesive interactions, to the topography of surface samples.

All of these correlations, however, share the lack of scale dependence in the topographical measurements. For example, a topographical image having dimensions of 1 μm x 1 μm and a resolution 256 pixels per line with 256 lines has a pixel area equal to 15.3 nm^2. An image of the same dimensions with a resolution of 512 pixels per line by 512 lines has a pixel area equal to 3.82 nm^2. This latter image represents the same substrate area, but contains four

times the number of samples as the former image. Since R_q is coupled to the number of samples in the data set, it is plausible that image resolution could have a significant effect on the credibility of the calculation.

Further, the size of the sampling probe (*e.g.,* an AFM tip) defines the precision with which the surface is measured. For example, a tip having a radius of curvature of 10 nm has a surface area of 628 nm^2, when modeled as a hemisphere of the same radius. Using the aforementioned 512 x 512 pixel image, we see that the sharpness of the tip is the limiting measurement factor, as this area is significantly larger than the size of a pixel in the captured image. Clearly, a resolution-independent correlation is required to provide an adequate representation of a surface.

Additionally, to correlate between the surface texture and the strength of an adhesive interaction, it is necessary to evaluate the number of interactions taking place within each sampling interval. For example, consider a bacterial cell having polymer grafting density of 10^{17} m^{-2}, or 0.1 nm^{-2}. Using a pixel of area 15.3 nm^2, each pixel will represent interactions with 1.53 bacterial exopolymers. Extending this measurement to the tip size limitation, we see that each measured sample is actually the superposition of interactions with more than 60 polymers. This is further complicated by the fact that these polymers are not evenly distributed across the cell surface, and do not necessarily have the same length or affinity for the probe. Therefore, we have a further need to characterise the surface under investigation in a manner independent of our ability to represent that surface experimentally.

The Discrete Bonding Model

Brown *et al.* [18, 92] have worked to overcome the limitations of existing characterisation methods and instruments by developing a virtual-tiling method, based in the fractal theory of Mandelbrot [71]. This technique, known as the Discrete Bonding Model (DBM), tiles triangles of equal area onto a topographical image, thereby providing a representation of the surface that is dependent on the size of the tiles, not upon the interval at which data were acquired. By incrementally decreasing the area of each triangle, the technique better represents the surface topography. This is shown in Figure 1.3.2.

Figure 1.3.2: Example of virtual tiling from the Discrete Bonding Model at three area scales. As the relative area increases, the projection of the original surface becomes more accurate.

Mathematical Basis of the Discrete Bonding Model

Utilising the assumption that each measurable force interaction, S_t, may be represented as the surface integral of multiple differential interaction forces, ds_s, we begin with the following expression, adapted from [19].

$$S_t = \frac{1}{A_p} \int_A ds_s \tag{1.21}$$

where A_p is the nominal projected area over which a measurable interaction occurs. In order to evaluate Equation 1.21, the entire topography must be differentiable, with integer spatial dimensions at every observational scale. In practice, however, these surfaces possess a non-integer, or fractal, dimension, meaning that the surface appears different at different observational scales. To visualise this, consider a sheet of paper. Held at arm's length, the sheet appears very smooth and uniform. Brought closer to the observer's eye, one may discern the macroscopic texture of the paper resulting from the manufacturing procedure. Under a microscope, this texture becomes even more pronounced. Since the sheet does not appear the same at all observational scales, it possesses a fractal dimension. Since surfaces will have non-integer dimensions at some observational scale, Equation 1.21 becomes very difficult to evaluate.

Assuming that the strength of a bond has a minimum and finite strength, S_s, and characteristic area, A_s, which also implies that a bonding phenomenon has a fundamental scale which is required for the phenomenon to occur, we may integrate 1.21 with respect to that fundamental scale.

$$S_t = \frac{N_t S_s}{A_p} + C \tag{1.22}$$

where N_t is the number of discrete adhesive events with strength S_s. We can further discretise N_t as a function of the total number of available bonding sites, since it is possible that some sites will not participate in adhesive events.

$$N_t = m_s \frac{A_{ts}}{A_s} \tag{1.23}$$

With A_{ts} defined as the total surface area evaluated at the scale of a single adhesive event. The ratio A_{ts}/A_s represents the total number of sites available for bonding. m_s is the fraction of total sites available for bonding, and varies between 0 and 1.

Combining Equations 1.22 and 1.23, we obtain the following.

$$S_t = m_s \frac{S_s}{A_s} \frac{A_{ts}}{A_p} + C \tag{1.24}$$

where the ratio $\frac{S_s}{A_s}$ describes a fundamental bond, and $\frac{A_{ts}}{A_p}$ characterises the surface at the fundamental scale of an interaction, A_s. This latter ratio is defined as the relative area. The virtual tiling method provides that the relative area is always greater than 1, as the tiles must be extremely small to perfectly map the input topography. C is a constant describing the adhesive (or repulsive) at a relative area of zero.

Application of the Discrete Bonding Model

While the DBM is shown above to be a useful and straightforward technique in the correlation between the adhesive strength and fundamental scale of an interaction, its application can be laborious. In general, only A_p is known, and specialised equipment (*e.g.,* the AFM) is required to estimate S_t. All other parameters are unknown, requiring rigorous iteration to obtain meaningful results.

Realising this, Brown *et al.* established Surfract (`http://www.surfract.com/`), a company which develops and maintains software (SFrax® and KFrax®) designed specifically to evaluate the DBM at many relative areas. This software is capable of importing a wide variety of file formats, including that of most common AFMs. With a topographical image as input, the SFrax® outputs a plot of the relative area against the area of each triangular patch. An example may be seen below.

So, to this point, we are able to correlate the relative area of an interaction to its virtual tiling scale. In order to determine the tensile strength of an interaction, we then plot the mean pull-off force, determined by AFM force cycle analysis, against the relative area for a number of topographical images at each area scale. Linear least squares regression of these data provide the least squares regression coefficient, R^2, for each area scale. Finally, a plot

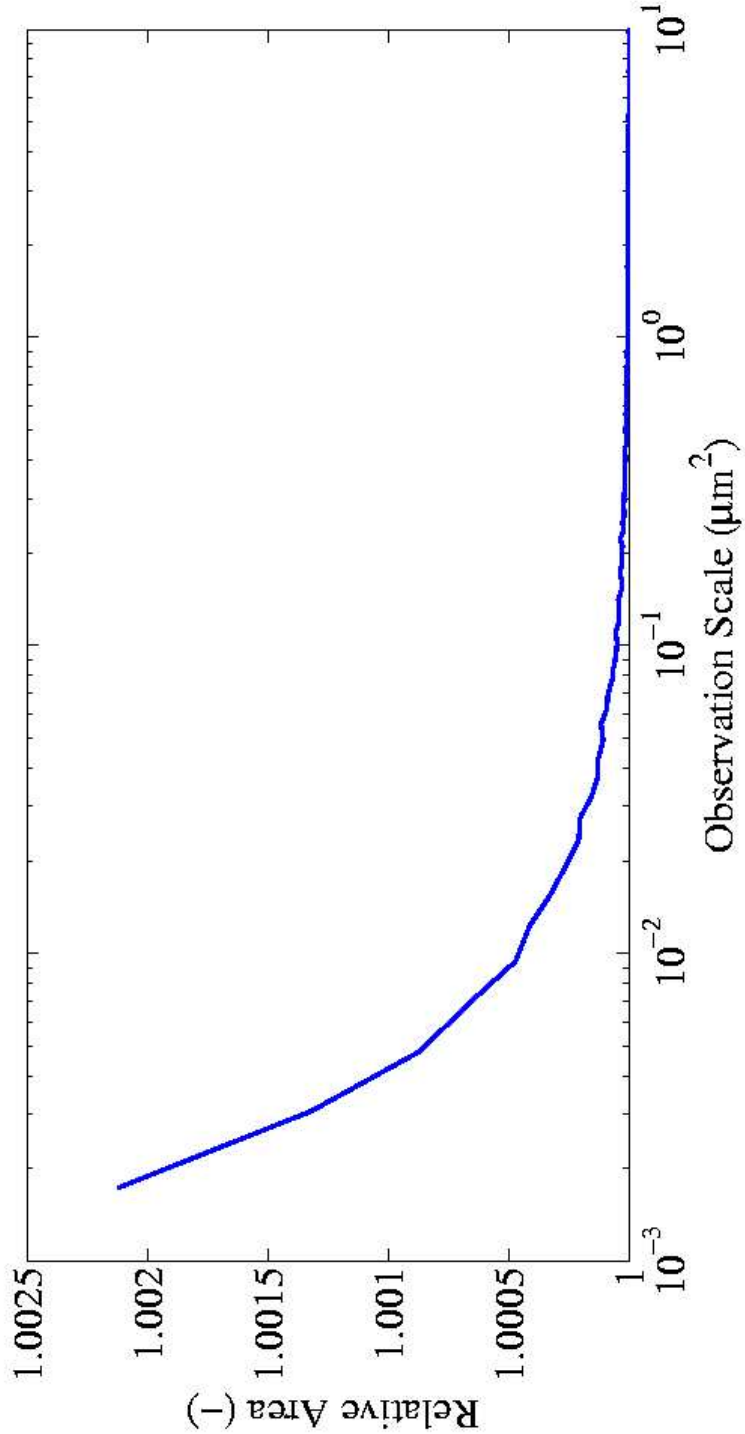

Figure 1.3.3: Example area scale plot for a 4 μm^2 topographical image of a dodecanethiol SAM on gold.

of R^2 against area scale, as shown in Figure 1.3.4, is generated. This is termed a Siegmann Plot.

Linear portions of the curve indicate area scales over which the surface appears complex, while nonlinear portions are considered smooth, from the point of view of the measuring device. A global maximum (*i.e.*, at an area scale of 0.0017301 μm^2 in Figure 1.3.4) within the complex portion of the plot indicates the fundamental area scale at which an interaction occurs.

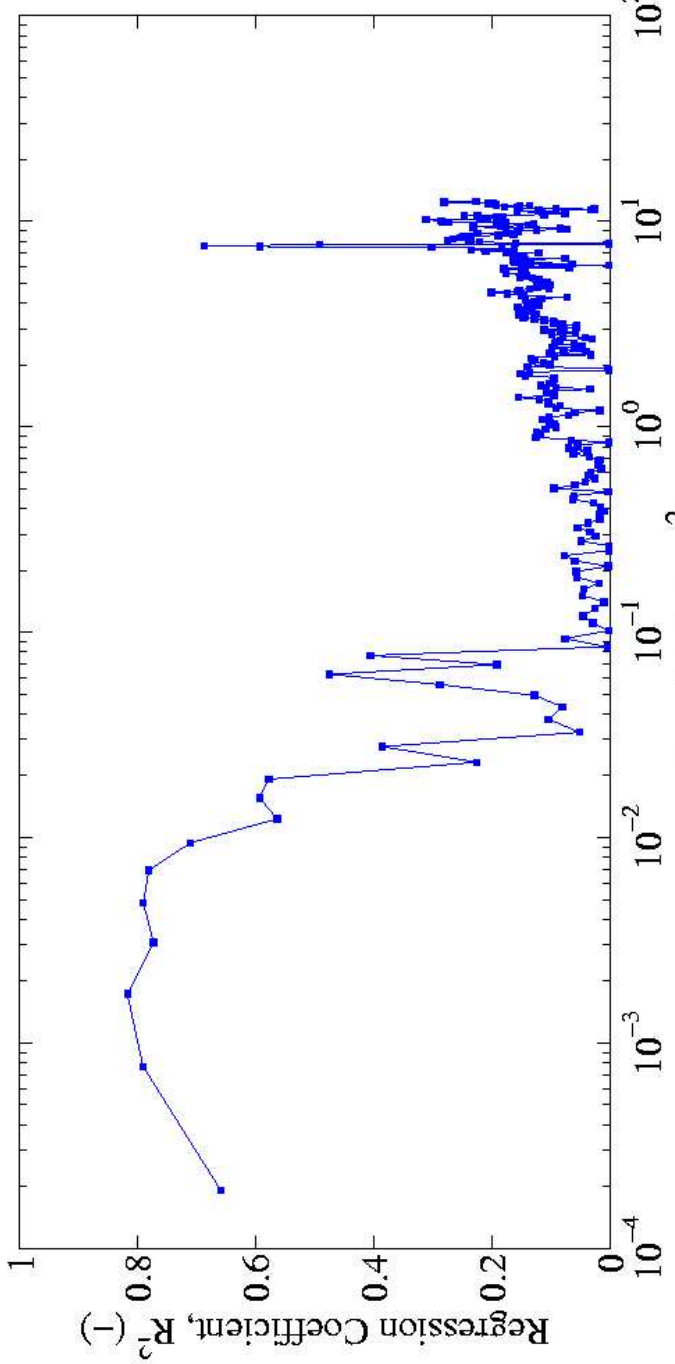

Figure 1.3.4: Example Siegmann plot. The maximum, which occurs in this example at an area scale of 0.0017301 μm^2, is indicative of the fundamental scale of adhesion for this interaction.

1.4 Summary

In the above review, the overlying issue of microbial adhesion and infection of biomedical implant devices was discussed 1.1. The atomic force microscope, described in 1.2, will be the primary tool for investigating both the topographical and adhesive properties of several microbial/biomaterial systems. Using the classical and novel mathematical theories described in 1.3, it is hypothesised that new light will be shed upon biomedical implant infections, in terms of the morphological, physicomechanical and physicochemical properties of both implant devices and the microbes that seek to colonise them. The following chapters of this dissertation describe several applications of AFM topographical and force capabilities to explaining how quickly, how strongly, and, most importantly, why opportunistic pathogenic microbes bind to these implants. Further, discussion is opened regarding methods by which microbial colonisation may be mitigated or eliminated. This work is meant to be neither the first nor the last step in this field of study. It is, however, an important step towards understanding how humans may control illness caused by organisms one one-millionth their size.

1.5 Bibliography

[1] Hooke's Law. Encyclopaedia Britannica. Encyclopaedia Britannica Premium Service, 2006. Available from: `http://wwwa.britannica.com/eb/article-9040985`.

[2] N. I. Abu-Lail. The Effect of Biopolymer Properties on Bacterial Adhesion: An Atomic Force Microscopy (AFM) Study. Doctoral Dissertation, Biological Interaction Forces Lab, Department of Chemical Engineering, Worcester Polytechnic Institute, 2003.

[3] N. I. Abu-Lail and T. A. Camesano. Role of ionic strength on the relationship of biopolymer conformation, DLVO contributions and steric interactions to bioadhesion of *Pseudomonas putida* KT2442. Biomacromolecules, 4:1000–1012, 2003.

[4] N. I. Abu-Lail and T. A. Camesano. Role of lipopolysaccharides in the adhesion, retention and transport of *Escherichia coli* JM109. Environmental Science and Technology, 37:2173–2183, 2003.

[5] A. E. Aiello, B. Marchall, S. B. Levy, P. Della-Latta, S. X. Lin, and E. Larson. Antibacterial cleaning products and drug resistance. Emerging Infectious Diseases, 11(10):1565–1570, 2005.

[6] S. Alexander. Adsorption of chain molecules with a polar head: A scaling description. Journal de Physique (Paris), 38(8):983–987, 1977.

[7] C. R. Arciola, D. Campoccia, S. Gamberini, M. E. Donati, and L. Montanaro. Presence of fibrinogen-binding adhesin gene in *Staphylococcus epidermidis* isolates from central venous catheter-associated and orthopaedic implant-associated infections. Biomaterials, 25:4825–4829, 2004.

[8] ASME B46.1. Chapter 10 - Surface Texture (Surface Roughness, Waviness and Lay). American Society of Mechanical Engineers, New York, NY, 2002.

[9] B. L. Bassler. How bacteria talk to each other: Regulation of gene expression by quorum sensing. Current Opinion in Microbiology, 2(6):582–587, 1999.

[10] G. Binnig, C. F. Quate, and C. Gerber. Atomic force microscope. Physical Review Letters, 56(9):930–933, 1986.

[11] G. Binnig, H. Rohrer, Ch. Gerber, and E. Weibel. Surface studies by scanning tunneling microscopy. Physics Review Letters, 49(1):57–61, 1982.

[12] G. Binnig, H. Rohrer, Ch. Gerber, and E. Weibel. Tunneling through a controllable vacuum gap. Applied Physics Letters, 40(2):178–180, 1982.

[13] R. Bos, H. C. van der Mei, and H. J. Busscher. 'Soft-particle' analysis of the electrophoretic mobility of a fibrillated and non-fibrillated oral streptococcal strain: *Streptococcus salivarius*. Biophysical Chemistry, 74:251–255, 1998.

[14] R. Bos, H. C. van der Mei, and H. J. Busscher. Physico-chemistry of initial microbial adhesive interactions - Its mechanisms and methods for study. FEMS Microbiology Reviews, 23:179–230, 1999.

[15] M Boström, D. R. M. Williams, and B. W. Ninham. Specific ion effects: Why DLVO theory fails for biology and colloid systems. Physical Review Letters, 87(16):1681031–1681034, 2001.

[16] W. R. Bowen, N. Hilal, R. W. Lovitt, and C. J. Wright. Direct measurement of the force of adhesion of a single biological cell using an atomic force microscope. Colloids and Surfaces A: Physicochemical and Engineering Aspects, 136:231–234, 1998.

[17] W. R. Bowen, R. W. Lovitt, and C. J. Wright. Direct quantification of *Aspergillus niger* spore adhesion in liquid using an atomic force microscope. Journal of Colloid and Interface Sciences, 228:428–433, 2000.

[18] C. A. Brown. Scale-area analysis and roughness: a method for understanding the topographic component of adhesive strength. In K. M. Liechti, editor, Seventeenth Annual Meeting and the Symposium on Particle Adhesion, pages 5–7, Orlando, FL, February, 1994. The Adhesion Society.

[19] C. A. Brown and S. Siegmann. Fundamental scales of adhesion and area-scale fractal analysis. International Journal of Machine Tools and Manufacture, 41:1927–1933, 2001.

[20] N. A. Burnham, O. P. Behrend, F. Oulevey, G. Gremaud, P.-J. Gallo, D. Gourdon, E. Dupas, A. J. Kulik, H. M. Pollock, and G. A. D. Briggs. How does a tip tap? Nanotechnology, 8:67–75, 1997.

[21] N. A. Burnham, X. Chen, C. S. Hodges, G. A. Matei, E. J. Thoreson, C. J. Roberts, M. C. Davies, and S. J. B. Tendler. Comparison of calibration methods for atomic-force microscopy cantilevers. Nanotechnology, 14:1–6, 2003.

[22] N. A. Burnham and R. J. Colton. Measuring the nanomechanical properties and surface forces of materials using an atomic force microscope. Journal of Vacuum Science and Technology, 7:2906–2913, 1989.

[23] N. A. Burnham, R. J. Colton, and H. M. Pollock. Interpretation of force curves in atomic force microscopy. Nanotechnology, 4:64–80, 1993.

[24] N. A. Burnham, G. Gremaud, A. J. Kulik, P.-J. Gallo, and F. Oulevey. Materials' properties measurements: Choosing the optimal scanning probe microscope configuration. Journal of Vacuum Sciene and Technology, 14(2):1308–1312, 1996.

[25] N. A. Burnham and A. J. Kulik. Surface Forces and Adhesion. In B. Bhushan, editor, Handbook of Micro/Nano Tribology, pages 247–271. CRC Press, Boca Raton, 2nd edition, 1999.

[26] H.-J. Butt and M. Jaschke. Calculation of thermal noise in atomic force microscopy. Nanotechnology, 6:1–7, 1995.

[27] H.-J. Butt, M. Kappl, H. Mueller, R. Paiteri, W. Meyer, and J. Ruhe. Steric forces measured with the atomic force microscope at various temperatures. Langmuir, 15:2559–2565, 1999.

[28] F. J. Caccavo and A. Das. Adhesion of dissimilatory Fe(III)-reducing bacteria to Fe(III) minerals. Geomicrobiology Journal, 19(2):161–177, 2002.

[29] T. A. Camesano and B. E. Logan. Probing bacterial electrosteric interactions using atomic force microscopy. Environmental Science and Technology, 34:3354–3362, 2000.

[30] H. B. G. Casimir and D. Polder. The influence of retardation on the London-van der Waals forces. Physical Review, 73:360–372, 1948.

[31] A. Centeno, C. P. Davis, M. S. Cohen, and M. M. Warren. Modulation of *Candida albicans* attachment to human epithelial cells by bacteria and carbohydrates. Infection and Immunity, 39(3):1354–1360, 1983.

[32] J. P. Cleveland, S. Manne, D. Bocek, and P. K. Hansma. A nondestructive method for determining the spring constant of cantilevers for scanning force microscopy. Reviews of Scientific Instruments, 64(2):403–405, 1993.

[33] J. W. Costerton. Overview of microbial biofilms. Journal of Industrial Microbiology, 15:137–140, 1995.

[34] J. W. Costerton, G. G. Geesey, and K.-J. Cheng. How bacteria stick. Scientific American, 238:86–95, 1978.

[35] J. W. Costerton, Z. Lewandowski, D. E. Caldwell, D. R. Korber, and H. M. Lappin-Scott. Microbial biofilms. Annual Review of Microbiology, 49:711–745, 1995.

[36] D. Davies. Understanding biofilm resistance to antibacterial agents. Nature Reviews Drug Discovery, 2:114–122, 2003.

[37] P. G. de Gennes. Polymers at an interface: A simplified view. Advances in Colloid and Interface Science, 27:189–209, 1987.

[38] A. J. de Kerchove and M. Elimelech. Relevance of electrokinetic theory for "soft" particles to bacterial cells: Implications for bacterial adhesion. Langmuir, 21:6462–6472, 2005.

[39] B. V. Derjaguin and L. Landau. Theory of the stability of strongly charged lyophobic sols and the adhesion of strongly charged particles in solutions of electrolytes. Acta Physicochimica (URSS), 14:633–662, 1941.

[40] R. M. Donlan. Biofilms: Microbial life on surfaces. Emerging Infectious Diseases, 8(9):881–890, 2002.

[41] W. A. Ducker and T. J. Senden. Measurement of forces in liquids using a force microscope. Langmuir, 8:1831–1836, 1992.

[42] Y. F. Dufrêne. Application of atomic force microscopy to microbial surfaces: From reconstituted cell surface layers to living cells. Micron, 32:153–165, 2001.

[43] Y. F. Dufrêne, C. J. P. Boonaert, H. C. van der Mei, H. J. Busscher, and P. G. Rouxhet. Probing molecular interactions and mechanical properties of microbial cell surfaces by atomic force microscopy. Ultramicroscopy, 86:113–120, 2001.

[44] I. V. Egorenkova, S. A. Konnova, Y. P. Fedonenko, L. A. Dykman, and V. V. Ignatov. Role of the polysaccharide components of *Azospirillum brasilense* capsules in bacterial adsorption on wheat seedling roots. Microbiology (Moscow, Russian Federation), 70(1):36–40, 2001.

[45] R. J. Emerson and T. A. Camesano. On the importance of precise calibration techniques for an atomic force microscope. Ultramicroscopy, 106(4-5):413–422, 2006.

[46] B. Gottenbos, H. C. van der Mei, and H. J. Busscher. Initial adhesion and surface growth of *Pseudomonas aeruginosa* on negatively and positively charged poly(methacrylates). Journal of Materials Science: Materials in Medicine, 10:853–855, 1999.

[47] B. Gottenbos, H. C. van der Mei, and H. J. Busscher. Initial adhesion and surface growth of *Staphylococcus epidermidis* and *Pseudomonas aeruginosa* on biomedical polymers. Journal of Biomedical Materials Research, 50:208–214, 2000.

[48] J. Gregory. Approximate expressions for retarded van der Waals interaction. Journal of Colloid and Interface Sciences, 83(1):138–145, 1981.

[49] A. G. Gristina. Biomaterial-centered infection: Microbial adhesion versus tissue integration. Science, 237:1588–95, 1987.

[50] H. C. Hamaker. London-van der Waals attraction between spherical particles. Physica (Amsterdam), 4:1058–1072, 1937.

[51] H. Hayashi, S. Tsuneda, A. Hirata, and H. Sasaki. Soft particle analysis of bacterial cells and its interpretation of cell adhesion behaviors in terms of DLVO theory. Colloids and Surfaces B: Biointerfaces, 22:149–157, 2001.

[52] S. O. Heard. Catheter-related infection: Diagnosis, prevention and treatment. Annals of the Academy of Medicine Singapore, 30:419–429, 2001.

[53] M. N. Helmus. Biomaterials in the Design and Reliability of Medical Devices. Tissue Engineering Intelligence. Eurekah.com/Landes Bioscience, Georgetown, TX, 2002.

[54] R. Hogg, T. W. Healy, and D. W. Fuerstenau. Mutual coagulation of colloidal dispersions. Transactions of the Faraday Society, 62:1638–1651, 1966.

[55] J. L. Hutter and J. Bechhoefer. Calibration of atomic-force microscope tips. Reviews of Scientific Instruments, 64(7):1868–1873, 1993.

[56] K. Hyonchol, H. Arakawa, T. Osada, and A. Ikai. Quantification of fibronectin and cell surface interactions by AFM. Colloids and Surfaces B: Biointerfaces, 25:33–43, 2002.

[57] Digital Instruments. Scanning Probe Microscopy Training Notebook. Technical report, Veeco Metrology Group, 1998.

[58] N. Khardori and M. Yassien. Biofilms in device-related infection. Journal of Industrial Microbiology, 15:141–147, 1995.

[59] A. S. Klainer. Use of Gram Stain in Clinical Infectious Diseases. Schering Group, Berlin, 1976.

[60] U. Landman, W. D. Luedtke, N. A. Burnham, and R. J. Colton. Atomistic mechanisms and dynamics of adhesion, nanoindentation and fracture. Science, 248:454–461, 27 April 1990.

[61] G. U. Lee, L. A. Chrisey, and R. J. Colton. Direct measurement of the forces between complementary strands of DNA. Science, 266(5186):771–773, 1994.

[62] O. Lesens, Y. Hansmann, D. Storck, and D. Christmann. Risk factors for metastatic infection in patients with *Staphylococcus aureus* bacteremia with and without endocarditis. European Journal of Internal Medicine, 14:227–231, 2003.

[63] A. S. Levin, S. F. Costa, N. S. Mussi, M. Basso, S. I. Sinto, C. Machado, D. C. Geiger, M. C. B. Villares, A. Z. Schreiber, A. A. Barone, and M. L. M. Branchini. *Candida parapsilosis* fungæmia associated with implantable and semi-implantable central venous catheters and the hands of healthcare workers. Diagnostic Microbiology and Infectious Disease, 30:243–249, 1998.

[64] S. B. Levy. The challenge of antibiotic resistance. Scientific American, 278(3):46–53, 1 March 1998.

[65] X. Li and B. E. Logan. Analysis of bacterial adhesion using a gradient force analysis and colloid probe atomic force microscopy. Langmuir, 20(20):8817–8822, 2004.

[66] S. K. Lower, C. J. Tadanier, and M. F. Hochella Jr. Measuring interfacial and adhesion forces between bacteria and mineral surfaces with biological force microscopy. Geochimica et Cosmochimica Acta, 64(18):3133–3139, 2000.

[67] S. K. Lower, C. J. Tadanier, and M. F. Hochella Jr. Dynamics of the mineral-microbe interface: Use of biological force microscopy in biogeochemistry and geomicrobiology. Geomicrobiology Journal, 18:63–76, 2001.

[68] A. Lupetti, A. Tavanti, P. Davini, E. Ghelardi, V. Corsini, I. Merusi, A. Boldrini, M. Campa, and S. Senesi. Horizontal transmission of *Candida parapsilosis* candidæmia in a neonatal intensive care unit. Journal of Clinical Microbiology, 40(7):2363–2369, 2002.

[69] J. B. Lyczak, C. L. Cannon, and G. B. Pier. Establishment of *Pseudomonas aeruginosa* infection: Lessons from a versatile opportunist. Microbes and Infection, 2:1051–1060, 2000.

[70] Q. Ma, Y. Zhai, J. C. Schneider, T. M. Ramseier, and M. H. Saier. Protein secretion systems of *Pseudomonas aeruginosa* and *P. fluorescens*. Biochimica et Biophysica Acta, 1611:223–233, 2003.

[71] B. B. Mandelbrot. Fractals, Form, Chance and Dimension. W. H. Freeman and Company, San Francisco, CA, 1977.

[72] L. A. Mermel, B. M. Farr, R. J. Sherertz, I. I. Raad, N. O'Grady, J. S. Harris, and D. E. Craven. Guidelines for the management of intravascular catheter-related infections. Clinical Infectious Diseases, 32(9):1249–1272, 2001.

[73] K. W. Michiels, C. L. Croes, and J. Vanderleyden. Two different modes of attachment of *Azospirillum brasilense* Sp7 to wheat roots. Journal of General Microbiology, 137(9):2241–2246, 1991.

[74] J. Munakata-Marr, P. L. McCarty, M. S. Shields, M. Reagin, and S. C. Francesconi. Enhancement of trichloroethylene degradation in aquifer microcosms bioaugmented with wild type and genetically altered *Burkholderia* (*Pseudomonas*) *cepacia* G4 and PR1. Environmental Science and Technology, 30:2045–2052, 1996.

[75] M. H. Nguyen, J. E. Peacock, A. J. Morris, D. C. Tanner, M. L. Nguyen, D. R. Snydman, M. M. Wagener, M. G. Rinaldi, and V. L. Yu. The changing face of candidæmia: Emergence of non-*Candida albicans* species and antifungal resistance. American Journal of Medicine, 100:617–623, 1996.

[76] I. Ofek and E. H. Beachey. Mannose binding and epithelial cell adherence of *Escherichia coli*. Infection and Immunity, 22(1):247–254, 1978.

[77] H. Ohshima and T. Kondo. Approximate analytic expression for the electrophoretic mobility of colloidal particles with surface-charge layers. Journal of Colloid and Interface Sciences, 130(1):281–282, 1989.

[78] Y.-L. Ong, A. Razatos, G. Georgiou, and M. M. Sharma. Adhesion forces between *E. coli* bacteria and biomaterial surfaces. Langmuir, 15:2719–2725, 1999.

[79] J. T. G. Overbeek. Colloid Science. Elsevier, New York, 1952.

[80] I. Palabiyikoglu, M. Oral, and M. Tulunay. *Candida* colonization in mechanically ventilated patients. Journal of Hospital Infection, 47:239–242, 2001.

[81] K. Pedersen. Biofilm development on stainless steel and PVC surfaces in drinking water. Water Research, 24(2):239–243, 1990.

[82] D. Raveh, B. Rudensky, Y. Schlesinger, S. Benenson, and A. M. Yinnon. Susceptibility trends in bacteraemias: Analyses of 7544 patient-unique bacteraemic episodes spanning 11 years (1990-2000). Journal of Hospital Infection, 55:196–203, 2003.

[83] A. Razatos, Y.-L. Ong, F. Boulay, D. L. Elbert, J. A. Hubbell, M. M. Sharma, and G. Georgiou. Force measurements between bacteria and poly(ethylene glycol)-coated surfaces. Langmuir, 16:9155–9158, 2000.

[84] A. Razatos, Y.-L. Ong, M. M. Sharma, and G. Georgiou. Evaluating the interaction of bacteria with biomaterials using atomic force microscopy. Journal of Biomaterial Science: Polymer Edition, 9(12):1361–1373, 1998.

[85] G. Reid. Microbial adhesion to biomaterials and infections of the urogenital tract. Colloids and Surfaces B: Biointerfaces, 2:377–385, 1994.

[86] J. E. Sader. Frequency response of cantilever beams immersed in viscous fluids with applications to the atomic force microscope. Journal of Applied Physics, 84(1):64–76, 1998.

[87] A. Safdar, D. S. Perlin, and D. Armstrong. Hematogenous infections due to *Candida parapsilosis*: Changing trends in fungæmic patients at a comprehensive cancer center during the last four decades. Diagnostic Microbiology and Infectious Disease, 44:11–16, 2002.

[88] S. Schelenz and G. French. An outbreak of multidrug-resistant *Pseudomonas aeruginosa* infection associated with contamination of bronchoscopes and and endoscope washer-disinfector. Journal of Hospital Infection, 46:23–30, 2000.

[89] J. H. Schenkel and J. A. Kitchener. A test of the Derjaguin-Verwey-Overbeek theory with a colloidal suspension. Transactions of the Faraday Society, 56:161–173, 1960.

[90] J.M. Schierholz and J. Beuth. Implant infections: A haven for opportunistic bacteria. Journal of Hospital Infection, 49:87–93, 2001.

[91] U. D. Schwarz, H. Hölscher, and R. Wiesendanger. Atomic resolution in scanning force microscopy: Concepts, requirements, contrast mechanisms, and image interpretation. Physical Review B, 62(19):13089–13097, 2000.

[92] S. Siegmann and C. A. Brown. Surface texture correlations with tensile adhesive strength of thermally sprayed coatings using area-scale fractal analysis. In E. Lugschneider and P.A. Kammer, editors, United Thermal Spray Conference - Proceedings DVS Verlag, Düsseldorf, Germany, 1999.

[93] K. C. Stover, X. Q. Pham, A. L. Erwin, S. D. Mizoguchi, P. Warrener, M. J. Hickey, F. S. L. Brinkman, W. O. Hufnagle, D. J. Kowalik, M. Lagrou, R. L. Garber, L. Goltry, E. Tolentino, S. Westbrock-Wadman, Y. Yuan, L. L. Brody, S. N. Coulter, K. R. Folger, A. Kas, K. Larbig, R. Lim, K. Smith, D. Spencer, G. K.-S. Wong, Z. Wu, I. Paulsen, J. Reizer, M. H. Saier, R. E. W. Hancock, S. Lory, and M. V. Olson. Complete genome sequence of *Pseudomonas aeruginosa* PA01: An opportunistic pathogen. Nature, 406:959–964, 2000.

[94] P. A. Suci, J. D. Vrany, and M. W. Mittelman. Investigation of interactions between antimicrobial agents and bacterial biofilms using attenuated total reflection Fourier transform infrared spectroscopy. Biomaterials, 19:327–339, 1998.

[95] S. Takashima and H. Morisaki. Surface characteristics of the microbial cell of *Pseudomonas syringae* and its relevance to cell attachment. Colloids and Surfaces B: Biointerfaces, 9:205–212, 1997.

[96] E. J. Thoreson. From Nanoscale to Macroscale: Using the Atomic Force Microscope to Quantify the Role of Few-Asperity Contacts in Adhesion. Doctoral Dissertation, Department of Physics Engineering, Worcester Polytechnic Institute, 2005.

[97] E. J. Thoreson and N. A. Burnham. Standard-deviation minimization for calibrating the radii of spheres attached to AFM cantilevers. Review of Scientific Instruments, 75:1359–1362, 2004.

[98] B. A. Todd, S. J. Eppell, and F. R. Zypman. Squeezing out hidden force information from scanning force microscopes. Applied Physics Letters, 79(12):1888–1890, 2001.

[99] A. Touhami, B. Hoffmann, A. Vasella, F. A. Denis, and Y. F. Dufrêne. Probing specific lectin-carbohydrate interactions using atomic force microscopy imaging and force measurements. Langmuir, 19(5):1745–1751, 2003.

[100] C. J. van Oss. Acid-base interfacial interactions in aqueous media. Colloids and Surfaces A: Physicochemical and Engineering Aspects, 78:1–49, 1993.

[101] C. J. van Oss. Interfacial Forces in Aqueous Media. Marcel Dekker, Inc., New York, NY, 1994.

[102] C. J. van Oss, M. K. Chaudhury, and R. J. Good. Additive and non-additive surface tension components and the interpretation of contact angles. Langmuir, 4:884–891, 1988.

[103] E. J. Verwey and J. T. G. Overbeek. Theory of the Stability of Lyophobic Colloids. Elsevier, Amsterdam, 1948.

[104] M. J. Vieira, R. Oliveira, L. Melo, M. M. Pinheiro, and V. Martins. Effect of metallic ions on the adhesion of biofilms formed by *Pseudomonas fluorescens*. Colloids and Surfaces B: Biointerfaces, 1:119–124, 1993.

[105] J.-L. Vincent, E. Anaissie, H. Bruining, W. Demajo, M. El-Ebiary, J. Haber, Y. Hiramatsu, G. Nitenberg, P.-O. Nyström, D. Pittet, T. Rogers, P. Sandven, G. Sganga, M.-D. Schaller, and J. Solomkin. Epidemiology, diagnosis and treatment of systemic *Candida* infection in surgical patients under intensive care. Intensive Care Medicine, 24:206–216, 1998.

[106] L. A. Wenzler, G. L. Moyes, G. N. Raikar, R. L. Hansen, J. M. Harris, and T. P. Beebe Jr. Measurements of single-molecule bond-rupture forces between self-assembled monolayers of organosilanes with the atomic force microscope. Langmuir, 13:3761–3768, 1997.

[107] S. C. Winans. Command, control and communication in bacterial pathogenesis. Trends in Microbiology, 6(10):382–383, 1998.

[108] M. C. Wolfgang, B. R. Kulasekara, X. Liang, D. Boyd, K. Wu, Q. Yang, C. G. Miyada, and S. Lory. Conservation of genome content and virulence determinants among clinical and environmental isolates of *Pseudomonas aeruginosa*. Proceedings of the National Academy of Sciences of the United States of America, 100(14):8484–8489, 2003.

[109] C. E. ZöBell and D. Q. Anderson. Observations on the multiplication of bacteria in different volumes of stored sea water and the influence of oxygen tension and solid surfaces. The Biological Bulletin, 71:324–342, 1936.

CHAPTER 2

Microbial Adhesion to Medical Implant Materials: An Atomic Force Microscopy Study

2.1 Abstract

Microbial infections of medical implants occur in more than 2 million surgical cases each year in the United States alone. These infections increase patient morbidity and mortality, as well as patient cost and recovery time. Many treatments are available, but none are guaranteed to remove the infection. The purpose of this work is to examine the initial events in microbial adhesion by simulating the approach and contact between a planktonic cell, immobilised on an Atomic Force Microscope (AFM) cantilever, and a biomaterial or biofilm substrate.

Distinct adhesive interactions exist between *Candida parapsilosis* and both unmodified silicone rubber and *Pseudomonas aeruginosa* biofilms. Using *C. parapsilosis* cells immobilised on AFM cantilevers with a silicone substrate, we have measured attractive inter-

actions with magnitude of 2.3 ± 0.25 nN (SD)[1] in the approach portion of the force cycle. On *P. aeruginosa* biofilms, the magnitude of the attractive force decreases to 2.0 ± 0.40 nN (SD), and is preceded by a 2.0 nN repulsion at approximately 75 nm from the cell surface. This repulsion may be attributed to steric and electrostatic interactions between the two microbial polymer brushes.

Future work will include modification of this system to better simulate *in vivo* conditions, extension of force curve analysis to adhesion-appropriate continuum contact models, examination of the effects of immobilised thiol-terminated oligosaccharides on adhesive behaviour, and investigation of cellular stains on adhesive properties.

Characterisation of cell-biomaterial and cell-cell interactions allows for a quantitative evaluation of the materials used for medical implantation. It also provides a link between the physicochemical and physicomechanical properties of these materials and the nanoscale interactions leading to microbial colonisation and infection. The goal of this research is to study this link and determine how best to exploit it to prevent microbial infections of medical implant materials.

[1] Values of error shown in this document reflect the standard deviation amongst repeated data sets. This is indicated by the symbol (SD).

2.2 Introduction

The development of the microbial biofilm and its importance in medical implant infections has been thoroughly discussed [11,38]. Causing over 2 million infections annually [16], which generate over $11 billion in additional patient costs [34], the biofilm, in a biomedical context, is a system which demands attention.

The application of atomic force microscopy (AFM) to biological systems seems advantageous and has been examined by several different groups, beginning with early work on DNA [24] that was later extended to ligand-receptor and whole-cell systems. AFM has been used to examine the physicochemical properties of microbial surfaces [12] and to characterise lectin-carbohydrate interactions at the nanoscale [39]. AFM probes, functionalised with either biomaterial spheres or confluent microbial lawns, were used to characterise bacterial-biomaterial interactions [32,33].

Single microbes, immobilised on AFM probes, have also been used to study a variety of surfaces. Bowen *et al.* [8] bound metabolically active *Saccharomyces cerevisiae* to the probe using a chemical adhesive. Also, Benoit *et al.* [4] measured discrete intercellular interactions by using *Dictyostelium discoideum* attached to the probe via a lectin. We propose to extend these prior techniques by attaching viable, clinically relevant microbes to the AFM cantilever. These cell probes will then be used to measure local interaction forces between the immobilised cell and both biomaterial and biofilm surfaces.

Many infectious systems can be polymicrobial, each strain contributing to the whole in some significant way [16, 22]. Therefore, our model microbial system is designed to study the interactions between *Pseudomonas aeruginosa*, a bacterium responsible for 99 % of bacteræmia cases, keratitis, and infections in cystic fibrosis patients [28], and *Candida parapsilosis*, an emerging nosocomial pathogen isolated in infections of central venous catheters and bronchoscopes [25, 31]. In our experiments, *Candida* cells are chemically immobilised onto AFM probes and used to quantify interactions with bare biomaterials and with biomaterials coated with a bacterial biofilm.

2.3 Materials and Methods

2.3.1 Microbial Growth and Storage

Lyophilized samples of *C. parapsilosis* (ATCC 90018) and *P. aeruginosa* (ATCC 10145) were acquired from the American Type Culture Collection (Manassas, VA, USA). *C. parapsilosis* was maintained on Sabouraud's Dextrose Agar (Emmons' Modification) (Sigma) plates, and grown in Complete Liquid Media (2 w/v% peptone, 1 w/v% yeast extract, 2 w/v% glycerol (Sigma) in distilled, deionized water [ddH_2O]). *P. aeruginosa* was maintained on Tryptic Soy Agar (Sigma) plates, and grown in Tryptic Soy Broth (Sigma). All plates were recultured every 14 days. Cells were incubated for 12 hours at 25 °C on a radially oriented tube-rotator (Glas-Col) in 25 mL vented tissue culture flasks (VWR) at approximately 0.45 xg. Cells were then transferred to 50 mL of their respective liquid growth media and grown in an orbital shaker bath (Lab-Line) at 37 °C and 160 RPM until late exponential growth phase (Optical density at 600nm $[O.D._{600}] = 0.5 \pm 0.05$).

2.3.2 Cell Morphology, Force Interactions and Cantilever Treatment

Cell cultures were imaged with a Dimension 3100 atomic force microscope with Nanoscope^{TM} IIIa controller (Digital Instruments, Santa Barbara, CA) to establish cell morphology and record interaction forces with silicon nitride probes (DNP-S, Digital Instruments) with nominal spring constants of 0.13 ± 0.02 $N \cdot m^{-1}$ (short, thin cantilevers) [10] or 0.25 ± 0.01 $N \cdot m^{-1}$ (short, fat cantilevers) [41].

To immobilise the cells for examination, the cells were chemisorbed to cleaned glass slides [10] by first coating the slides with poly-L-lysine (Sigma). In a Petri dish, 1 mL of poly-L-lysine was pipetted over each slide and placed in a laminar flow hood to dry for 10 minutes. While the slides dried, 30 mL of cell culture was divided between 2 centrifuge tubes and wrapped in Parafilm^{TM} to prevent leakage. Tubes were centrifuged at 1360 xg for 15 minutes, after which time the supernatant was eluted and replaced with a like volume of 0.1 M 2-(N-Morpholino)ethanesulfonic acid (MES) buffer (Aldrich) at pH = 7.1. Tubes were vortexed to resuspend the cell pellets, and the contents were poured over the dry glass

slides. The Petri dish was then covered and placed on a shaker table for 20 minutes to allow the cells to adhere.

After 20 minutes, the slides were placed on filter paper to remove excess liquid. Slides were affixed to the AFM stage using double-sided carbon tape, and the AFM was configured for TappingMode^{TM} in liquid per the manufacturer's instructions. AFM images were captured for each cell found, and five force cycles per cell were recorded with the drive amplitude set to zero (approximating contact mode) for analysis. For consistency in measurements, force curves were measured at the same point on each cell, defined as the intersection of segments drawn axially and radially across the topographical image [42]

Prior to cell probe fabrication, cantilevers were placed under ultraviolet light for 5 min to remove any adsorbed water and/or hydrocarbons, which may be present from the manufacturing process. Cantilevers were then held in forceps and sonicated for 1 min in ddH_2O, followed by sonication for 1 min in reagent grade ethanol (Aldrich). They were then placed tips-up on a clean glass microscope slide. 50 µL of 1-hexadecanethiol (HDT) stock solution (10 mM in reagent-grade ethanol) was then pipetted onto the tips.

Cells were attached to the AFM tips using 1-hexadecanethiol (HDT). This chemical has been used extensively in attaching cells to different substrata, since it readily forms a self-assembled monolayer (SAM) on a variety of glasslike and metal substrata [26, 30]. The HDT is dissolved in reagent-grade ethanol, and, as the ethanol evaporates, the molecules orient such that the thiol moiety forms a covalent sulfide linkage to the cantilever surface, with the alkyl chain extending into the bulk phase. Microbial cells, which carry a negative net charge under physiological conditions, will therefore possess charged carboxyl and/or hydroxyl groups. When these groups contact the methyl terminus of the HDT chain, a covalent ester bond is formed, anchoring the cells to the tip.

2.3.3 Cell Probe Preparation

Attachment of a single *C. parapsilosis* cell to an AFM cantilever was accomplished using a custom-designed micromanipulator with extension arm (stages from Edmund Industrial Optics, Barrington, NJ). The unit was capable of translating in three axes with 1 µm accuracy. A single silicon nitride chip, with two triangular cantilevers, was attached to the

extension arm using double-sided tape. 25 μL of cell culture at an approximate cell density of 1x10^{11} cells $\cdot$ mL^{-1} was delivered via pipette to a channel of comparable volume etched into a PTFE block. The cantilever was oriented over the cell culture droplet such that both the tips on the cantilever and the droplet were simultaneously visible under a stereoscope (SMZ-10A, Nikon). The cantilever was then moved vertically downwards to the droplet surface until the tips were submerged, and left for 5 minutes to allow cell adhesion to the HDT anchors.

The cantilever was carefully withdrawn from the droplet, dried for 5 minutes in a laminar flow hood, and viewed with an optical microscope (Eclipse E400, Nikon) equipped with an ultraviolet ($\lambda = 330 - 380$ nm) filter cube to verify attachment. *C. parapsilosis* is weakly autofluorescent in UV wavelengths, eliminating the need for chemical staining to verify attachment. We found that the short, fat cantilever gave the best reproducibility in immobilising the cells.

2.3.4 Scanning Electron Microscopy

In order to further verify cell adhesion and orientation on the cantilevers, six cellular probes were prepared for analysis with a scanning electron microscope (Amray 1610 Turbo, Bedford, MA). After treatment, cantilever chips were placed in a desiccator for 4 days to dehydrate the chemisorbed cells. They were then mounted on an SEM sample holder with carbon tape and placed in a Desk II Cold Sputtercoater (Denton Vacuum, Moorestown, NJ) and coated for 20 seconds at 45 mA. Gold-coating of the samples is necessary to increase overall sample electron density, making the cells visible to the electron beam.

After coating, the samples were placed in the SEM chamber, which was then closed and isolated to a vacuum pressure of $10^{-6} - 10^{-7}$ torr (abs). The SEM was calibrated at an acceleration potential of 20 kV, and each intact cantilever was examined at four points (each cantilever leg, the base between the legs, and the tip) for the presence of bound cells. Images were captured for each cell, at magnifications of 5.0 kX to 15.0 kX.

It should be noted that this experiment was done only to verify attachment, and identify preferred attachment sites. Since the cells were not chemically fixed prior to desiccation in this experimentation, we expected significant morphological changes as the cells dried.

2.3.5 Approach Interactions at the Cell–Biomaterial Interface

With the cell probes prepared, it was now possible to measure the interactions between a biomaterial surface and the probe. Silicone rubber was chosen as a representative implant material for this study. Medical-grade silicone rubber tubing (VWR, 0.25" I.D.) was cut with sterile scissors to approximately 1 inch in length, and then sliced to allow access to the inner luminal surface. The section of silicone was then taped flat to the bottom half of a Petri dish to prevent curling. A 2 cm^2 area of silicone in the center of the dish was sufficiently flat for examination with the AFM. With a cell probe mounted in the AFM fluid cell, we manually focused the AFM optics on the sample surface. When the cantilever was approximately 2 mm from the sample surface, MES buffer (pH = 7.1) was pipetted to cover the cell probe.

After setting software parameters according to the manufacturer's instructions for fluid-based operation in TappingMode^{TM}, the AFM was engaged. Force cycles were recorded for 8 - 10 different areas with 3 data sets taken on each area. Biomaterials were also examined using an unmodified probe to compare with cell probe data, and surface roughness data were recorded to identify local surface features that could affect cell adhesion. Further, the biomaterials were examined using a probe coated with HDT only, to serve as an additional control for the effect of HDT-coated probes on force-separation interactions. In order to compare the affinities for each substrate (a bare probe with a cell bound to glass, and a functionalised probe on bare silicone and on a biofilm grown for three days on silicone), the retraction portion of each force cycle was processed. The magnitudes of the pull-off forces show the relative strengths of binding to each substrate after contact.

2.3.6 Approach Interactions at the Cell–Biofilm Interface

As an extension to the experimentation in Section 3.5, it was now of interest to characterise the interactions between spore probes and biofilms grown on silicone rubber. The parallel plate flow cell (Model FC-71, BioSurface Technologies Corporation, Bozeman, MT) (Figure 2.3.1) was opened and cleaned, after which a coupon of silicone rubber was fixed into the channel with double-sided tape.

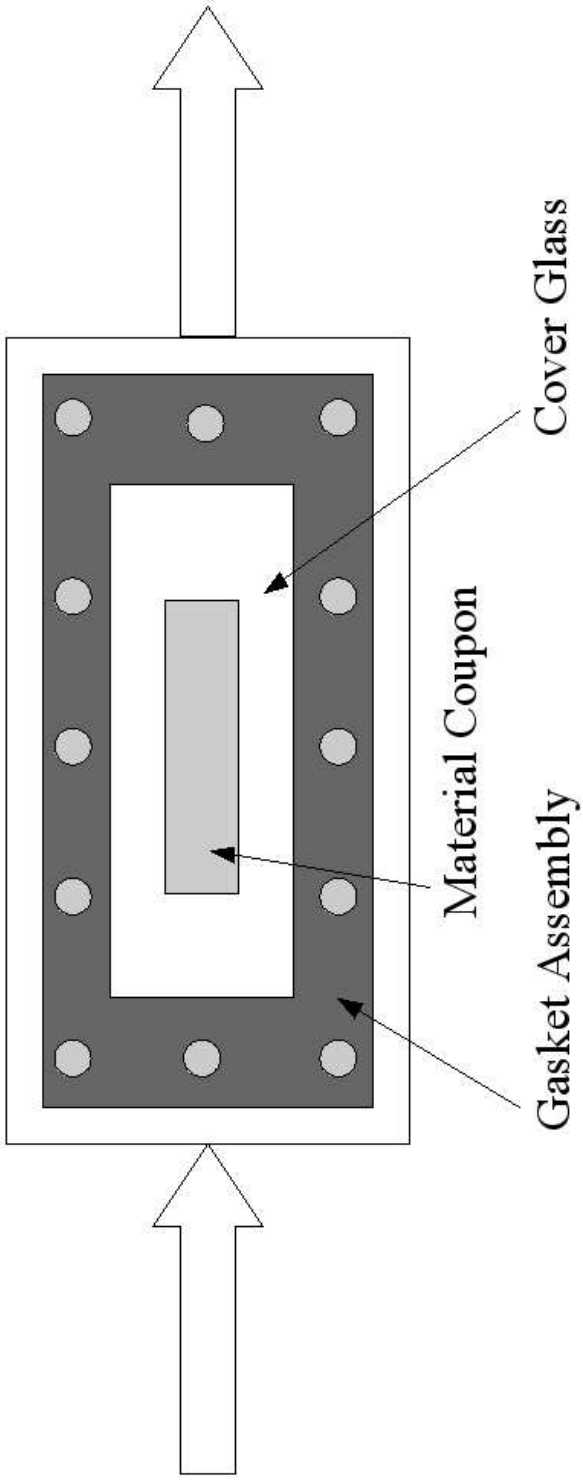

Figure 2.3.1: Schematic of the parallel-plate flow chamber used for biofilm growth. A channel etched into the base allows for placement of a biomaterial coupon inside the chamber without disrupting flow. Shear effects were minimised by setting the fluid velocity to 380 cm $\cdot$ min^{-1}, which correlates to $N_{Re} \approx 200$.

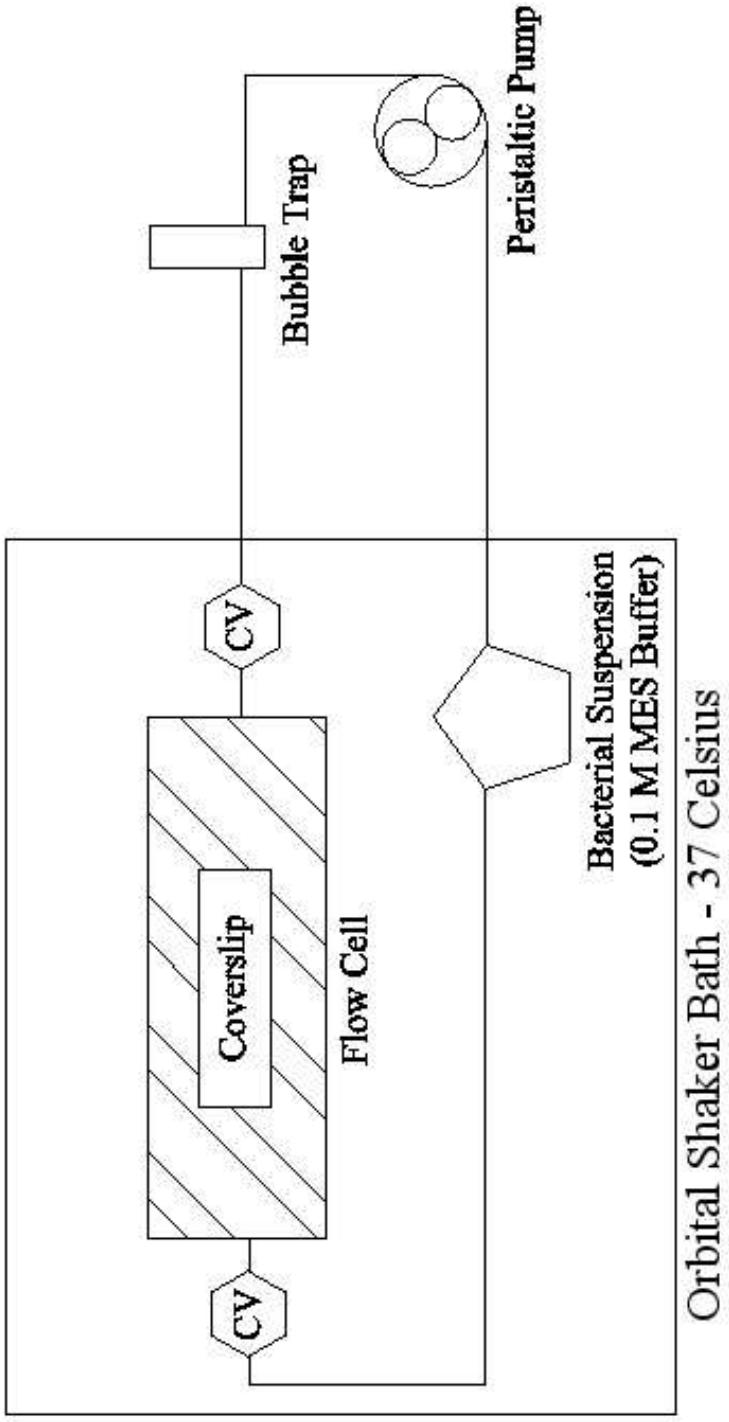

Figure 2.3.2: Schematic of the fluid circuit used to grow biofilms. The circuit is maintained at 37 °C to emulate *in vivo* conditions. Bacteria are suspended in MES buffer with no growth factors, allowing for examination of the initial events in biofilm formation without significant cellular reproduction.

The rubber was pressed gently with tweezers to ensure adhesion to the tape. A standard #2 (24 x 60 mm) microscope cover slip was then placed over the channel, followed by the flow cell gasket. The flow cell cover was then replaced, and screws were tightened to within two full turns of their final position. 0.125" I.D. silicone rubber tubing was fitted over the two access ports and secured with cable ties. Check valves were then placed in-line, and the entire unit was autoclaved at 121 °C for 20 minutes to sterilise. After cooling, the screws were tightened to prevent leakage during the experiment. The flow cell was held in a custom support brace inside the shaker bath cover and secured with silicone screws. The check valves were then connected to the feed and drain lines for the fluid circuit.

A 60 mL sample of *P. aeruginosa* ($O.D._{600} \approx 0.5$) was divided into four 15 mL centrifuge tubes, and sealed with Parafilm^{TM}. The tubes were centrifuged at 1360 xg for 15 minutes (25 °C), after which time the supernatant was eluted and replaced with a like volume of 0.1 M MES buffer (pH = 7.1). The tubes were re-sealed, vortexed to resuspend the cell pellet, and then added to a 250 mL flask of MES buffer. Additional MES buffer was added to the flask to bring the final volume in the flask to 250 mL. This flask served as a bacterial reservoir for use in the fluid circuit, shown in Figure 2.3.2.

The peristaltic pump (Manostat "Vera" Varistaltic Pump, Fisher Scientific) was fitted with 0.25" I.D. silicone rubber tubing and set to speed 4. This corresponds to a fluid velocity of 94.75 $\mathrm{cm \cdot min^{-1}}$, or a fluid Reynolds number of approximately 100. The low flowrate minimises the effect of shear on the nascent biofilm while still allowing the pump to operate in a non-pulsatile regime. The fluid circuit was maintained at 37 °C in an orbital shaker bath (Lab-Line), with minimal heat loss by convection in the tubing outside the bath. Cells were kept in suspension in the flask by agitation at 160 RPM. A bubble trap was installed in the feed line to damp any pulsatile behaviour caused by the peristaltic pump. The tubing was necked to 0.125" I.D. before the bubble trap for connection to the other units in the circuit. This increases the fluid velocity to 380 $\mathrm{cm \cdot min^{-1}}$, corresponding to $N_{Re} \approx 200$. The final level of fluid in the flask was recorded at the beginning of experimentation and checked hourly to verify that the circuit was not leaking. All connections in the circuit were secured with cable ties and wrapped with Parafilm^{TM} to prevent leakage.

Biofilms were allowed to grow for 1 or 3 days in the flow cell. After this time, the pump

was stopped and the check valves disconnected to maintain hydration of the biomaterial sample. The flow cell was then removed from the circuit and brought to the AFM, where the screws, cover, gasket and microscope coverslip were carefully removed. With a reserve of MES buffer at hand to periodically replenish any evaporating liquid, the AFM was configured with a cell probe and operated as before. The procedure was repeated with an unmodified cantilever for comparison.

2.3.7 Electrophoretic Mobility Analysis

In order to characterise the interaction energy profiles of the two model microbes, it was necessary to determine their surface potentials as a function of solution ionic strength. This quantity, taken as equal to the zeta potential of the microbes, may be related to the microbial electrophoretic mobility by Equation 1.8, or, if the microbes are considered soft, by Equation 1.13. The electrophoretic mobilities and surface potentials of both *C. parapsilosis* and *P. aeruginosa* were measured using a zeta potential analyser (Zeta PALS, Brookhaven, Holtsville, NY). Mid-exponential growth phase cultures were centrifuged at 1360 xg and resuspended in MES buffer (25 °C, pH = 7.1). Measurements were taken as a function of buffer ionic strength (Deionized water [I.S. $\approx$ 1x10^{-6} M], 0.02, 0.04, 0.06, 0.08, and 0.1 M). All measurements were recorded four times and averaged.

2.3.8 Microbial Interaction Energy Analysis

To determine the contribution of London-van der Waals forces to the interaction energy profiles, it is necessary to determine the Hamaker constant describing the microbe-AFM probe-fluid system. Being a function of the free energy components of the microbes, we may obtain the Hamaker constant by measuring the contact angles of microbial lawns under various liquids. Contact angles were recorded for both microbes under three liquids (water, formamide and diiodomethane) using a Rame-Hart NRL Contact Angle Goniometer (Model #100, Mountain Lakes, NJ) with 80 readings taken on both sides of each liquid droplet and averaged. Using Equation 1.11 and the contact angle data, we may solve three instances of the equation simultaneously to return values for the three surface free energy components (γ_M^{LW}, γ_M^+ and γ_M^-). The Hamaker constant is then calculated from Equation 1.12, and the

contribution of London-van der Waals interactions to the final energy profile is evaluated from Equation 1.9.

2.4 Experimental Results

2.4.1 Microbial Growth Curves

Growth curves for *P. aeruginosa* and *C. parapsilosis* are shown in Figure 2.4.1 and Figure 2.4.2, respectively. The absorbance data obtained were fitted using an exponential regression, since cells must be harvested from culture in the mid- to late-exponential phase of growth. Assuming a first-order logarithmic relationship between absorbance and cell growth, the form of this regression will follow the equation:

$$A_m = A_0 \, exp(\mu t) \tag{2.1}$$

where A_m is the measured optical density of the culture, A_0 is the optical density at time = 0 hrs, t is elapsed time, and μ is the specific growth rate, which is obtained from the regression of the data.

2.4.2 Cell Morphologies and Example Force Cycles

P. aeruginosa cells are rod-shaped, $2-3$ μm long and ≈1 μm in diameter. Measurements of the forces between the unmodified silicon nitride probe and individual cells of *P. aeruginosa* during the approach of the probe to the cell show interactions beginning at 80 nm from the cell surface (Figure 2.4.3). Only repulsive interactions exist for this cell during the approach portions of the force cycle, and reach a maximum value of 7 nN at the point of zero separation.

Morphologically, *C. parapsilosis* cells are spherical, with diameters of $4-6$ μm. The approach curves describing the interactions between an unmodified silicon nitride probe and individual cells of *C. parapsilosis* are shown in Figure 2.4.4. Interactions start at ≈80 nm from the cell surface, with a characteristic adhesion of 0.9 ± 0.4 nN at 55 nm, with a 6 nN repulsion at the cell surface.

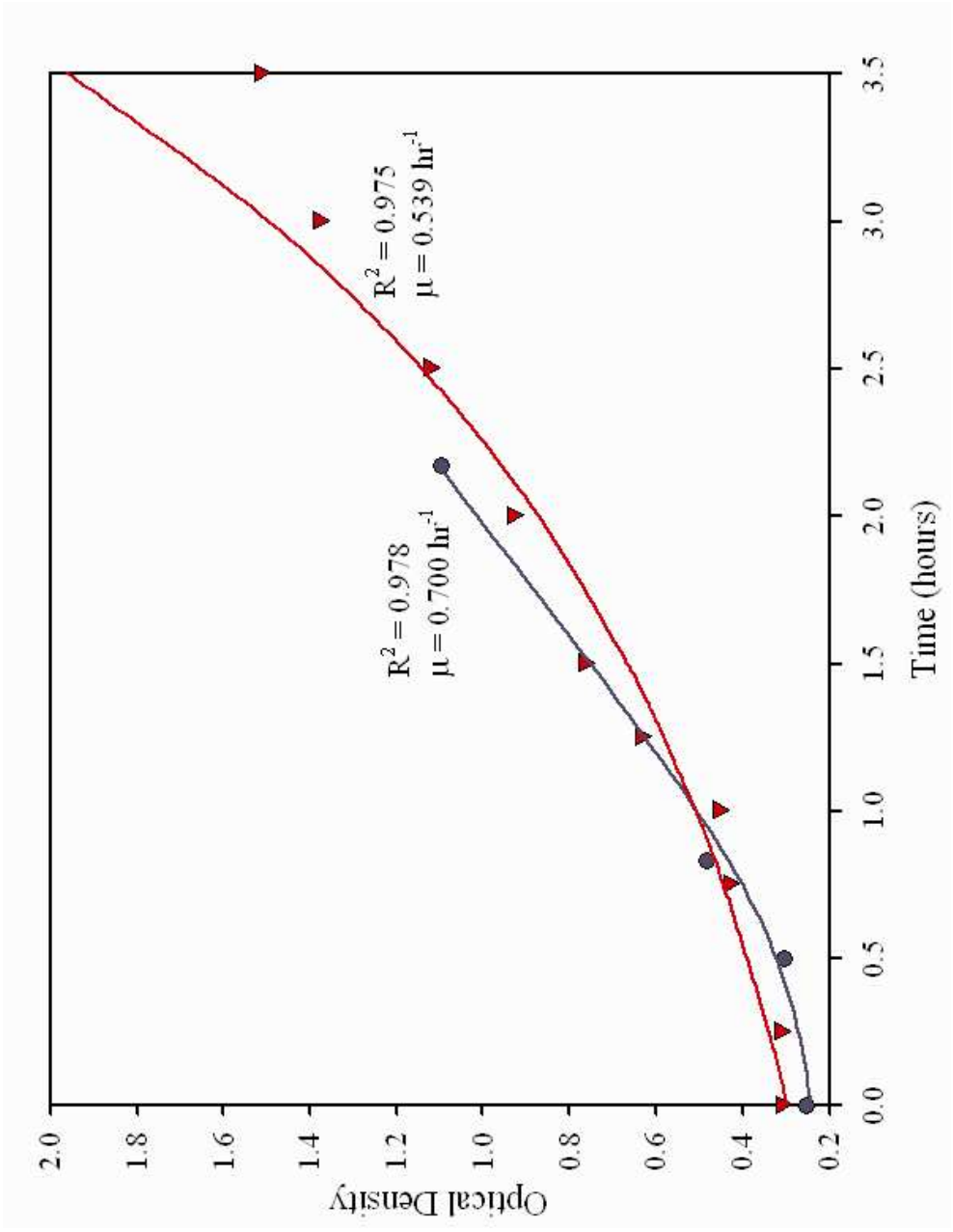

Figure 2.4.1: Growth curves and exponential regressions for *P. aeruginosa*. Different data sets represent duplicate experiments at the same experimental conditions.

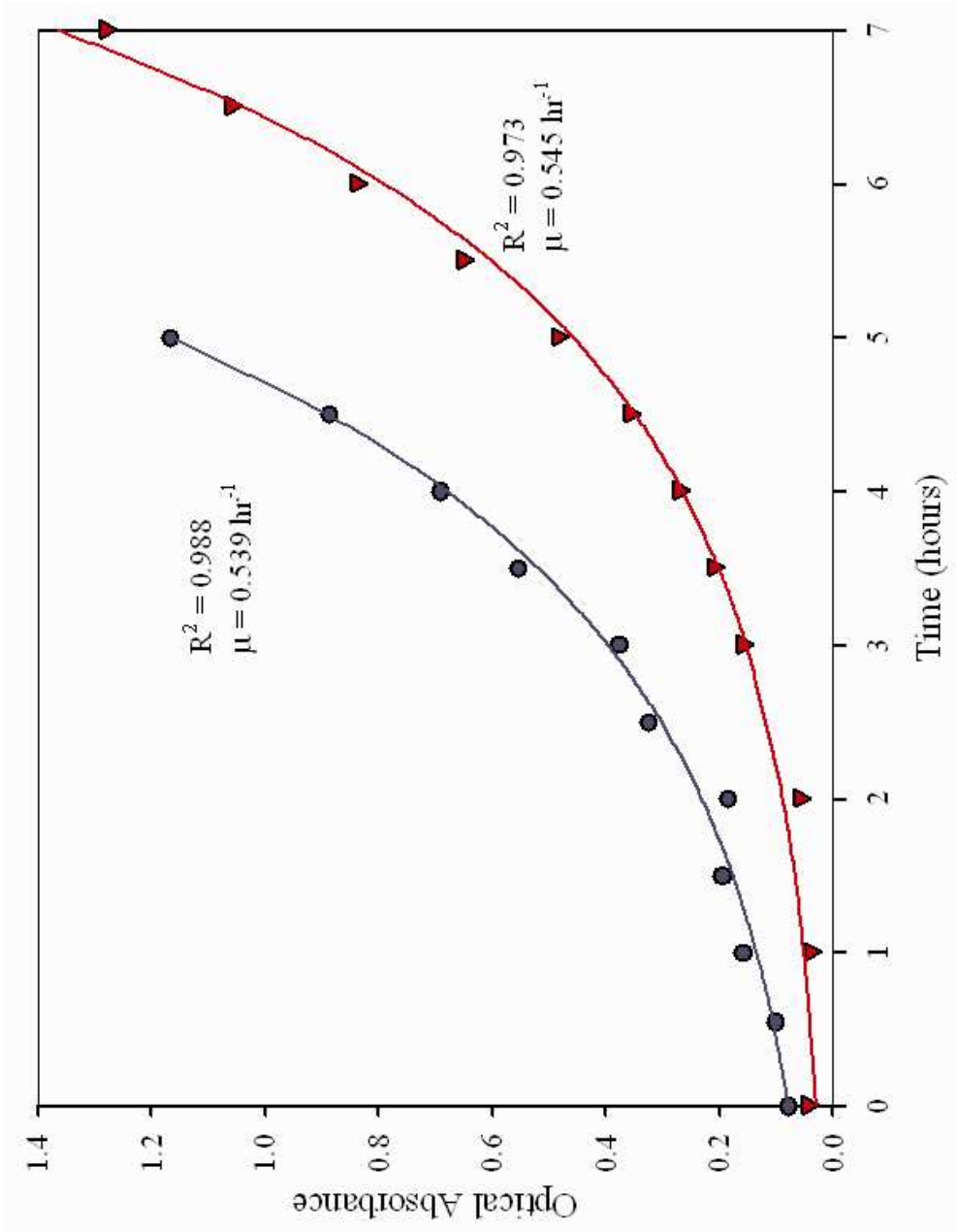

Figure 2.4.2: Growth curves and exponential regressions for *C. parapsilosis*. Different data sets represent duplicate experiments at the same experimental conditions.

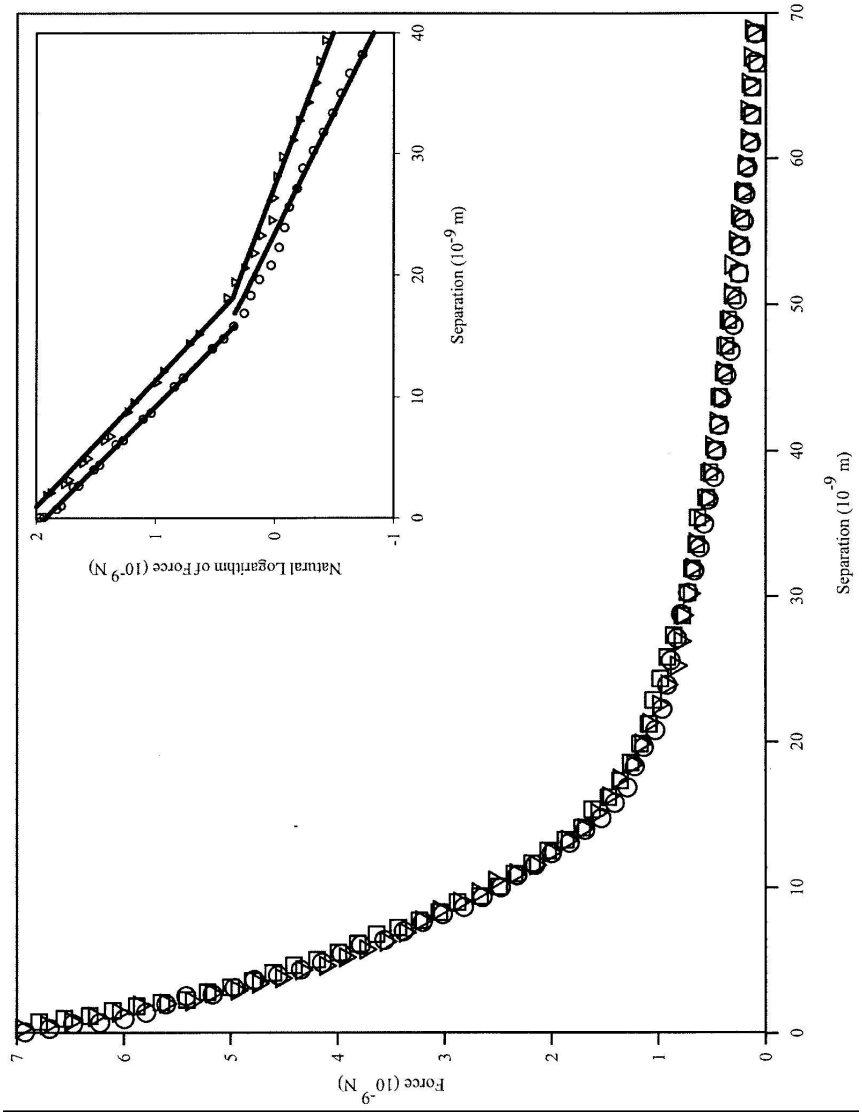

Figure 2.4.3: *P. aeruginosa* approach curves with an unmodified silicon nitride probe. Data shown represent five measurements on a single cell with the average of the five also plotted. Interactions begin at 80 nm from the cell surface, and are purely repulsive in nature. Repulsion at zero separation distance reaches a value of 8.5 ± 1.5 nN. The inset figure shows a semilogarithmic plot of force versus separation, where an inflection point is apparent at a separation of 17 nm. This may be indicative of a multi-polymer brush, or a change in the physicomechanical properties of the brush as separation distance decreases.

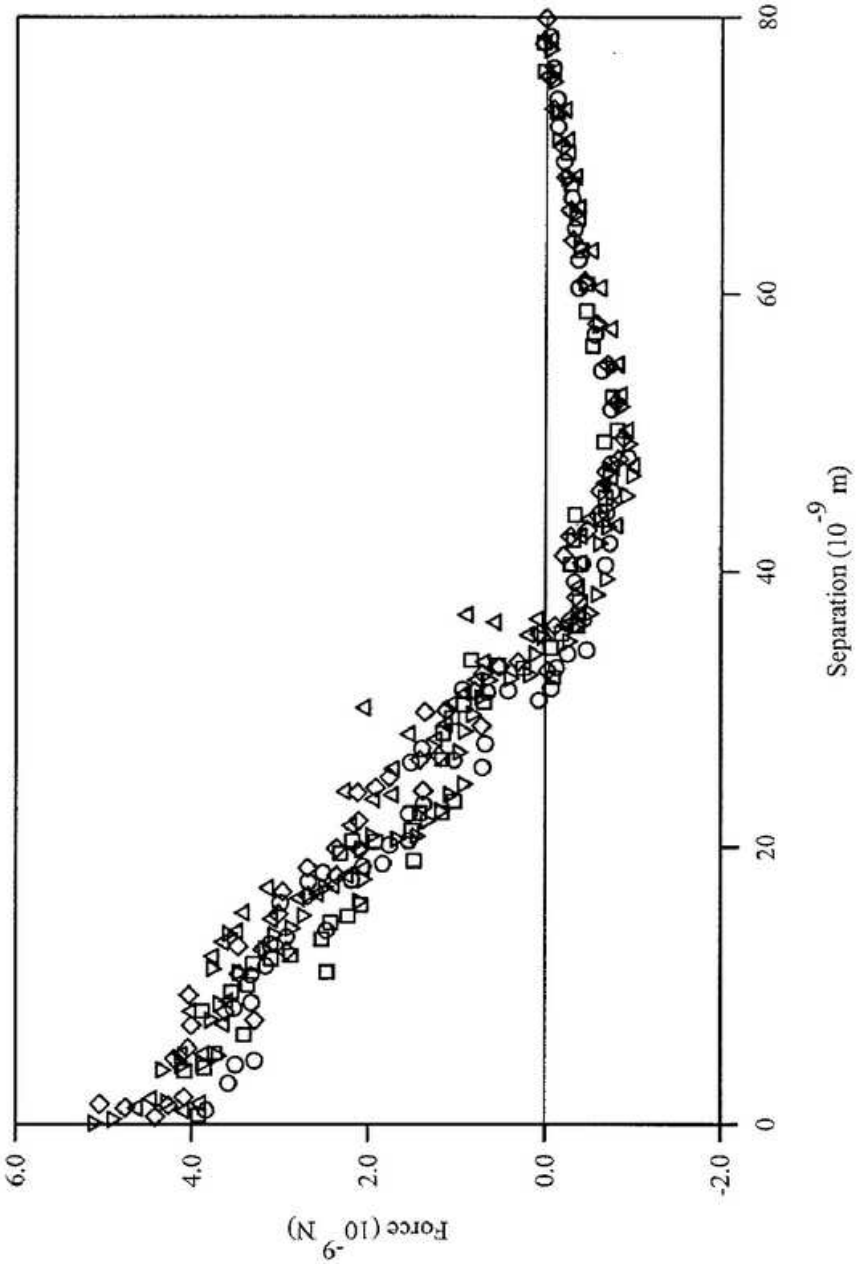

Figure 2.4.4: *C. parapsilosis* approach curves with an unmodified silicon nitride probe. Data shown represent five measurements on a single cell with the average of the five also plotted. An attractive interaction begins at 80 nm from the cell surface with a final magnitude of 1 nm. Repulsion at zero separation distance reaches a value of 4.5 ± 0.3 nN.

2.4.3 Cell Probe Preparation and SEM Analysis

After preparation of the cell probes, we verified adhesion and placement of the cells on the cantilevers. Examination of the cellular probes with SEM showed cells bound to the cantilever, with multiple cells present in some cases (Figure 2.4.5).

It should be noted that, while structures matching the morphology of a *C. parapsilosis* cell were evident, a more rigorous assay should be performed in this verification step. The key issue that must be addressed is that of hydration, *viz.*, that after cells were attached, it was necessary to hold the cantilevers in a desiccator for several days to remove moisture and enhance adhesion of the gold coating prior to SEM analysis. This would, presumably, cause a "deflating" of the cell body as the water is removed. More complex chemical treatment of the cantilevers would be necessary to maintain cell morphology after desiccation.

Control AFM experiments using incrementally modified probes may be seen in Figure 2.4.6. Data for the bare probe using a glass substrate show clean interaction with the surface, with attractive minima beginning $10 - 15$ nm from the point of zero separation. Tips modified with hexadecanethiol show attractive events of slightly smaller magnitude, and also being $5 - 10$ nm further from the surface, as compared to the bare tips. Interactions for the *C. parapsilosis*-modified probe are widely different from both control experiments, having attractive force magnitudes much less than the bare and HDT-modified probes. Also, the interactions begin at ≈ 80 nm from the point of zero separation, and are followed by repulsive interactions, presumably attributable to cell surface structures. The profile of this latter experiment agree with those seen for *C. parapsilosis* bound to glass and examined with a bare silicon nitride probe (Figure 2.4.4), and also exhibit force magnitudes ≈ 0.5 nN smaller than those experiments.

2.4.4 Approach Interactions at the Cell-Biomaterial Interface

On examination of the silicone rubber with a cell probe, distinct attractive profiles (areas of negative force) are evident in each approach curve (Figure 2.4.7). Interactions begin at 60 nm from the cell surface, and reach a magnitude of approximately 2.5 nN at the cell surface. Both the magnitude and the distance of these interactions are larger than for a bare

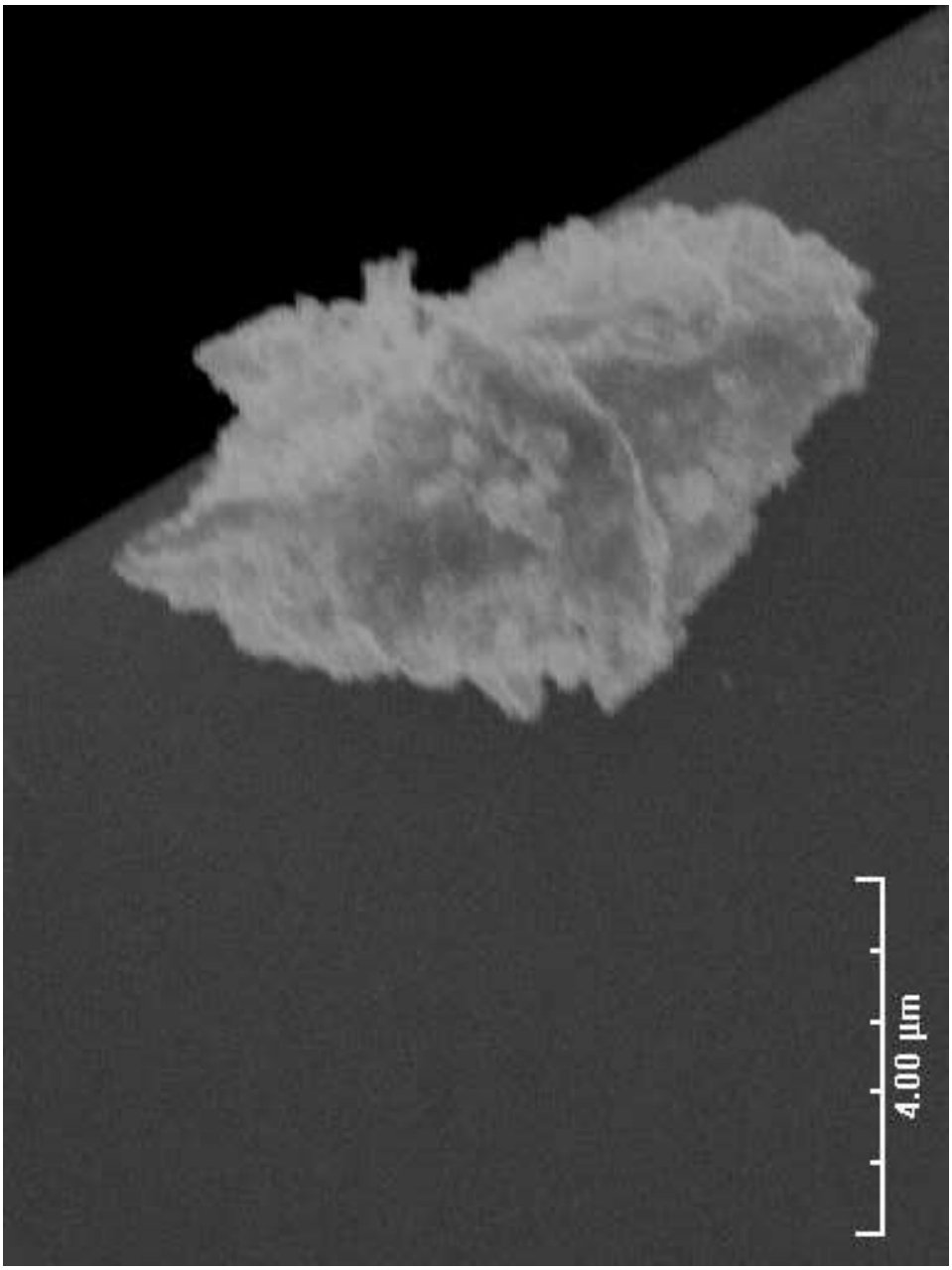

Figure 2.4.5: Scanning electron micrograph of a single, dehydrated *C. parapsilosis* cell bound to a DNP-S AFM cantilever. Image magnification is 7.0 kX.

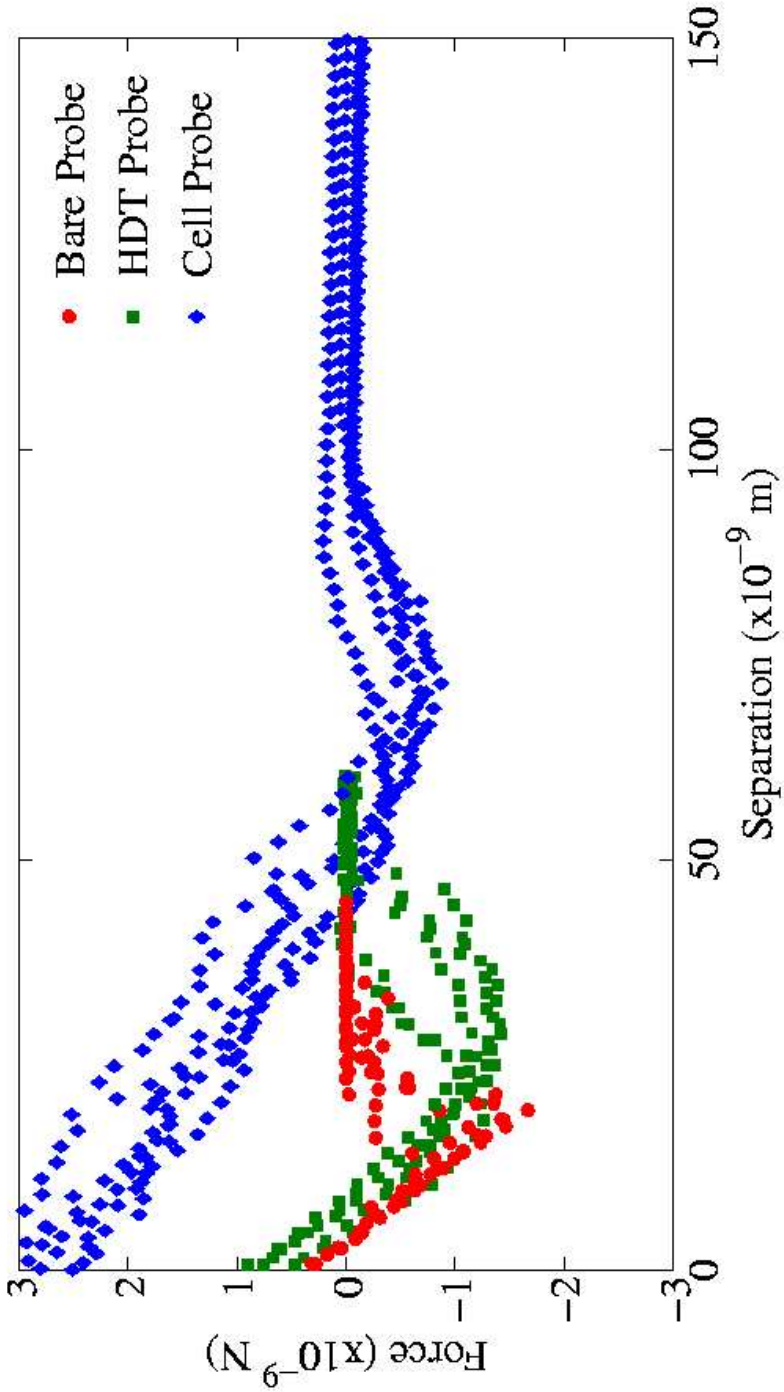

Figure 2.4.6: Control studies for cell probes. For the bare tips, we see clear attractive events taking place starting at $10 - 15$ nm from the substrate surface. Tips coated with HDT have a less regular profile, are slightly smaller in magnitude, and also begin $5 - 10$ nm further from the point of zero separation as compared to the bare tip. Cell probes have a widely different profile, with the attractive interaction beginning ≈ 80 nm from the point of zero separation, and include a repulsive segment after the attraction. This profile is consistent with that seen for *C. parapsilosis* bound to glass using an unmodified probe (Figure 2.4.4.

probe and one modified with HDT.

This range of force interactions may result from heterogeneity in the biomaterial surface, allowing the immobilised cell to interact with discrete areas of the substrate. Surface roughness may be characterised by imaging a representative area of the material using an unmodified cantilever (Figure 2.4.8).

The image is then processed to obtain the Root Mean Square roughness (R_q), which is based on Equation 2.2 [20]. The R_q value obtained from this equation represents the standard deviation of height differences within a given area.

$$R_q = \sqrt{\frac{\sum_{i=1}^{M} (Z_i - Z_{Ave})^2}{M}} \tag{2.2}$$

where Z_i is the height in a given area, Z_{Ave} is the average height of the entire area, and M is the number of points in that area. Ten images (*v.i.* Figure 2.4.8) were processed according to Equation 2.2 to calculate an average R_q of 40 ± 12 nm (SD) on silicone rubber.

The surface also shows distinct repeating domains, which may influence the interactions of microbial surface structures with the biomaterial, showing different affinities for a "peak" or a "valley". To investigate this qualitatively, we compared the retraction portions of the force cycles (Figure 2.4.9) for a bare cantilever on cells bound to glass, and with functionalised probes on bare silicone and a biofilm grown for 3 days on silicone. Data shown represent the different force-distance interactions seen for three substrate/probe combinations.

The strongest interactions occur in the biofilm/cell probe system, with an attractive magnitude of ≈35 nN at 40 nm from the surface. Further, this system shows multiple minima in the retraction curve, indicating that multiple polymers take part in the total interaction. For the silicone rubber/cell probe system, we see a single peak with magnitude of ≈18 nN, suggesting that only a single polymer plays a significant role in this interaction. The fact that the interaction occurs over such a long range also indicates that the polymer is elastic and flexible. Both of these interactions are an order of magnitude stronger than those seen for *C. parapsilosis* probed with an unmodified DNP-S probe.

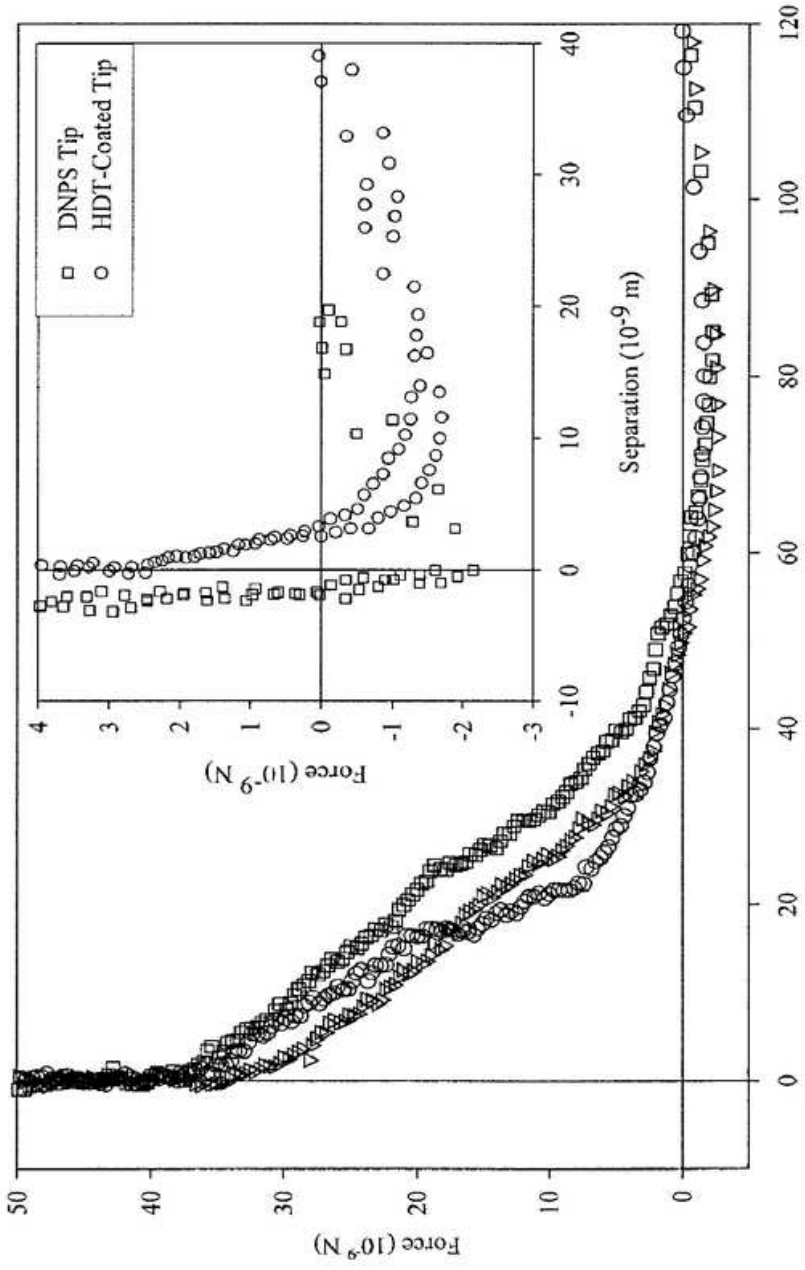

Figure 2.4.7: Approach curves for a *C. parapsilosis*-modified cantilever approaching a bare silicone rubber surface. The inset figure shows curves for a bare cantilever (squares) and an HDT-coated cantilever (circles) on the same material. Attractive events exist for each system. The modified probe has the strongest interactions with the cell-modified cantilever, and the weakest interactions with the HDT-modified cantilever.

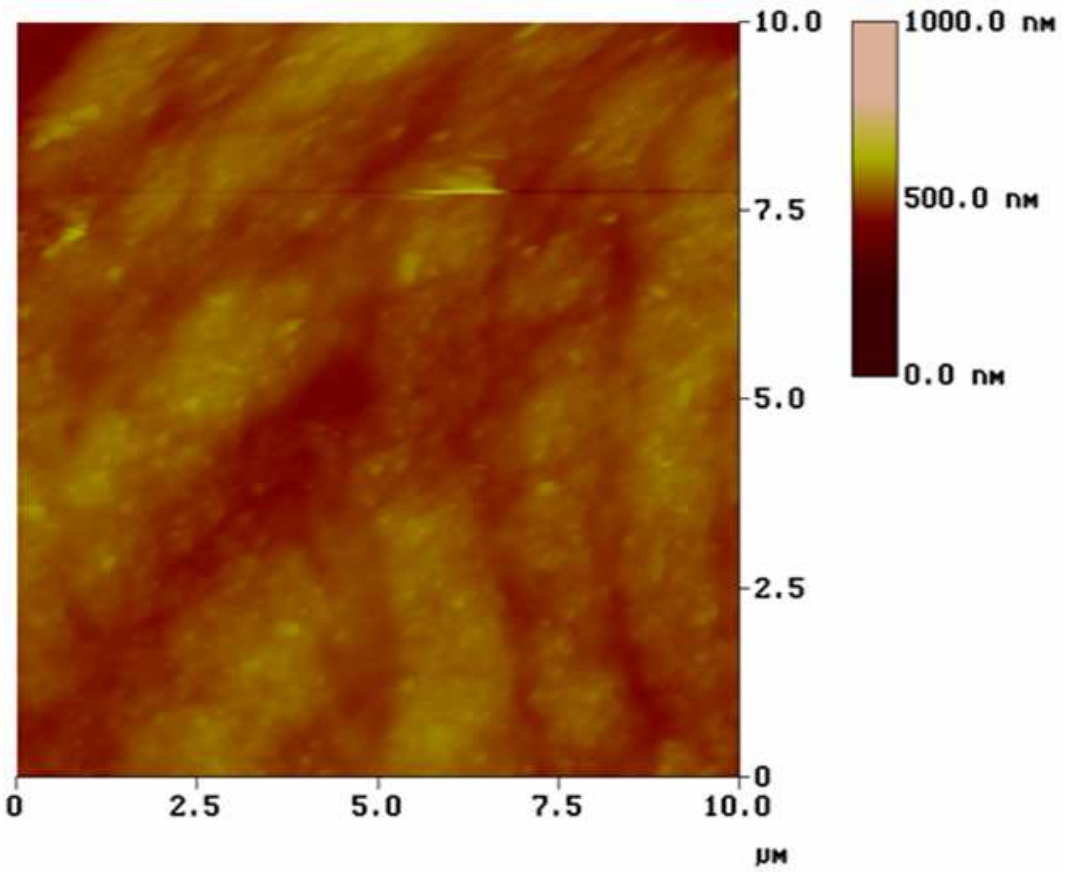

Figure 2.4.8: TappingMode^{TM} AFM image of silicone rubber under 100 mM MES buffer (pH = 7.1). The image shows distinct domains on the surface of the material, offering different areas (possibly with different adhesive affinities) for microbes to adhere. Since the cell is large compared to these domains, it is likely that it will interact simultaneously with more than one of these domains.

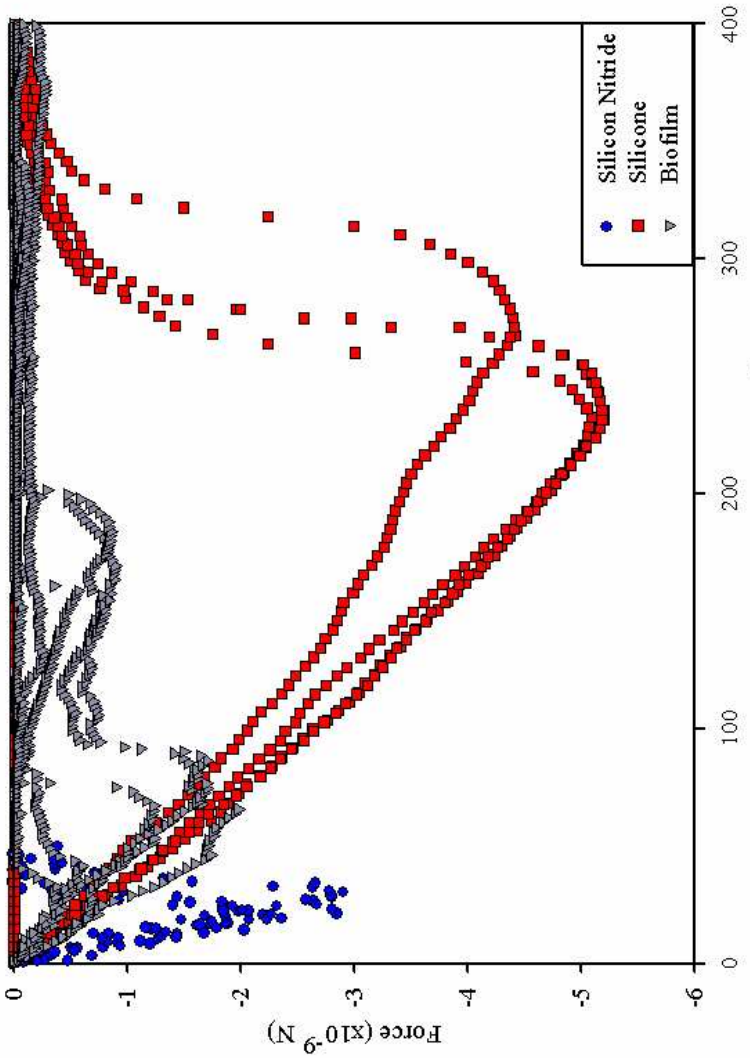

Figure 2.4.9: Retraction for *C. parapsilosis*-modified probes on different substrata. One can see that the cells show the highest affinity for silicone rubber, with a pull-off distance of ≈240 nm and an adhesive force of 4.5 – 5.5 nN. Pull-off distances in a biofilm system are significantly shorter, and occur in different places, indicating a number of different polymers interacting with the cell probe. Interactions between the bare silicon nitride cantilever and *C. parapsilosis* are shown for comparison.

2.4.5 Approach Interactions at the Cell-Biofilm Interface

AFM approach curves using a modified probe to examine a nascent biofilm surface may be seen in Figure 2.4.10. Data shown are representative of a biofilm grown for 3 days. Interactions begin at ≈250 nm from the biofilm surface, initially showing repulsion. This repulsion reaches a maximum magnitude of 2.8 nN, and is immediately followed by an attractive interaction with a maximum magnitude of 5 nN. Data were identical for biofilm growth experiments lasting 1 and 3 days in the parallel plate flow chamber, suggesting that, without growth factors, adhesion and detachment of bacteria to the surface reach a steady state relatively quickly.

2.4.6 Electrophoretic Mobility Analysis

Over the range of ionic strengths, the zeta potential for *P. aeruginosa* increases from −7.96 mV at 20 mM to −3.35 mV at 100 mM (Table 2.4.1).

We see more variation as a function of ionic strength among the data for *C. parapsilosis*, which covers a range of zeta potentials from −6.28 to − 3.35 mV. Further, the data do not follow a steady increasing trend, as do data for *P. aeruginosa*. As expected, for both microbes, lower values for zeta potentials are calculated using soft-particle theory compared to rigid DLVO with the Smoluchowski equation. The exception is at low ionic strengths, where soft-particle DLVO theory is least able to represent experimental results [1].

2.4.7 Microbial Interaction Energy Analysis

Using two polar (water and formamide) and one non-polar (diiodomethane) liquids, contact angles on microbial lawns may be translated into surface free energy components. Both microbes are relatively hydrophilic, but *C. parapsilosis* ($\theta_W = 15.17 \pm 11.5^\circ$ (SD)) is more hydrophilic than *P. aeruginosa* ($\theta_W = 24.42 \pm 1.5^\circ$ (SD)) (Table 2.4.2). These values, and the corresponding surface free energy components, differ significantly from published values for *P. aeruginosa* Olin [15] and *C. parapsilosis* Strain 294 and Strain 289 [14]. Since values for the strains examined in this study were not available, differences in contact angle are expected, owing to differences between the strains.

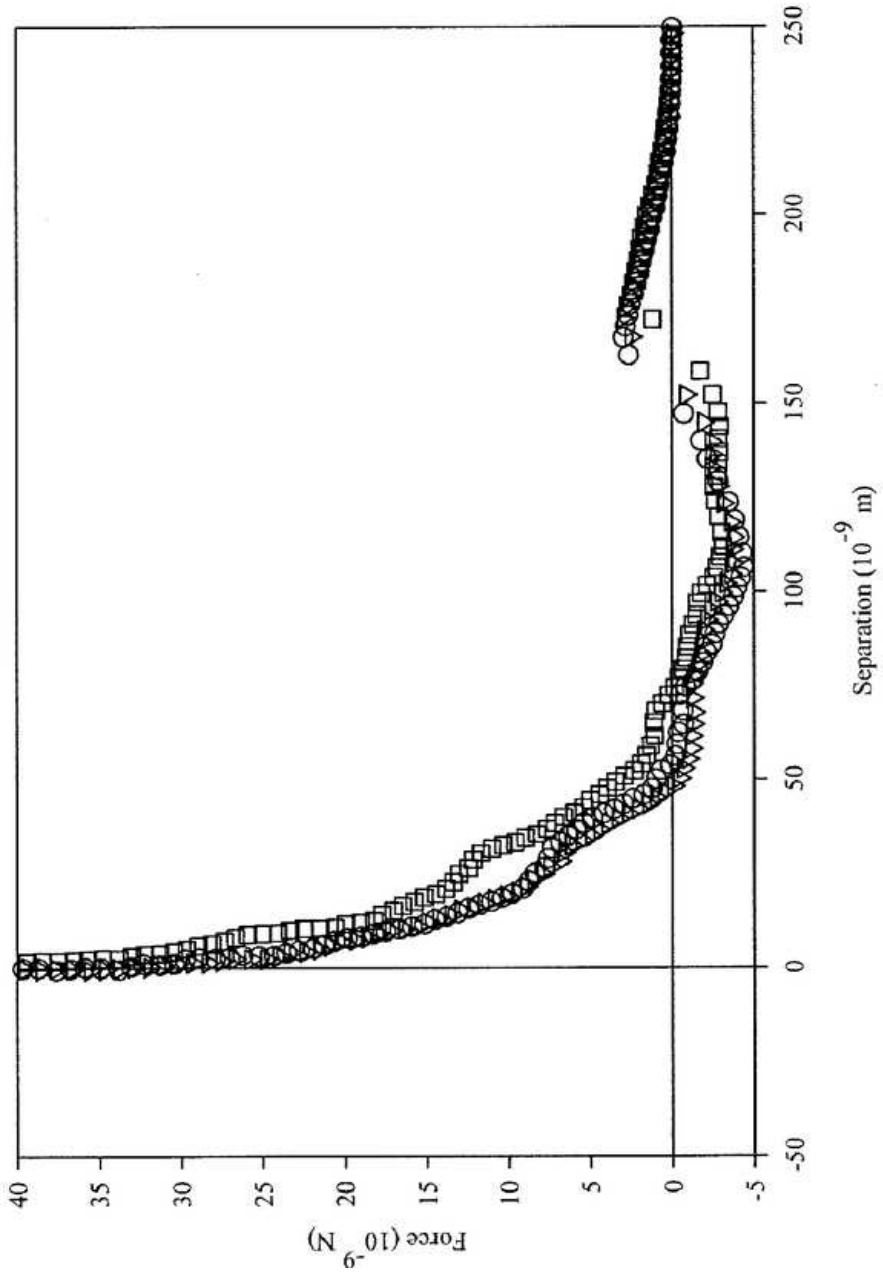

Figure 2.4.10: Approach curves with a *C. parapsilosis*-modified probe on a bacterial biofilm grown for three days on silicone rubber. A repulsive interaction begins at ≈250 nm from the cell surface. Repulsions are followed by attractive events, with magnitudes of 3.7 ± 0.64 nN at ≈115 nm.

Table 2.4.1: Zeta potential measurements for *C. parapsilosis* and *P. aeruginosa*

Note[1]	**pH**	ζ_{Smol}[2] (x10^3 V)	**EM**[3] (x10^8 $m^2 \cdot V^{-1} \cdot s^{-1}$)	Ψ_0[4] (x10^3 V)
C. parapsilosis				
20 mM	6.81	-5.1	-0.39 ± 0.01	-6.2
40 mM	6.84	-4.5	-0.35 ± 0.18	-3.1
60 mM	6.99	-3.4	-0.26 ± 0.11	-2.1
80 mM	7.01	-6.3	-0.49 ± 0.10	-1.6
100 mM	7.03	-4.7	-0.37 ± 0.10	-1.3
P. aeruginosa				
20 mM	6.95	-8.0	-0.62 ± 0.14	-10.3
40 mM	6.98	-6.7	-0.52 ± 0.07	-5.3
60 mM	6.99	-4.4	-0.34 ± 0.08	-3.6
80 mM	7.01	-5.4	-0.42 ± 0.28	-2.7
100 mM	7.01	-3.4	-0.26 ± 0.10	-2.2

[1] All samples were grown at 37 °C until $OD_{600} = 0.5$ and suspended in MES buffer with varying ionic strength to a cell concentration of 1 x 10^8 cells $\cdot mL^{-1}$

[2] Zeta potential as calculated from the Smoluchowski Equation

[3] Average electrophoretic mobility of microbial culture (n=4) with standard deviations of repeated data sets

[4] Surface potential as calculated from the soft-particle DLVO theory; this is equivalent to the zeta potential of the solution [40]

Simultaneous solution of three instances of the van Oss-Chaudhury-Good equation yields the three surface tension components (Table 2.4.2). The values of the apolar surface tension component are then used to calculate the Hamaker constants (Equation 1.12), which have values of $[6.71 \pm 0.12]\text{x}10^{-20}$ J (SD) for *C. parapsilosis*, and $[5.12 \pm 0.03]\text{x}10^{-20}$ J (SD) for *P. aeruginosa*. Values for both strains are in good agreement ($< 1\text{x}10^{-21}$ J variation) with literature values of similar strains [14, 15].

Interaction energy curves for *P. aeruginosa* and *C. parapsilosis* may be seen in Figure 2.4.11 and Figure 2.4.12, respectively. Shown are the total, van der Waals and electrostatic interactions, as calculated from soft-particle DLVO and classical DLVO theories in 100 mM MES buffer.

For classical DLVO calculations, the Smoluchowski equation 1.8 was used for calculation of microbial surface potentials. *C. parapsilosis* shows no energy barrier preventing adhesion using soft-particle theory, and, in fact, an adhesion of 5.86 k_BT is predicted by the model. An electrostatic repulsion of 18.4 k_BT, located at 0.3 nm, exists in the calculation based on classical theory. *P. aeruginosa* shows a 4.83 k_BT electrostatic repulsion at 0.1 nm using classical DLVO theory, while at the same distance this repulsion has a magnitude of 7.00 k_BT using soft-particle DLVO theory. For both microbes, these small repulsions are greatly outweighed by van der Waals interactions, showing overall negative interaction energy, *e.g.,* attraction, at very small separation distances. Neither classical nor soft-particle DLVO theory agrees with the behaviour seen in AFM force curves (Figure 2.4.3 and Figure 2.4.4). The models used, however, only account for van der Waals and electrostatic interactions. The fact that there is little difference between the two theories also indicates that the softness of the sample is unimportant in the overall interactions of the microbes. As such, the behaviour shown in the force curves are not significantly influenced by either electrostatic or London-van der Waals interactions.

2.4.8 Steric Interactions with the Microbial Polymer Brush

The approach curves were fitted using a scaling model for a polymer brush interacting with a bare, flat surface, with the grafted polymer density and equilibrium polymer length as fitting parameters. Graphical fits may be seen in Figure 2.4.13 for *C. parapsilosis* and

Table 2.4.2: Microbial contact angle and surface tension data

Parameter[1]	*C. parapsilosis*	*P. aeruginosa*
pH	7.03	7.01
θ_W (°)[2]	15.17 ± 11.5	24.42 ± 1.5
θ_F (°)[3]	13.41 ± 1.4	32.28 ± 3.9
θ_D (°)[4]	46.63 ± 1.2	61.69 ± 0.3
γ_M^{LW} ($\mathrm{mJ \cdot m^{-2}}$)[5]	36.13 ± 0.65	27.56 ± 0.15
γ_M^+ ($\mathrm{mJ \cdot m^{-2}}$)[6]	1.96 ± 0.39	2.05 ± 0.57
γ_M^- ($\mathrm{mJ \cdot m^{-2}}$)[7]	51.94 ± 6.42	60.29 ± 3.55
A (10^{20}) J	6.71 ± 0.12	5.12 ± 0.03

[1] Microbes were examined under three liquids (water, formamide, and diiodomethane). By using the van Oss-Chaudhury-Good equation for the three liquids [40], the three components of surface tension may be calculated. Hamaker constants (A) follow directly from values of γ_M^{LW}. Standard deviations of repeated data sets are shown.

[2] Contact angle of microbial lawn under $\mathrm{ddH_2O}$.

[3] Contact angle of microbial lawn under formamide.

[4] Contact angle of microbial lawn under diiodomethane.

[5] Apolar (Lifshitz-van der Waals) component of microbial surface free energy.

[6] Electron-accepting parameter of the polar microbial surface free energy.

[7] Electron-donating parameter of the polar microbial surface free energy.

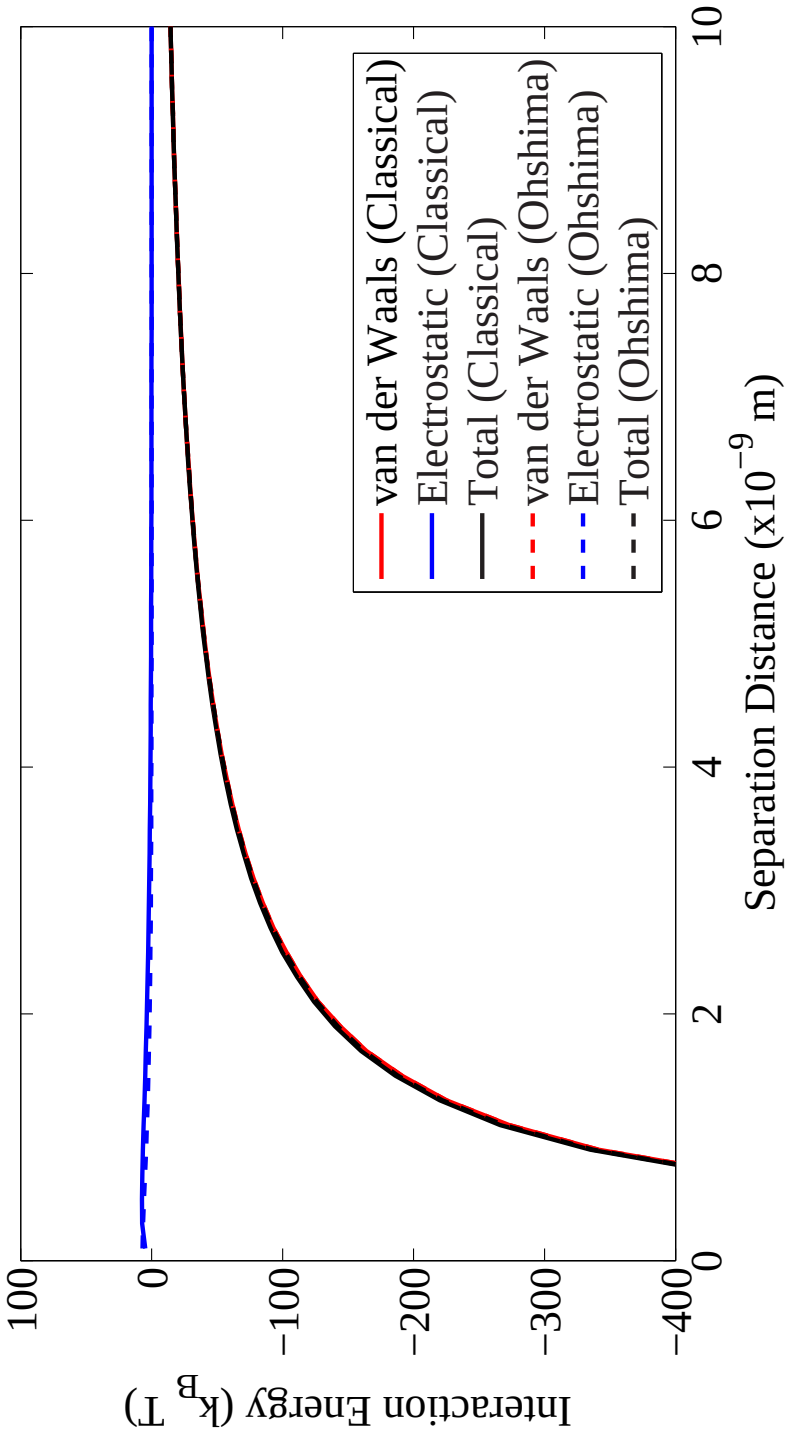

Figure 2.4.11: Interaction energies for *P. aeruginosa* in 100 mM MES buffer. Shown are total energy and the individual contributions for van der Waals and electrostatic interactions, with the differences between soft-particle (blue) and classical (red) DLVO theories. The two show nearly identical results, save for small differences in electrostatic interactions at very short (<4 nm) separation distances.

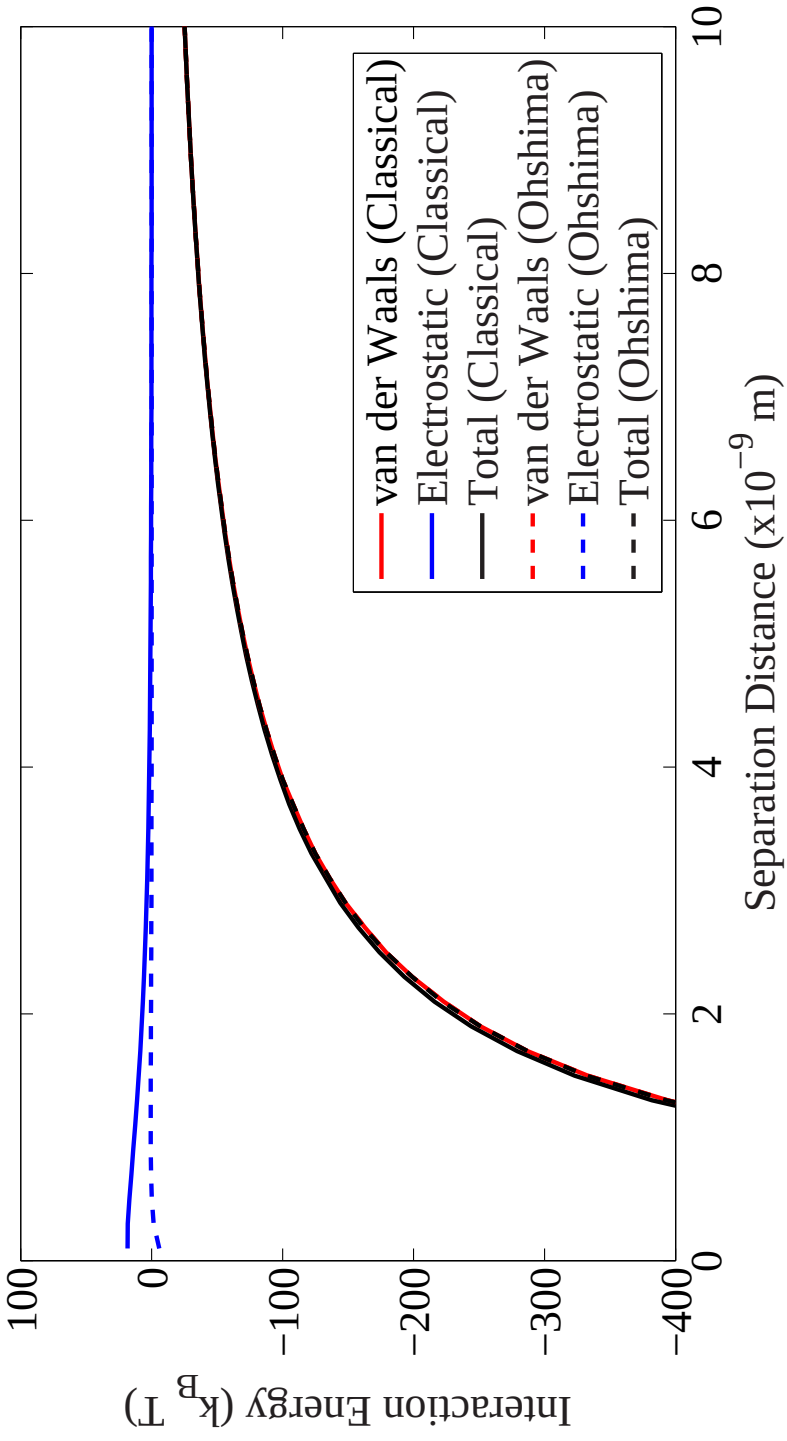

Figure 2.4.12: Interaction energies for *C. parapsilosis* in 100 mM MES buffer. Shown are total energy and the individual contributions for van der Waals and electrostatic interactions, with the differences between soft-particle (blue) and classical (red) DLVO theories. The two show nearly identical results, save for small differences in electrostatic interactions at very short (<4 nm) separation distances.

in Figure 2.4.14 for *P. aeruginosa*. The steric model behaves as a decaying exponential function, and, as such, adhesive behaviour (*e.g.,* forces < 0 for the case of *C. parapsilosis*) cannot be predicted by the model. The repulsive portion of these data is fitted with the steric, with the regression ending before the first negative point.

C. parapsilosis force-distance interactions demonstrate excellent agreement with the steric model for the repulsive portion of the curve (Figure 2.4.13). Values of the fitting parameters for this microbe may be seen in Table 2.4.3.

For *P. aeruginosa*, model fits showed excellent mathematical agreement with the collected data. It was evident, however, that the fit appeared poor at separation distances of ≈20 nm from the surface. To verify that the data indeed followed a decaying exponential function, the natural logarithm of the force was plotted against the separation distance (Figure 2.4.3, inset).

The result of this treatment showed an inflection point in the data set at the distance where the basic steric model fails to fit the data well. As such, we formulated an extension to the steric model which accounts for two polymer layers, each having a different grafting density and equilibrium polymer brush length. Fits with this extended model are shown in Figure 2.4.14, and the fitting parameters may be seen in Table 2.4.3.

For *P. aeruginosa*, fitting with the two-brush model postulated in Equation 1.19, we see excellent agreement with the data sets (R^2 >0.95). The model produces four values for the fitting parameters (shown in Table 2.4.3). Qualitatively, these correspond to the two polymer brushes suggested by the model, with the longer brush having a lower grafting density, and the shorter a higher density. Modeling the cell as a cylinder of radius 1 μm with two hemispherical endcaps, also of radius 1 μm, the grafting density for *P. aeruginosa* is 7.86x10^4 polymers $\cdot$ cell^{-1} of the longer polymers, and 3.96x10^5 polymers $\cdot$ cell^{-1} of the shorter polymers.

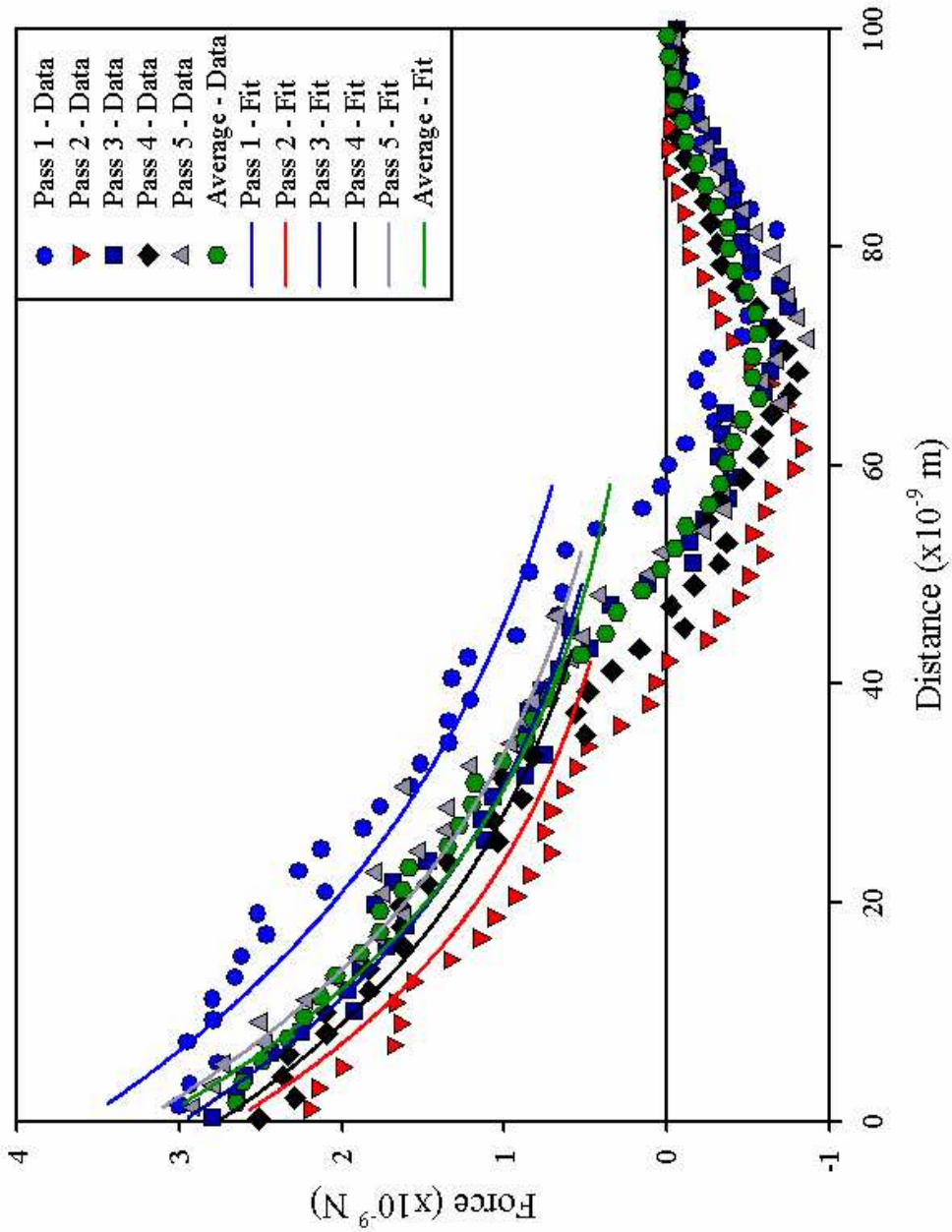

Figure 2.4.13: *C. parapsilosis* approach curves with an unmodified silicon nitride probe. Only the repulsive portion of the curve may be fitted with the model.

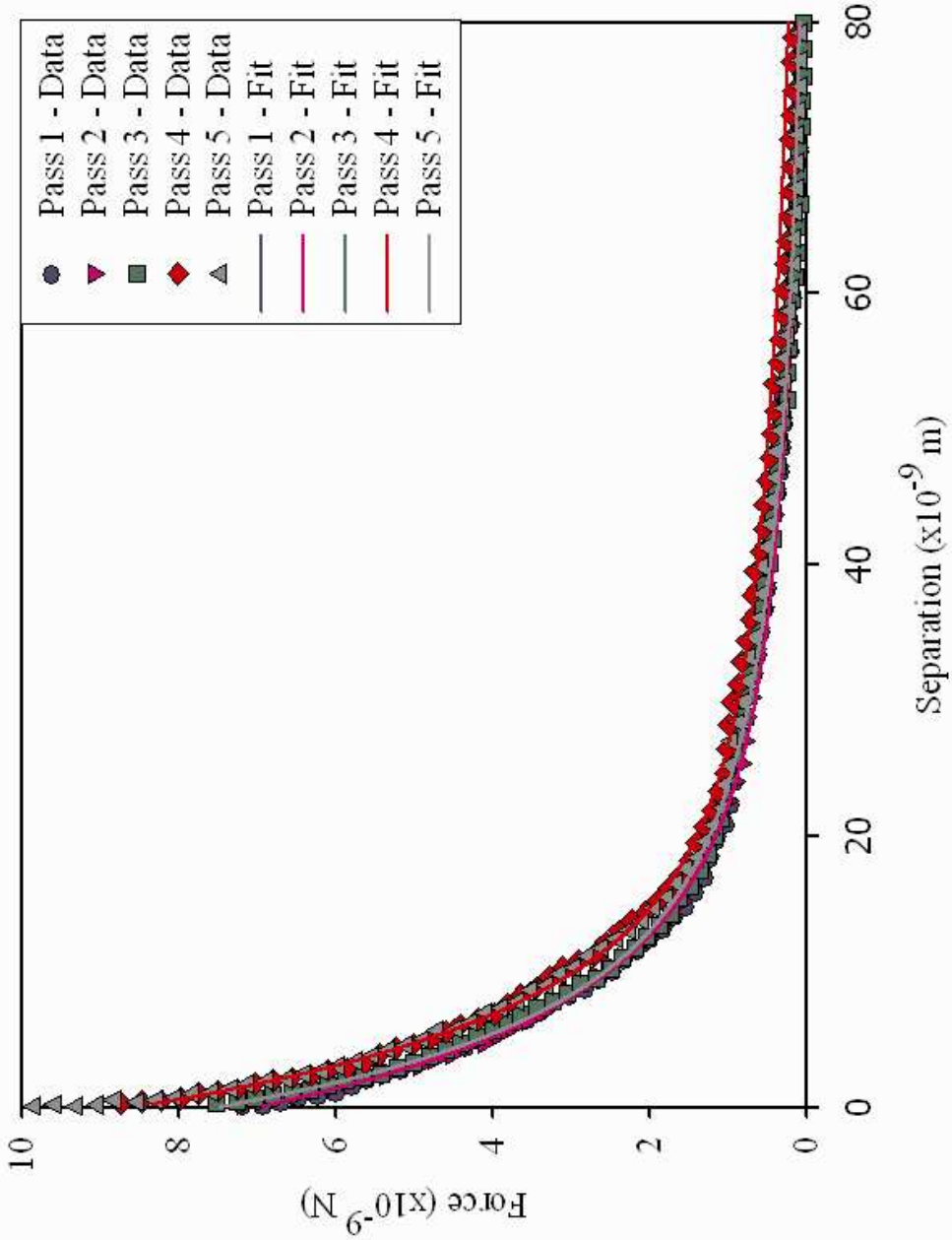

Figure 2.4.14: *P. aeruginosa* approach curves with an unmodified silicon nitride probe. The model is valid for the entire range of the interaction.

Table 2.4.3: Quantification of equilibrium polymer lengths and polymer grafting density for *P. aeruginosa* as obtained by the steric model

Sample[1]	Probe	Γ_1/Γ_2[2] (10^{-16} m^{-2})	L_1/L_2[3] nm	R^2
P. aeruginosa	DNP-S	2.48/7.49	92.6/24.0	1.00
C. parapsilosis	DNP-S	3.12	157	0.91
Silicone	HDT	12.4	0.88	0.88
Silicone	*C. parapsilosis*	11.1	130	0.96
Biofilm	*C. parapsilosis*	11.5	109	0.98

[1] Five measurements were taken for each sample-probe combination and fitted with either the basic or modified steric model. R^2 values are also presented. Γ_2 and L_2 were calculated only for *P. aeruginosa*.

[2] Polymer grafting density per unit area.

[3] Equilibrium polymer length of microbial surface features

2.5 Discussion

2.5.1 Microbial Growth Curves

For valid comparison between experiments, it is vital to harvest and examine cells at the same point in their growth cycle, *viz.*, at the same optical density, each time cells are grown. *P. aeruginosa* reaches an acceptable point in its exponential growth phase ($O.D._{600} = 0.50 \pm 0.07$) in $1.5 - 2.5$ h, while *C. parapsilosis* reaches its ideal growth phase ($O.D._{600} = 0.55 \pm 0.06$) in $3.5 - 5.0$ h. As can be seen in Figure 2.4.1 and Figure 2.4.2, the growth behaviour of the cells follows an exponential trend. Microbial growth, however, is dependent upon a variety of factors (*e.g.,* temperature, nutrient availability, initial number of cells in culture, the number of viable cells present, etc...), and, as such, small variations between cultures must be expected.

2.5.2 Cell Probe Preparation and SEM Analysis

A major goal in formulating this immobilisation technique was to minimise the area of the cell that would be chemically treated. An ongoing debate in the scientific community regards whether cells may be exposed to different chemicals before analysis without changing their surface properties. Several groups have shown that treatment in this manner can alter cell wall flexibility, and may also alter the adhesive properties of the cell [9, 18, 19]. Early experimentation (Figure 2.5.1) showed distinct differences in force cycles between microbial cells treated with various fluorescent and visible-spectrum stains and those that were not stained. In this example, cells were treated with different concentrations of the stain Neutral Red, which is described as a "supravital stain" [27], meaning it does not promote apoptosis or lysis when introduced into vital cell cultures. The stain is commonly used in cellular viability and adhesion assays, and is widely considered to be nontoxic for cells [5, 13, 23].

While the cell will likely survive treatment with Neutral Red, its surface properties are altered. As such, we believe that minimising chemical treatment of the cell surface with any agent will give results most closely approximating those found *in vivo*. Further investigation of the physicochemical properties of microbial cell walls and their structures and their relationship to chemical treatment may prove to be exceptionally interesting.

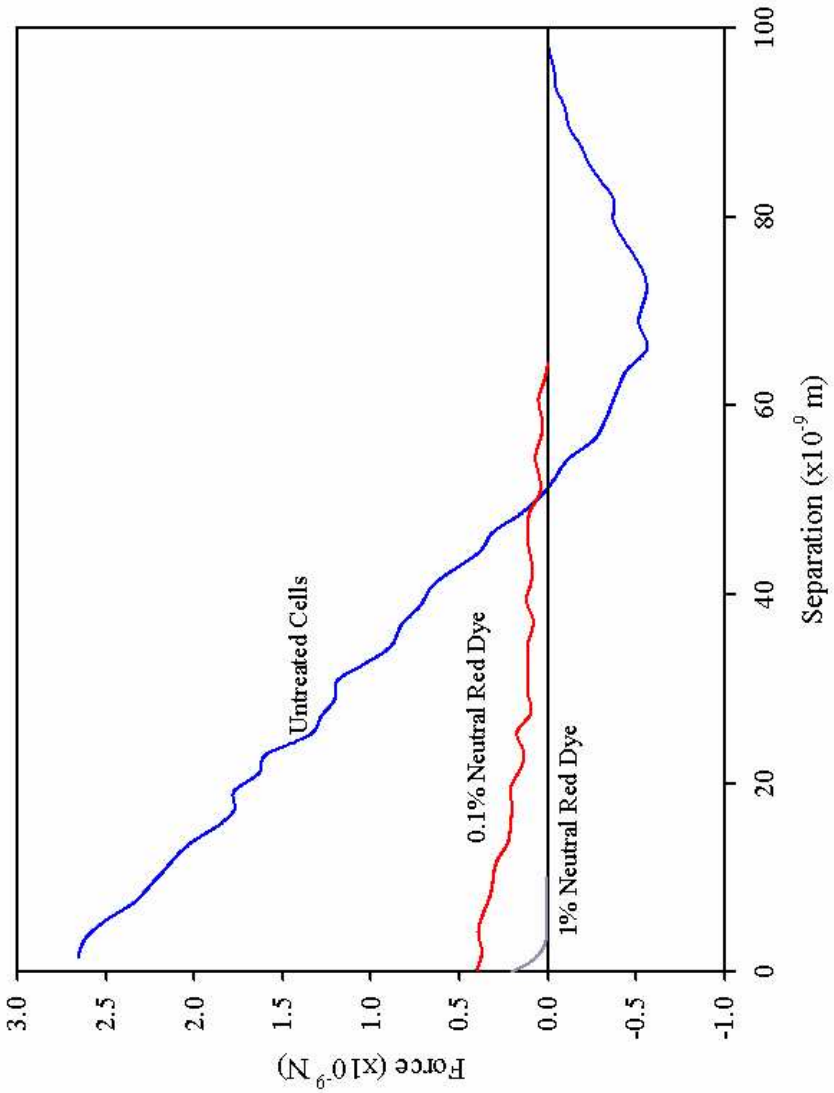

Figure 2.5.1: Illustration of the effects of the chemical stain Neutral Red on AFM force curves. It is clear that the presence of the stain changes the nature of the probe-sample interactions. The decrease in surface repulsion between samples suggests the force is dependent on the concentration of stain present.

Examination of the cellular probes with SEM showed cells bound to the cantilever with multiple cells present in some cases. Since the height of the tips is small (≈2.5 μm) relative to the height of the cells, the chemisorbed *Candida* would be the major bodies interacting with the sample surfaces. It was also noted that, while the cells were not perfectly aligned at the apex of each cantilever, the tips themselves were, in all cases, off-center as well. Any variations in force curves due to this misalignment of the tip are corrected for during the laser alignment procedure. The same technique should be directly applicable to correcting for an off-center cell chemisorbed to the cantilever.

2.5.3 Approach Interactions at the Cell–Biomaterial Interface

For a modified probe interacting with a biomaterial, attractive interactions exist within the range of equilibrium polymer lengths for *C. parapsilosis*. The domains evident on the silicone suggest that the heterogeneity of the surface could lead to a variety of interactions, depending on whether the cell surface structures interact with high or low points on the biomaterial surface. Therefore, it is possible that long, proteinaceous surface structures (*e.g.,* flagella, fimbriae), if present, may interact with these domains before the majority of the polymers on the cell surface. The role of such structures in lectin-ligand binding to specific sites has been investigated by a number of groups [36, 37, 39]. These groups have demonstrated that cell surface structures are critical in certain lock-and-key mechanisms, and that the lectins interact with specific saccharide residues. Singh *et al.* [37] discussed the existence of cell-cell interactions in terms of specific biological systems, including bacteria, plants and yeasts. While no evidence has been found in the open literature examining such structures on *C. parapsilosis*, various other yeasts (*Kluyveromyces bulgaricus*, *Saccharomyces cerevisiae*, *S. ludwigii* and *Brandeiraea simplicifolia*) were shown to produce them.

Structures protruding from the cell surface would also be able to specifically interact with either high or low points on the surface, since these structures are very narrow as compared to the domains on the materials. However, the cell itself is large as compared to these domains, and the majority of the adhesions occur within the range of equilibrium polymer lengths for the cell. Affinities, as shown in the retraction curves in Figure 2.4.9, demonstrate unique values for each substrate. The strongest interactions occur with bare silicone, with only one

peak in the retraction curve. This indicates that only one type of polymer is interacting with the probe, as compared to the multiple peaks for functionalised probes on a biofilm substrate. So, while long cell surface structures may interact with different portions of the biomaterial surface, the similarity of interactions over several areas leads us to believe that a bulk or average area of contact will play the dominant role in cellular adhesion.

It is therefore within reason to say that the polymer brush, which is distributed across the cell surface and has a thickness that may be mathematically quantified, is the main feature of the cell interacting with the biomaterial. Further, since a distinct inflection occurs where adhesion ends and repulsion begins, we may conclude that the point of maximum adhesion (most negative force) is the maximum compression force of the polymers on the cell surface. After this point, the brush cannot be compacted further, and begins pushing back against the probe loading force as the probe comes into contact with the material surface.

2.5.4 Approach Interactions at the Cell–Biofilm Interface

Interactions between a modified probe and a nascent biofilm also exhibit a characteristic attraction on approach. However, immediately before this attraction, a long-range (250 nm) repulsion takes place. This can be attributed to a combination of electrostatic double layer effects associated with the polymer brushes on each microbe, as well as steric effects.

As the "planktonic" *C. parapsilosis* moves closer to the surface, the strong attractive interaction begins to dominate. This suggests that an initial energy barrier must be overcome to reach an energetic minimum favoring sessile behaviour. Therefore, the planktonic microbe must have sufficient force, associated with bulk flow, gravitational settling or the cell's inherent mobility, to initially bind to a biofilm.

Attractive peaks correlate to the equilibrium polymer lengths of *P. aeruginosa*, occurring at shorter distances than those seen for a modified probe and a bare biomaterial surface. The magnitudes of these interactions are as much as 3x greater than those seen for a modified probe-bare biomaterial system. This behaviour suggests that planktonic cells have a higher affinity for binding to surfaces on which a biofilm is already growing, and that the cells, once bound, will have a greater probability of remaining bound, since a perturbation of greater magnitude will be required to dislodge the cell.

Microbial adhesion to medical implant materials and biofilms growing on those materials is a complex topic, but one that is essential to the prevention and elimination of implant-associated infections. Using AFM and supporting technologies, it is possible to characterise how strongly a microbial cell interacts with a bare or biofilm-coated biomaterial surface. Application of mathematical models allows for quantification of interaction energies that are useful in constructing new theories and in designing materials that protect the host from microbial colonisation.

2.5.5 Microbial Interaction Energy Analyses

Microbial surface potentials were calculated using classical DLVO theory and the soft-particle DLVO equations. DLVO calculations based on assuming the zeta potential equal to the surface potential (*e.g.,* classical DLVO calculations) predicted higher values for surface potential compared to potentials calculated from the soft-particle equations. Departure from the experimental measurements was most significant in solutions with low salt concentrations.

Results of the classical and soft-particle DLVO equations for *C. parapsilosis* are shown in Figure 2.4.12. For the latter expression, the values of spatial charge density and softness were evaluated by plotting calculated (Equation 1.13) versus experimental electrophoretic mobility (data not shown). ZN and $\frac{1}{\lambda}$ were varied such that a linear regression of the data points yielded a slope of unity and a zero intercept. The regression coefficient for this treatment was very low ($R^2 = 0.219$), with $ZN = -0.0196\,\mathrm{mol}\cdot\mathrm{L}^{-1}$. Based on the regression coefficient, it follows that ≈22 % of the variation between the experiment and the mathematical model are due to solvent ion effects and microbial softness. This result, however, is not completely unexpected. Fungal cell walls often contain cellulose, chitin, or both [29], which greatly increases cell wall rigidity, and these polymers may also be expressed as extracellular structures. So, while various bacterial strains, such as *E. coli* [3], *P. putida*, *P. aeruginosa* [17], and *S. salivarius* [6], show better agreement with soft-particle DLVO theory, *C. parapsilosis* would presumably interact as a more rigid particle. In this case, there is no significant benefit to applying the soft-particle theory.

Since *P. aeruginosa* (Figure 2.4.11) does not contain these rigid materials, we expected to see a better agreement with soft-particle DLVO theory. This was true, with soft-particle

theory providing a fit with $R^2 = 0.671$ and $ZN = -0.0336$ mol $\cdot$ L^{-1}. The model fit is not as accurate as has been observed for other bacteria [3], perhaps because more data, especially at low ionic strengths, is necessary to completely characterise the system.

On the whole, neither classical nor soft-particle DLVO theory quantitatively predicts the interactions seen for either *P. aeruginosa* or *C. parapsilosis*. This may be due to the fact that only three types of interactions (electrostatic, van der Waals, and softness effects) were accounted for in the model. It may be beneficial in the future to include other interactions in the mathematical model to obtain a clearer picture of the forces involved in the behaviour of these two microbes.

Further investigation of DLVO-type interactions may have included the use of extended DLVO theory (XDLVO) [40, 43, 44], which adds terms describing steric, acid-base and/or solvation interactions to the classical DLVO interactions. This formulation has proven useful in many colloidal systems, including analysis of zeolite nucleation and growth [35] and fungal adhesion to random copolymers of sulfonated polystyrene [21]. Both of these studies showed that the solvation or acid-base terms of the XDLVO theories are significant contributors to the total interaction energy profile for these specific cases. However, both studies were conducted at relatively high ionic strengths (622 mM and 150 mM, respectively). As was shown by Boström [7], the classical theory, and its extensions, cause a significant screening of electrostatic forces at high ionic strength. These interactions would presumably be dominant in high ionic strength systems, but, as is shown in the studies of Schoeman [35] and Kang [21], consistently remain near zero. This has been attributed to a negligible importance of electrostatic interactions in these systems (*op. cit.*); however, it is more likely a fundamental failure of the model to truly represent the system under investigation. In general, the permutations of the DLVO theory have been shown to represent the experimental systems well in low ionic strength (< 0.05 mM, but their relevance to biological systems produces misleading and non-representative results. Additionally, recent work in our group has shown that XDLVO produces unrealistically high energy barriers at low separation distances for *P. putida* KT2442 [2]. While acid-base interactions may take place between charged species on the microbial surface, these previous results have prompted us to neglect their effect in the overall interaction energy profiles.

2.5.6 Steric Interactions with the Microbial Polymer Brush

For *C. parapsilosis*, we see excellent agreement between the repulsive data points and the steric model. This demonstrates that, after the interactions causing attraction take place (Figure 2.4.13), steric interactions due to the microbial polymer brush become dominant. Where this model is incapable of fitting attractive interactions and the classical and soft DLVO theories did not predict an attractive minimum in the energy profiles, the source of the attractive interaction seen for *C. parapsilosis* has still not been identified.

The two-brush steric model fits the repulsive regions of the approach curves for *P. aeruginosa* very well, indicating that steric forces play a significant role as the probe approaches the cells (Figure 2.4.14). Physically, this model represents the interactions of an elastic polymer brush with a surface (in this case, the AFM probe), where the force increases as the brush is further compressed. So, the increasing repulsive force seen as the probe approaches the cell is indicative of cell surface structures pushing back against the cantilever due to their own inherent elasticity and increasing rigidity.

There were no attractive interactions seen for *P. aeruginosa*. Qualitatively similar results have been observed from AFM measurements on *E. coli* JM109 [3], *Burkholderia cepacia* G4, and *P. putida* KT2442 [10]. The hydrophobicity and surface potentials of *P. putida* and *P. aeruginosa* are similar, and it is not surprising that strong repulsive interactions are observed between the polymer brush and the AFM probe for both bacterial strains.

2.6 Conclusions

We examined two medically-important microbes in order to characterise their affinity for biomaterial and biofilm surfaces. Steric interactions play significant roles in the approach of silicon nitride probes to both *C. parapsilosis* and *P. aeruginosa*. These interactions do not, however, explain the adhesive interactions seen for *C. parapsilosis*. Further, the adhesions are not mathematically predicted by soft-particle or classical DLVO interaction energy analysis. As such, other forces must be responsible for the adhesions present in the force cycles.

Planktonic microbes show adhesive interactions with bare and biofilm-coated biomaterial surfaces, with a clear point of maximum adhesive strength visible in the approach portions of the force cycles. These occur at approximately the same distance for both, with biofilm-coated surfaces causing a stronger adhesive interaction. In biofilm systems, however, there is an initial repulsion that must be overcome before an adhesion may take place.

We have also demonstrated that established methods of force curve analysis show inconsistencies when involving a polymer brush on the sample, the probe, or both. Additional experimentation is necessary to accurately quantify the role of the polymer brush in AFM approach curves involving attraction, but application of the constant compliance region as the reference point in defining zero separation should be an adequate approximation of the sample surface.

The procedure to examine this model system allows us to characterise cell-biomaterial and cell-cell interactions at the scales of force and distance at which they occur. We are refining our immobilisation technique so that single cells can be attached to the probe. Further examination of different systems of microbes and materials will provide quantitative data for the design of new materials that are less susceptible to microbial attack, and will save many dollars and many lives in the process.

2.7 Bibliography

[1] N. I. Abu-Lail. The Effect of Biopolymer Properties on Bacterial Adhesion: An Atomic Force Microscopy (AFM) Study. Doctoral Dissertation, Biological Interaction Forces Lab, Department of Chemical Engineering, Worcester Polytechnic Institute, 2003.

[2] N. I. Abu-Lail and T. A. Camesano. Role of ionic strength on the relationship of biopolymer conformation, DLVO contributions and steric interactions to bioadhesion of *Pseudomonas putida* KT2442. Biomacromolecules, 4:1000–1012, 2003.

[3] N. I. Abu-Lail and T. A. Camesano. Role of lipopolysaccharides in the adhesion, retention and transport of *Escherichia coli* JM109. Environmental Science and Technology, 37:2173–2183, 2003.

[4] M. Benoit, D. Gabriel, G. Gerisch, and H. E. Gaub. Discrete interactions in cell adhesion measured by single-molecule force spectroscopy. Nature Cell Biology, 2:313–317, 2000.

[5] E. Borenfreund and J. A. Puerner. A simple quantitative procedure using monolayer cultures for cytotoxicity assay (HTD/NR-90). Journal of Tissue Culture Methods, 9:7–9, 1984.

[6] R. Bos, H. C. van der Mei, and H. J. Busscher. 'Soft-particle' analysis of the electrophoretic mobility of a fibrillated and non-fibrillated oral streptococcal strain: *Streptococcus salivarius*. Biophysical Chemistry, 74:251–255, 1998.

[7] M Boström, D. R. M. Williams, and B. W. Ninham. Specific ion effects: Why DLVO theory fails for biology and colloid systems. Physical Review Letters, 87(16):1681031–1681034, 2001.

[8] W. R. Bowen, R. W. Lovitt, and C. J. Wright. Atomic force microscopy study of the adhesion of *Saccharomyces cerevisiae*. Journal of Colloid and Interface Sciences, 237:54–61, 2001.

[9] G. A. Burks, S. B. Velegol, E. Paramonova, B. E. Lindenmuth, J. D. Feick, and B. E. Logan. Macroscopic and nanoscale measurements of the adhesion of bacteria with varying outer layer surface composition. Langmuir, 19(6):2366–2371, 2003.

[10] T. A. Camesano and B. E. Logan. Probing bacterial electrosteric interactions using atomic force microscopy. Environmental Science and Technology, 34:3354–3362, 2000.

[11] J. W. Costerton, P. S. Stewart, and E. P. Greenberg. Bacterial biofilms: A common cause of persistent infections. Science, 284:1318–1322, 1999.

[12] Y. F. Dufrêne, C. J. P. Boonaert, H. C. van der Mei, H. J. Busscher, and P. G. Rouxhet. Probing molecular interactions and mechanical properties of microbial cell surfaces by atomic force microscopy. Ultramicroscopy, 86:113–120, 2001.

[13] D. A. Flick and G. E. Gifford. Comparison of *in vitro* cell cytotoxic assays for tumor necrosis factor. Journal of Immunological Methods, 68:167–175, 1984.

[14] A. M. Gallardo-Moreno, E. Garduno, M. L. Gonzalez-Martin, C. Perez-Giraldo, J. M. Bruque, and A. C. Gomez-Garcia. Analysis of the hydrophobic behaviour of different strains of *Candida parapsilosis* under two growth temperatures. Colloids and Surfaces B: Biointerfaces, 28:119–126, 2003.

[15] D. Grasso, B. F. Smets, K. A. Strevett, B. D. Machinist, C. J. van Oss, R. F. Giese, and W. Wu. Impact of physiological state on surface thermodynamics and adhesion of *Pseudomonas aeruginosa*. Environmental Science and Technology, 30:3604–3608, 1996.

[16] A. G. Gristina. Biomaterial-centered infection: Microbial adhesion versus tissue integration. Science, 237:1588–95, 1987.

[17] H. Hayashi, S. Tsuneda, A. Hirata, and H. Sasaki. Soft particle analysis of bacterial cells and its interpretation of cell adhesion behaviors in terms of DLVO theory. Colloids and Surfaces B: Biointerfaces, 22:149–157, 2001.

[18] J. H. Hoh and C. A. Schoenenberger. Surface morphology and mechanical properties of MDCK monolayers by atomic force microscopy. Journal of Cell Science, 107:1105–1114, 1994.

[19] D. Hopwood. Theoretical and practical aspects of glutaraldehyde fixation. Histochemical Journal, 4(4):267–303, 1972.

[20] Digital Instruments. Scanning Probe Microscopy Training Notebook. Technical report, Veeco Metrology Group, 1998.

[21] S. Kang and H. Choi. Effect of surface hydrophobicity on the adhesion of *S. cerevisiae* onto modified surfaces by poly(styrene-ran-sulfonic acid) random copolymers. Colloids and Surfaces B: Biointerfaces, 46:70–77, 2005.

[22] N. Khardori and M. Yassien. Biofilms in device-related infection. Journal of Industrial Microbiology, 15:141–147, 1995.

[23] F. C. Kull and P. Cuatrecasas. Preliminary characterization of the tumor cell cytotoxin in tumor necrosis serum. Journal of Immunology, 126:1279–1283, 1981.

[24] G. U. Lee, L. A. Chrisey, and R. J. Colton. Direct measurement of the forces between complementary strands of DNA. Science, 266(5186):771–773, 1994.

[25] A. S. Levin, S. F. Costa, N. S. Mussi, M. Basso, S. I. Sinto, C. Machado, D. C. Geiger, M. C. B. Villares, A. Z. Schreiber, A. A. Barone, and M. L. M. Branchini. *Candida parapsilosis* fungæmia associated with implantable and semi-implantable central venous catheters and the hands of healthcare workers. Diagnostic Microbiology and Infectious Disease, 30:243–249, 1998.

[26] D. Losic, J. G. Shapter, and J. J. Gooding. Concentration dependence in microcontact printing of self-assembled monolayers (SAMs) of alkanethiols. Electrochemical Communications, 3:722–726, 2001.

[27] C. W. Löwik, M. J. Alblas, M. van de Ruit, S. E. Papapoulos, and G. van der Pluijm. Quantification of adherent and nonadherent cells cultured in 96-well plates using the supravital stain Neutral Red. Analytical Biochemistry, 213:426–433, 1993.

[28] J. B. Lyczak, C. L. Cannon, and G. B. Pier. Establishment of *Pseudomonas aeruginosa* infection: Lessons from a versatile opportunist. Microbes and Infection, 2:1051–1060, 2000.

[29] M. T. Madigan, J. M. Martinko, and J. Parker. Biology of Microorganisms. Prentice Hall, Upper Saddle River, NJ, 9th edition, 2000.

[30] M. Mrksich, C. S. Chen, Y. Xia, L. E. Dike, D. E. Ingber, and G.M. Whitesides. Controlling cell attachment on contoured surfaces with self-assembled monolayers of alkanethiols on gold. Proceedings of the National Academy of Sciences of the United States of America, 93(20):10775–10778, 1996.

[31] I. Palabiyikoglu, M. Oral, and M. Tulunay. *Candida* colonization in mechanically ventilated patients. Journal of Hospital Infection, 47:239–242, 2001.

[32] A. Razatos, Y.-L. Ong, F. Boulay, D. L. Elbert, J. A. Hubbell, M. M. Sharma, and G. Georgiou. Force measurements between bacteria and poly(ethylene glycol)-coated surfaces. Langmuir, 16:9155–9158, 2000.

[33] A. Razatos, Y.-L. Ong, M. M. Sharma, and G. Georgiou. Evaluating the interaction of bacteria with biomaterials using atomic force microscopy. Journal of Biomaterial Science: Polymer Edition, 9(12):1361–1373, 1998.

[34] J.M. Schierholz and J. Beuth. Implant infections: A haven for opportunistic bacteria. Journal of Hospital Infection, 49:87–93, 2001.

[35] B. J. Schoeman. Analysis of the nucleation and growth of TPA-silicalite-1 at elevated temperatures with the emphasis on colloidal stability. Microporous and Mesoporous Materials, 22:9–22, 1998.

[36] N. Sharon and H. Lis. Lectins as cell recognition molecules. Science, 246(4927):227–234, 1989.

[37] R. S. Singh, A. K. Tiwary, and J. F. Kennedy. Lectins: Sources, activities and applications. Critical Reviews in Biotechnology, 19(2):145–178, 1999.

[38] P. S. Stewart and J. W. Costerton. Antibiotic resistance of bacteria in biofilms. The Lancet, 358:135–138, 2001.

[39] A. Touhami, B. Hoffmann, A. Vasella, F. A. Denis, and Y. F. Dufrêne. Probing specific lectin-carbohydrate interactions using atomic force microscopy imaging and force measurements. Langmuir, 19(5):1745–1751, 2003.

[40] C. J. van Oss. Interfacial Forces in Aqueous Media. Marcel Dekker, Inc., New York, NY, 1994.

[41] S. B. Velegol and B. E. Logan. Contributions of bacterial surface polymers, electrostatics and cell elasticity to the shape of AFM force curves. Langmuir, 18:5256–5262, 2002.

[42] S. B. Velegol, S. Pardi, X. Li, D. Velegol, and B. E. Logan. AFM imaging artifacts due to bacterial cell height and AFM tip geometry. Langmuir, 16:851–857, 2003.

[43] W. Wu. Application of the extended DLVO theory - The stability of alatrofloxacin mesylate solutions. Colloids and Surfaces B: Biointerfaces, 14:57–66, 1999.

[44] W. Wu, R. F. Giese, and C. J. van Oss. Stability versus flocculation of particle suspensions in water - Correlation with the extended DLVO approach for aqueous systems, compared with the classical DLVO theory. Colloids and Surfaces B: Biointerfaces, 14:47–55, 1999.

CHAPTER 3

Microstructure of Cell Wall-Associated Melanin in the Human Pathogenic Fungus *Cryptococcus neoformans*

3.1 Abstract

Melanin is a virulence factor for many pathogenic fungal species, including *Cryptococcus neoformans*. Melanin is deposited in the cell wall, and melanin isolated from this fungus retains the shape of the cells, resulting in hollow spheres called "ghosts". In this study, atomic force, scanning electron, and transmission electron microscopy revealed that melanin ghosts are covered with roughly spherical granular particles approximately $40 - 130$ nm in diameter, and that the melanin is arranged in multiple concentric layers. Nuclear magnetic resonance cryoporometry indicated melanin ghosts contain pores with diameters between 1 and 4 nm, in addition to a small number of pores with diameters near 30 nm. Binding of monoclonal antibodies to melanin reduced the apparent measured volume of these pores,

suggesting a mechanism for their antifungal effect. We propose a model of cryptococcal melanin structure whereby the melanin granules are held together in layers. This structural model has implications for cell division, cell wall remodeling, and antifungal drug discovery.

3.2 Introduction

Cryptococcus neoformans is a frequent cause of life-threatening fungal disease in immunocompromised patients [36]. This yeast-like fungus is remarkable in being an encapsulated eukaryotic human pathogen, of which there are few known examples [5, 19]. Cryptococcal infections are presumably contracted by inhalation of infectious particles that reside in the environment. In the majority of healthy hosts, the infection is contained in the lungs. However, in individuals with impaired immunity, dissemination can occur, frequently to the central nervous system. Like many fungal infections, cryptococcosis is notoriously difficult to treat. Therefore, it is important to understand factors that contribute to virulence for the development of more effective therapies.

One key factor that contributes to the pathogenesis of *C. neoformans*, as well as other fungi, is melanin [9,30]. Comparison of melanized and nonmelanized strains of *C. neoformans* in animal models of infection reveals that non-melanotic *C. neoformans* strains are less virulent, thereby establishing the importance of melanin to virulence [22, 42]. Melanin has been found to affect the immune system. Fungal melanins are immunogenic and can elicit antibodies that inhibit fungal growth [2, 32, 35, 39]. Furthermore, melanization is associated with decreased levels of inflammatory cytokines in animal models of infection [18, 26]. Melanization decreases the rate of phagocytosis and killing of *C. neoformans* by macrophages [46] and increases resistance to microbicidal peptides *in vitro* [14]. Together, these studies suggest that melanin in *C. neoformans* increases virulence by reducing the vulnerability of fungal cells to host defense mechanisms and interfering with the development of effective immune responses. In addition to increasing resistance of *C. neoformans* to immune defenses, melanin also reduces the efficacy of certain antifungal drugs [20, 45, 49]. Thus, melanization has clinical implications for *C. neoformans* infections in terms of both the immune response and the ability to use and develop newer antifungal drugs.

Melanization occurs in the environment [34] and is important for survival. Melanin protects *C. neoformans* from various environmental conditions, such as the presence of toxins, extreme temperatures, and ultraviolet radiation [15,38,48,50]. Additionally, melanin provides defense from environmental predation by microorganisms such as the nematode,

Caenorhabditis elegans, and the amoeba *Acanthamoeba castellani* [27,43]. Thus, melanin has a protective role in *C. neoformans* both in the host and in the environment. Melanin in *C. neoformans* is found in the cell wall [29, 46]. Synthesis of melanin is dependent on a laccase enzyme and the presence of exogenous substrates, such as L-3,4-dihydroxyphenylalanine (L-dopa) and epinephrine [37, 54]. Although the details of melanin structure are largely unknown, it is believed to be a cross-linked polymer of phenol and indole subunits [7, 24]. Melanin is a highly stable compound and can be isolated from cells by harsh chemical treatments that degrade other cellular components such as the cell wall, lipids, and proteins. Such treatment produces hollow melanin shells called "ghosts" that retain the spherical shape of the cells [47].

The presence of melanin in *C. neoformans* leads to challenges in the treatment of this disease. The effects of melanization on the basic biological mechanisms of the organism, including how nutrients are transported across the melanin layer and how cells bud through melanin, are not understood. To formulate a model of how these processes occur, it is necessary to determine the structure of the melanin layer. Unfortunately, melanins are poorly characterised because they are insoluble amorphous materials not suitable for crystallization or solution studies. To gain structural insights, complementary techniques were applied to the study of melanin. These included atomic force microscopy (AFM) and scanning electron microscopy (SEM) for imaging of the melanin surface, transmission electron microscopy (TEM) for cross-sectional analysis of melanin ghosts, and nuclear magnetic resonance (NMR) cryoporometry for determination of the porosity of melanin. On the basis of results from these studies, we propose a model of melanin structure composed of multiple layers of densely packed granules whereby pores and channels are formed in the spaces between melanin particles. This model has implications for the mechanism of budding of melanized cells and the antifungal action of melanin-binding antibodies.

3.3 Experimental Procedures

3.3.1 *C. neoformans* Strains and Media

C. neoformans serotype D strain 24067 was obtained from the American Type Culture Collection (Manassas, VA). *C. neoformans* serotype D strain Cap67, containing a mutation in the CAP59 gene, was generously provided by J. Kwon-Chung [10]. The cells were grown in defined chemical media [minimal medium, 15 mM dextrose, 10 mM $MgSO_4$, 29.4 mM KH_2PO_4, 13 mM glycine, and 3 μM thiamine (pH 5.5)] with 1 mM L-dopa, epinephrine, or dopamine (Sigma-Aldrich, St. Louis, MO). Cultures (500 mL) were incubated in the dark at 30 °C in 1 L Erlenmeyer flasks in a rotary shaker at 150 RPM for the indicated times.

3.3.2 Antibodies

Melanin-binding antibodies and their use have been described previously [40]. Briefly, mice were immunised with L-dopa melanin ghosts. Spleen cells from mice producing antibodies to melanin were fused to myeloma cells to generate hybridomas for the production of monoclonal antibodies to melanin. MAb 5C11, recognising mycobacterial lipoarabinomannan, was used as a control [16].

3.3.3 Preparation of Melanin Ghosts from Cells Grown *in vitro*

C. neoformans strain 24067 was cultured in defined chemical media with 1 mM L-dopa, epinephrine, or dopamine at 30 °C for the indicated times. Melanin ghosts were isolated by enzymatic digestion of the cell wall, proteolysis, chloroform extraction, and boiling in concentrated HCl as described previously [41].

3.3.4 *In Vivo* Melanin Ghost Isolation

BALB/c mice were infected by intravenous injection in the tail vein with 5 x 10^5 *C. neoformans* strain 24067 cells. After 21 days, infected mice were sacrificed and melanin ghosts were isolated from infected tissues. The brains of infected mice were homogenised by mechanical grinding. Tissues were then treated with 1.0 $mg \cdot mL^{-1}$ proteinase K (Boehringer Mannheim

Co., Indianapolis, IN) at 65 °C for 4 h, incubated in 4.0 M guanidine thiocyanate for at least 2 h at room temperature with frequent vortexing, and then boiled in 6.0 M HCl for 1 h. The resulting material was washed three times with phosphate-buffered saline (PBS) [8 $g \cdot L^{-1}$ NaCl, 0.2 $g \cdot L^{-1}$ KCl, 0.2 $g \cdot L^{-1}$ KH_2PO_4, and 1.2 $g \cdot L^{-1}$ Na_2HPO_4 (pH 7.4)] and prepared for SEM as described below.

3.3.5 Nuclear Magnetic Resonance Cryoporometry

Melanin ghosts were prepared from cells grown for 4, 7, or 10 days in the presence of a substrate (*e.g.,* 1 mM L-dopa or epinephrine). For the melanin antibody studies, melanin ghosts were isolated from cells grown for 10 days in the presence of L-dopa. Ghosts were incubated with SuperBlock (Pierce, Rockford, IL) to prevent nonspecific binding and then incubated with a melanin-binding or control antibody at a concentration of 10 $\mu g \cdot mL^{-1}$ prior to analysis. In addition, commercially prepared synthetic tyrosine melanin and *Sepia officinalis* melanin were analysed (Sigma-Aldrich).

To analyse pore size by NMR cryoporometry, samples were frozen in water, and then slowly warmed at a rate of 0.2 $K \cdot min^{-1}$. The change in melting point temperature was measured from the amplitude of the NMR signal from the protons in liquid water and used to determine porosity as a function of pore size using the Gibbs-Thomson equation [21,51,52].

The NMR cryoporometry measurements were made using a fast-recovery NMR relaxation spectrometer, constructed by J. B. W. Webber at the University of Kent (Canterbury, Kent, United Kingdom), with gas-flow temperature control (liquid nitrogen to 500 K), which had been modified for highly precise (≈1 mK) relative temperature measurements [51]. Samples were prepared in flame-sealed thin-walled silica tubes, with the measurement copper-constantan thermocouple soldered to a non-shorting copper foil around the sample, and the thermal EMF measured relative to a matched thermocouple in melting ice. NMR cryoporometry offers a number of advantages over the similar thermoporosimetry technique, including the ability to measure arbitrarily slowly and to improve both pore size resolution and the signal-to-noise ratio. These NMR cryoporometry measurements show a pore volume resolution of around 5 $nL \cdot Å^{-1}$.

3.3.6 Scanning Electron Microscopy

Melanin ghosts were isolated from *C. neoformans* cultures grown for 1, 2, or 3 weeks in the presence of 1 mM L-dopa or dopamine or from animals as described above. Following melanin ghost isolation, samples were fixed in 2.5 % glutaraldehyde in 0.1 M cacodylate (pH 7.4). After being fixed, samples were dehydrated through a graded series of ethanol and critical point dried using liquid carbon dioxide in a Tousimis Samdri (Rockville, MD) 795 critical point drier. Samples were then sputter coated with gold-palladium (Desk-II; Denton Vacuum Inc., Cherry Hill, NJ). Imaging was performed with a JEOL (Peabody, MA) JSM-6400 scanning electron microscope using an accelerating voltage of 10 kV. Images were acquired with analySIS (Soft Imaging System GmbH, Münster, Germany). For SEM of acapsular cells, cultures (250 mL) of *C. neoformans* strain Cap67 were grown for 2 weeks in the dark in defined chemical media with or without 1 mM L-dopa in 500 mL Erlenmeyer flasks at 30 °C and 150 rpm. Cells were washed in PBS, fixed in 2.5 % glutaraldehyde in 0.1 M cacodylate, dehydrated, and coated as described for melanin ghosts.

3.3.7 Transmission Electron Microscopy

Melanin ghosts were fixed in 2 % glutaraldehyde in 0.1 M cacodylate at room temperature for 2 h, followed by overnight incubation in 4 % formaldehyde, 1 % glutaraldehyde, and 0.1 % PBS. The samples were subjected to postfixation for 90 min in 2 % osmium, serially dehydrated in ethanol, and embedded in Spurrs epoxy resin. Sections ($70 - 80$ nm thick) were cut on a Reichart Ultracut UCT microtome and stained with 0.5 % uranyl acetate and 0.5 % lead citrate. Samples were viewed in a JEOL 1200EX transmission electron microscope at 80 kV.

3.3.8 Atomic Force Microscopy

For AFM studies, melanin ghosts were isolated from *C. neoformans* cultures grown for 7, 14, or 21 days in the presence of L-dopa. Glass slides for AFM were cleaned as described elsewhere [8]. Melanin ghosts were immobilised on glass slides by mixing poly-L-lysine with a suspension of melanin ghosts [1 mL of a 10 % (w/v) suspension added to 9 mL of ghost

suspension containing between 5 x 10^8 and 1 x 10^9 ghosts/mL] and pipetting the mixture onto glass slides.

AFM imaging was performed with a Digital Instruments Dimension 3100 (Veeco Instruments, Santa Barbara, CA) atomic force microscope with a Nanoscope IIIa controller. AFM was performed in air or water at room temperature under normal atmospheric pressure. Images were recorded in intermittent contact mode. For air experiments, cantilevers were TESPA (TappingMode^{TM} Etched Silicon Probes with an Aluminum Backing-Layer) from Digital Instruments (Santa Barbara, CA), with a nominal spring constant of 100 $N \cdot m^{-1}$. In liquid, cantilevers were DNP-S (triangular silicon nitride probes with a gold backing layer), with a nominal spring constant of 0.13 $N \cdot m^{-1}$.

All cantilevers were cleaned under UV light for 5 min prior to experiments to remove adsorbed water and hydrocarbons. The scan rate was 1.001 Hz. The number of samples was 256 lines/image and 256 pixels/line (65,536 total samples). The AFM laser diode wavelength and Z-direction step height were calibrated according to [6]. Imaging parameters were calibrated according to the manufacturer's specifications using a 180 nm pitted calibration standard (SHS-200, Digital Instruments). Data were analysed using Nanoscope IIIa software (version 4.43 r8, Digital Instruments) and Scanning Probe Imaging Processor (SPIP) software (Image Metrology, Denmark). To determine granule size diameter, the edges of the granules were marked on the sectional analysis of the image and corresponding coordinates used to measure granules.

3.4 Results

3.4.1 Overall Structure of Melanin Ghosts

Melanin ghosts were isolated from melanized *C. neoformans* cells grown in liquid media containing L-dopa for 1, 2, or 3 weeks. Samples were imaged by SEM and AFM. The isolated ghosts retained the spherical shape of the cells (Figure 3.4.1). However, some collapsing of the melanin ghosts was observed by AFM (Figure 3.4.2D).

3.4.2 High-Resolution Surface Structure of Melanin

Two complementary imaging methods were used to visualise the surface of melanin ghosts isolated from C. neoformans: high-resolution SEM and AFM (Figures 3.4.1 and 3.4.2, respectively). The most striking feature apparent from these images was the granular nature of the melanin surface (Figures 3.4.1A and 3.4.2B,C,E,F), a feature that was not described in previous studies [40, 47]. The ghost surface consisted of irregularly shaped granules with a geometry that approximated tightly packed spheres. Occasionally, ghosts were observed with the granules in an ordered linear arrangement (Figure 3.4.2E,F). The size of the granules was estimated by measurements from both the SEM and AFM images (Figure 3.4.3). SEM measurements revealed a diameter of 74 ± 13 nm for granules from 1 week melanin ghosts and 82 ± 21 nm for granules from 3 week ghosts, a small, but statistically significant difference in size ($P < 0.05$). By contrast, AFM measurements yielded an average particle diameter of 57 ± 12 nm for granules from 1 week ghosts, 81 ± 31 nm for granules from 2 week ghosts, and 49 ± 8 nm for granules from 3 week ghosts. For SEM, 20 granules from each ghost were measured and 4-5 ghosts were analysed. For AFM, 5-12 granules from each ghost were measured and 1-2 ghosts were analysed.

Since the isolation of melanin ghosts requires harsh chemical treatments that could theoretically alter the melanin structure, we attempted to study the surface structure of melanin as it is found in intact cells by visualising melanized and nonmelanized *C. neoformans* cells using SEM (Figure 3.4.4) and AFM (data not shown). Since *C. neoformans* normally has a polysaccharide capsule that prevents surface inspection of the cell wall, an acapsular strain, Cap67, was used in this analysis [10]. When viewed in the SEM, the surfaces of both the

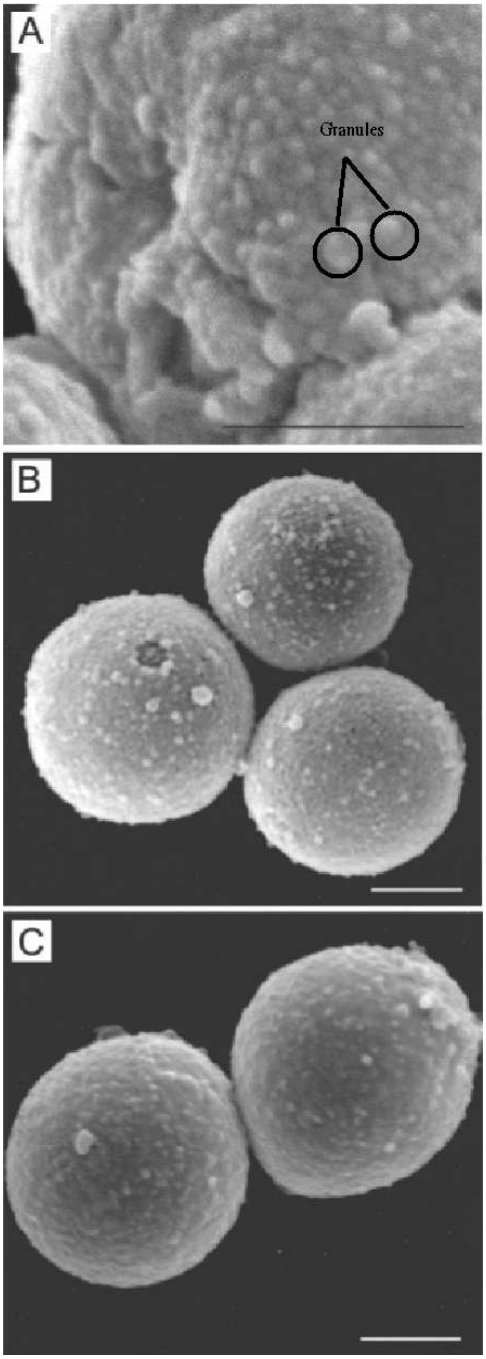

Figure 3.4.1: SEM of granules on the surface of melanin ghosts. Scale bars are 1 μm. (A) High-resolution micrograph of melanin ghosts isolated from the 1 week culture of *C. neoformans* strain 24067 grown in the presence of L-dopa. (B) Melanin ghosts isolated from *C. neoformans* strain 24067 grown in the presence of dopamine for 10 days. (C) Melanin ghosts isolated from *C. neoformans*-infected mouse tissue harvested 21 days post-infection.

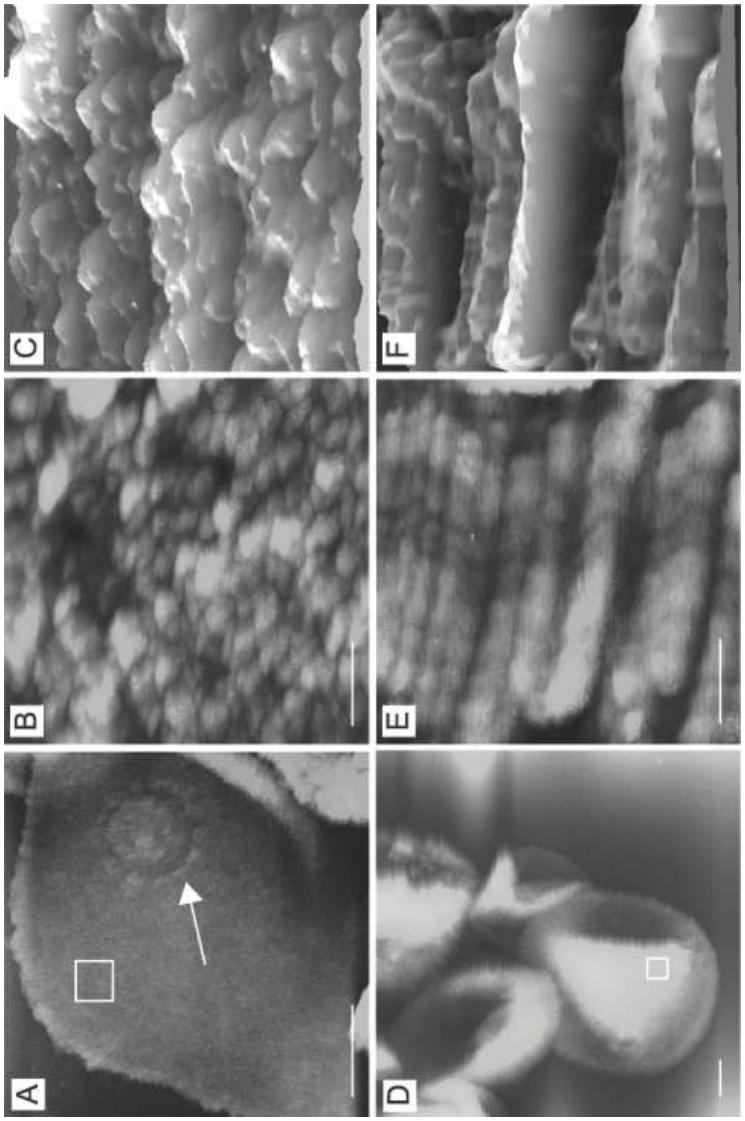

Figure 3.4.2: AFM surface analysis of melanin ghosts. Melanin ghosts were isolated from the 3 week culture of *C. neoformans* strain 24067 grown in the presence of L-dopa. AFM height images, showing the surface topology of melanin ghosts, are shown. (A) Overall shape of the melanin ghost imaged by AFM. The arrow points to a bud scar. The scale bar is 1 µm. (B) Close-up analysis of the surface indicated by the small rectangle in panel A. The scale bar is 100 nm. Images created using Nanoscope IIIa software (version 4.43 r8, Digital Instruments). (C) Three-dimensional rendering of the surface in panel B. This image was created with SPIP (Image Metrology). (D) Overall shape of melanin ghosts imaged by AFM. Ghosts are somewhat collapsed. The scale bar is 1 µm. (E) Close-up analysis of the surface indicated by the small rectangle in panel D. The scale bar is 100 nm. Images created using Nanoscope IIIa software (version 4.43 r8, Digital Instruments). (F) Three-dimensional rendering of the surface in panel E. This image was created using SPIP (Image Metrology).

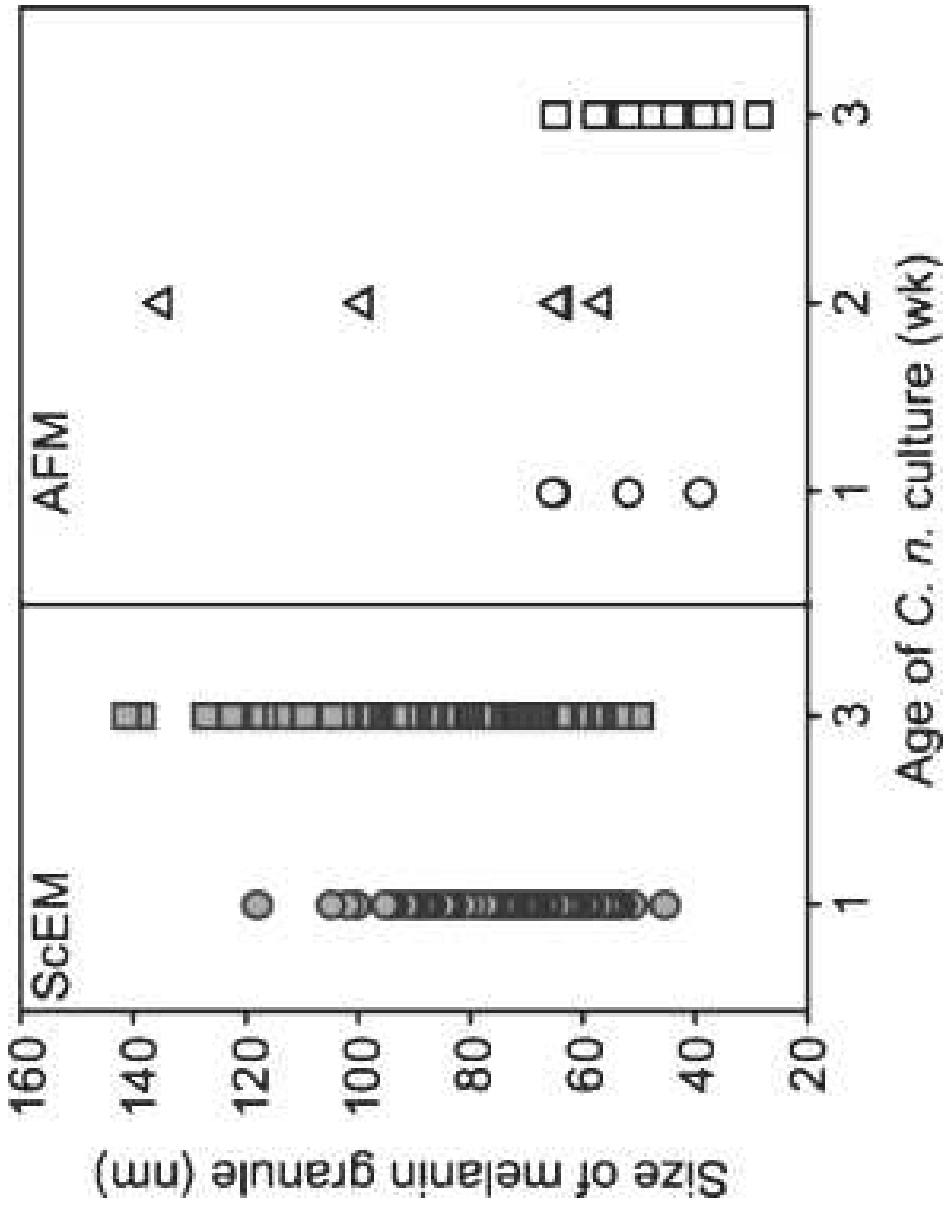

Figure 3.4.3: Analysis of melanin ghost granule size. The sizes of granules on the surface of 1, 2, and 3 week melanin ghosts were measured using SEM and AFM images as described in Experimental Procedures (all data points are plotted). Data from SEM are shown at the left and from the AFM at the right: circles, 1 week samples; triangles, 2 week samples; and squares, 3 week samples.

melanized (Figure 3.4.4A) and nonmelanized (Figure 3.4.4B) cells were similar. Both appeared fairly smooth. This suggests that, in the cell, melanin was partially obscured by outer components of the cell wall. Consequently, it was not feasible to compare the surface structure of melanin ghosts to the surface of melanin in cells by these techniques.

Differences in the granularity of melanin were apparent around bud scars, which were manifested by significant increases in the granule size in areas near bud scars relative to other parts of the ghost surface (Figure 3.4.5A,B). Larger granules were observed near the bud scars. By AFM, the average particle size for the 3 week samples was 49 ± 8 nm far from the bud scars and 96 ± 29 nm near the bud scars ($P < 0.05$) (Figure 3.4.5C). Between 7 and 8 granules near bud scars from each of two different melanin ghosts were measured. AFM analysis of the average roughness revealed the same trend.

The root-mean-square roughness (R_q) of the ghost surface far away from the bud scar was 4.1 nm, whereas near the bud scar the roughness was 7.1 nm (data not shown).

$$R_q = \sqrt{\frac{\sum_{i=1}^{M} (Z_i - Z_{Ave})^2}{M}} \tag{3.1}$$

where Z_{Ave} is the average height within the given area, Z_i is a discrete height within the area, and M is the number of points in the given area [13]. The same significant variation was apparent from SEM of melanin ghosts. The average size of the granules near bud scars was 136 ± 8 nm for 3 week melanin ghosts, compared to 82 ± 21 nm for granules far from bud scars ($P < 0.05$) (Figure 3.4.5C). Between 12 and 19 granules near bud scars on each of three different melanin ghosts were measured. The difference in melanin granule size around bud scars may be due to alterations in the underlying cell wall architecture since similar structures were visible in acapsular cells, both melanized and nonmelanized (Figure 3.4.4 and data not shown).

3.4.3 Melanin Shell of *C. neoformans* Is Composed of Layers

Melanin ghosts were sectioned and visualised by TEM to gain insight into their cross-sectional structure. The TEM images revealed that the walls of the melanin ghosts were composed of two to five concentric layers (Figure 3.4.6B,D,F). Each layer was $50 - 75$ nm

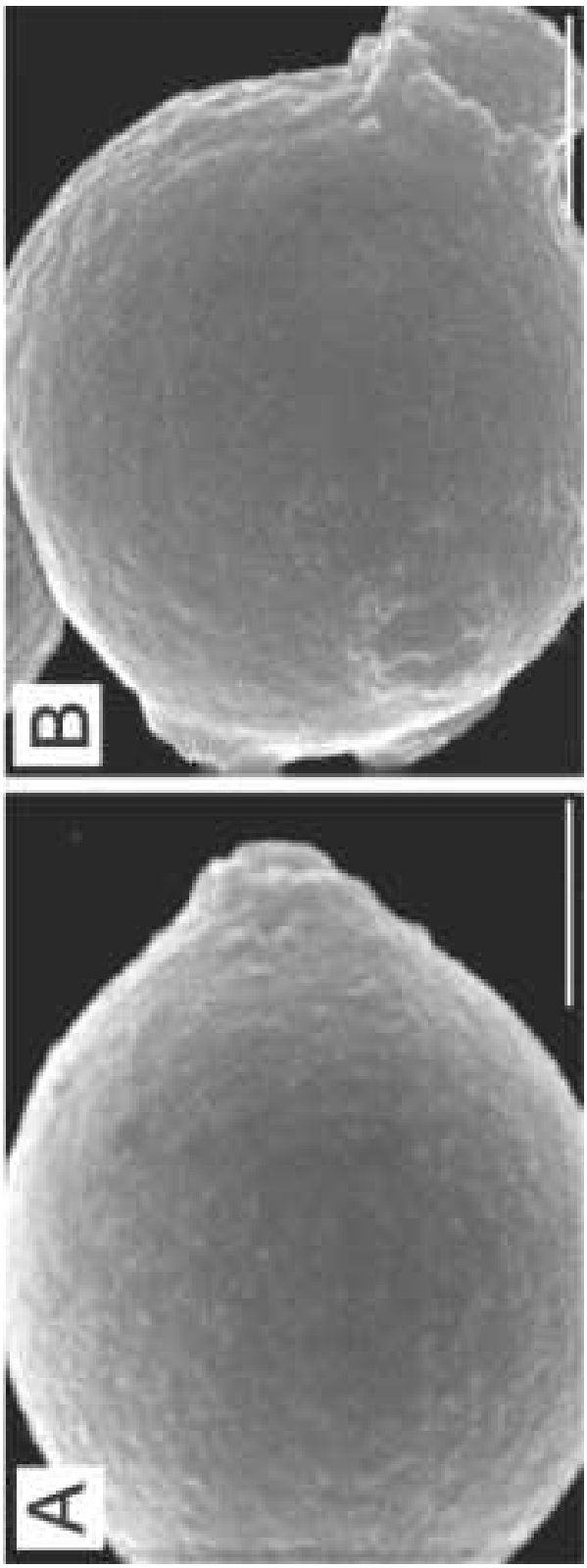

Figure 3.4.4: Melanin in *C. neoformans* is partially covered by portions of the cell wall. (A) SEM images of melanized acapsular *C. neoformans*. Strain Cap67 was grown for 2 weeks in minimal media with L-dopa and then washed and fixed as described in Experimental Procedures. Scale bars are 1 µm. (B) SEM images of nonmelanized acapsular *C. neoformans*. Strain Cap67 was grown for 2 weeks in minimal media and then washed and fixed as described in Experimental Procedures. Scale bars are 1 µm.

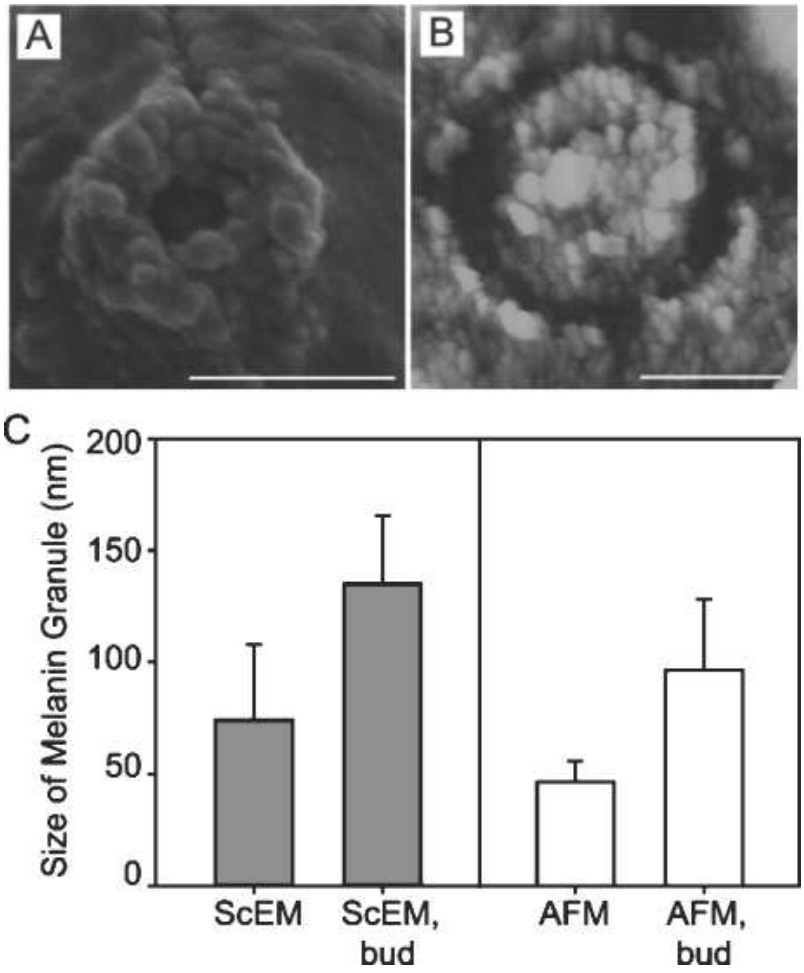

Figure 3.4.5: Melanin granules are larger near bud scars. (A) High-resolution SEM of melanin ghosts isolated from the 1 week culture of *C. neoformans* strain 24067 grown in the presence of L-dopa. The scale bar is 1 μm. (B) AFM image of bud scar from melanin ghost isolated from the 3 week culture of *C. neoformans* strain 24067 grown in the presence of L-dopa. The scale bar is 0.5 μm. (C) Melanin granules were measured from SEM and AFM images for areas near (SEM, bud, and AFM, bud) or far (SEM and AFM) from bud scars. Melanin ghosts isolated from 3 week *C. neoformans* cultures were analysed. Graphs indicate the average size ± the standard deviation of melanin granules.

wide, and the average thickness of the melanin ghost wall was 200 ± 98 nm. The thickness of the melanin was measured for 1, 2, and 3 week samples, and average thicknesses were found to be 164 ± 82 nm (n=42), 220 ± 81 nm (n=26), and 241 ± 114 nm (n=30), respectively (Figure 3.4.6G). One week melanin ghost shells were significantly different from 2 week ($P < 0.05$) and 3 week melanin ghosts ($P < 0.05$). Ghosts from budding cells showed that the melanin layer around the bud was thinner than that of the mother cell. An increase in thickness was observed for larger buds (Figure 3.4.7A-F). SEM analysis of similar ghosts showed that the surface of the buds was often smoother than that of the mother cell (Figure 3.4.7G). This suggests that, in early buds, melanin deposition was not complete. Together, these results are consistent with an increase in melanin thickness over time.

3.4.4 Melanin Ghosts Have Pores

NMR cryoporometry was used to analyse the porosity of *C. neoformans* melanin. In this method, porosity was determined based on the change in melting point temperature of water in a pore versus a large volume [21, 52]. The melting point was measured by the amplitude of the NMR signal from the protons in liquid water. Cells were grown in liquid media containing L-dopa for 4, 7, or 10 days, and melanin ghosts were isolated. Samples were mechanically crushed with a mortar and pestle prior to analysis. By this technique, a pore was identified by the contained water melting at a lower temperature than the bulk water present around the melanin shells. The relative amplitudes of the pore water signal and the total water signal were recorded. Thus, the volume of this pore-contained water was directly measurable, as the total volume of the water in the sample was known from gravimetric measurements. Additional measurements were taken with commercially available melanin from *S. officinalis* ink sacs and synthetic tyrosine.

Of the *C. neoformans* melanin samples, day 4 melanin ghosts had the greatest porosity (a sharp peak of 41 $\mu L \cdot Å^{-1} g^{-1}$ at 16.4 Å). Day 7 melanin ghosts showed a broad peak of lower porosity (11 $\mu L \cdot Å^{-1} g^{-1}$ in the $10 - 20$ Å region), and day 10 melanin ghosts had a more complex structure (15 $\mu L \cdot Å^{-1} g^{-1}$ $\approx$10 Å, with additional porosity up to 50 Å). Melanin from *S. officinalis* ink sacs had a slightly lower peak porosity than the day 4 melanin ghosts (a sharp peak of 29 $\mu L \cdot Å^{-1} g^{-1}$ at 12.5 Å). In contrast, the synthetic tyrosine melanin had

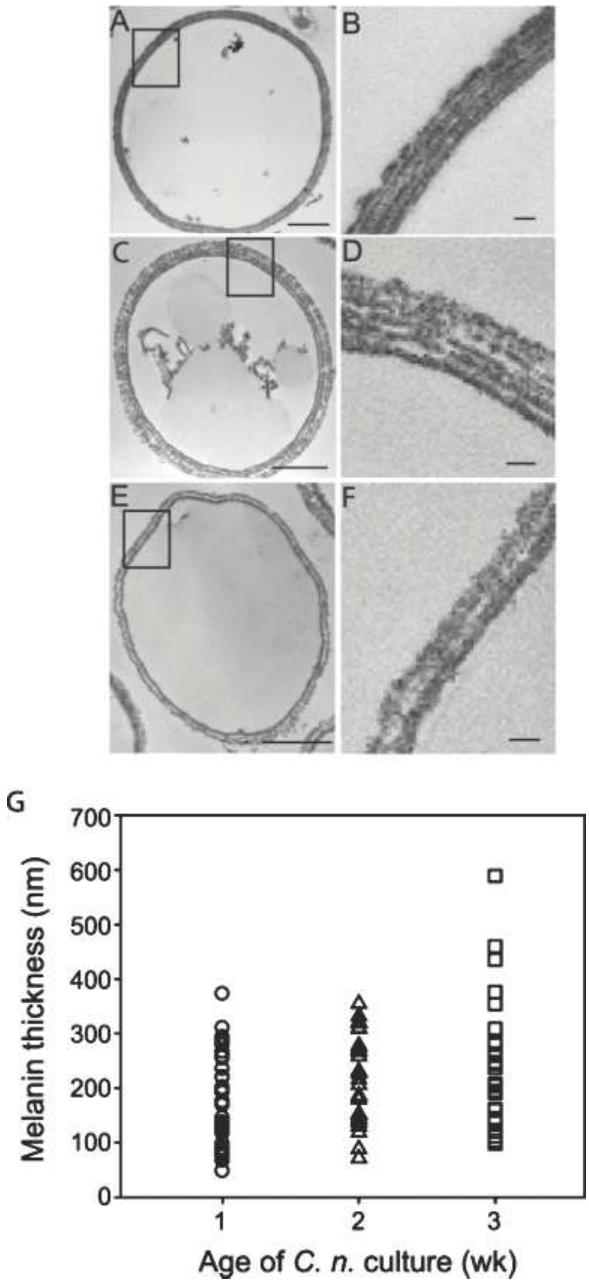

Figure 3.4.6: Melanin in *C. neoformans* is arranged in layers. Transmission electron micrographs of three representative melanin ghosts. (A, C, and E) Cross section of melanin ghosts. Scale bars are 1 μm. (B, D, and F) Close-up of areas indicated by rectangles in panels A, C, and E, respectively. Scale bars are 100 nm. (G) The thickness of melanin shell was measured for 1, 2, and 3 week melanin ghosts, and all data points are plotted: circles, 1 week samples; triangles, 2 week samples; and squares, 3 week samples.

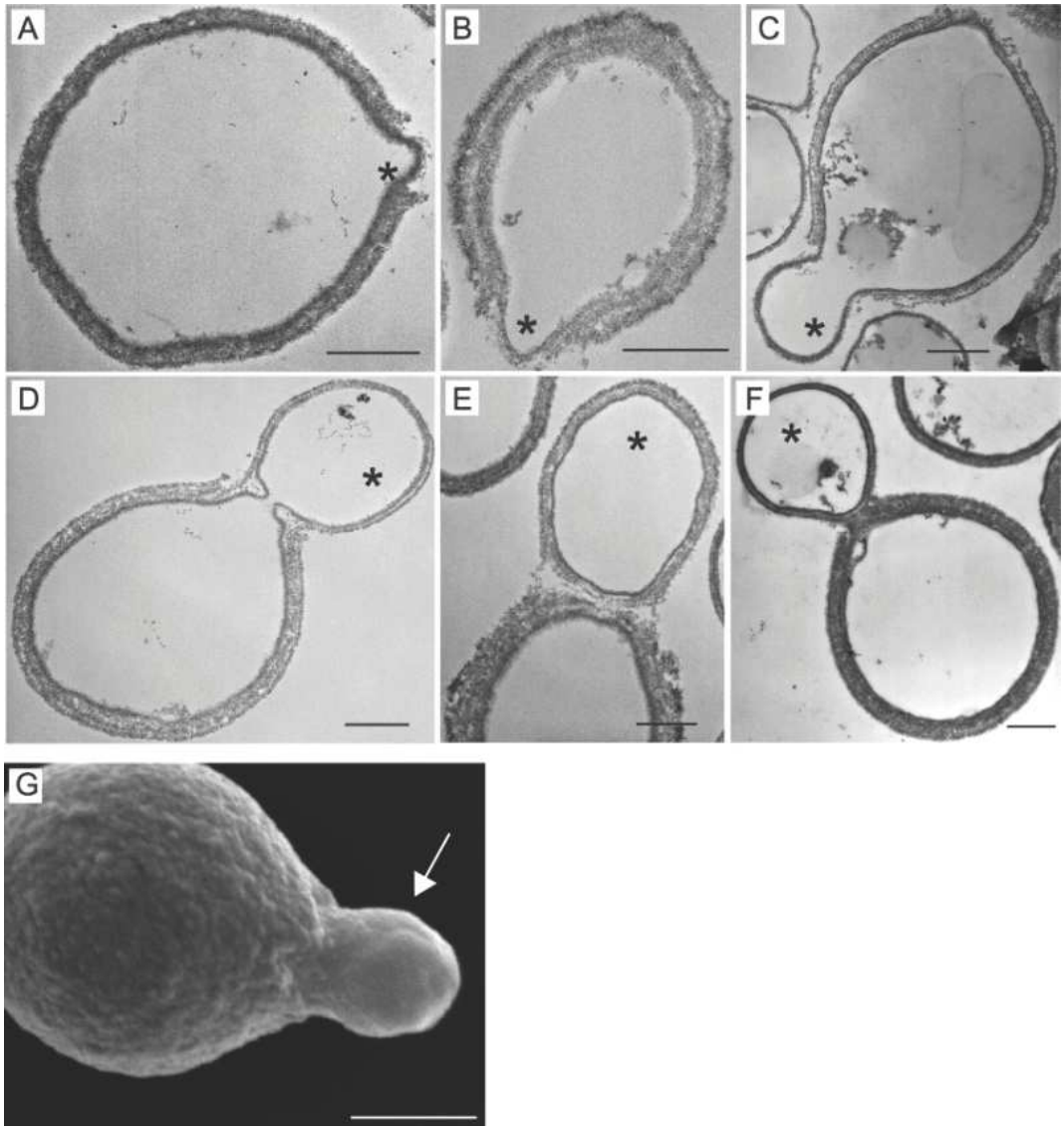

Figure 3.4.7: Melanin layer is thinned around buds. (A–F) Transmission electron micrographs of melanin ghosts made from cells in various stages of budding. An increase in melanin thickness with increasing bud size relative to the mother cell is apparent. Buds are marked with asterisks. Scale bars are 1 μm. (G) SEM of a melanin ghost from a budding cell showing that melanin is smoother around the bud (white arrow).

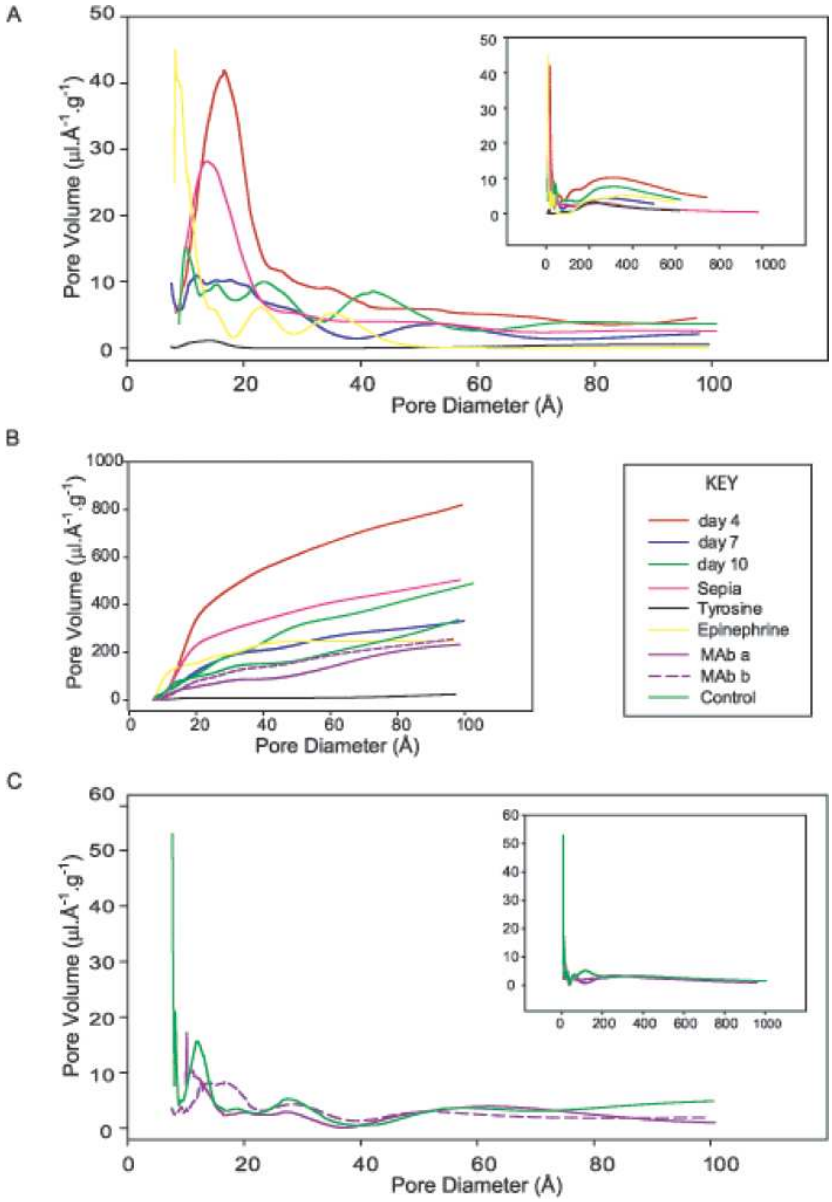

Figure 3.4.8: NMR cryoporometry of *C. neoformans* melanin ghosts. The color key is beside panel B. (A) Pore distribution graphs for the following melanin samples: *C. neoformans* melanin ghosts isolated from cells grown for 4 (day 4), 7 (day 7) or 10 days (day 10) in the presence of L-dopa, melanin from *S. officinalis* (Sepia), synthetic melanin made from tyrosine (Tyrosine) or *C. neoformans* melanin ghosts made from cells grown for 10 days in the presence of epinephrine (Epinephrine). The inset shows the pore distribution over a larger diameter range. (B) Pore integrals for samples in panel A. Pore volume was integrated with respect to pore diameter. (C) Pore distribution graphs for 10 day L-dopa-derived melanin ghosts incubated with control antibody (control) or melanin-binding antibody (Mab a and b). The results of two experiments are shown for the melanin-binding antibody. The inset shows the pore distribution over a large diameter range.

the lowest peak porosity (1.1 $\mu L \cdot Å^{-1} g^{-1}$ at 14 Å) (Figure 3.4.8A). Additional porosity was distributed in broad peaks in the 300 Å range for all samples (Figure 3.4.8A, inset).

With this technique, it is also possible to estimate pore diameter. For all three *C. neoformans* melanin samples, the peak porosity was distributed in pores with diameters ranging from $10 - 20$ Å. The day 10 sample also had pores of ≈40 Å. The change in porosity as a function of melanization and time is indicated by the peaks in the pore distribution graph (Figure 3.4.8A). This can also be seen from the pore integral graph (Figure 3.4.8B). When pore volume was integrated with respect to pore diameter, a rapid increase in the integral was seen in the range of $10 - 50$ Å, corresponding to the presence of pores of that diameter. *S. officinalis* melanin had pores of similar size.

3.4.5 The Antibody to Melanin Reduces Porosity

Prior studies showed that addition of melanin-binding antibody to melanized cells arrested cell growth [39]. We hypothesised that this phenomenon may reflect plugging of melanin pores by specific antibody, a phenomenon that could interfere with cellular nutrition or replicative functions. When melanin ghosts were incubated with a monoclonal antibody against melanin, the total porosity was reduced compared to that with the control antibody. For the control antibody, a peak porosity of ≈16 $\mu g \cdot Å^{-1} g^{-1}$ was observed for pores with a diameter of ≈12 Å. With the melanin antibody, the porosity was 8 $\mu L \cdot Å^{-1} g^{-1}$ for pores of this diameter (Figure 3.4.8C).

3.4.6 Melanins Made from Various Substrates Have Similar Structures

Since *C. neoformans* can synthesise melanin from a variety of substrates, we evaluated the porosity and surface structure of melanin ghosts generated from other substrates. Melanin from *C. neoformans* grown in the presence of epinephrine had a porosity distribution similar to that of melanin made from L-dopa. The pore volume of epinephrine-derived melanin ghosts was distributed in pores ≈10 Å in diameter (Figure 3.4.8A). To compare the surface structure, *C. neoformans* strain 24067 was grown in the presence of dopamine for 14 days

and melanin ghosts were isolated. SEM of the isolated ghosts revealed a granular surface for the dopamine ghosts similar to that with L-dopa (Figure 3.4.1B). We next examined the surface of melanin ghosts isolated from infected mouse brain tissue. *In vivo*, *C. neoformans* is thought to use various neurotransmitters from the host as substrates for melanin production [33]. Ghosts were isolated from mouse brain 21 days after infection by intravenous injection with 5 x 10^5 *C. neoformans* cells. SEM analysis of ghosts recovered from mouse tissue revealed a granular surface similar to that of cells grown *in vitro* (compare panels B and C of Figure 3.4.1).

3.5 Discussion

Determining the structure of melanin in the *C. neoformans* cell wall is essential to understanding the function of melanin with regard to both cell growth and virulence. Previous studies found that melanin can protect fungal cells against insults that this organism is likely to encounter in both the environment and animal hosts. How melanin affects the structure and function of the fungal cell is a fundamental question in the biology of *C. neoformans* and other fungi that melanize their cell wall. In this study, we applied multiple techniques to address the problem of melanin structure: AFM and SEM to examine the surface structure of melanin, TEM to study melanin in cross section, and NMR cryoporometry to analyse the porosity of melanin. The results are internally consistent and provide information for modeling the structure of the melanized cell wall and the budding process in melanized cells. Furthermore, these results may serve as a basis for future investigations into the cellular structures of diverse melanized microbes.

The AFM and SEM images revealed that the surface of melanin ghosts derived from melanized *C. neoformans* cells is composed of discrete granules with roughly uniform dimensions. Depending on the imaging technique that was used, the melanin particles ranged in size from 40 to > 100 nm with the average particle diameter being 76 ± 23 nm based on all measurements using both SEM and AFM. A significant difference was found for granule size measured by SEM versus AFM for 3 week melanin ghosts. The larger measurements for SEM may be explained by the fact that samples are coated with $10 - 15$ nm of gold-palladium prior to viewing in the EM, or by the intrinsic magnification error of the microscope (5 %). Alternatively, the differences may be due to the fact that the measurements were made from a small number of melanin ghosts, and may reflect natural variation in granule size.

The observation that melanin ghosts from melanized *C. neoformans* are composed of assemblies of smaller melanin particles is consistent with published reports on the structure of melanin from other biological sources. Melanin produced in the ink sacs of the cuttlefish *S. officinalis* consisted of particles 150 nm in diameter by AFM imaging [12]. Other studies using high-resolution SEM and TEM methods showed that melanin from *S. officinalis* and bovine eye was comprised of aggregates of smaller particles approximately 20 nm in diameter

[11,25]. Melanin granules have also been reported in other fungi. Scytalone-derived melanin in *Verticillium dahliae* formed 100 nm granules in the cell wall when observed by SEM and TEM [53]. In *Histoplasma capsulatum*, L-dopa-derived granules have been reported [31].

Hence, the structure of melanin in *C. neoformans* ghosts and in other biological sources may be similar and composed of small particles that differ in their three-dimensional organization. Sections of melanin ghosts were analysed by TEM, revealing that the melanin ghosts are composed of two to five layers arranged in a concentric manner to form the melanin ghost wall. When melanin ghosts from budding cells were examined by TEM, the melanin around the bud was thinner than that of the mother cell. As bud size increased relative to the mother cell, the melanin also appeared to increase in thickness. Together, these data are consistent with an increase in melanin thickness with age, possibly by the addition of more layers of similar-sized particles. Furthermore, the TEM images of melanin ghosts from budding cells support the hypothesis that melanin is degraded or remodeled in budding of *C. neoformans*. This is particularly apparent from the image of the smallest bud in which it appears that a break has been made in the melanin, allowing the bud to emerge (Figure 3.4.7A).

On the basis of the microscopy results, we propose that melanin in the *C. neoformans* cell wall is composed of one or more layers of closely packed granules. This is supported by the observation that the surfaces of the melanin ghosts were covered with granular particles $\approx$75 nm in diameter, and by the fact that discrete layers that can be viewed by TEM were approximately the same width of one granule diameter. A question raised by this model is how the melanin granules are held together. One possibility is that they are simply cross-linked together. Alternatively, they could be held together by a lattice or scaffold composed of melanin and/or proteins and polysaccharides. The existence of such a scaffold would have implications for growth and budding of melanized *C. neoformans*, since remodeling of melanin during the budding process could be achieved by degradation of the scaffold. Furthermore, it implies the existence of enzymes required for building and degrading the scaffold. The substructure of the melanin shell could be examined using TEM at resolutions higher than those employed for this research. Qualitative information regarding the presence of a cross-linked melanin layer, or of a scaffold holding melanin granules within its matrix,

could be derived from such analysis. The chemical identity of the scaffold material, if present, could be determined using gas chromatography and mass spectroscopy, after separation of the scaffold from the melanin granules. The melanin layers observed in melanin ghosts are reminiscent of cell wall layers observed for *C. neoformans* cells [1, 44]. Multilaminate structures are a general feature of fungal cell walls [3]. Thus, there exist structures in the fungal cell wall that could serve to direct the deposition of melanin into layers.

Since melanized cells continue to replicate and do not show an obvious growth defect relative to nonmelanized cells [38], we surmised that they must have pores for nutrient acquisition. However, no large pores were visible by microscopy. One possibility is that, rather than having conventional pores, nutrients and other molecules pass through the melanin layer by diffusing through the spaces between the granules. NMR cryoporometry was utilised to determine the porosity of melanin ghosts from *C. neoformans*. NMR cryoporometry revealed that melanin ghosts had pores and that their porosity decreased with the increasing age of the culture from which the ghosts were generated. This may reflect increased synthesis of melanin and/or crosslinking with time. In addition, the studies revealed a complex pore distribution. Most of the pore volume was distributed in relatively small pores $10 - 20$ Å in diameter. However, some pore volume was also distributed in larger pores 300 Å in diameter.

Antibody studies provided additional insights into melanin porosity. Melanin ghosts were incubated with melanin binding antibodies prior to performance of the NMR cryoporometry analysis, and we found a reduction in the measured pore volume of melanin, for pores less than 20 Å in diameter. The most straightforward explanation for this phenomenon is that the antibody binds to the melanin granules and blocks the pore by physical occupation. By contrast, the melanin-binding antibody had no effect on pore volume of pores 300 Å in diameter, suggesting that these pores were inaccessible to the antibody (Figure 3.4.8C, inset). Together, these results suggest that melanin ghosts have two sets of pores: (1) smaller, external pores accessible to antibody and (2) larger internal pores inaccessible to antibody.

The NMR cryoporometry results have implications for the arrangement of melanin granules, which approximate microspheres. The predicted volume for a closely packed hexagonal array of spheres is approximately one-fifth the size of the sphere, 15 nm in this case [51].

Therefore, the NMR cryoporometry results imply that the granules in melanin ghosts are of an irregular shape and arrangement. Therefore, we propose a model of melanin structure and function in which irregularly shaped melanin granules are fused in layers (Figure 3.5.1). The spaces between granules are represented by the small pores observed with NMR cryoporometry.

By contrast, the internal spaces between layers are larger, represented by the larger-sized pores. Such a structure enables the melanin to act as a "sieve," allowing certain molecules to pass through, but restricting the passage of larger molecules into the cell. This function is augmented by the fact that melanin also binds and sequesters many such molecules [17]. The ability of melanin to bind various molecules can be explained by the highly charged and aromatic melanin surface [28, 35].

This model implies that melanin porosity is a property of the arrangement of melanin particles, and consequently, there appears to be no need for specialised pore structures to permit nutrient acquisition. The measured pore size of $10 - 20$ Å is similar to the size of glucose and amino acid molecules. Larger molecules, such as amphotericin B, which has been found to form large aggregates, might be too large to fit in the pores [23]. Hence, the resistance of melanized cells to amphotericin B may reflect inability of this drug to penetrate the cell wall. The measured and predicted pore sizes suggest a theoretical limit to the size of antifungal drugs which can be expected to be effective against melanotic fungi.

Prior studies have shown that addition of melanin-binding antibodies to melanized *C. neoformans* cells arrests their growth but has no effect on nonmelanized cells [39]. Since nutrition is essential for growth and nutrient acquisition by melanized cells would almost certainly require competent pores, the ability of a specific antibody to reduce pore size could account for the observed growth arrest. Pore blocking by a specific antibody resulting in a starvation state would represent a novel protective function for antibody-mediated inhibition of *C. neoformans*.

NMR cryoporometry has been used to study cross-linking in polymer systems [4]. There have also been a number of studies of pore sizes in zeolite skeletons. A caveat of the NMR cryoporometry results is that the melanin ghost preparation may affect the porosity of melanin from *C. neoformans*. However, this application of NMR cryoporometry to the

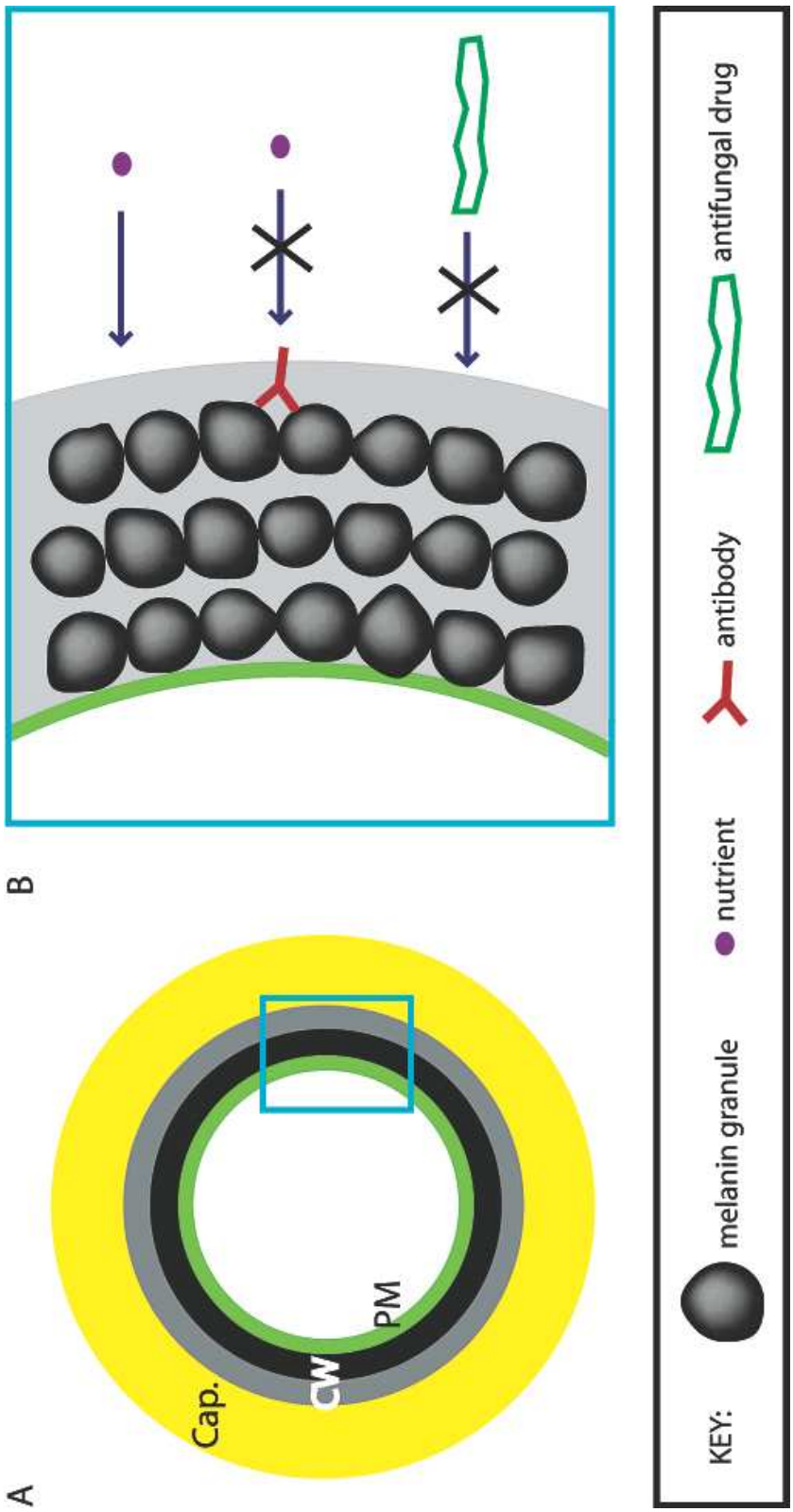

Figure 3.5.1: Model of melanin structure of *C. neoformans*. (A) Cross-sectional depiction of the *C. neoformans* cell. The polysaccharide capsule (Cap.) surrounds the cell. Melanin (black) is localised to the cell wall (CW), next to the plasma membrane (PM). (B) Cross-sectional depiction of melanin microstructure in the cell wall of *C. neoformans*. The melanin is comprised of multiple layers of granular particles. According to the model, small nutrient molecules, such as sugars and amino acids, can enter the cell by passing through spaces between the melanin particles. Antibody binding to melanin may prevent passage of nutrients by blocking such spaces. In addition, the large size of certain antifungal drugs may prevent their passage through the tight spaces between melanin granules.

study of pores in melanin shells of fungi is a novel application of this technique to the biological world. These melanin ghosts offer a clean system for NMR cryoporometry, as there are no changes to the bulk melting point caused by dissolved components in the water. All changes to the melting point arise from the Gibbs-Thomson dimensional effects on the thermodynamics of the system. However, given that the technique of cryoporometry does not require desiccation of the sample, there is now a clear interest in investigating the extent to which it can be applied to the study of other, nonmelanized biological systems. This study has shown that NMR cryoporometry has the necessary sensitivity for measuring the size and volume of pores in biological polymers, and thus potentially is a technique with a large number of new applications in the biological field.

3.6 Bibliography

[1] Y. Al-Doory. The ultrastructure of *Cryptococcus neoformans*. Sabouraudia, 9:115–118, 1971.

[2] D. S. Alviano, A. J. Franzen, L. R. Travassos, C. Holandino, S. Rozental, R. Ejzemberg, C. S. Alviano, and M. L. Rodrigues. Melanin from *Fonsecæa pedrosoi* induces production of human antifungal antibodies and enhances the antimicrobial efficacy of phagocytes. Infection and Immunity, 72(1):229–37, 2004.

[3] J. M. Aronson. The Cell Wall. In G. C. Ainsworth and A. S. Sussman, editors, The Fungal Cell, volume I of The Fungi: An Advanced Treatise, pages 49–76. Academic Press, New York and London, 1965.

[4] M. Baba, J.-M. Nedelec, J. Lacoste, and J.-L. Gardette. Calibration of cyclohexane solid-solid-phase transition thermoporosimetry and application to the study of crosslinking of elastomers upon aging. Journal of Non-Crystalline Solids, 315:228–238, 2003.

[5] K. L. Buchanan and J. W. Murphy. What makes *Cryptococcus neoformans* a pathogen? Emerging and Infectious Diseases, 4(1):71–83, 1998.

[6] N. A. Burnham, X. Chen, C. S. Hodges, G. A. Matei, E. K. Thoreson, C. J. Roberts, M. C. Davies, and S. J. B. Tendler. Comparison of calibration methods for atomic-force microscopy cantilevers. Nanotechnology, 14:1–6, 2003.

[7] M. J. Butler and A. W. Day. Fungal melanins: A review. Canadian Journal of Microbiology, 44:1115–1136, 1998.

[8] T. A. Camesano and B. E. Logan. Probing bacterial electrosteric interactions using atomic force microscopy. Environmental Science and Technology, 34:3354–3362, 2000.

[9] A. Casadevall, A. L. Rosas, and J. D. Nosanchuk. Melanin and virulence in *Cryptococcus neoformans*. Current Opinion in Microbiology, 3(4):354–8, 2000.

[10] Y. C. Chang and K. J. Kwon-Chung. Complementation of a capsule-deficient mutation of *Cryptococcus neoformans* restores its virulence. Molecular and Cell Biology, 14(7):4912–9, 1994.

[11] C. M. Clancy, J. B. Nofsinger, R. K. Hanks, and J. D. Simon. A hierarchical self-assembly of eumelanin. Journal of Physical Chemistry B, 104(33):7871–7873, 2000.

[12] C. M. Clancy and J. D. Simon. Ultrastructural organization of eumelanin from *Sepia officinalis* measured by atomic force microscopy. Biochemistry, 40(44):13353–60, 2001.

[13] Digital Instruments. Scanning Probe Microscopy Training Notebook. Veeco Metrology Group, 1998.

[14] T. L. Doering, J. D. Nosanchuk, W. K. Roberts, and A. Casadevall. Melanin as a potential cryptococcal defence against microbicidal proteins. Medical Mycology, 37(3):175–81, 1999.

[15] J. Garcia-Rivera and A. Casadevall. Melanization of *Cryptococcus neoformans* reduces its susceptibility to the antimicrobial effects of silver nitrate. Medical Mycology, 39(4):353–7, 2001.

[16] A. Glatman-Freedman and A. Casadevall. Monoclonal antibodies to surface antigens of *Mycobacterium tuberculosis* and their use in a modified enzyme-linked immunosorbant spot assay for detection of mycobacteria. Journal of Clinical Microbiology, 34(11):2795–2802, 1996.

[17] H. Z. Hill. The function of melanin or six blind people examine an elephant. Bioessays, 14(1):49–56, 1992.

[18] G. B. Huffnagle, G. H. Chen, J. L. Curtis, R. A. McDonald, R. M. Strieter, and G. B. Toews. Down-regulation of the afferent phase of T cell-mediated pulmonary inflammation and immunity by a high melanin-producing strain of *Cryptococcus neoformans*. Journal of Immunology, 155(7):3507–16, 1995.

[19] C. M. Hull and J. Heitman. Genetics of *Cryptococcus neoformans*. Annual Review of Genetics, 36:557–615, 2002.

[20] R. Ikeda, T. Sugita, E. S. Jacobson, and T. Shinoda. Effects of melanin upon susceptibility of *Cryptococcus* to antifungals. Microbiology and Immunology, 47(4):271–7, 2003.

[21] C. L. Jackson and G. B. McKenna. The melting behavior of organic materials confined in porous solids. Journal of Chemical Physics, 93(12):9002–9011, 1990.

[22] K. J. Kwon-Chung, I. Polacheck, and T. J. Popkin. Melanin-lacking mutants of *Cryptococcus neoformans* and their virulence for mice. Journal of Bacteriology, 150(3):1414–21, 1982.

[23] M. T. Lamy-Freund and W. F. Reed. Characterization and time dependence of amphotericin B: Deoxycholate aggregation by quasielastic light scattering. Journal of Pharmaceutical Sciences, 80(3):262–266, 1991.

[24] K. Langfelder, M. Streibel, B. Jahn, G. Haase, and A. A. Brakhage. Biosynthesis of fungal melanins and their importance for human pathogenic fungi. Fungal Genetics and Biology, 38(2):143–58, 2003.

[25] Y. Liu and J. D. Simon. The effect of preparation procedures on the morphology of melanin from the ink sac of *Sepia officinalis*. Pigment Cell Research, 16(1):72–80, 2003.

[26] N. Mohagheghpour, N. Waleh, S. J. Garger, L. Dousman, L. K. Grill, and D. Tuse. Synthetic melanin suppresses production of proinflammatory cytokines. Cell Immunology, 199(1):25–36, 2000.

[27] E. Mylonakis, F. M. Ausubel, J. R. Perfect, J. Heitman, and S. B. Calderwood. Killing of *Caenorhabditis elegans* by *Cryptococcus neoformans* as a model of yeast pathogenesis. Proceedings of the National Academy of Science of the United States of America, 99(24):15675–80, 2002.

[28] J. D. Nosanchuk and A. Casadevall. Cellular charge of *Cryptococcus neoformans*: Contributions from the capsular polysaccharide, melanin, and monoclonal antibody binding. Infection and Immunity, 65(5):1836–41, 1997.

[29] J. D. Nosanchuk and A. Casadevall. Budding of melanized *Cryptococcus neoformans* in the presence or absence of L-dopa. Microbiology, 149(Pt 7):1945, 2003.

[30] J. D. Nosanchuk and A. Casadevall. The contribution of melanin to microbial pathogenesis. Cell Microbiology, 5(4):203–23, 2003.

[31] J. D. Nosanchuk, B. L. Gomez, S. Youngchim, S. Diez, P. Aisen, R. M. Zancope-Oliveira, A. Restrepo, A. Casadevall, and A. J. Hamilton. *Histoplasma capsulatum* synthesizes melanin-like pigments *in vivo* and during mammalian infection. Infection and Immunity, 70:5124–5131, 2002.

[32] J. D. Nosanchuk, A. L. Rosas, and A. Casadevall. The antibody response to fungal melanin in mice. Journal of Immunology, 160(12):6026–31, 1998.

[33] J. D. Nosanchuk, A. L. Rosas, S. C. Lee, and A. Casadevall. Melanisation of *Cryptococcus neoformans* in human brain tissue. Lancet, 355(9220):2049–2050, 1998.

[34] J. D. Nosanchuk, J. Rudolph, A. L. Rosas, and A. Casadevall. Evidence that *Cryptococcus neoformans* is melanized in pigeon excreta: Implications for pathogenesis. Infection and Immunity, 62:5477–5479, 1999.

[35] J. D. Nosanchuk, P. Valadon, M. Feldmesser, and A. Casadevall. Melanization of *Cryptococcus neoformans* in murine infection. Molecular and Cell Biology, 19(1):745–50, 1999.

[36] J. R. Perfect and A. Casadevall. Cryptococcosis. Infectious Disease Clinics of North America, 16(4):837–74, v–vi, 2002.

[37] I. Polacheck, V. J. Hearing, and K. J. Kwon-Chung. Biochemical studies of phenoloxidase and utilization of catecholamines in *Cryptococcus neoformans*. Journal of Bacteriology, 150:1212–1220, 1982.

[38] A. L. Rosas and A. Casadevall. Melanization affects susceptibility of *Cryptococcus neoformans* to heat and cold. FEMS Microbiology Letters, 153(2):265–72, 1997.

[39] A. L. Rosas, J. D. Nosanchuk, and A. Casadevall. Passive immunization with melanin-binding monoclonal antibodies prolongs survival of mice with lethal *Cryptococcus neoformans* infection. Infection and Immunity, 69(5):3410–2, 2001.

[40] A. L. Rosas, J. D. Nosanchuk, M. Feldmesser, G. M. Cox, H. C. McDade, and A. Casadevall. Synthesis of polymerized melanin by *Cryptococcus neoformans* in infected rodents. Infection and Immunity, 68(5):2845–2853, 2000.

[41] A. L. Rosas, J. D. Nosanchuk, B. L. Gomez, W. A. Edens, J. M. Henson, and A. Casadevall. Isolation and serological analyses of fungal melanins. Journal of Immunological Methods, 244(1-2):69–80, 2000.

[42] S. D. Salas, J. E. Bennett, K. J. Kwon-Chung, J. R. Perfect, and P. R. Williamson. Effect of the laccase gene CNLAC1, on virulence of *Cryptococcus neoformans*. Journal of Experimental Medicine, 184(2):377–86, 1996.

[43] J. N. Steenbergen, H. A. Shuman, and A. Casadevall. *Cryptococcus neoformans* interactions with amoebae suggest an explanation for its virulence and intracellular pathogenic strategy in macrophages. Proceedings of the National Academy of Science of the United States of America, 98(26):15245–50, 2001.

[44] H. Stoetzner and C. Kemmer. The morphology of *Cryptococcus neoformans* in human cryptococcosis. A light-,phase-contrast and electron-microscopic study. Mycopathologia et Mycologia Applicata, 45(3):327–35, 1971.

[45] D. van Duin, A. Casadevall, and J. D. Nosanchuk. Melanization of *Cryptococcus neoformans* and *Histoplasma capsulatum* reduces their susceptibilities to amphotericin B and caspofungin. Antimicrobial Agents and Chemotherapy, 46(11):3394–400, 2002.

[46] Y. Wang, P. Aisen, and A. Casadevall. *Cryptococcus neoformans* melanin and virulence: Mechanism of action. Infection and Immunity, 63(8):3131–6, 1995.

[47] Y. Wang, P. Aisen, and A. Casadevall. Melanin, melanin "ghosts," and melanin composition in *Cryptococcus neoformans*. Infection and Immunity, 64(7):2420–4, 1996.

[48] Y. Wang and A. Casadevall. Decreased susceptibility of melanized *Cryptococcus neoformans* to UV light. Applied and Environmental Microbiology, 60(10):3864, 1994.

[49] Y. Wang and A. Casadevall. Growth of *Cryptococcus neoformans* in presence of L-dopa decreases its susceptibility to amphotericin B. Antimicrobial Agents and Chemotherapy, 38(11):2648–50, 1994.

[50] Y. Wang and A. Casadevall. Susceptibility of melanized and nonmelanized *Cryptococcus neoformans* to nitrogen- and oxygen-derived oxidants. Infection and Immunity, 62(7):3004, 1994.

[51] J. B. W. Webber. Characterizing Porous Media, Appendix H. Doctoral Dissertation, University of Kent, Canterbury, Kent, UK, 2000.

[52] J. B. W. Webber, J. H. Strange, and J. C. Dore. An evaluation of NMR cryoporometry, density measurement and neutron scattering methods of pore characterization. Magnetic Resonance Imaging, 19:395–399, 2001.

[53] M. H. Wheeler, W. J. Tolmsoff, and Meola S. Ultrastructure of melanin formation in *Verticillium dahliae* with (+)-scytalone as a biosynthetic intermediate. Canadian Journal of Microbiology, 22:702–711, 1976.

[54] P. R. Williamson. Biochemical and molecular characterization of the diphenol oxidase of *Cryptococcus neoformans*: Identification as a laccase. Journal of Bacteriology, 176(3):656–64, 1994.

CHAPTER 4

On the Importance of Precise Calibration Techniques for an Atomic Force Microscope

4.1 Abstract

Proper calibration of any instrument is vital to an investigator's ability to compare laboratory experiments, as well as to draw quantitative relations between experimental results and the real world. For the atomic force microscope, knowledge of quantities such as the probe spring constant, the piezoactuator voltage/height response, and the probe radius of curvature is necessary when transforming raw data into height, separation, and force. These parameters are also prerequisites when applying mathematical models to the collected data. In this communication, we adapt existing techniques of quantifying these parameters to our equipment and show differences between the adjusted parameters and those provided by the manufacturer.

The total statistical uncertainty within the measurement of a force magnitude is $\approx 80\%$ using manufacturers' values. After adjustment, this contribution drops to approximately 1%. The uncertainty in the radius of the probe falls from 20% (manufacturer's values) to 3% after calibration. The combined effect of quantifying these parameters, which had previously not been explored in concert, demonstrates the necessity of properly understanding one's equipment in order to generate reproducible and credible experimental results.

4.2 Introduction

Atomic force microscopy (AFM) has evolved into an elegant tool for topographical imaging [13,15], as well as for measuring force-separation interactions between a probe and substrate [1, 8]. Recently, the basic probe-sample system has been extended by chemical or physical modification of the probe with organic molecules [2,22], polymeric materials [1,11] and whole, metabolically active microbial cells [3, 12] in order to model environmentally and medically relevant systems.

In many cases, however, investigators neglect to properly calibrate the requisite quantities used to convert the raw data signal of the AFM into physically meaningful parameters, such as sample height, tip-sample separation, probe spring constant and probe radius of curvature. Knowledge of these quantities is necessary to obtain any true sense of accuracy and precision within and amongst a group of experiments, as well as to compare experimental data amongst different researchers. It is further necessary to have precise values of these quantities when applying mathematical models to collected data sets.

In this communication, we describe various techniques, adapted from previous research [5, 27], used to quantify the parameters necessary for proper translation of AFM data into physically meaningful data. The concerted effect of the calculated parameters has never been qualitatively or quantitatively examined. As such, we will extend the previous work to demonstrate the effect of the piezoactuator travel distance and cantilever spring constant on the approach and retraction portions of a force-separation cycle, as well as the influence of the probe radius of curvature on the results of a mathematical model. The importance of this latter quantity is shown in the application of the classical Derjaguin-Landau-Verwey-Overbeek (DLVO) theory of colloid stability [10, 28], which models the energy profiles of London-van der Waals and electrostatic interactions as two surfaces (in this case, a hypothetical model surface and an AFM probe) are brought into contact.

The techniques described are specific to our instrument (Dimension 3100 AFM with Nanoscope® IIIa controller, Digital Instruments, Santa Barbara, CA, USA), available software (Nanoscope® v. 4.43 r8, Digital Instruments; Matlab® v. 7.0 R14 (The Mathworks, Natick, MA, USA)) and probes (Mikromasch, Portland, OR, USA). However, with

minor adaptations, these techniques may be extended to a number of other instrument/software/probe combinations.

4.3 Calibration Parameters

In the vernacular of this document, the term "calibration" is defined as the process of determining a series of operational parameters of the AFM system, independent of manufacturers' reported values. Further, "calibration" includes the application of those parameters to recorded data sets and mathematical models. Of particular importance to the verity of our measurements, we describe the quantification of the true tip-sample separation distance, the cantilever spring constant, and the tip radius of curvature. These are described qualitatively below, and in mathematical terms in Section 4.4.

4.3.1 Sample Height and Tip-Sample Separation

During topographical imaging, the voltage applied to the vertical components of the AFM piezoactuator is adjusted via the proportional-integral (PI) feedback loop while the piezoactuator raster-scans the tip across the surface in the X-Y plane [18, 19]. In contact mode, the loop serves to maintain a constant cantilever deflection/tip-sample interaction force. In intermittent contact mode, the loop maintains a constant cantilever oscillation amplitude. Deviations from the setpoint and the resulting response of the piezoactuator are interpreted by the controller as height. In force mode, the raster motion is stopped (*viz.*, no voltage is applied to the X and Y components of the piezoactuator) and the piezoactuator only moves in the positive and negative vertical directions via a known ramped voltage. The ramp is reported in terms of tip-sample separation and/or indentation.

Based on the AFM configuration, the software translates voltage into separation distance via a series of internal algorithms and calibration parameters. Unless the AFM is adequately calibrated, however, this distance may not accurately represent the actual motion of the piezoactuator through space. The software is not capable of accounting for piezoactuator nonlinearity (*e.g.,* hysteresis, creep, thermal deformation during the voltage ramp, or the specific mechanical properties of the piezoactuator).

A hardware correction to piezoactuator nonlinearity employs closed Z-loop control of the actuator, which has a much faster response compared to the open-loop PI control found on most AFMs. Closed-loop control is available in most newer instruments. However, the vast majority of AFMs in use today still rely on PI control. Therefore, it is important to realise that the separation reported by the AFM software is in actuality a multiplicative conversion from voltage to distance, and may not accurately represent the tip-sample separation.

To account for piezoactuator nonlinearity, it is necessary to quantify the actual distance traveled by the AFM laser light and compare it to the software-reported value. The technique was adapted from [5], and modified to take advantage of more precise equipment. This included an optical spectrum analyser connected to a fiber-optic network, which was also employed by the previous authors (*op. cit.*) when the network became available.

4.3.2 Probe Radius of Curvature

Knowledge of the radius of curvature of the AFM probe is essential to several mathematical models [7, 10, 28]. However, manufacturers' reports of this value can vary by more than a factor of three [19], leading to inaccuracy and uncertainty in subsequent calculations. It is, therefore, essential to determine the probe radius of curvature before and after each experiment, both to characterise this parameter accurately for mathematical modeling and to account for wear of the tip after repeated contact with the sample surface.

Thoreson and Burnham [27] have recently formulated a simple method to extract the probe radius of curvature from topographical image data taken on a step grating (TGZ01, Mikromasch) using beads $2 - 60$ µm in diameter. The method provides 9% accuracy and 4% precision as compared to direct measurement of the sphere radius using a calibrated microscope. These values may be verified optically, as the feature size is greater than the wavelength of light in the visible spectrum ($\approx 390 - 780$ nm). However, standard AFM tips, which have radii on the order of 10 nm, require a non-optical method. High resolution electron microscopy can provide the required precision, but incur high capital and maintenance costs, and require significant operational expertise. Further, these techniques often require the destructive preparation of the sample, making them useless for subsequent AFM experiments. By applying a simple mathematical regression to the extrapolated tip profile,

it is possible to obtain a precise measurement with minimal asset commitment. The original technique is modified to account for a paraboloid, as opposed to a spherical, probe geometry.

4.3.3 Probe Spring Constant

The probe spring constant is by far the most important, as well as the least frequently measured, parameter in force spectroscopy. Assuming the validity of Hooke's Law, the spring constant relates the cantilever deflection to the interaction force. Manufacturers of AFM probes routinely provide a nominal value of the cantilever spring constant, but rarely describe the method by which it was measured, or the standard deviation associated with those measurements. Those that do provide a range of values that may span a full order of magnitude. Many calibration methods are available to the researcher, but these often do not adequately characterise the properties of the probe.

For example, Cleveland *et al.* [9] developed a widely-used method of calculating the cantilever spring constant. By attaching a known mass to the end of the cantilever, the researcher may record changes in its resonant frequency. Then, using these data and the bulk physical properties of the cantilever (geometry, density), one may apply a simple analytical expression to calculate the spring constant. This method, however, requires that the cantilever itself be an isotropic continuum. Therefore, it cannot account for spatial variations in the physical properties of the cantilever, or for the contribution of reflective metal layers to the mechanical functionality of the probe as a whole.

So-called "thermal" techniques, including that developed by Hutter and Bechhoefer [17], require that the thermal distribution spectrum of the cantilever (mean square amplitude fluctuations versus frequency) be captured. In this method, it is assumed that the thermal properties of the cantilever follow a Lorentzian function in the frequency domain, with fluctuations arising from alternate sources (*e.g.,* white noise) superposing linearly to produce the final spectrum. With the additional assumption that the cantilever's fluctuations at resonance occur at frequencies measurably different from those of the background noise sources, one may subtract each background element to obtain the Lorentzian. Integration of the mean square amplitude with respect to frequency yields power, which is inversely proportional to the spring constant of the cantilever. Thermal techniques are considered more

precise than geometric methods, as they are based in standard physical theories, are independent of the cantilever material and geometry, and require no additional measurements of the surroundings. These techniques require additional calibration of the AFM (*viz.*, knowledge of the piezoactuator voltage/height response), but, as this is a requirement common to force cycle analysis, its application should be straightforward to most AFM users.

A hybrid thermal/geometric method has been developed by Sader *et al.* [24, 25] and Green *et al.* [14], in which the cantilever spring constant in the fundamental flexural resonance mode is related to the plan view dimensions of the cantilever as well as its resonant frequency, the density of the surrounding medium (usually air), and the imaginary portion of a hydrodynamic function [23], which is dependent upon the local Reynolds' number. This method has been shown to work extremely well for rectangular cantilevers over a wide range of spring constants, and does not require rigorous calibration of the AFM to be applicable. However, precise measurements of the cantilever plan dimensions, fluid density and the fluid Reynolds' number are essential to credible results from this model, and therefore limit its practical use.

The method used in this paper was adapted from [5], and is purely thermal in its formulation. This method was chosen primarily for its simplicity of application, *viz.*, it is necessary only to obtain the thermal noise spectrum of the cantilever at its fundamental resonant frequency without the explicit calculation of the cantilever geometry or any other factors. The noise spectrum in the frequency domain is fitted as the sum of inverse frequency and white noise, as well as a peak describing the resonant behaviour of the cantilever as that of a simple harmonic oscillator. Nonlinear least-squares regression of the spectrum yields numerical results which may be used to directly calculate the normal cantilever spring constant. Specific mathematics regarding the model are described in Section 4.4.

4.4 Materials and Methods

4.4.1 Sample Height and Tip-Sample Separation

The beam from the AFM laser diode was reflected into a fiber optic wire and passed to an optical spectrum analyser (AQ6317B, Ando Electric Co, Ltd, Newnan, GA, USA), which measured the actual diode wavelength. Next, a cantilever was mounted into the standard contact mode holder (DAFMCH, Digital Instruments), and the laser aligned half on/half off the cantilever. This generates an interference pattern in the force cycles which may be used to determine the software-reported value of distance.

The AFM was engaged in contact mode and translated vertically using the step motor by at least 50 μm to remove interactions between the probe and sample. In force mode, one sees a periodic interference pattern resulting from the misaligned laser. Software parameters were adjusted such that three periods of the oscillation ($N_{int} = 3$) were visible in the viewing window. Ten interference patterns were captured.

Interference patterns were plotted as piezoactuator displacement on the abscissa and raw photodiode voltage, in terms of Least Significant Bits (LSB), on the ordinate. The LSB is a numerical representation of the digital voltage signal from the photodiode detector, ranging from 0 to 65,536. ΔZ_M, shown in Equation 4.1 as the wavelength of the interference peaks, serves as a reference point describing distance as extrapolated from the potential difference from the piezoactuator.

$$\Delta Z_M = \frac{\Delta z}{N_{int}} \tag{4.1}$$

where Δz is the total piezoactuator displacement as recorded by the AFM software, and N_{int} is the number of interference wavelengths within that displacement range. Δz is chosen such that only an integer multiple of interference wavelengths are used in the calculation of ΔZ_M.

ΔZ_P is related to the actual distance traveled by the laser beam, as calculated from the known laser diode wavelength. Since any signal recorded by the AFM in an interference pattern must be the result of constructive interference (*viz.*, the split waveforms must sum to an integer multiple of the wavelength at the photodetector surface), we may calculate

ΔZ_P according to Equation 4.2.

$$\Delta Z_P = \frac{\lambda}{1 + cos(2\theta)} \tag{4.2}$$

where λ is the laser wavelength (nm) and θ is the angle of repose of the cantilever in the holder (rad). This latter quantity was measured as $10 \pm 0.1°$ with a calibrated optical microscope.

The ratio $\Delta Z_P / \Delta Z_M$ represents the separation correction factor.

$$\frac{\Delta Z_P}{\Delta Z_M} = \frac{\lambda}{1 + cos(2\theta)} \frac{N}{\Delta z} \tag{4.3}$$

where all variables are defined as above. Variation of this quantity from unity shows that the actual piezoactuator displacement does not agree with that reported by the software.

4.4.2 Probe Radius of Curvature

To measure the radius of curvature of the AFM probe, we used a 20 nm step-height grating (TGZ01, Mikromasch). This grating is comprised of parallel silicon steps, 20 nm in height. This specific step height was chosen to be on the same order of magnitude as the expected tip radius. If the step were significantly larger than the radius, dilation effects between the tip and step will produce an artificially large result. The microscope was configured according to manufacturer's specifications, and engaged in contact mode. It is important that the vertical bars of the grating are orthogonal to the fast scan direction. To verify this, we recorded a relatively low magnification topographical image (20 x 20 μm) and measured the angle of the receding edge of the grating features. If this angle differed from orthogonality by more than 2°, the AFM was withdrawn and the grating manually rotated.

After proper sample alignment, the scan size was adjusted such that only the receding edge of each step was scanned (approx. 2 x 2 μm). Scanning the advancing edge of the feature can introduce torsional artifacts to the image and affect data analysis. Image data (256 x 256 pixel resolution) were exported from the AFM software and converted to height. Topographical data were imported into a spreadsheet program, and the 256 lines of the scan image were averaged. The vertical minimum of the averaged data was then calculated, the value of which was subtracted from all points to allow for easier mathematical treatment.

The original method [27] used spherical glass beads attached to the cantilevers, and could, therefore, fit the averaged data with the equation for a circular arc. However, typical silicon or silicon nitride AFM tips are microfabricated such that the tip of the probe is very sharp, enhancing image resolution. As such, the lateral profile of these probes is either paraboloid or polyhedral. Based on the shape of the averaged data curves, we found that a paraboloid model best described our experimental system.

A translated parabola has an apex at (h, k) in the Cartesian plane, with F defined as the length of the chord connecting (h, k) and (h, c), the focal point. Since the distance from any point on the parabola to the focus is constant [4], we chose to use this length as the minimising parameter. This is parallel to use of the radius of a circle in [27]. To evaluate c, we apply the equation for a translated, downward-opening parabola:

$$c = -\frac{(x-h)^2}{4(z-k)} \tag{4.4}$$

D, the distance between point F and each point on the parabola, is calculated from:

$$D = \sqrt{(x-c)^2 + z^2} \tag{4.5}$$

Using the coordinates of the apex as the two fitting parameters for the model, we may now calculate D for each point in the data set. The radius of the probe is then calculated by minimising the standard deviation of the length of the focal chord according to:

$$\delta D = \sqrt{\frac{N\sum_{i=1}^{N} D_i^2 - \left(\sum_{i=1}^{N} D_i\right)^2}{N(N-1)}} = 0 \tag{4.6}$$

Standard deviation minimisation is performed using the Solver add-in from Microsoft Excel®.

4.4.3 Probe Spring Constant

Cantilevers used for analysis (Mikromasch CSC38, Mikromasch NSC36, Digital Instruments DNP-S, and Digital Instruments TESPA) were mounted in the tip holder (DAFMCH, Digital Instruments). The laser was aligned to the free end of the cantilever and centered

using the fine adjust knobs on the side of the scanner. It is essential to eliminate as many external noise sources as possible prior to and during data capture to ensure a precise measurement. As such, the AFM used in this experimentation is equipped with an acoustical isolation chamber which surrounds the instrument, minimising external thermal, optical and mechanical/vibrational influences. The instrument is seated on a floating air table, which also reduces external noise levels.

After the laser was properly aligned, the isolation chamber was closed and the AFM was engaged in contact mode. Entering force mode, a tip-sample interaction was located by adjusting the deflection ramp location ("Z Scan Start" parameter in the Nanoscope^{TM} software). Before capturing the curve, a line was drawn parallel to the contact regime of the force curve (defined as the region in which cantilever deflection is equal to piezoactuator displacement at high load). This step sets the sensitivity parameter, which provides a relationship between cantilever deflection (nm) and the potential change across the photodetector (V).

Next, using the step motor, the scanner was translated vertically by at least 100 µm to remove any tip-substrate interactions. The AFM was allowed to scan for at least 30 min prior to measurement to allow the system to come to thermal equilibrium. To capture the noise spectrum, several parameters were set to eliminate as many noise sources as possible. Proportional and integral gains were set to zero and the deflection setpoint to 1, removing the influence of the feedback loop on the X- and Y-components of the piezoactuator. Image resolution was set to 512 x 512 pixels (this is the maximum allowable array size in most widely available spreadsheet packages). The capture channel was set to Deflection, and the scan rate set to its maximum (for the Dimension 3100, this is 61 Hz). Finally, the scan size was set to zero, removing the influence of the X- and Y-components of the piezoactuator. Five noise spectra were captured for each cantilever and exported as comma-delimited spreadsheets with the header intact. Dynamic changes in the noise spectra, and therefore the spring constant, were measured after 30 min of scanning a borosilicate glass microscope slide in contact mode. The influence of cantilever oscillation was also investigated by measuring the spring constant of the cantilever after an additional 30 min scan in intermittent contact mode.

Custom Matlab® scripts were developed to analyse the data according to [5]. An adap-

tation was made at the suggestion of the authors (*op. cit.*) to add a correction factor to their Equation 4.7. This modified equation is formulated such that one need not measure the entire frequency spectrum ($-\infty \rightarrow \infty$), but may instead measure within the bandwidth of the instrument (*op. cit.*). In order to convert data from mean square voltage to mean square amplitude based on the actual frequency resolution of the instrument (122 Hz), the equation was modified to:

$$\left\langle x^2\left(\nu\right)\right\rangle = \left[\frac{\lambda}{\Delta Z_P\left(1+\cos\left(2\theta\right)\right)}\right]^2\left[\frac{1}{\cos(\theta)}\right]^2\left[\frac{\Delta Z_M}{\Delta V_M}\right]^2\left\langle \Delta V^2\left(\nu\right)\right\rangle \tag{4.7}$$

where $\left\langle x^2\left(\nu\right)\right\rangle$ is the mean square amplitude of the noise signal in the Fourier domain, $\left\langle \Delta V^2\left(\nu\right)\right\rangle$ is the mean square voltage in the Fourier domain, and $\Delta Z_M/\Delta V_M$ is the sensitivity calculated from the slope of the contact region. All other parameters are defined as above. It is important to note that the frequency range of the instrument is a major limitation in measuring spring constant values. According to the Nyquist-Shannon Sampling Theorem [21], an analog signal (*viz.*, the noise spectrum of the AFM system) must be sampled at at least twice the frequency of the signal's bandwidth in order to adequately represent the original signal in digital form. Since the maximum data acquisition rate for the Nanoscope IIIa controller is 61 Hz, we are limited to a resonant frequency range of less than 30.5 kHz.

After converting to mean square amplitude, we performed a least-squares curve fit over one-half the valid frequency range. The relevant equation from [5], defining the mean square amplitude as the linear superposition of $1/f$ noise, white noise and the mean square amplitude at kinetic resonance, is:

$$\left\langle x^2\left(\nu\right)\right\rangle = \frac{A}{\nu} + B + \frac{\left\langle x^2\left(\nu_k\right)\right\rangle}{Q^2}\frac{1}{\left\{\left[1-\left(\frac{\nu}{\nu_k}\right)^2\right]^2+\left[\frac{\nu}{\nu_k Q}\right]^2\right\}} \tag{4.8}$$

where A and B are constants modifying $1/f$ and white noise, respectively, $\left\langle x^2\left(\nu_k\right)\right\rangle$ is the mean square amplitude at kinetic resonance, Q is the dimensionless quality factor, and ν_k is the kinetic resonance frequency. These five quantities are used as fitting parameters in the regression with the frequency, ν, as the input data.

We may then calculate the cantilever spring constant, k_c, based on the mean square amplitude fluctuations at kinetic resonance:

$$k_c = \frac{12}{\alpha_i^4 \pi} \frac{k_B T Q}{\langle x^2 (\nu_k) \rangle} \frac{\Delta\nu}{\nu_k} \tag{4.9}$$

where k_B is the Boltzmann constant, T is absolute temperature, and $\Delta\nu$ is the frequency resolution of the AFM. α_i is a dimensionless quantity describing the vibrational mode of the cantilever, detailed in [6, 20]. For this experimentation, we will assume that the cantilever remains in its first vibrational mode. This means that the cantilever may only oscillate about its fixed end, with the free end tracing the vibration and no other oscillation points along the length of the beam. At higher frequency ranges, it is possible to enter higher vibrational modes. However, with this instrument, it is unlikely that those frequencies will be reached under normal operation. For the first vibrational mode, α_1 is equal to 1.8751, reducing Equation 4.9 to:

$$k_c = 1.272 \text{ x } 10^{-21} \frac{Q}{\langle x^2 (\nu_k) \rangle} \frac{\Delta\nu}{\nu_k} \tag{4.10}$$

4.4.4 Differences Between Calibrated and Uncalibrated Results

The influence of the spring constant and piezoactuator step calibration may be most clearly seen in force-separation plots. As an example, the AFM was configured for contact mode in air with a Mikromasch CSC38 cantilever, using the center cantilever. The cantilever was scanned over a borosilicate glass microscope slide at a scan rate of 1 Hz. Data sets were analysed four times: 1) Without the inclusion of the calibration factors, 2) With the spring constant but without the piezoactuator correction, 3) With the piezoactuator correction but without the measured spring constant and 4) With both calibration factors. Analysis was carried out using a series of custom Matlab® scripts, and modified for the four scenarios described.

4.5 Results

4.5.1 Sample Height and Tip-Sample Separation

The manufacturer's value of the AFM laser diode wavelength was 670 nm. Measurements from the optical spectrum analyser gave a value of 673.4 ± 0.1 nm. Analysis of the interference patterns (Figure 4.5.1) showed an average interference wavelength of 365.1 ± 7.98 nm.

The ratio $\Delta Z_P / \Delta Z_M$ was 1.09 ± 0.004, meaning that for each nanometer of distance recorded by the AFM software, the piezoactuator actually moves 1.09 nm. This is a significant difference between expected and actual, and should be accounted for in data analysis.

4.5.2 Probe Radius of Curvature

An example of the probe radius calculation may be seen in Figure 4.5.2. The nominal radius of curvature of the probe is < 10 nm. However, in several cases, we saw values significantly higher than expected. For the Mikromasch CSC38 (silicon with aluminum back coating; Cantilever B), the average radius was 10.3 ± 0.01 nm ($N_D = 10$) for new cantilevers. After scanning a silicon calibration grating at 1 Hz (approximately 2 hours for each cantilever), the tip radius had increased to 13.4 ± 0.14nm Similar results were seen for the Mikromasch NSC36 (silicon with aluminum back coating; Cantilever B) ($N_D = 5$) and Digital Instruments TESPA (silicon with aluminum back coating; $N_D = 3$) tips. For the Digital Instruments DNP-S tips (silicon nitride with gold back coating; Short, thin cantilever), the average radius was found to be 14.6 ± 0.21 nm ($N_D = 10$). After scanning the calibration grating for 2 hours, the radius increased to an average of 20.2 ± 0.58 nm.

4.5.3 Probe Spring Constant

The probe spring constant was determined by the nonlinear least-squares regression of a plot of mean square amplitude against frequency (Figure 4.5.3).

For the Mikromasch CSC38 (Cantilever B; nominal $k_c = 0.03\ \mathrm{N \cdot m^{-1}}$), the average spring constant of a new cantilever was $0.042 \pm 0.001\ \mathrm{N \cdot m^{-1}}$ ($N_D = 15$).

We also observed that the spring constant changes dynamically. After scanning a silicon calibration grating for 30 minutes in contact mode, the spring constant of the CSC38 had de-

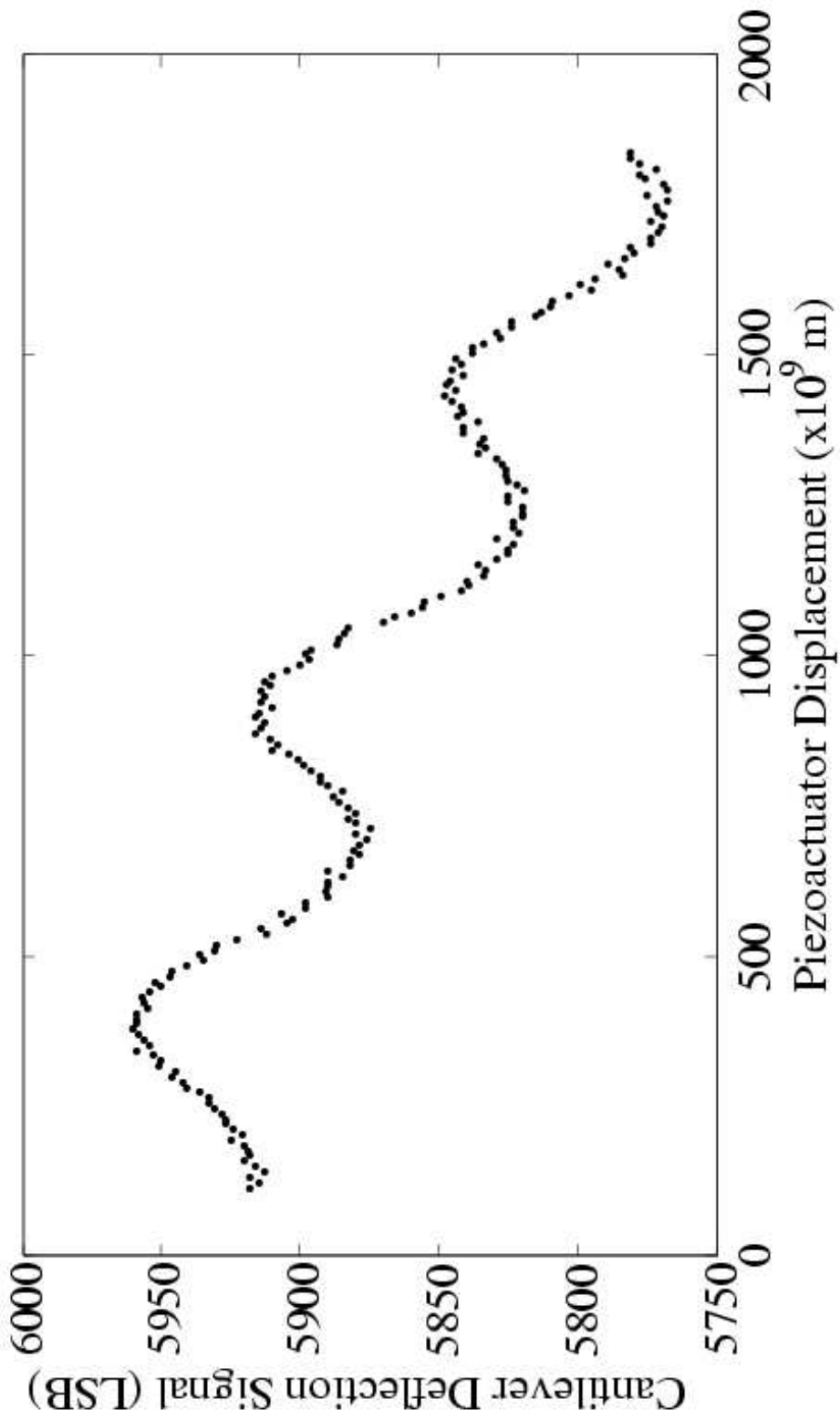

Figure 4.5.1: Example interference pattern plot. By taking the total displacement and dividing by the number of peaks ($N_{int} = 3$), we are able to determine ΔZ_M for the piezoactuator correction factor.

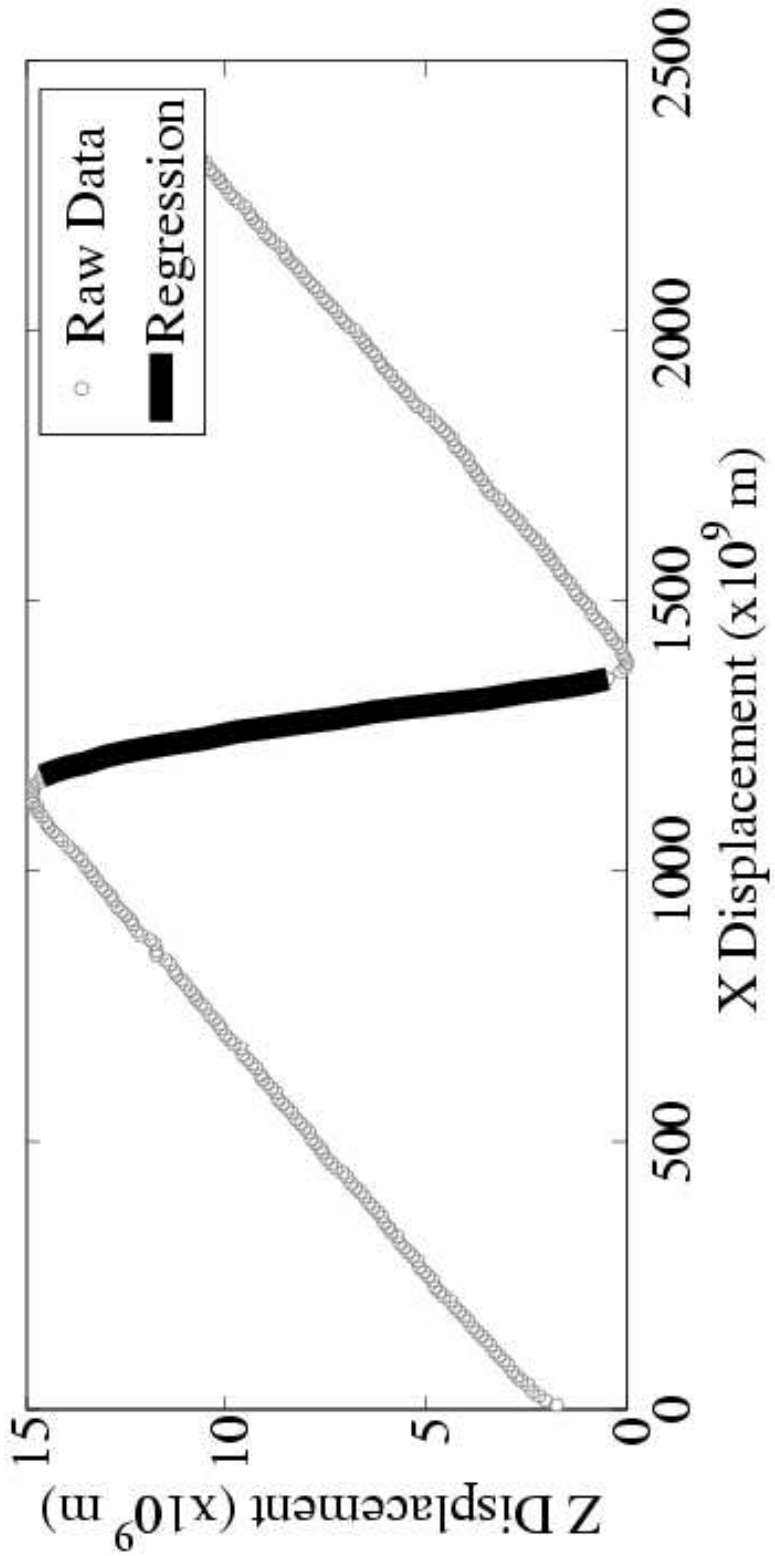

Figure 4.5.2: Example radius of curvature plot. The raw data are shown as open circles, and the minimised fit is shown as a solid line. The profile of the data, which is in reality square, is a result of a first-order planefit in the AFM software. This operation removes tilt artifacts from the image, which are a result of the large topographical differences in the sample surface.

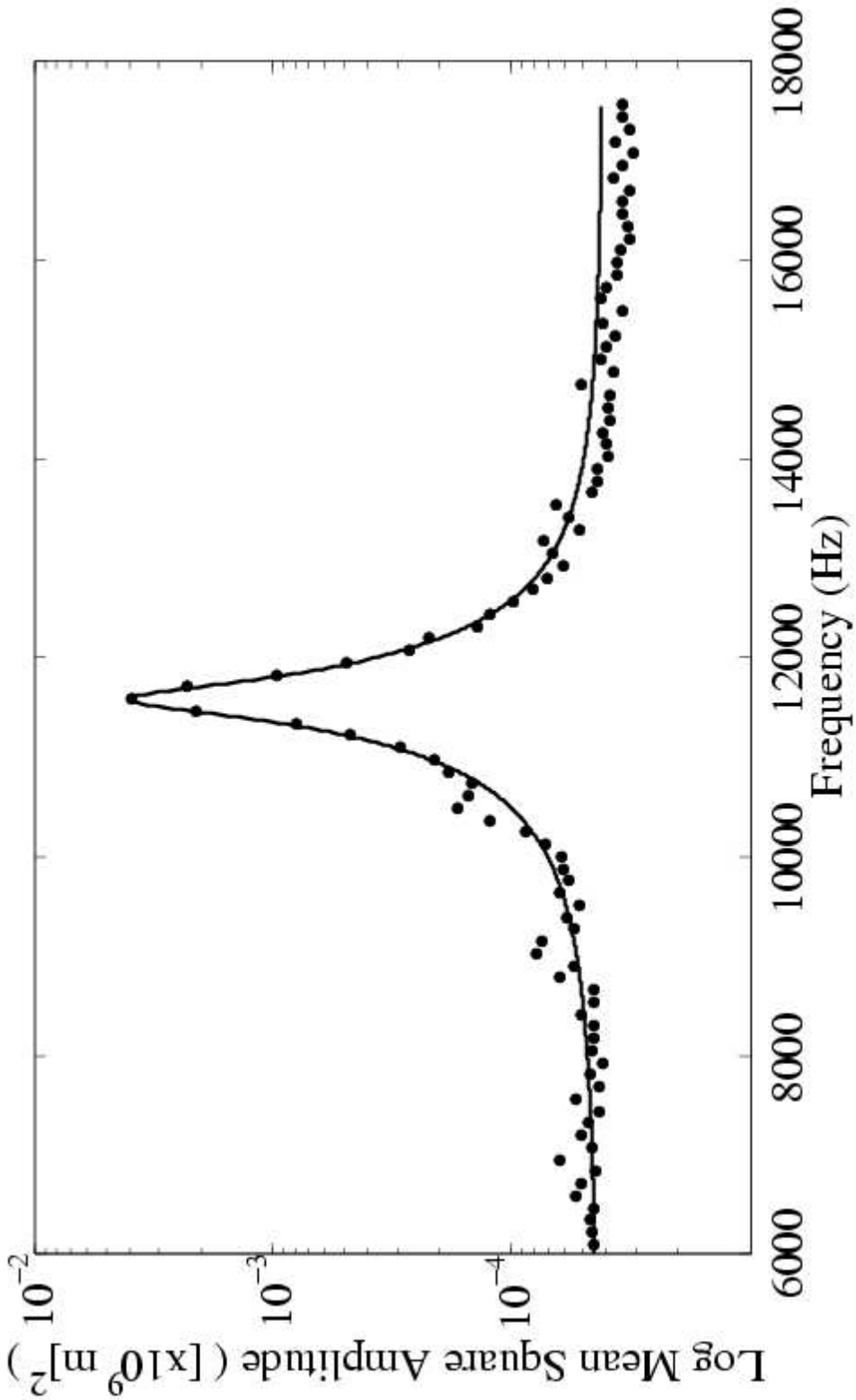

Figure 4.5.3: Plot of mean square amplitude against frequency. The raw data, as processed by the method described, are shown as solid circles. The nonlinear least-squares curve fit of the data is shown as a solid line. This fit corresponds to $k_c = 0.041\ \mathrm{N \cdot m^{-1}}$.

creased to $0.040 \pm 0.001\ \mathrm{N \cdot m^{-1}}$. After an additional 30 minutes of scanning in intermittent contact mode, the spring constant was measured as $0.036 \pm 0.001\ \mathrm{N \cdot m^{-1}}$. This behaviour may be seen in Figure 4.5.4. Data were collected in parallel to explore cantilever dynamics if the same cantilever were used in multiple experiments, but in different operational modes.

4.5.4 Differences Between Calibrated and Uncalibrated Results

One extremely useful feature of the AFM is its ability to measure force-separation interactions in a wide variety of experimental systems. The cantilever spring constant and the separation correction factor are the most important quantities in characterising the magnitudes of both force and distance, respectively. The effect of the spring constant and separation measurements may be seen in the force-separation curve in Figure 4.5.5.

We can see the effect of the changes in probe radius of curvature over time by applying the measured values to existing mathematical models. The classical formulation of the Derjaguin-Landau-Verwey-Overbeek theory of colloid stability [10, 28] describes the interaction energy profile as the separation distance between two bodies decreases. Specifically, the theory accounts for interactions due to electrostatic double layer and London-van der Waals forces. We applied the formulation for sphere-sphere geometry found in [16], using the parameters in Table 4.5.1.

The probe radius of curvature was calculated as the average of five measurements using the Mikromasch CSC38 cantilever B. The manufacturer's reported radius was less than 10 nm. Our initial measurement was 10.3 nm. After scanning a silicon calibration grating for 2 h, the radius had increased to 13.4 nm. The effect of varying the probe radius of curvature may be seen in Figure 4.5.6 in the context of the classical DLVO theory.

4.5.5 Statistical Uncertainty Analysis

Tables 4.5.2 and 4.5.3 detail the quadrature uncertainty analysis ([26]) of uncalibrated and calibrated data sets, respectively.

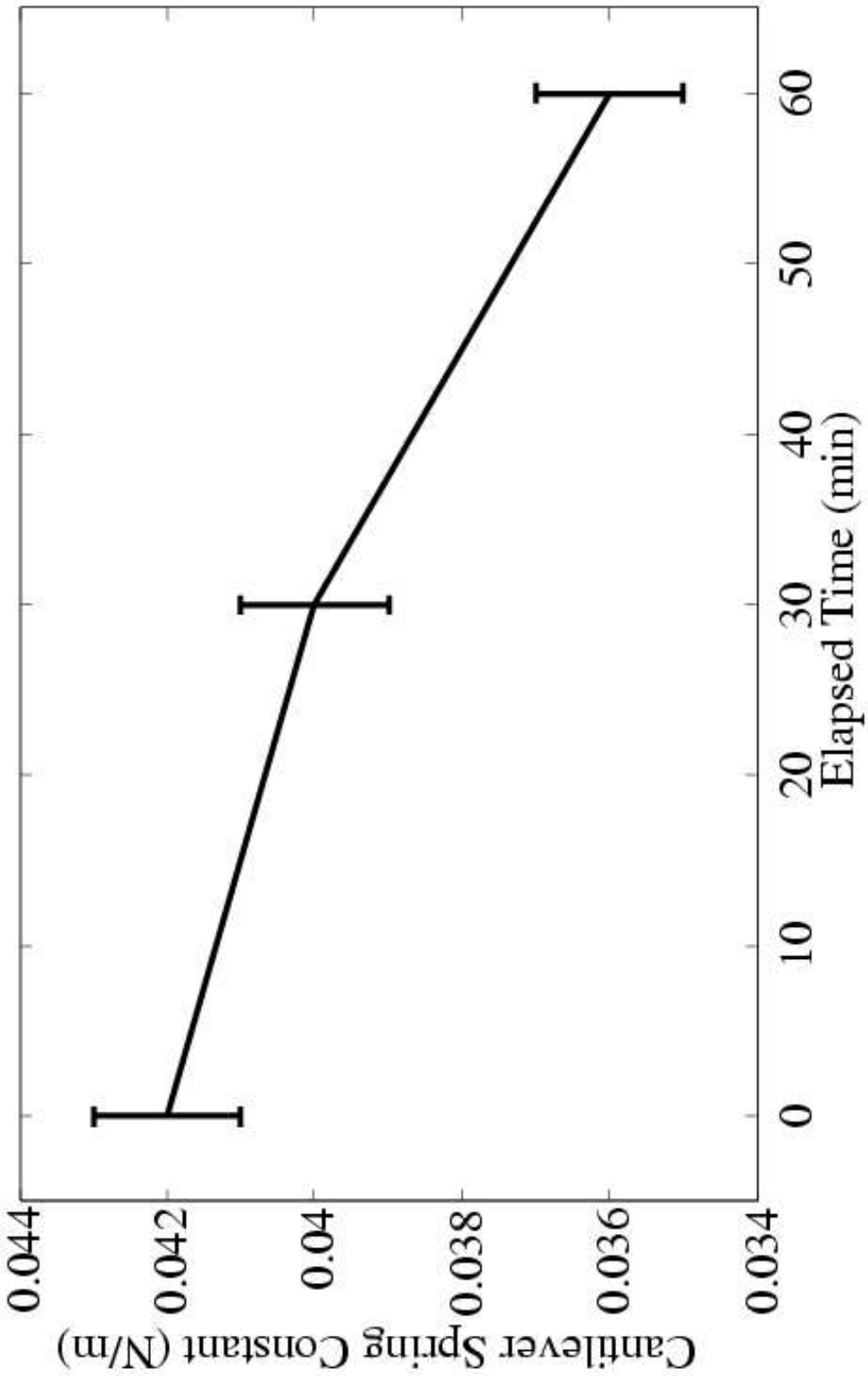

Figure 4.5.4: Plot of the dynamic behaviour of the cantilever spring constant. The substrate was a silicon sample grating (STR10, Digital Instruments). The first 30 minutes of scanning were performed in contact mode, after which time the AFM was withdrawn, engaged in intermittent contact mode, and allowed to scan for a further 30 minutes.

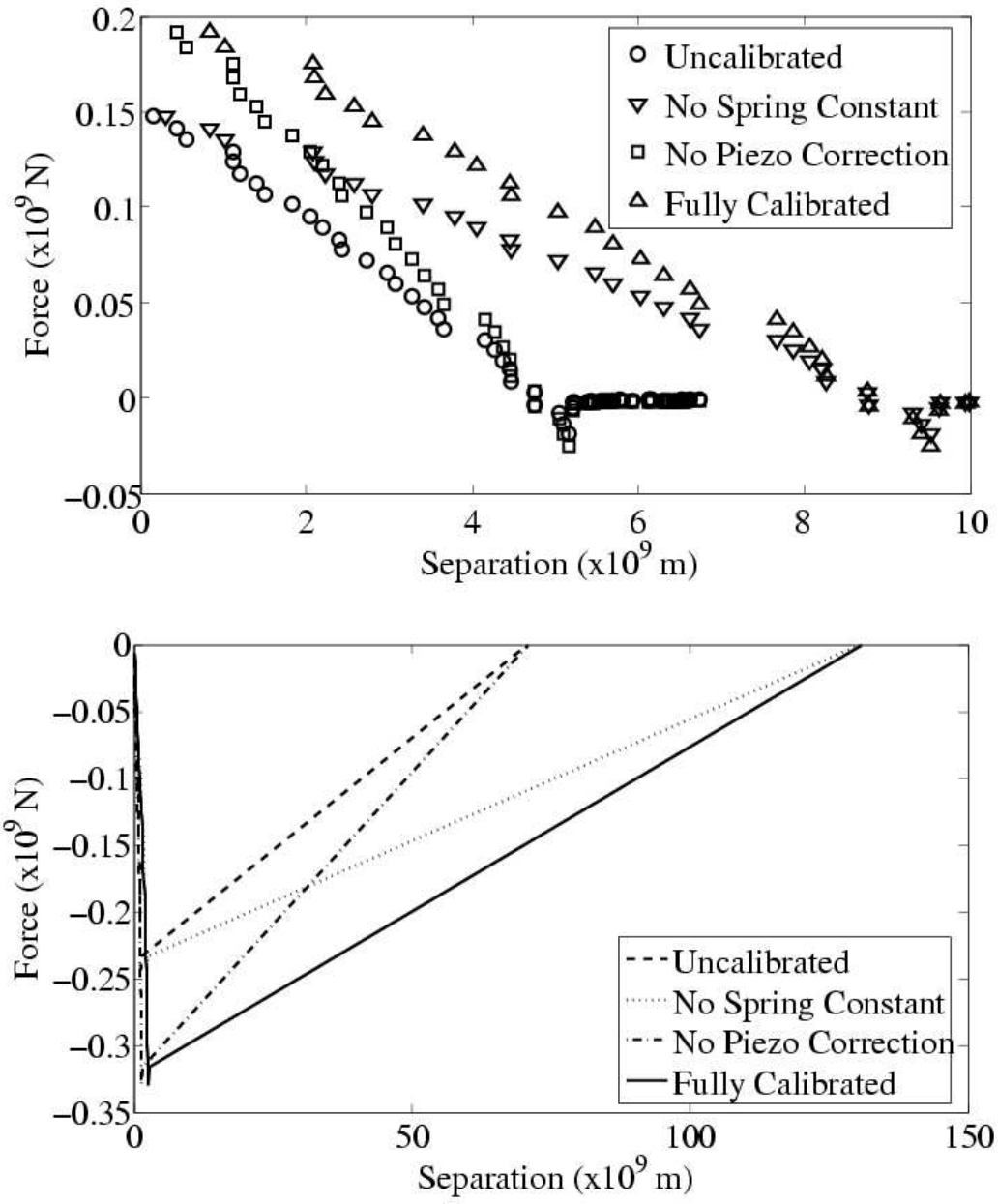

Figure 4.5.5: Comparison of the effect of the calibration factors on an AFM force curve. The top plot shows the approach curve, and the bottom curve the retraction curve, for a silicon tip on a borosilicate glass microscope slide. Data are representative of 50 force cycles recorded in air for the system. The vertical region of stiff contact is not shown to highlight the features of the interaction in the positive separation quadrants.

Table 4.5.1: Parameters used in the classical DLVO model to describe the effect of probe radius of curvature on the interaction energy profile.

Parameter	**Value**
Hamaker Constant (J)	6 x 10^{-21}
Sample Radius (nm)	1000
Sample Surface Potential (V)	-0.01
Probe Surface Potential (V)	-0.1
Salt Concentration ($\mathrm{mol \cdot L^{-1}}$)	0.1

Table 4.5.2: Statistical uncertainty of an AFM measurement without instrument calibration. Data shown are for a Mikromasch CSC38 chip, cantilever B.

		Uncertainty	**Value**
Spring Constant			
	($\mathrm{N \cdot m^{-1}}$)		
Uncertainty	0.04		
Value	0.05	0.78	0.05
Piezoactuator Correction			
	($\mathrm{nm \cdot nm^{-1}}$)		
Uncertainty	0		
Value	1	0.00	1
Probe Radius			
	(nm)		
Uncertainty	2		
Value	10	0.20	10

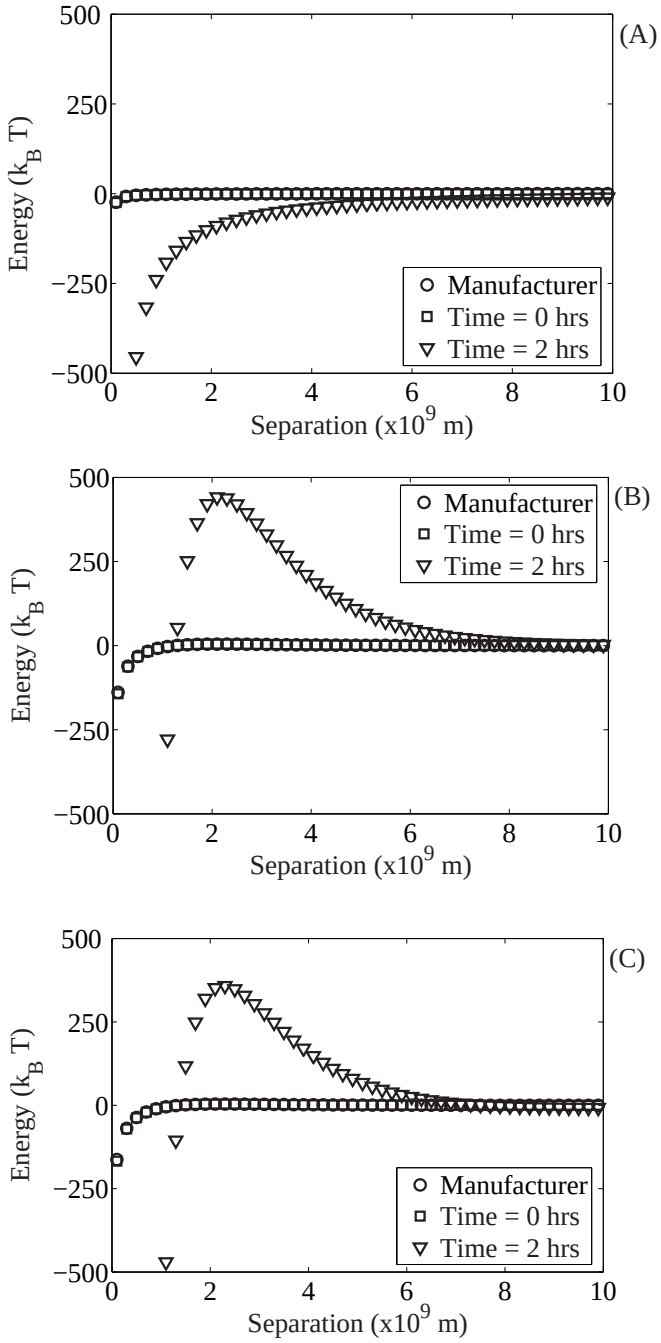

Figure 4.5.6: Classical DLVO component analysis showing the effects of the probe radius of curvature. The typical manufacturer's value is compared to the initially measured value, and the value obtained after two hours scanning a silicon substrate. Panels represent (A) London-van der Waals interactions, (B) Electrostatic double layer interactions, and (C) Total energy interaction profile.

Table 4.5.3: Statistical uncertainty of an AFM measurement with instrument calibration. Data shown are for a Mikromasch CSC38 cantilever B.

				Uncertainty	**Value**
ΔZ_M **Displacement**					
Quantity	Ramp Size				
	(nm)				
Uncertainty	1.95			0.001	365.1
Value	2000				(nm)
ΔZ_P **Displacement**					
Quantity	λ	θ			
	(nm)	(°)			
Uncertainty	0.1	0.1		0.01	347.2
Value	673.4	10			(nm)
ΔZ_P / ΔZ_M **Correction**					
Quantity	ΔZ_M	ΔZ_P			
	(nm)	(nm)			
Uncertainty	0.001	0.01		0.001	1.09
Value	365.1	347.2			(-)
Spring Constant					
Quantity	λ	θ	ΔZ_P		
	(nm)	(°)	(nm)		
Uncertainty	0.1	0.1	0.01	0.01	0.05
Value	673.4	10	347.2		$(\mathrm{N \cdot m^{-1}})$
Probe Radius					
Quantity	Height	Resolution			
	(nm)	(nm)			
Uncertainty	0.6	3.9		0.03	10.3
Value	20	2000			(nm)

4.6 Discussion

4.6.1 Differences Between Calibrated and Uncalibrated Results

For the three factors investigated in this communication, we see large variations from the typical manufacturer's values in all cases. The static and dynamic variation of the values from the typical manufacturers' values may be seen in Table 4.6.4. For the voltage/height response, the difference is approximately constant at ±5%.

The effect of proper calibration of the cantilever spring constant and piezoactuator correction factor is shown dramatically in Figure 4.5.5. Using the minima of the interaction peaks in the approach and retraction curves as reference points, we can quantify the differences according to the analysis scenario in Table 4.6.5.

In particular, the calculation of the piezoactuator step correction has a significant effect on the force curves and their interpretation. Approach cycles show a nearly twofold increase in the distance to the attractive minimum, with a small increase in the magnitude after including the measured spring constant. Retraction curves show a similar increase in the magnitude of the adhesive interaction as a result of the spring constant and the distance to the minimum. Additionally, there is a twofold increase in the distance over which the adhesion persists as the cantilever more gradually returns to its rest position. Taking the two factors together, it is obvious that the interactions being recorded by the AFM are, in fact, stronger and persist further than one would see if the manufacturers' indications were used. While this exact scenario may not be true of every instrument, we can see that knowledge of these fundamental properties of the AFM allows the researcher to better represent the system under study.

An interesting result is the dynamic change in both tip radius of curvature and cantilever spring constant. The former may be explained by wear of the tip over time as it is scanned across a relatively rigid substrate. Namely, as the tip raster-scans across the substrate, material is removed from the tip, increasing the radius of curvature of the probe over time. This effect is similar to the wear seen as a sharp pencil point is repeatedly used. Layers of material are removed, as a result of friction and breaking of intercrystalline bonds, progressively dulling the point. Assuming that the profile of the tip remains constant (*viz.*,

Table 4.6.4: Evidence of the variation and dynamic behaviour of the three AFM parameters investigated. Values shown are taken from measurements on the Mikromasch CSC38 Cantilever B, and record the percent variation from manufacturers' specification of the radius of curvature and spring constant as a function of time.

Time (h)$\longrightarrow$	0	0.5	1	2
Radius	$> 3\%$	-	-	25%
Spring Constant	40%	33%	20%	-

Table 4.6.5: Comparison of force curve peak separation and magnitude as calculated from each of the four data analysis techniques. We can see that the piezoactuator correction has a significant effect on the magnitude of the separation, but an inconsiderable influence on the magnitude of the force. Conversely, measurement of the spring constant drastically affects the magnitude of the force, but is of little importance in the separation measurement.

		Separation (x10^{-9} m)	**Force** (x10^{-9} N)
Approach			
	Uncalibrated	5.16	-0.019
	Fully Calibrated	9.53	-0.025
	No Piezo Correction	5.16	-0.025
	No Spring Constant	9.54	-0.019
Retraction			
	Uncalibrated	6.63	-0.242
	Fully Calibrated	12.24	-0.329
	No Piezo Correction	6.63	-0.329
	No Spring Constant	12.24	-0.242

paraboloid), the radius may be recalibrated for use in subsequent mathematical analysis of the substrate.

Conversely, it is possible that the tip could collect material from the substrate, creating a larger radius of curvature value. Such wear and contamination may be apparent in topographical images, as well as in force cycle analysis. This also manifests in the DLVO model (Figure 4.5.6), in the form of a radius-dependent electrostatic energy barrier. In this example, the profile of the tip may remain constant, or accrete surface materials in an amorphous fashion. While the tip may be recalibrated as in the wearing example, should the profile become amorphous, it would become necessary to either chemically clean the tip, or to replace it with a fresh probe.

The explanation of the change in probe spring constant is somewhat more complicated. In terms of materials science, we may hypothesise in terms of the stress and strain to which the cantilever is exposed, both during topographical imaging and force cycle capture. The cantilever itself will wear out over time as intercrystalline stresses accumulate, overcoming the elasticity of the spring. This will occur gradually as the material of the cantilever changes in response to imposed stresses. This change may be quantified through the use of force-calibrated cantilevers such as those used in [5]. These beams were obtained from Veeco Metrology Group (CLFC-NOBO and CLFC-NOMB) and characterised by the National Institute of Standards and Technology (NIST, Gaithersburg, MD, USA), and may be used independently to verify the model.

We see an increase in the rate of change of the spring constant as we change modes from contact to intermittent contact mode. In this latter mode, the cantilever is oscillated at or near its resonant frequency, where the amplitude of the oscillation serves as the setpoint of the feedback loop. At resonance, we expect intercrystalline stresses to change more rapidly. Further, as we are inducing a rapid, periodic deflection, the more rapid decrease in spring constant may be attributed to more rapid wear of the material over time.

4.6.2 Statistical Uncertainty Analysis

We see in Tables 4.5.2 and 4.5.3 that a significant uncertainty exists between the uncalibrated and calibrated data sets.

Namely, by calibrating the piezoactuator response, and the cantilever spring constant, experimental uncertainty the in the magnitude of a measured force due to these three properties yields a value of ≈1%. Using a spring constant based on the range given by the manufacturer, and assuming a 1:1 ratio between ΔZ_P and ΔZ_M (*viz.*, the piezoactuator moves by the same amount as measured by the software), we see the uncertainty increases dramatically to ≈80% for this system. The uncertainty in measuring the radius of curvature of the probe, and therefore its contribution to the uncertainty in subsequent mathematical analyses, is 20% for the uncalibrated probe, and only 3% for the calibrated probe. This increase is due almost solely to the uncertainty inherent in the value of the spring constant. The range given spans an order of magnitude, or approximately 80% base uncertainty. With each quantity summed in quadrature towards the final value of experimental uncertainty, precise calculation of the cantilever spring constant becomes the determining factor in the overall precision of the experiment and of the final data sets.

It should be noted that, while our relative uncertainty in the probe radius is calculated as 3%, that determined by Thoreson and Burnham [27] was 9%. This should not suggest that our technique is better than that from *op. cit.*, as the methods were identical. Thoreson and Burnham investigated the radii of various microspheres, ranging in size from 2 μm to 60 μm. The data presented in this work are based solely on the Mikromasch CSC38(B) tip. It is likely that, while variations exist for this latter probe, they are not so significant as the combined effects of radii spanning an order of magnitude, as in the former. Differences in sample size (number of tips measured) may also have lowered the value of our relative uncertainty. Were we to combine calculations for several different probes, it is likely that the relative uncertainty will increase with a wider distribution of tip radii.

4.6.3 Recommendations for Calibration Frequency

The AFM manufacturer often provides a calibration schedule for the instrument. In the case of the Dimension 3100, it is recommended that we calibrate the vertical components of the piezoactuator on a monthly basis, and the X- and Y-components twice yearly, according to a silicon calibration grating (STR10 pit grating, 180 ± 5.4 nm, Digital Instruments). For the quantities described here, we provide further recommendations that may be easily and

quickly added to the researcher's existing calibration and experimentation regimes.

The wavelength of the laser diode will change as the diode itself ages. However, since this quantity is not expected to change greatly over time, it will be sufficient to measure the wavelength on a biannual or annual basis at the same time as the full piezoactuator calibration. If an optical spectrum analyser is not available, then a geometric method of determining the laser wavelength (for example, the original method described in [5]) may be used, although a rigorous error analysis will be necessary and some precision will be lost.

The piezoactuator correction factor is a weak function of the laser wavelength, and more significantly a function of the vertical calibration parameters in the AFM software. Further, the response (*viz.*, the piezoactuator sensitivity) will change as the piezoelectric material ages. Since these parameters will change on a monthly basis if the manufacturer's calibration schedule is followed, it is recommended that the interference wavelength and the voltage/height correction factor be calculated in sequence at the same time.

As has been shown, the probe radius of curvature and spring constant have very high variability, both in static and dynamic measurements. Therefore, we recommend that both parameters be measured at the beginning and end of each experiment. The two values may then be averaged, and the variability described in terms of the standard deviation of the two values.

While many different types of AFM exist, the underlying principles are identical. In general, an AFM has a piezoelectric component, an optical laser component, and a software component which allows the user to record images and force cycles. In order to perform the above analyses, it is only necessary to identify the means by which each AFM records these quantities. Most importantly, it is essential to understand the data file format such that recorded quantities may be easily interconverted between the raw format and values of deflection, separation and force. Once this is adequately understood, the previously discussed calibration factors are easily determined, and the overall accuracy and precision of the instrument may be reliably reported.

4.7 Conclusions

We have shown the importance of quantifying several AFM parameters before beginning analysis of one's recorded data sets, as well as provided recommendations for calibration frequency. The quantities explored here, while often identified by the manufacturer, can and do change dynamically and must be measured before the researcher is able to precisely report their final data sets. While some uncertainty will always remain in any data processing, these few simple and easily-adaptable techniques allow for greater precision and accuracy in the researcher's data analysis.

4.8 Bibliography

[1] N. I. Abu-Lail and T. A. Camesano. Role of lipopolysaccharides in the adhesion, retention and transport of *Escherichia coli* JM109. Environmental Science and Technology, 37:2173–2183, 2003.

[2] M. Benoit, D. Gabriel, G. Gerisch, and H. E. Gaub. Discrete interactions in cell adhesion measured by single-molecule force spectroscopy. Nature Cell Biology, 2:313–317, 2000.

[3] W. R. Bowen, N. Hilal, R. W. Lovitt, and C. J. Wright. Direct measurement of the force of adhesion of a single biological cell using an atomic force microscope. Colloids and Surfaces A: Physicochemical and Engineering Aspects, 136:231–234, 1998.

[4] G. L. Bradley and K. J. Smith. Calculus. Prentice Hall, Upper Saddle River, NJ, 1995.

[5] N. A. Burnham, X. Chen, C. S. Hodges, G. A. Matei, E. J. Thoreson, C. J. Roberts, M. C. Davies, and S. J. B. Tendler. Comparison of calibration methods for atomic-force microscopy cantilevers. Nanotechnology, 14:1–6, 2003.

[6] H. J. Butt and W. Jaschke. Calculation of thermal noise in atomic force microscopy. Nanotechnology, 6:1–7, 1995.

[7] H.-J. Butt, M. Kappl, H. Mueller, R. Paiteri, W. Meyer, and J. Ruhe. Steric forces measured with the atomic force microscope at various temperatures. Langmuir, 15:2559–2565, 1999.

[8] T. A. Camesano and B. E. Logan. Probing bacterial electrosteric interactions using atomic force microscopy. Environmental Science and Technology, 34:3354–3362, 2000.

[9] J. P. Cleveland, S. Manne, D. Bocek, and P. K. Hansma. A nondestructive method for determining the spring constant of cantilevers for scanning force microscopy. Reviews of Scientific Instruments, 64(2):403–405, 1993.

[10] B. V. Derjaguin and L. Landau. Theory of the stability of strongly charged lyophobic sols and the adhesion of strongly charged particles in solutions of electrolytes. Acta Physicochimica (URSS), 14:633–662, 1941.

[11] Y. F. Dufrêne. Application of atomic force microscopy to microbial surfaces: From reconstituted cell surface layers to living cells. Micron, 32:153–165, 2001.

[12] R. J. Emerson and T. A. Camesano. A nanoscale investigation of pathogenic microbial adhesion to a biomaterial. Applied and Environmental Microbiology, 70(10):6012–6022, 2004.

[13] M. Grandbois, W. Dettmann, M. Benoit, and H. E. Gaub. Affinity imaging of red blood cells using an atomic force microscope. Journal of Histochemistry and Cytochemistry, 48(5):719–724, 2000.

[14] Green C. P., H. Lioe, J. P. Cleveland, R. Proksch, P. Mulvaney, and J. E. Sader. Normal and torsional spring constants of atomic force microscopes. Review of Scientific Instruments, 75:1988–1996, 2004.

[15] H. G. Hansma, K. J. Kim, D. E. Laney, R. A. Garcia, M. Argaman, M. J. Allen, and S. M. Parsons. Properties of biomolecules measured from atomic force microscopy images: A review. Journal of Structural Biology, 119:99–108, 1997.

[16] R. Hogg, T. W. Healy, and D. W. Fuerstenau. Mutual coagulation of colloidal dispersions. Transactions of the Faraday Society, 62:1638–1651, 1966.

[17] J. L. Hutter and J. Bechhoefer. Calibration of atomic-force microscope tips. Reviews of Scientific Instruments, 64(7):1868–1873, 1993.

[18] Digital Instruments. Dimension 3100 Manual Ver. 4.43b. Technical report, Veeco Metrology Group, 1997.

[19] Digital Instruments. Scanning Probe Microscopy Training Notebook. Technical report, Veeco Metrology Group, 1998.

[20] R. Lévy and M. Maaloum. Measuring the spring constant of atomic force microscope cantilevers: thermal fluctuations and other methods. Nanotechnology, 13:33–37, 2002.

[21] H. Nyquist. Certain topics in telegraph transmission theory. American Institute of Electrical Engineers. Transactions., 47:617–644, 1928.

[22] M. Rief, F. Oesterhelt, B. Heymann, and H. E. Gaub. Single molecule force spectroscopy on polysaccharides by atomic force microscopy. Science, 275:1295–1297, 1997.

[23] J. E. Sader. Frequency response of cantilever beams immersed in viscous fluids with applications to the atomic force microscope. Journal of Applied Physics, 84:64–76, 1998.

[24] J. E. Sader, J. W. M. Chon, and P. Mulvaney. Calibration of rectangular atomic force microscopy cantilevers. Review of Scientific Instruments, 70:3967–3969, 1999.

[25] J. E. Sader, I. Larson, P. Mulvaney, and L. F. White. Method for the calibration of atomic force microscope cantilevers. Review of Scientific Instruments, 66:3789–3798, 1995.

[26] J. R. Taylor. An Introduction To Error Analysis. University Science Books, Sausalito, CA, 1997.

[27] E. J. Thoreson and N. A. Burnham. Standard-deviation minimization for calibrating the radii of spheres attached to AFM cantilevers. Review of Scientific Instruments, 75:1359–1362, 2004.

[28] E. J. Verwey and J. T. G. Overbeek. Theory of the Stability of Lyophobic Colloids. Elsevier, Amsterdam, 1948.

CHAPTER 5

Atomic Force Microscopic Studies of Fibronectin Immobilised by Monoclonal Antibodies on Glass

5.1 Abstract

Specific bacterial adhesion on to implanted medical devices occurs through receptor:ligand interactions with adsorbed proteins (*e.g.,* fibronectin and fibrinogen), a critical first step in a cascade of processes leading to biofilm formation, virulence and infection, and potentially death. A protocol to quantify the specific receptor:ligand interaction for the model system of the bacterium, *Staphylococcus epidermidis*, binding to the immobilised protein, fibronectin (i-FN), is presented. The protocol allows one to control the surface orientation of the FN molecule by using surface-immobilised monoclonal antibodies that bind at different epitopes on FN. FN molecular orientation was verified by SA and surfaces were characterised by surface coverage and topography by atomic force microscopy (AFM). Bacterial static adhe-

sion studies were carried out on surfaces that displayed the FN molecule tethered by either its N- or C-terminus, as described in a subsequent study [21]. Results indicate a significant preferential specific adhesion of *S. epidermidis* to i-FN anchored by the C-terminus. FN tethered in the reverse manner significantly inhibited *S. epidermidis* adhesion.

5.2 Introduction

Specific bacterial adhesion to biological (host tissues) and synthetic (biomedical devices) substrata, through receptor:ligand interactions with adsorbed proteins (*e.g.,* fibronectin and fibrinogen), is a critical first step in a cascade of processes leading to host tissue invasion or biofilm formation, virulence and infection, and potentially death.

Defining the binding interactions between a bacterial receptor and its surface ligand currently requires an assortment of time-consuming molecular tools, applied under very strictly controlled *in vitro* or *in vivo* conditions that can only provide qualitative results. Our goal is to integrate a battery of complementary tools to quantify the molecular binding interactions between bacterial receptors and their corresponding surface-bound ligand. We will combine *(a)* direct molecular determination of the binding epitopes for both receptor:ligand pairs with *(b)* atomic force microscopy (AFM) to quantify receptor:ligand binding in the model system of *Staphylococcus epidermidis* binding to immobilised fibronectin (i-FN).

5.2.1 Background

A number of complex biological phenomena are governed by dynamic processes that occur at interfaces including: cell-to-cell adhesion, immune response to bacterial infection, and bacterial adhesion to and infection of mammalian cells and biomedical implants. Specific adhesion of cells to biological and synthetic surfaces through adsorbed proteins, such as fibrinogen and fibronectin (FN), is critical to biomedical and biotechnological applications [1, 14, 19, 28, 42, 43, 50, 51]

Bacteria, transported to the substratum either by inherent motility or fluid flow, can adhere either nonspecifically (governed by electrostatic forces acting between the cell and surface) or specifically (governed by cell surface structures). Certain cell surface molecules, termed "receptors" can bind to specific molecules, termed "ligands," found on the substratum. Both specific and nonspecific interactions can lead to biofilm formation [5, 37, 40] and host immune response [45]. Bacterial infections caused by adhesion to medical implants have been observed in a variety of systems, including prosthetic heart valves, urinary catheters, and ocular prostheses [11]. *Staphylococcus epidermidis*, normally a benign skin flora, is one

of the most frequently isolated bacterial pathogens in hospitals and widely considered to be one of the predominant causes of indwelling medical device infection [53].

5.2.2 Role of FN in Bacterial Colonisation

After implantation, biomedical implants are coated with a complex, multi-component fluid, whose constituents can serve as binding ligands to the receptors of colonising bacteria. Fibronectin (FN) plays an important role in many physiological processes and is one of the most extensively studied blood plasma proteins. FN is an adhesive glycoprotein (≈440 kDa) found in the blood and the extracellular matrix that is a key player in cell adhesion. It is also one of the main plasma proteins responsible for forming a conditioning film on implanted biomaterials. Plasma FN is a dimer of two similar polypeptides linked by two disulfide bonds at their C-termini. The individual chains are approximately $60 - 70$ nm in length and $2 - 3$ nm in thickness, each chain with a molecular weight of $220 - 250$ kDa [35]. FN is also a key extracellular matrix protein involved in epithelial cell adherence to the underlying solid matrix, and promotes macrophage and fibroblast adhesion. Several *Staphylococcus* and *Streptococcus* strains, however, also possess receptors for FN [21]. In the case of *Staphylococcus aureus*, two FN-binding receptors have been identified and sequenced, which allow the microbe to attach within the heparin-, fibrin- and collagen-binding domains located near the N-terminus of the protein [33, 46]. *Staphylococcus epidermidis* shows similar adhesive characteristics for FN-coated surfaces, although the specific receptor proteins have not been identified. No C-terminal binding receptors have been identified, demonstrating regioselectivity of *Staphylococcus* for FN.

Several different soluble FN-binding adhesins have been previously described for Group A *Streptococci* (GAS), and these FN adhesins have been implicated in adherence to and invasion of epithelial cells [48] and in *in vivo* virulence [9]. By contrast, Group B *Streptococci* (GBS) do not bind to soluble FN [47]. Several pathogens bind specifically only to immobilised FN (i-FN) and not to soluble FN (s-FN). These include the Gram-positive organisms *Streptococcus sanguis* and *S. pneumoniae* [49] and the Gram-negative bacteria *Porphyromonas gingivalis* and *p*-fimbriated strains of *E. coli* [54]. Tamura and Rubens have previously demonstrated that GBS bind specifically to only i-FN [47]. This specific inter-

action with i-FN may play an important role in adherence of bacteria to FN on epithelial cells or on FN immobilised on biomedical implants. s-FN is present in plasma and exists in concentrations of $>0.25\ \mathrm{g \cdot L^{-1}}$ [12]. s-FN can block the interaction of bacteria bearing s-FN receptors to i-FN [10], suggesting that these bacteria would not bind to i-FN in the presence of bodily fluids. A recent study with *Staphylococcus aureus* demonstrated that blockage of s-FN receptors occurs when they are grown in peritoneal dialysis fluid isolated from humans [31], suggesting that this phenomenon occurs *in vivo*. Another study demonstrated that s-FN adhesins actually led to a decrease in *S. aureus* virulence [36], suggesting that opsonization by FN may play an important role *in vivo*. Interestingly, FN does not opsonize GBS, which lack s-FN receptors [56].

Taken together, these findings suggest two separate advantages for i-FN-specific adhesins. First, they allow bacteria to bind to i-FN present on epithelial cells or biomedical implants *in vivo*. Secondly, having only i-FN receptors would allow such bacteria to avoid the opsonic effects of s-FN. Prior studies have identified i-FN adhesins for *S. pneumoniae* (PavA) and *E. coli* (*p*-fimbriae). Studies have revealed a decreased virulence for *pavA* mutants of *S. pneumoniae* and *p*-fimbriae mutants of *E. coli* [10, 30, 31, 34, 56]. However, a careful structure/function analysis has not been performed to determine whether the FN-binding properties of these proteins are responsible for their virulence phenotype.

The interaction of bacteria with FN is believed to contribute significantly to the virulence of a number of microorganisms, including *Staphylococci* and *Streptococci* [16,20,27]. Several FN-binding receptors (FN-BR) of *Staphylococci* and *Streptococci* share similar structural organisation and mechanisms of ligand recognition. Binding of *S. aureus* (SA) [32, 46] to FN has been more extensively characterised than that of *S. epidermidis*. The primary fibronectin-binding site of SA is located in the FN − 29 kDa N-terminal domain [22]. It has also been found that SE binds to FN-coated materials, although the identity of the specific FN-binding adhesin is unknown [2, 20, 55]. Several studies have indicated that SE binds preferentially to the heparin binding domains near the C-terminus, although these studies did not actually quantify bacterial adhesion to FN-modified substrata [2, 3, 18, 22].

5.3 Materials and Methods

The techniques used in the various stages of fabricating the oriented FN surfaces are identical to those described in [21]. This manuscript deals primarily with the study of *Staphylococcus epidermidis* adhesion to the oriented FN surfaces which are characterised according to AFM topographical measurement techniques described herein.

5.3.1 Reagents

EZ-Link® Sulfo-NHS-LC-biotin was purchase from Pierce (Rockford, IL). Streptavidin from *Streptomyces avidini* and (3-Aminopropyl)triethoxysilane, 99 % were purchased from Sigma (St. Louis, MO). All other reagents were purchased from Sigma unless otherwise specified.

Fibronectin

Purified human plasma fibronectin was purchased from Chemicon International, Inc. (Temecula, CA). Lyophilized protein was reconstituted and stored according to manufacturer's protocol. FN was thawed (in a 37 °C water bath) and diluted immediately prior to use. The purity was verified by sodium dodecyl sulphate polyacrylamide gel electrophoresis (SDS-PAGE).

5.3.2 Monoclonal Antibodies to Human Plasma FN

Monoclonal antibodies to the N-terminus (Mab.1936, designated Anti-N) and the C-terminus (Mab.1935, designated Anti-C) of human plasma FN were purchased from Chemicon International, Inc. Mab.1936 specifically recognises the N-terminal fibrin- and heparin-binding 29 kDa domain. Mab.1935 recognises the C-terminal domain, which contains the second fibrin binding site. Mab.1935 distinguishes between two major proteolytic fragments (140 kDa and 160 kDa), but not between the A and B chains. The Mab.1935 binding site on FN also encompasses the C-terminal heparin binding fragment. These antibodies have been extensively characterised for their specificity to epitopes at their respective termini of the FN molecule [23–26]. Binding activity of antibodies was verified via end point ELISA.

5.3.3 Biotin-Labeling of Antibodies Via Amine Groups

Biotin labeling of Mabs was performed following the manufacturer's suggested protocol for Sulfo-NHS-LC-Biotin (Pierce). Antibodies were buffer exchanged into PBS (sodium chloride 7.85 $g \cdot L^{-1}$, sodium phosphate (dibasic) 0.65 $g \cdot L^{-1}$, sodium phosphate (monobasic) 0.15 $g \cdot L^{-1}$; pH 7.4) using 50 MWCO Millipore microconcentrators. A stock solution of 10 $mg \cdot mL^{-1}$ Sulfo-NHS-LC-Biotin (MW 556.59 $g \cdot mol^{-1}$) in PBS was made. Mabs in PBS solution were transferred into 2 mL siliconised microcentrifuge tubes. Biotin solution was added to create a 20:1 ratio of biotin to Mab. Tubes were placed on ice for 2 h. Samples were transferred into 50 MWCO microconcentrators and buffer exchanged samples three times with PBS. Antibody concentrations were measured using NanoOrange Protein Quantitation Kit (Pierce) following the manufacturer's protocol. Biotin-labeled antibody activity (Anti-Cb and Ant-Nb) was verified via ELISA using horseradish peroxidase conjugated to streptavidin (Sigma) and the QuantaBlu Substrate system (Pierce).

5.3.4 Peroxidase-Labeling of Antibodies

Anti-N Mabs were peroxidase-labeled using the EZ-Link® Activated Peroxidase Antibody Labeling Kit (Pierce). Manufacturer's protocol was followed with adjustments made to accommodate less than 0.3 mg of IgG. Activity of peroxidase-labeled Anti-N against FN was verified via ELISA (data not shown). Anti-C antibodies were treated with peroxidase using the manufacturer's protocol but the Mabs did not retain their activity. It is possible that the antigen-binding site was blocked or that conformational changes occurred during the labeling process [17], deactivating the antibodies.

5.3.5 Model Substrate Preparation

Streptavidin Layer Formation and Antibody Immobilisation

For the purposes of AFM imaging, circular borosilicate glass coverslips (5 mm diameter) were used. For protein binding assays, borosilicate glass beads (3 mm diameter) were used. Glass was chosen because it is inexpensive and can be easily functionalised with a stable silane layer. For the purposes of testing protein binding via chemical assay, borosilicate

glass beads (3 mm diameter) were used. In a chemical safety hood, glass coverslips or glass beads were cleaned with Piranha solution (70 % H_2SO_4, 30 % H_2O_2 (30 %)), rinsed extensively with 18 mΩ MilliQ ultrapure water, and allowed to dry for 30 min at 100 °C. Silanization of glass was performed in an Atmosbag^{TM} filled with zero-grade nitrogen to protect moisture-sensitive chemicals. Glass coverslips or beads were immersed for 5 min in a 2 % aminopropyltriethoxysilane (APTES, Sigma) / 95 % aqueous ethanol solution (previously stirred for 15 min per manufacturer's protocol). Samples were extensively rinsed with ethanol and dried for 30 min at 100 °C in a vacuum oven. Silanised glass samples were stored in a vacuum dessicator and protected from light until used, usually within 24 h. Select samples of all substrata were characterised by water contact angle method and XPS analysis at the NESAC/BIO facility at the University of Washington.

Prior to coating glass samples with streptavidin, silanised glass was first coated with biotin. Biotinylation of glass prior to coating with streptavidin yields a uniform monolayer of oriented streptavidin molecules that are biologically active and not denatured [52]. Silanised glass samples were added one each to wells of a 96-well plate. 100 µL of a 500 $\mu g \cdot mL^{-1}$ solution of Sulfo-NHS-LC-biotin in PBS were pipetted into each well. Samples were incubated overnight at room temperature. Biotinylated glass was rinsed with MilliQ ultrapure water and dried. 100 µL of 10.0 $\mu g \cdot L^{-1}$ streptavidin (Sigma) in PBS was added to each well (containing one biotinylated silanised glass sample) and samples were incubated overnight at room temperature. Samples were rinsed extensively with PBST (PBS with 0.05% Tween 20) to remove any unbound streptavidin. The amount of streptavidin that bound to beads at 10 $\mu g \cdot mL^{-1}$ was quantified using NanoOrange Protein Quantitation kit (Pierce).

Streptavidin-coated samples were then added one each to wells of a 96-well plate. Biotinylated antibodies were diluted to 2.5 $\mu g \cdot mL^{-1}$ (Anti-C) and 2.8 $\mu g \cdot mL^{-1}$ (Anti-N) in 2% BSA blocking buffer. Samples prepared for AFM were rinsed with PBST. 100 µL of antibody solution was added to each well and incubated for 2 h at 37 °C. Samples were rinsed extensively with PBST using a continuous wash method (10 $mL \cdot min^{-1}$ for 30 s) to remove any unbound antibodies. Total antibody bound to streptavidin-coated glass was not quantified. However, ELISA studies did verify the presence and activity of Mabs on the glass surface.

Coupling of FN to Treated Glass

FN was diluted in 2 % BSA blocking buffer (or PBST for AFM studies) to either 10 $\mu g \cdot mL^{-1}$ (for bound Anti-C surfaces) or 12.4 $\mu g \cdot mL^{-1}$ (for bound Anti-N surfaces). Antibody-modified glass samples were added one each to wells of a 96-well plate. One hundred microliters of FN solution was added to each well and incubated at 37 °C for 3 h. Samples were rinsed extensively with PBST with a continuous wash at 10 $mL \cdot min^{-1}$ for 30 s to remove any unbound protein.

Concentrations of FN solutions necessary to bind equivalent quantities of FN to each surface were determined ^{125}I-labelled FN assay (see below). Due to the different affinity of the two Mabs for FN, slightly different liquid phase concentrations were necessary to affect equivalent amounts of immobilised FN. Samples were incubated for 3 h at 37 °C then rinsed with PBST using a continuous wash.

Quantification of FN on Immobilised Biotinylated IgG

Glass beads were prepared as detailed above at the University of Connecticut (Storrs, CT, USA). One hundred µL of ^{125}I-FN with a specific activity of 0.74 $\mu Ci \cdot \mu g^{-1}$ were diluted to 10.0, 2.0 and 0.4 $\mu g \cdot mL^{-1}$ in 2 % BSA blocking buffer, then added to appropriate wells and incubated for 3 h at 37 °C. Beads were rinsed with PBST using a continuous wash for 30 s. Beads were then transferred to poly(propylene) tubes where ^{125}I-FN was quantified using a LKB Wallac automatic γ counter. Samples were prepared in triplicate. Results show that ^{125}I-FN binds to the surface in a dose-depended fashion. Using a linear calibration between bound ^{125}I-FN and ^{125}I-Fn in solution, adjustments were made in liquid-phase FN concentration to achieve approximately the same amount of FN bound to both Anti-C and Anti-N presenting surfaces.

Verification of FN Orientation

Orientation of FN using Mabs bound on a substratum was verified using a "double" sandwich ELISA technique. A double sandwich ELISA comprises a "capture" Mab bound to a surface (either the biotinylated Anti-N or Anti-C Mab, bound to the streptavidin surface). The antigen (FN) is then applied followed by the second "detector" Mab, a peroxidase-labeled

Anti-N Mab. If the FN is indeed oriented so that the molecule is bound to the surface via the selected terminus, the secondary antibody should display lower binding activity if it is specific to the bound terminus and higher binding activity if it is specific to the unbound terminus.

Streptavidin-coated beads were added one each to the wells of a 96-well microtiter plate. Two hundred μL of 2% BSA blocking buffer were added to each well and plates incubated for 1 h at room temperature. Beads were rinsed in place once with PBST and then 100 μL of biotinylated Mab (either Anti-C or Anti-N, in concentrations 2.5 $\mu g \cdot mL^{-1}$ (Anti-Cb) and 2.8 $\mu g \cdot mL^{-1}$ (Anti-Nb)) were added to each well. Wells were then incubated at 37 °C for 3 h. Beads were rinsed extensively with PBST using a continuous wash. One hundred microliters of FN, serially diluted to various concentrations in 2% BSA blocking buffer, were added to each well and plates were again incubated at 37 °C for 2 h. After rinsing with PBST in a continuous wash, 100 μL of peroxidase-labeled Anti-N Mab (2.7 $\mu g \cdot mL^{-1}$) diluted in PBST were added to each well, incubated at 37 °C for 2 h, and rinsed extensively. One hundred fifty μLof QuantaBlu Substrate (Pierce) were added to each well and after 30 min, 100 μL of solution from each well were transferred to clean wells and the fluorescence was read using a Molecular Devices SpectraMax Gemini EM microplate spectrofluorometer.

5.3.6 Atomic Force Microscopy

AFM was used to examine the oriented FN surfaces in more detail. All samples were examined with a Dimension 3100 atomic force microscope with a Nanoscope IIIa controller (Digital Instruments, Santa Barbara, CA) at Worcester Polytechnic Institute. Images were acquired in TappingMode^{TM} in air or liquid (PBS) in ambient conditions. Cantilevers used were silicon (cantilever B from tip number NSC36/AL BS, MikroMasch, Portland, OR), 90 μm in length, and have a manufacturer's reported spring constant of $0.8 \pm 0.2\ N \cdot m^{-1}$. The tip curvature radius is < 10 nm. AFM was used to evaluate the various substrata for homogeneity of protein coverage as well as Root-Mean-Square surface roughness (R_q). Samples imaged in air were rinsed briefly with MilliQ Ultrapure^{TM} water to remove any adsorbed PBS and allowed to dry before imaging.

All images were processed by a first-order flattening algorithm, which removes image

artifacts resulting from bowing and scanner drift. This option is available in the Nanoscope® software, which was also used to generate surface roughness measurements. Images were acquired at a scan rate of 1 Hz with 256 x 256 pixel images typically 2 μm x 2 μm in size. Surfaces studied were clean glass, silanised glass, biotinylated silanised glass, streptavidin bound to silanised glass, IgG bound to streptavidin, and FN bound to immobilised IgG. The amount of FN bound to the IgG surfaces was estimated to be approximately 11.7 $\mathrm{pg} \cdot \mathrm{mm}^{-2}$.

5.3.7 Statistical Analysis

Statistical analysis of AFM topographical data was performed using the statistical analysis software package SPSS 12.0 for Windows. Differences were considered statistically significant when $P < 0.005$. All values are expressed as mean ± SD (see Figure 5.4.9).

5.4 Results

5.4.1 Biochemical Assays

To confirm the activity of our immobilised biotinylated monoclonal antibodies, an end point ELISA was performed (Figure 5.4.1). ELISA results demonstrate that both immobilised Anti-C and Anti-N antibodies were able to bind FN in a dose-dependent fashion. We have also shown that these antibodies do not bind to BSA-coated polystyrene (results available upon request). Figure 5.4.1 indicates that both Mabs react to FN in a dose-dependent fashion. The streptavidin liquid concentration that was used for all surfaces is 10 $\mu g \cdot mL^{-1}$, which results in a surface streptavidin density of $18 \pm 3.0\%$ $pmol \cdot cm^{-2}$; a uniform monolayer on the glass surface.

To verify presence of biotinylated Mabs bound to the streptavidin-coated glass, an ELISA was carried out using a secondary antibody labeled with alkaline-phosphatase (Figure 5.4.2). While this ELISA did not quantify the amount of bound IgG, it verify the presence of IgG and shows that the biotinylated antibodies (either Anti-C or Anti-N) did bind to streptavidin-coated glass in a dose-dependent fashion. Total FN bound per area to the Mab-modified beads was quantified using ^{125}I-FN on surfaces with either immobilised Anti-N or immobilised Anti-C MAbs (Figure 5.4.3). At concentrations below 2 $\mu g \cdot mL^{-1}$, there is no significant difference in the amount of FN bound to either surface. Orientation of FN bound to Mabs on glass was verified using peroxidase-labeled Anti-N Mabs (Figure 5.4.4). Attempts to peroxidase label Anti-C antibodies were unsuccessful most likely due to blockage of the active sites by peroxidase. This could possibly be corrected by appropriate site-labeling of the peroxidase on the IgG molecule. Activity of the detector Anti-N Mabs is significantly higher when the FN is bound to the surface by the C-terminus.

5.4.2 Topography Analysis Using AFM

A schematic representation of the polylaminar surfaces generated may be seen in Figure 5.4.5. After each layering step, AFM topographies were measured to ensure confluence and identify specific features of each deposited species.

Images of silanised glass surface (Figure 5.4.6a) revealed a relatively smooth surface

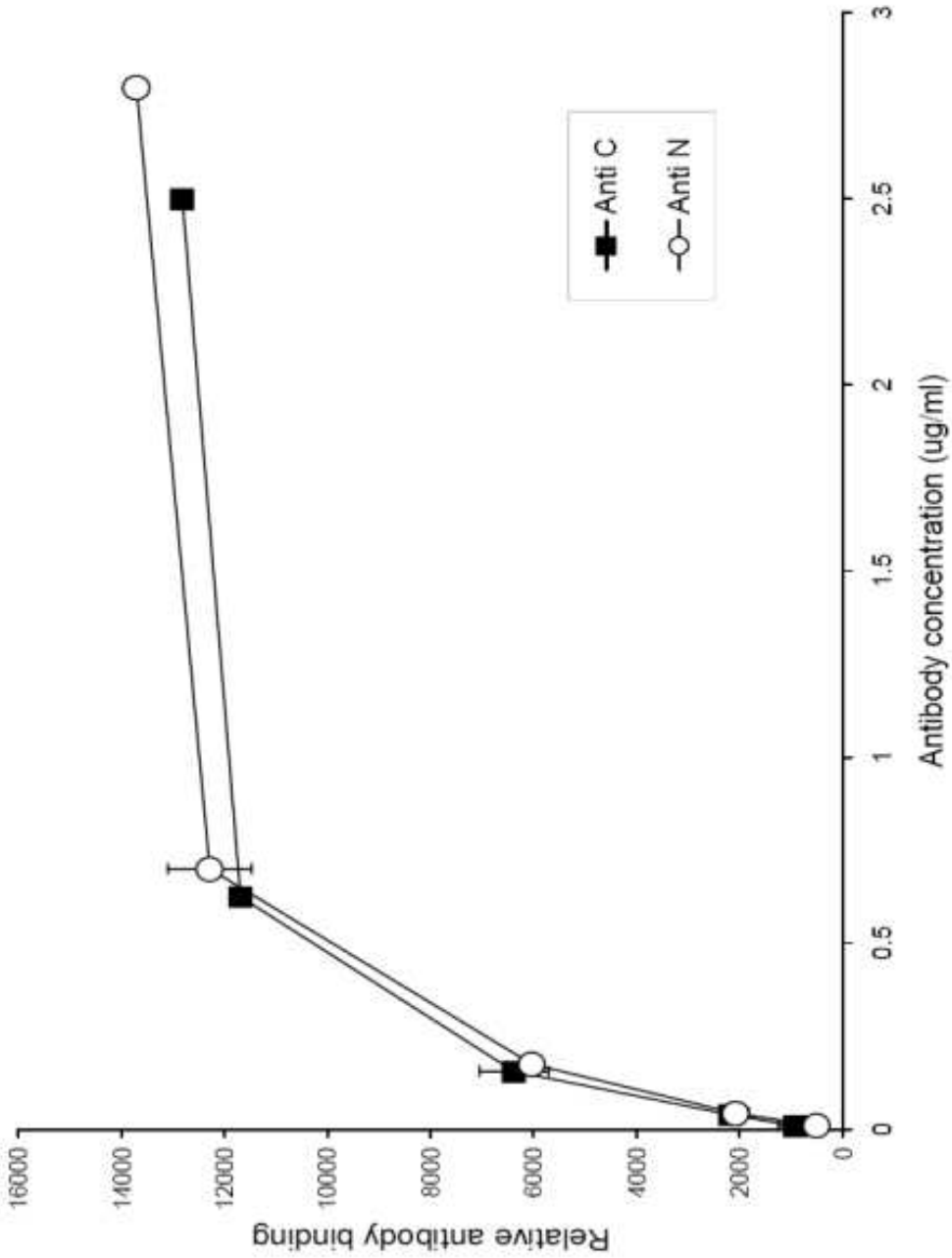

Figure 5.4.1: ELISA with biotin IgG. Amount of i-FN was assumed constant for both trials at an identical liquid FN concentration = 1.0 $\mu g \cdot mL^{-1}$. (RFU-Relative Fluorescent Units)

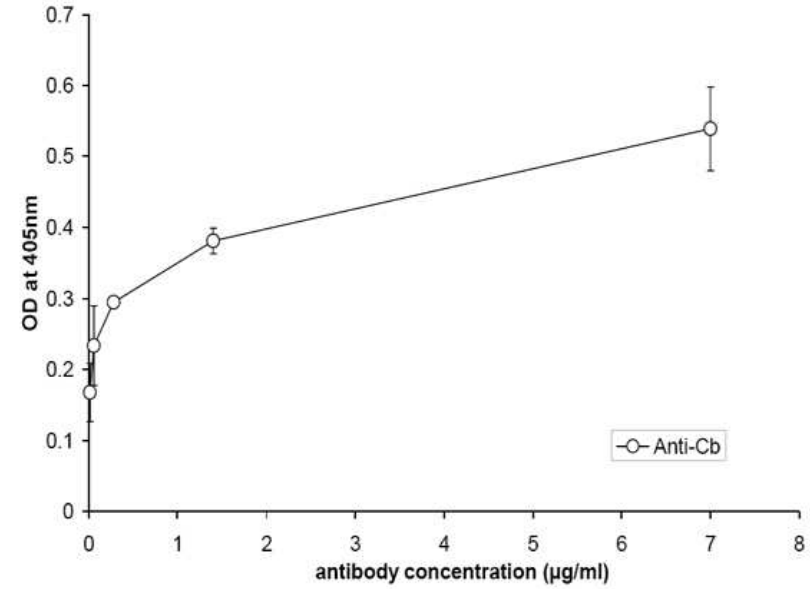

(a)

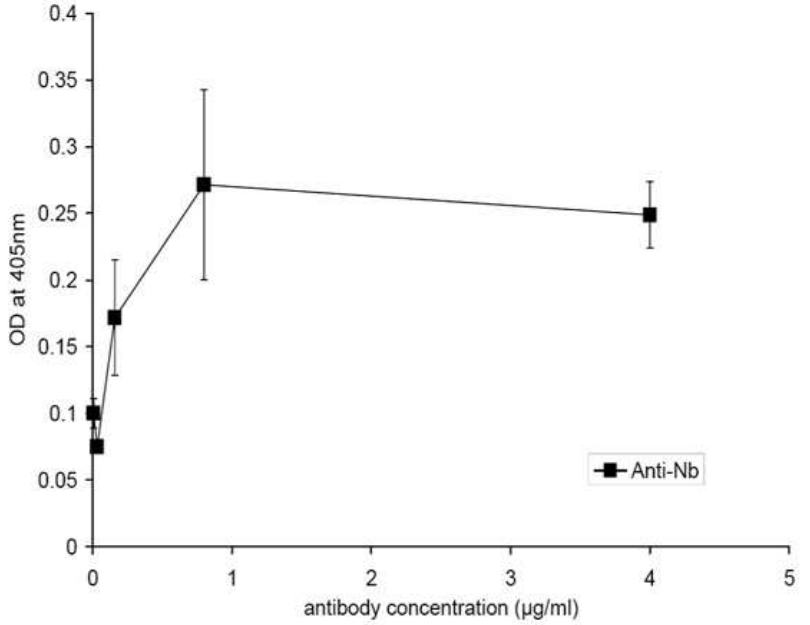

(b)

Figure 5.4.2: An ELISA was performed with biotinylated IgG (a. Anti-C or b. Anti-N) on streptavidin-coated beads and alkaline-phosphatase labeled goat anti-mouse secondary antibody.

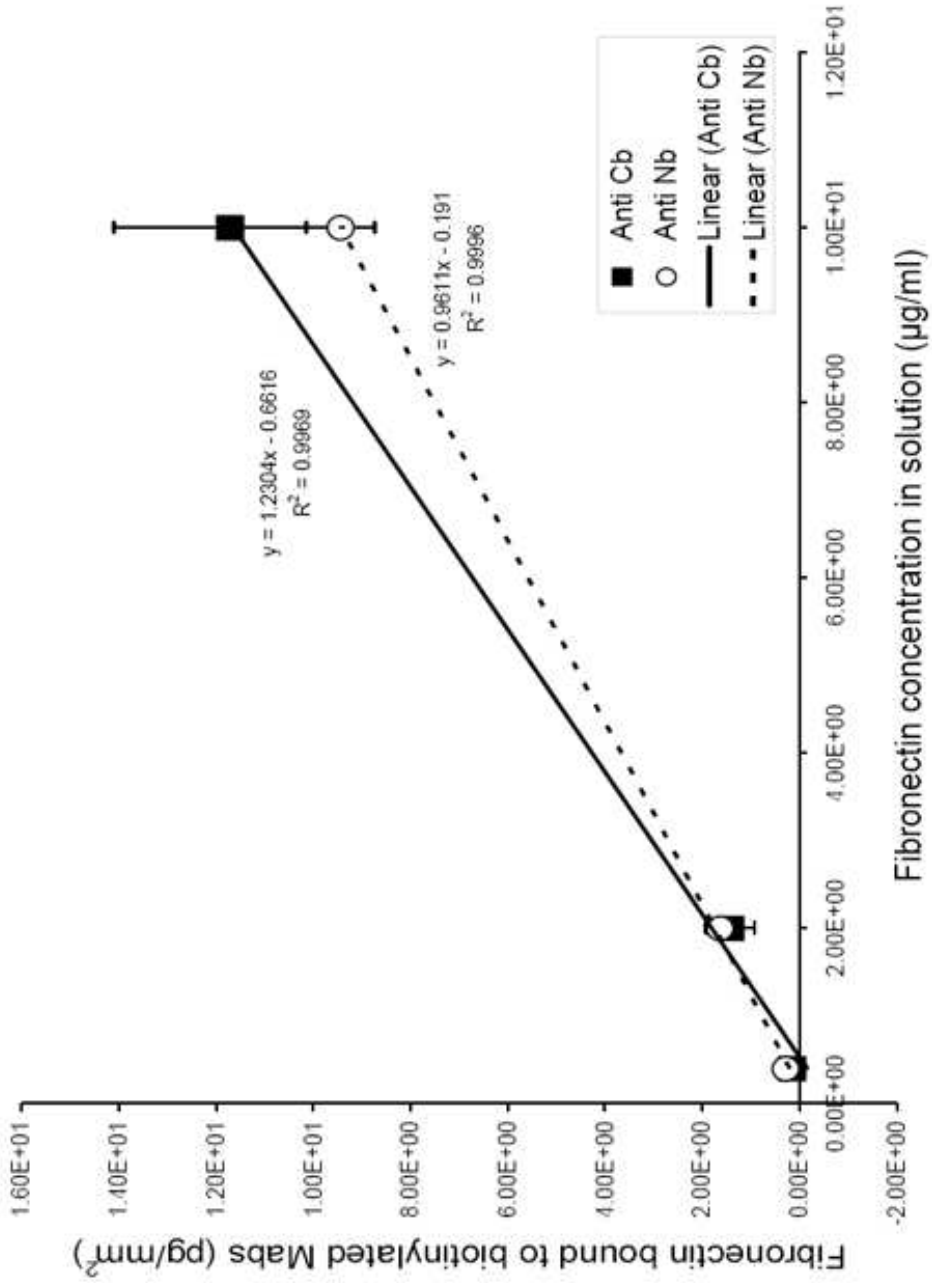

Figure 5.4.3: ^{125}I-FN binding to biotinylated-Mabs immobilised to streptavidin coated glass.

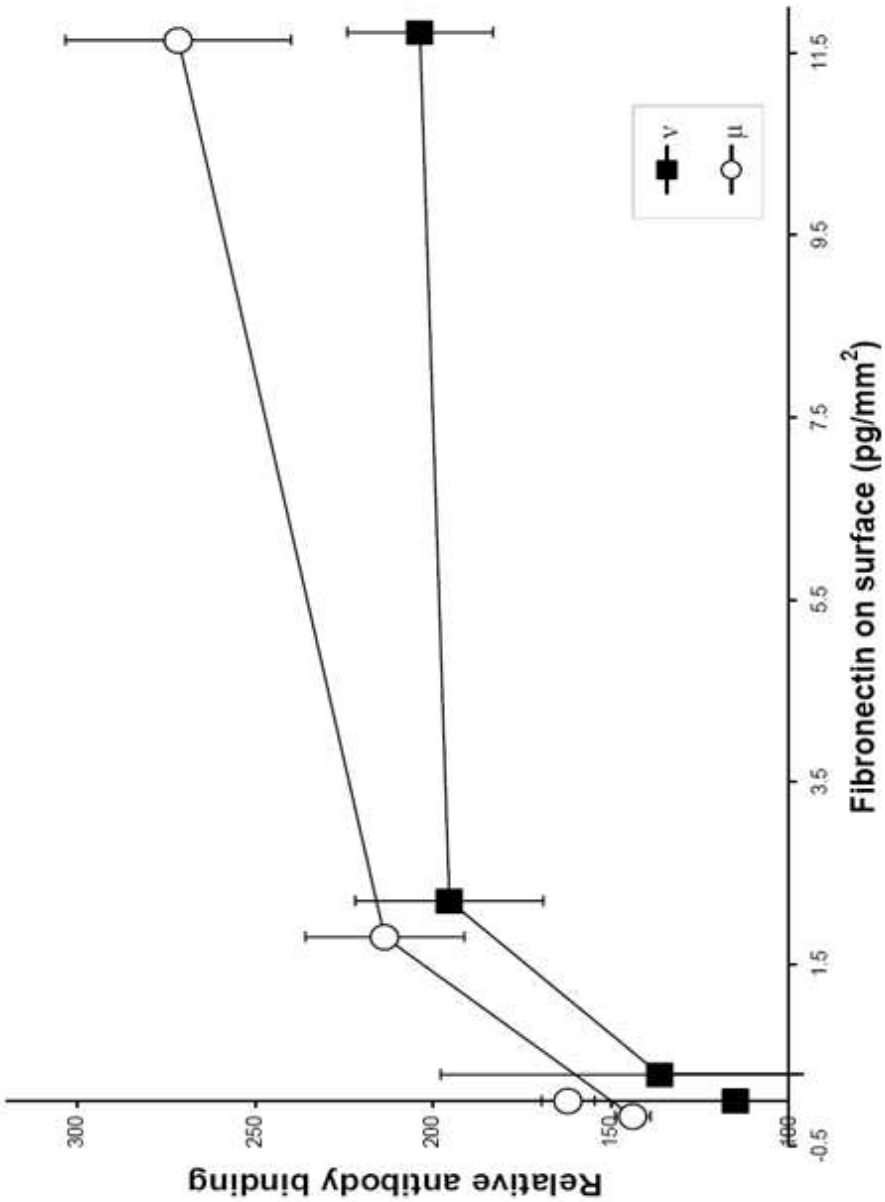

Figure 5.4.4: Sandwich ELISA demonstrating orientation of i-FN. ν = i-FN immobilised by its N-terminus to Anti-N Mab. μ = i-FN immobilised by its C-terminus to Anti-C Mab. I-FN in either case was interrogated using peroxidase-labeled Anti-N Mabs. Anti-C Mabs were unable to retain anti-FN activity after peroxidase-labeling most likely due to blockage of the active sites.

Figure 5.4.5: Schematic diagram of the FN binding substrate. Streptavidin was coated onto silanised glass slides, to which biotinylated monoclonal antibodies were bound. The antibodies were specific to the N- or C-terminus of the FN molecule, allowing for orientation of the protein on the surface.

with no large aggregates in observed areas of 2x2 μm and an average R_q of 0.57 ± 0.132 nm which is larger than that of clean glass ($R_q = 0.34 \pm 0.069$ nm). Images of silanised glass immersed in 500 $\mu g \cdot mL^{-1}$ Sulfo-NHS-LC-biotin (Figure 5.4.6b) also revealed a smooth surface with few aggregates. Images of streptavidin-coated coverglass (Figure 5.4.6c) show what appears to be a protein monolayer with few small aggregates and a surface roughness of 2.76 ± 0.151 nm in an area of 2x2 μm. Streptavidin has previously been shown to have a height of approximately 2 nm [39]. Images of biotinylated Anti-N Mabs bound to streptavidin-glass (Figure 5.4.7a) showed more aggregates than the Anti-C bound surface (Figure 5.4.7b) but had a lower R_q. More scan lines are visible in the images of the Anti-C Mabs. Images of FN/Mab complexes (Figure 5.4.8) reveal that the FN is bound discretely, rather than in a continuous layer. There appear to be some aggregates on the surfaces, although it is not clear if these aggregates are due to aggregated IgG or FN. When FN is bound to the immobilised antibody layers, there is a large increase in R_q compared to the antibody-bound surfaces (increased by 5.36 for Anti-C surface and 2.04 for Anti-N surface). It is not possible to determine orientation of the FN in the AFM images by inspection. The R_q value increased as each protein layer was added. The large increases in surface roughness, in comparison to the streptavidin layer, indicate that there are significant regions on the surface with unfilled Mab and discrete places of i-FN/Mab.

The average height of FN/Anti-C Mab complexes is 62 ± 18.8 nm and the average width is 141 ± 35.2 nm. The average height of FN/Anti-N Mab complexes is 29.9 ± 7.50 nm and the average width is 127.9 ± 30.20 nm. These values were calculated using SPIP software (The Scanning Probe Image Processor v. 3.0.1.0, Image Metrology, Denmark). Ten areas per image were evaluated for height and width using the Line Profile option. Four images were examined. The broad width is caused by the convolution of the tip (< 10 nm) on the border of the object [8]. Figure 5.4.9 summarises R_q results as calculated by the Nanoscope® software.

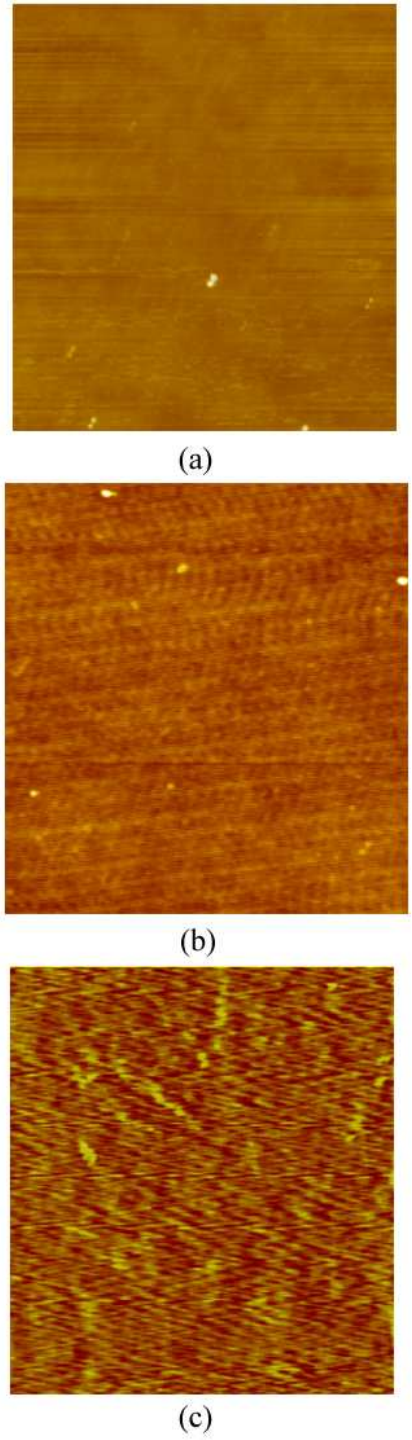

Figure 5.4.6: (a) Amine-silanised glass. Vertical scale is 12.5 nm. (b) Biotinylated silanised glass coverslip. Vertical scale is 7.3 nm. (c) Streptavidin-coated (10 $\mu g \cdot mL^{-1}$) biotinylated coverslip. Vertical scale is 41.42 nm. All images are 2x2 μm in area.

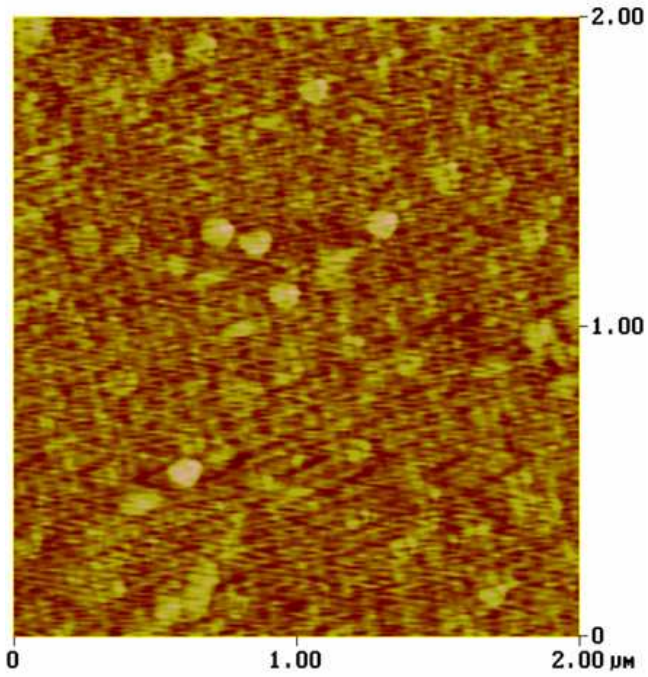

(a)

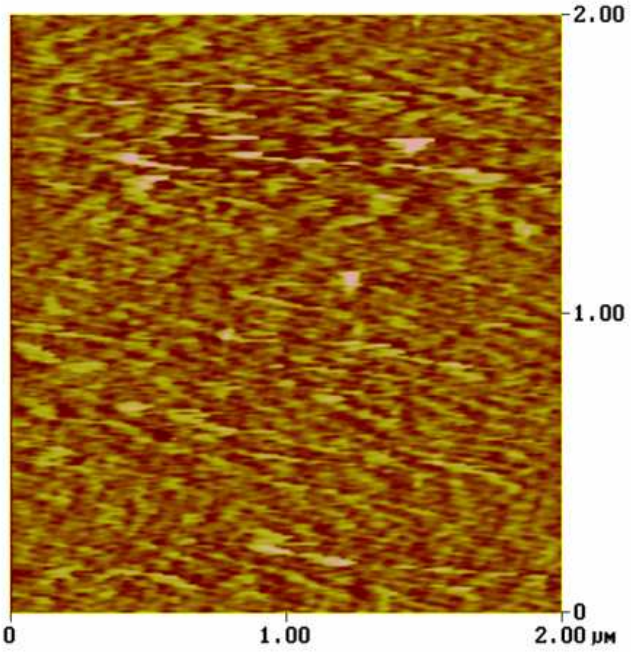

(b)

Figure 5.4.7: (a) Biotinylated Anti-N IgG bound to streptavidin. The image is 2x2 µm and the vertical scale is 27 nm. (b) Biotinylated Anti C IgG bound to streptavidin. The image is 2x2 µm in area and the vertical scale is 62.8 nm. Images were taken in TappingMode^{TM} in air.

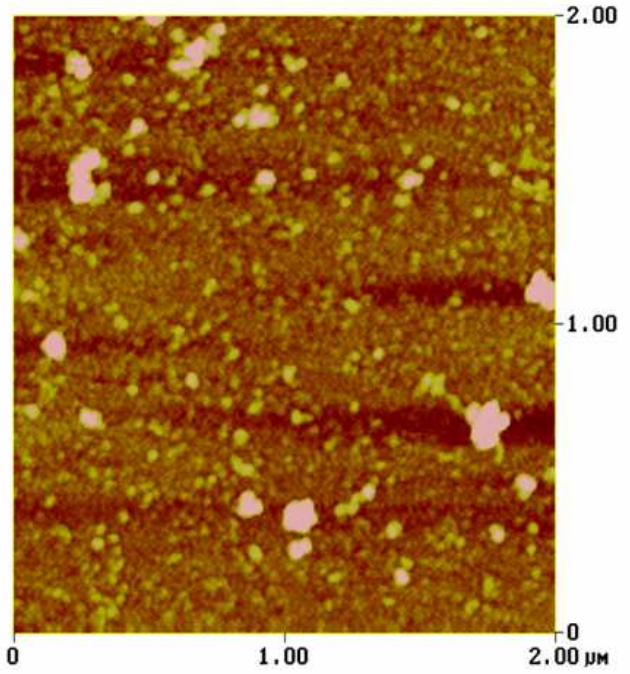

(a)

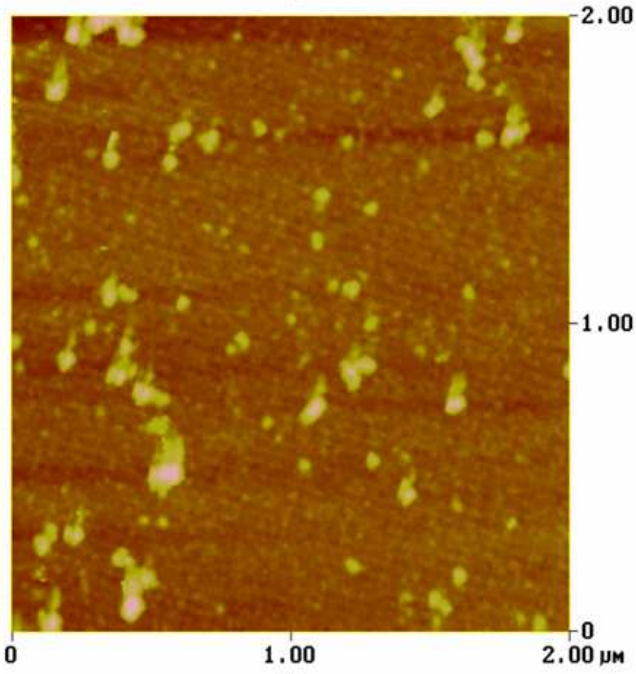

(b)

Figure 5.4.8: (a) FN bound to biotinylated AntiN IgG. The image is 2x2 µm and the vertical scale is 58 nm. (b) FN bound to biotinylated AntiC IgG. The image is 2x2 µm and the vertical scale is 136 nm. Images were taken in TappingMode^{TM} in air. The amount of FN bound to the IgG surfaces was estimated to be approximately 11.7 pg $\cdot$ mm^{-2}.

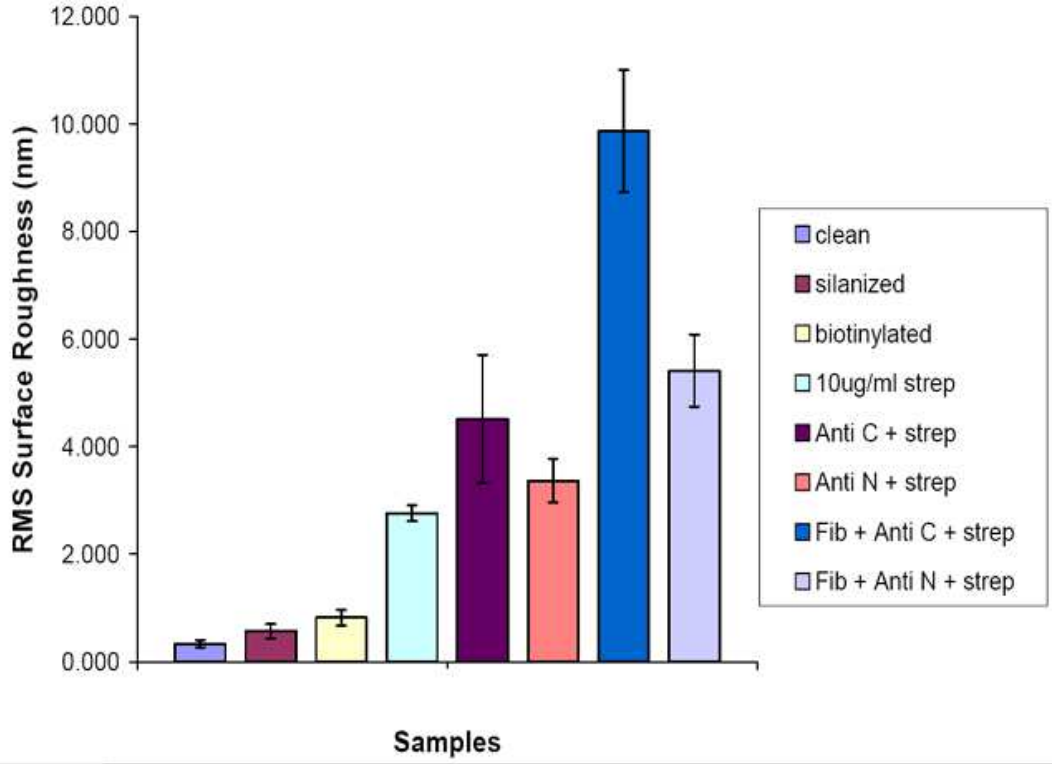

Figure 5.4.9: RMS roughness of samples with various surface treatments. Values were calculated from Nanoscope® software and data was acquired in air. Analysis of these data comparing the number of cells bound to the substrate to the surface texture (R_q) using One Way ANOVA shows a statistically significant difference within the sampled populations ($P < 0.005$)

5.5 Discussion

Monoclonal antibodies were biotin-labeled and immobilised to glass surfaces using the biotin-streptavidin system. Unlike physical adsorption techniques [6, 7], antibody immobilisation in this way can prevent the Mabs from denaturing on the surface and consequently preserve biological activity. Thus, the Mabs were specific to either the -COOH or the NH_2-C- or N- terminus of FN and were used to specifically orient i-FN molecules. There are several methods to immobilise antibodies to a surface. To increase biological activity, antibodies can be biotin labeled at the Fc portion then coupled to an immobilised streptavidin layer, thus orienting the IgG molecule with its active sites facing away from the surface. It was determined that the Anti-N Mab used here could not be successfully biotin-labeled via the carbohydrate moiety, most likely due to a lack of sufficient carbohydrates in the Fc portion. Consequently, we chose to bind biotin to the IgG amine groups using Sulfo-NHS-LC-Biotin (Pierce). Peluso *et al.* [44] showed that the orientation of the intact antibody did not significantly impact the specific activity of the bound antibody on a streptavidin-coated glass surface.

Our surfaces were characterised using several methods. Biochemical assays, such as ELISA, were used to verify presence and activity of bound protein. FN was quantified using ^{125}I-FN and its orientation was verified via sandwich ELISA. The ELISA showed low but measurable activity of the N-terminal-bound FN for the Anti-N Mab, which may be due to the presence of some FN aggregates passively adsorbed on the glass surface or to Anti-N Mabs detecting a secondary binding site on FN. Unlike FN's C-termini, which are linked together in FN molecule by two disulfide bonds, the two N-termini are not. Thus, while it is possible a FN molecule is bound by the Anti-N Mab at one N-terminus, the other NH_2-terminus is still available for binding. A similar result was also seen in the study by Klueh *et al.* [26]. Another explanation of Anti-N Mab binding to Anti-N tethered i-FN is the existence of some FN aggregation. Although precautions were taken in the handling of FN to minimise aggregation, AFM images did show the existence of some areas of aggregation (see below).

Topographies of the various protein/Mab films as well as R_q measurements were exam-

ined using AFM. AFM is a useful tool for investigating the structure and surface characteristics of biomolecules, because it allows for the study of surfaces at high resolution. AFM data complements other methods, such as ELISA, and reveals information about levels of protein adsorption, aggregation, and surface coverage [38]. Comparison of the number of cells adhered to the substrate as a function of the calculated R_q showed a statistically significant difference ($P < 0.005$) for all populations sampled. This indicates that the variability in the measurements is attributable to differences in the surface morphology and topography, and is not dominated by random sampling variability.

We were able to visualise our protein-coated surfaces and detect differences on the surfaces as each protein layer was added. IgG and FN are large molecules several nanometers in size [4, 57]. All AFM images were acquired in TappingMode$^{\text{TM}}$, which results in reduced lateral forces on the sample in comparison to contact mode and is useful for imaging soft biological samples, such as proteins, without damage [38]. Previous AFM studies of immobilised antibodies on a surface via an intermediate protein layer have been conducted for biosensor development [8,29,41]. In those studies, a monolayer of either Protein A or Protein G was used to immobilise IgG. A study by You and Lowe [57] provided similar images for antibodies physically adsorbed to a silanised mica surface. Their study examined antibodies either physically adsorbed or covalently bound using glutaraldehyde. The glutaraldehyde not only covalently links the IgG to the silane surface, it also crosslinks IgG molecules via their primary amine groups.

Images of Anti-C Mab and Anti-N Mab surfaces collected in air show distinct differences. The Anti-C Mab surface show more artifacts (*e.g.,* scan lines) than the Anti-N Mab surfaces. There are several factors that can influence the presence of artifacts. These factors range may include from piezoelectric piezoactuator hysteresis, acoustic or other vibrational oscillations, to contamination of the probe or probe contamination [38]. The artifacts in these images are most likely caused by contamination of the tip by protein. The surfaces were extensively rinsed with PBS containing 0.05% Tween 20, which should remove any non-specifically bound proteins as well as reduce protein aggregates [29]. The Anti-C Mab is of the IgG1 subclass and the Anti-N Mab is of the IgG3 subclass. There are some differences in antibody characteristics between the two subclasses. IgG3 antibodies have an elongated hinge region (4

times longer than IgG1) that allows for greater flexibility. It is possible that some differences in the morphology of the surfaces could be explained by differences in the structure of the two antibody subclasses. Since the antibodies were biotin-labeled via their amine groups, their specific orientation on the surface is not known. Several studies have shown that antibodies exposed to a surface presenting a layer of immobilised protein A or protein G will bind in clusters [8, 29, 41].

The average height of FN/Mab complexes was also determined. Differences in height between Anti-C and Anti-N-held i-FN complexes could be attributed to differences in fibronectin orientation or possibly to the differences in Mab isotype. Since the FN has been kept at physiological conditions, it is most likely in compact form [4]. Elongated FN molecules have been found to have a length of 123 ± 28 nm. Molecules in compact form would have smaller dimensions. The dimensions of IgG have been measured to be 10.5 nm in height and the tip-to-tip distance from each Fab active site is 14.2 nm [8].

Results of bacterial adhesion assays, as described in [21], indicate that while there is some binding of SE seen when FN is bound to the surface by its N-terminal, SE binds preferentially to FN oriented with its C-termini bound to the surface. The number of bacteria bound to the N-terminal-bound FN does not vary drastically by surface density, but this may be due to the close values of FN surface density. There exists nonspecific adhesion to the surfaces with only streptavidin and IgG.

5.6 Conclusions

In this study, we engineered surfaces that specifically orient fibronectin molecules for the purpose of studying bacterial response to oriented protein in the hopes to better understand receptor:ligand interactions. The two oriented FN surfaces appear comparable in their distribution of FN molecules. There was a difference in average height between the complexes observed on the FN/ Anti-N Mab surface and the FN/Anti-C Mab surface. Some aggregates were visible on each surface despite effects to minimise aggregation. These surfaces could be useful in future studies of bacterial response to oriented proteins.

Adhesion of *Staphylococcus epidermidis* RP62A to these engineered surfaces was also examined. It is evident from our studies that *S. epidermidis* RP62A binds preferentially to fibronectin when it is bound by its C-terminus. While binding to the N-terminal-bound fibronectin surface has not been eliminated, it is reduced when compared with the C-terminus bound fibronectin surface. It is known that the orientation and conformation of proteins is affected by the properties of the surface [15]. While there have been studies that examine the influence of FN orientation and conformation on mammalian cell adhesion and spreading [13], there is still much to be learned about the bacterial response. This information can be critical in the development of biomaterials that resist colonisation by microorganisms.

5.7 Bibliography

[1] J. M. Anderson. Chapter 4 - mechanisms of inflammation and infection with implanted devices. Cardiovascular Pathology, Volume 2(Issue 3, Supplement 1):Pages 33–41., 1993.

[2] C. R. Arciola, Y. Bustanji, M. Conti, D. Campoccia, L. Baldassarri, B. Samori, and L. Montanaro. *Staphylococcus epidermidis*-fibronectin binding and its inhibition by heparin. Biomaterials, 24(18):3013–9, 2003.

[3] C. R. Arciola, D. Campoccia, and L. Montanaro. Effects on antibiotic resistance of *Staphylococcus epidermidis* following adhesion to polymethylmethacrylate and to silicone surfaces. Biomaterials, 23(6):1495–502, 2002.

[4] M. Bergkvist, J. Carlsson, and S. Oscarsson. Surface-dependent conformations of human plasma fibronectin adsorbed to silica, mica, and hydrophobic surfaces, studied with use of atomic force microscopy. Journal of Biomedical Materials Research, 64A(2):349–56, 2003.

[5] M. R. Brown, D. G. Allison, and P. Gilbert. Resistance of bacterial biofilms to antibiotics: a growth-rate related effect? Journal of Antimicrobial Chemotherapy, 22(6):777–80, 1988.

[6] J. E. Butler, L. Ni, W. R. Brown, K. S. Joshi, J. Chang, B. Rosenberg, and E. W. Jr. Voss. The immunochemistry of sandwich ELISAs – VI. greater than 90% of monoclonal and 75% of polyclonal anti-fluorescyl capture antibodies (CAbs) are denatured by passive adsorption. Molecular Immunology, 30(13):1165–75, 1993.

[7] J. E. Butler, L. Ni, R. Nessler, K. S. Joshi, M. Suter, B. Rosenberg, J. Chang, W. R. Brown, and L. A. Cantarero. The physical and functional behavior of capture antibodies adsorbed on polystyrene. Journal of Immunological Methods, 150(1-2):77–90, 1992.

[8] M. C. Coen, R. Lehmann, P. Groning, M. Bielmann, C. Galli, and L. Schlapbach. Adsorption and bioactivity of Protein A on silicon surfaces studied by AFM and XPS. Journal of Colloid and Interface Science, 233(2):180–189, 2001.

[9] H. S. Courtney, D. L. Hasty, Y. Li, H. C. Chiang, J. L. Thacker, and J. B. Dale. Serum opacity factor is a major fibronectin-binding protein and a virulence determinant of M type 2 *Streptococcus pyogenes*. Molecular Microbiology, 32(1):89–98, 1999.

[10] H. S. Courtney, I. Ofek, W. A. Simpson, D. L. Hasty, and E. H. Beachey. Binding of *Streptococcus pyogenes* to soluble and insoluble fibronectin. Infection and Immunity, 53(3):454–9, 1986.

[11] R. M. Donlan. Biofilms and device-associated infections. Emerging Infectious Diseases, 7(2):277–81, 2001.

[12] W. M. Dunne and E. M. Burd. Fibronectin and proteolytic fragments of fibronectin interfere with the adhesion of *Staphylococcus epidermidis* to plastic. Journal of Applied Bacteriology, 74(4):411–6, 1993.

[13] A. J. Garcia, M. D. Vega, and D. Boettiger. Modulation of cell proliferation and differentiation through substrate-dependent changes in fibronectin conformation. Molecular Biology of the Cell, 10(3):785–98, 1999.

[14] C. Greene, D. McDevitt, P. Francois, P. E. Vaudaux, D. P. Lew, and T. J. Foster. Adhesion properties of mutants of *Staphylococcus aureus* defective in fibronectin-binding proteins and studies on the expression of *fnb* genes. Molecular Microbiology, 17(6):1143–52, 1995.

[15] F. Grinnell and M. K. Feld. Fibronectin adsorption on hydrophilic and hydrophobic surfaces detected by antibody binding and analyzed during cell adhesion in serum-containing medium. Journal of Biological Chemistry, 257(9):4888–93, 1982.

[16] A. G. Gristina, C. D. Hobgood, L. X. Webb, and Q. N. Myrvik. Adhesive colonization of biomaterials and antibiotic resistance. Biomaterials, 8(6):423–6, 1987.

[17] G. T. Hermanson. Bioconjugate Techniques. Academic Press, San Diego, CA, 1996.

[18] S. D. Holmes, K. May, V. Johansson, F. Markey, and I. A. Critchley. Studies on the interaction of *Staphylococcus aureus* and *Staphylococcus epidermidis* with fibronectin using

surface plasmon resonance (BIAcore). Journal of Microbiological Methods, 28(1):77–84, 1997.

[19] K. House-Pompeo, Y. Xu, D. Joh, P. Speziale, and M. Hook. Conformational changes in the fibronectin binding MSCRAMMs are induced by ligand binding. Journal of Biological Chemistry, 271(3):1379–84, 1996.

[20] M. Hussain, C. Heilmann, G. Peters, and M. Herrmann. Teichoic acid enhances adhesion of *Staphylococcus epidermidis* to immobilized fibronectin. Microbial Pathogenesis, 31(6):261–70, 2001.

[21] R. A. Jarvis and J. D. Bryers. Effects of controlled fibronectin surface orientation on subsequent *Staphylococcus epidermidis* adhesion. Journal of Biomedical Materials Research Part A, 75A:41–55, 2005.

[22] D. Joh, E. R. Wann, B. Kreikemeyer, P. Speziale, and M. Hook. Role of fibronectin-binding MSCRAMMs in bacterial adherence and entry into mammalian cells. Matrix Biology, 18(3):211–23, 1999.

[23] U. Klueh. Characterization of protein orientation on surfaces. Master's Thesis, University of Connecticut, 2000.

[24] U. Klueh, J. D. Bryers, and D. L. Kreutzer. Binding and orientation of fibronectin on polystyrene surfaces using immobilized bacterial adhesin-related peptides. Journal of Biomedical Materials Research, 67A(1):36–43, 2003.

[25] U. Klueh, S. Goralnick, J. D. Bryers, and D. L. Kreutzer. Binding and orientation of fibronectin on surfaces with collagen-related peptides. Journal of Biomedical Materials Research, 56(3):307–23, 2001.

[26] U. Klueh, T. Seery, D. G. Castner, J. D. Bryers, and D. L. Kreutzer. Binding and orientation of fibronectin to silanated glass surfaces using immobilized bacterial adhesin-related peptides. Biomaterials, 24(22):3877–84, 2003.

[27] P. Kuusela, T. Vartio, M. Vuento, and E. B. Myhre. Binding sites for *Streptococci* and *Staphylococci* in fibronectin. Infection and Immunity, 45(2):433–6, 1984.

[28] J. M. Kuypers and R. A. Proctor. Reduced adherence to traumatized rat heart valves by a low-fibronectin-binding mutant of *Staphylococcus aureus*. Infection and Immunity, 57(8):2306–12, 1989.

[29] W. Lee, B. K. Oh, Y. Min Bae, S. H. Paek, W. Hong Lee, and J. W. Choi. Fabrication of self-assembled Protein A monolayer and its application as an immunosensor. Biosensors and Bioelectronics, 19(3):185–92, 2003.

[30] H. Lindmark and B. Guss. SFS, a novel fibronectin-binding protein from *Streptococcus equi*, inhibits the binding between fibronectin and collagen. Infection and Immunity, 67(5):2383–8, 1999.

[31] R. C. Massey, S. R. Dissanayeke, B. Cameron, D. Ferguson, T. J. Foster, and S. J. Peacock. Functional blocking of *Staphylococcus aureus* adhesins following growth in *ex vivo* media. Infection and Immunity, 70(10):5339–45, 2002.

[32] R. C. Massey, M. N. Kantzanou, T. Fowler, N. P. Day, K. Schofield, E. R. Wann, A. R. Berendt, M. Hook, and S. J. Peacock. Fibronectin-binding Protein A of *Staphylococcus aureus* has multiple, substituting, binding regions that mediate adherence to fibronectin and invasion of endothelial cells. Cell Microbiology, 3(12):839–51, 2001.

[33] R. C. Massey, M. N. Kantzanou, T. Fowler, N. P. Day, K. Shofield, E. R. Wann, A. R. Berendt, M. Hook, and S. J. Peacock. Fibronectin-binding protein A of *S. aureus* has multiple, substituting, binding regions that mediate adherence to fibronectin and invasion of endothelial cells. Cell Microbiology, 3:839–851, 2001.

[34] M. H. McCafferty, M. Lepow, T. M. Saba, E. Cho, H. Meuwissen, J. White, and S. F. Zuckerbrod. Normal fibronectin levels as a function of age in the pediatric population. Pediatric Research, 17(6):482–5, 1983.

[35] J. McDonagh. Plasma fibronectin: Structure and Function, volume 5 of Hematology. Marcel Dekker, Inc., New York, NY, 1985.

[36] M. C. McElroy, D. J. Cain, C. Tyrrell, T. J. Foster, and C. Haslett. Increased virulence of a fibronectin-binding protein mutant of *Staphylococcus aureus* in a rat model of pneumonia. Infection and Immunity, 70(7):3865–73, 2002.

[37] J. Mills, L. Pulliam, L. Dall, J. Marzouk, W. Wilson, and J. W. Costerton. Exopolysaccharide production by viridans *Streptococci* in experimental endocarditis. Infection and Immunity, 43(1):359–67, 1984.

[38] V.J. Morris, A.R. Kirby, and A.P. Gunning. Atomic Force Microscopy for Biologists. Imperial College Press, London, 1999.

[39] C. S. Neish, I. L. Martin, R. M. Henderson, and J. M. Edwardson. Direct visualization of ligand-protein interactions using atomic force microscopy. British Journal of Pharmacology, 135(8):1943–50, 2002.

[40] J. C. Nickel, J. Heaton, A. Morales, and J. W. Costerton. Bacterial biofilm in persistent penile prosthesis-associated infection. Journal of Urology, 135(3):586–8, 1986.

[41] B. K. Oh, Y. K. Kim, W. Lee, Y. M. Bae, W. H. Lee, and J. W. Choi. Immunosensor for detection of *Legionella pneumophila* using surface plasmon resonance. Biosensors and Bioelectronics, 18(5-6):605–11, 2003.

[42] J. M. Patti, B. L. Allen, M. J. McGavin, and M. Hook. MSCRAMM-mediated adherence of microorganisms to host tissues. Annual Review of Microbiology, 48:585–617, 1994.

[43] J. M. Patti and M. Hook. Microbial adhesins recognizing extracellular matrix macromolecules. Current Opinion in Cell Biology, 6(5):752–8, 1994.

[44] P. Peluso, D. S. Wilson, D. Do, H. Tran, M. Venkatasubbaiah, D. Quincy, B. Heidecker, K. Poindexter, N. Tolani, M. Phelan, K. Witte, L. S. Jung, P. Wagner, and S. Nock. Optimizing antibody immobilization strategies for the construction of protein microarrays. Analytical Biochemistry, 312(2):113–24, 2003.

[45] A. Reisner, N. Hoiby, T. Tolker-Nielsen, and S. Molin. Microbial pathogenesis and biofilm development. Contributions to Microbiology, 12:114–31, 2005.

[46] C. Signas, G. Raucci, K. Jonsson, P. E. Lindgren, G. M. Anantharamaiah, M. Hook, and M. Lindberg. Nucleotide sequence of the gene for a fibronectin-binding protein from *Staphylococcus aureus*: use of this peptide sequence in the synthesis of biologically active peptides. Proceedings of the National Academy of Sciences of the United States of America, 86(2):699–703, 1989.

[47] G. S. Tamura and C. E. Rubens. Group B streptococci adhere to a variant of fibronectin attached to a solid phase. Molecular Microbiology, 15(3):581–9, 1995.

[48] Y. Terao, S. Kawabata, E. Kunitomo, J. Murakami, I. Nakagawa, and S. Hamada. Fba, a novel fibronectin-binding protein from *Streptococcus pyogenes*, promotes bacterial entry into epithelial cells, and the fba gene is positively transcribed under the Mga regulator. Molecular Microbiology, 42(1):75–86, 2001.

[49] M. van der Flier, N. Chhun, T. M. Wizemann, J. Min, J. B. McCarthy, and E. I. Tuomanen. Adherence of *Streptococcus pneumoniae* to immobilized fibronectin. Infection and Immunity, 63(11):4317–22, 1995.

[50] P. Vaudaux, D. Pittet, A. Haeberli, P. G. Lerch, J. J. Morgenthaler, R. A. Proctor, F. A. Waldvogel, and D. P. Lew. Fibronectin is more active than fibrin or fibrinogen in promoting *Staphylococcus aureus* adherence to inserted intravascular catheters. Journal of Infectious Diseases, 167(3):633–41, 1993.

[51] P. E. Vaudaux, P. Francois, R. A. Proctor, D. McDevitt, T. J. Foster, R. M. Albrecht, D. P. Lew, H. Wabers, and S. L. Cooper. Use of adhesion-defective mutants of *Staphylococcus aureus* to define the role of specific plasma proteins in promoting bacterial adhesion to canine arteriovenous shunts. Infection and Immunity, 63(2):585–90, 1995.

[52] R. A. Vijayendran and D. E. Leckband. A quantitative assessment of heterogeneity for surface-immobilized proteins. Analytical Chemistry, 73(3):471–80, 2001.

[53] C. Vuong and M. Otto. *Staphylococcus epidermidis* infections. Microbes and Infection, 4(4):481–9, 2002.

[54] B. Westerlund, I. van Die, C. Kramer, P. Kuusela, H. Holthofer, A. M. Tarkkanen, R. Virkola, N. Riegman, H. Bergmans, and W. et al. Hoekstra. Multifunctional nature of P fimbriae of uropathogenic *Escherichia coli*: mutations in *fsoE* and *fsoF* influence fimbrial binding to renal tubuli and immobilized fibronectin. Molecular Microbiology, 5(12):2965–75, 1991.

[55] R. J. Williams, B. Henderson, L. J. Sharp, and S. P. Nair. Identification of a fibronectin-binding protein from *Staphylococcus epidermidis*. Infection and Immunity, 70(12):6805–10, 2002.

[56] K. D. Yang, N. H. Augustine, L. A. Gonzalez, J. F. Bohnsack, and H. R. Hill. Effects of fibronectin on the interaction of polymorphonuclear leukocytes with unopsonized and antibody-opsonized bacteria. Journal of Infectious Diseases, 158(4):823–30, 1988.

[57] H. X. You and C. R. Lowe. AFM studies of protein adsorption 2. Characterization of Immunoglobulin G adsorption by detergent washing. Journal of Colloid and Interface Science, 182:586–601, 1996.

CHAPTER 6

A Microscale Correlation Amongst Surface Chemistry, Texture and the Adhesive Strength of *Staphylococcus epidermidis*

6.1 Abstract

Staphylococcus epidermidis is among the most commonly isolated microbes from medical implant infections, particularly in the colonisation of blood-contacting devices. Past research has rigorously studied the influence of surface wettability and traditional engineering parameters, such as average or root-mean-square roughness, on microbial adhesive strength. These approaches have met with limited success. In this study, we explore these traditional approaches by studying the molecular-level interactions between *S. epidermidis* and a vari-

ety of chemically and texturally distinct model substrata. These included metals, aliphatic and aromatic self-assembled monolayers, and polymeric and proteinaceous materials.

Interaction forces between a single, metabolically active microbial cell and each substrate were measured using atomic force microscopy. Correlations between adhesive strength and surface texture (root mean square roughness, R_q) show weak relationships for most surfaces ($R^2 < 20\%$). These measurements also show scale-dependence, as values of R_q and R^2 varied unpredictably with the scan size of the image. For simple aliphatic molecules, the water contact angle explained $> 95\%$ of the variation in the values of the adhesive strength. However, the correlation decreased significantly for more complex aromatic molecules ($R^2 < 65\%$) and irregularly-deposited proteins and polyamino acids ($R^2 < 55\%$).

Making the *a priori* assumption that the texture of a surface must influence its adhesive capabilities to some extent, and seeing that conventional parameters such as R_q poorly characterise the interactions, and vary with observational scale, we chose to apply a novel surface characterisation method based in Mandelbrot fractal theory. Preliminary correlations between this model, which describes a range of observational scales independent of the scale defined by the recorded topographical image, and the adhesive strength show stronger correlations amongst the recorded data sets. However, additional analysis, specifically accounting for the elasticity of the microbial exopolymer brush and cell wall, may further validate the choice of this model in characterising microbial adhesive affinity in terms of the binding surface texture.

6.2 Introduction

Microbial infections of medical implants occur in more than 2 million surgical cases each year in the United States, increasing patient morbidity, mortality, cost and recovery time [2,12,26]. While many methods exist to treat these infections, surgical excision of the infected device is the only certain cure [19, 21]. Clinically, it is of interest to determine the factors affecting microbial adhesion, the precursor to infection, and to formulate adhesion-resistant materials that are effective over protracted time periods.

6.2.1 Background

Past research has provided two heuristics in the design of medical implant devices related to biocompatibility and biostability *in vivo*. First, devices having low wettability (*viz.*, hydrophobic materials with large water contact angles) are the most successful candidates for implantation, as they are chemically distinct from water-based somatic fluids, proteins and cells. This is generally an incorrect assumption, as implantation of these foreign bodies often elicits an immune response from the host, leading to leukocyte activation and subsequent protein sorption. Often, this response provides an ideal conditioning layer to which planktonic microbes may attach, grow and disseminate. Hydrophilic materials, such as polished metals and oxidized plastics, demonstrate higher resistance to microbial colonisation [22]. These materials, however, lack the mechanical flexibility and biocompatibility necessary for the majority of implant sites [1].

A further guideline in medical device design has been to consider extremely smooth surfaces as both biostable and biocompatible, as well as anti-adhesive for microbes [29, 33, 34]. The decreased surface area available for adhesion decreases the probability of colonisation by either somatic immune factors or pathogenic microbes, but, given sufficient time, any implanted material will be made chemically and texturally indistinct from the somatic environment. Quirynen *et al.* [34] have suggested that an optimal surface texture may be fabricated, leading to a surface which is resistant to microbial colonisation.

6.2.2 Current Research

In recent years, cell surface hydrophobicity and charge have received significant attention as a determining factor in establishing the propensity of a bacterium to adhere to a surface [5, 10, 43]. Hydrophobicity is determined by fluid (generally water) contact angles measured on dried microbial lawns [10], while the surface charge is reported in terms of the electrophoretic mobility of a microbial suspension in buffered media of varying ionic strength [43]. In conjunction with the Derjaguin-Landau-Verwey-Overbeek (DLVO) theory of colloid stability [14, 42], these parameters may be used to calculate the energy profiles arising from London-van der Waals and electrostatic interactions. Extensions to the classical theory have been developed to account for exopolymeric steric interactions [11], acid-base interactions [41], and various other possible specific and non-specific interaction mechanisms.

Similarly, researchers have identified the texture of the material surfaces as the causative agents in initial microbial colonisation. It has been shown, particularly in the case of polymeric materials, that the roughness of the surface allows for an increase in both microbial and somatic cell adhesive strength [4, 13, 20].

A shortcoming to these methods has consistently been the lack of any clear relationship between the macroscopic measurements of fluid contact angle or electrophoretic mobility and the microscopic or nanoscopic behaviour of the microbial cell wall structures. Vadillo-Rodriguez *et al.* [40] have recently explored possible correlations between macroscale measurements and microscale behaviour as measured by atomic force microscopy (AFM). In many cases, clear relationships between macroscale measurements and microscale force interaction profiles cannot be derived.

6.2.3 Objective

The main objective of this research was to determine quantitatively the main factors influencing the adhesion of *Staphylococcus epidermidis* to a variety of substrates as a precursor to *in vivo* studies addressing the design of novel biomedical implant materials. Where macroscale correlations have proved elusive, we explored their use in conjunction with atomic force microscopy (AFM) techniques, specifically in comparing results obtained from macroscale

contact angle experiments and microscale image analysis to characterise the surface texture.

Model surfaces were modified with a variety of chemically and texturally distinct films, including self-assembled monolayers (SAMs), poly-amino acids and proteins. Using an AFM probe functionalised with a single, metabolically active *S. epidermidis* cell, we are able to quantitatively measure the adhesive strength of the cell to each surface after contact. Adhesive strength measurements were correlated to both the relative hydrophobicity (contact angle) of each surface, and to the root-mean-square roughness (R_q) of each surface. This latter is calculated from topographical images of each surface at a fixed scan area using a bare AFM probe.

We have also applied a Discrete Bonding Model [7,37], which relates the adhesive strength of an interaction to a fractal representation of each topographical image. This technique offers many benefits, as it partially overcomes the resolution-dependence of the AFM images, and is able to identify the area scale at which individual interactions occur.

6.3 Materials and Methods

Substrates of interest to this study include a variety of chemically distinct self-assembled monolayers, polymeric, proteinaceous and metallic surfaces. In addition to the gold (Au) and stainless steel (SS) control surfaces, we include the species described in Table 6.3.1. These are also shown schematically in Figure 6.3.1.

6.3.1 Preparation of Self-Assembled Monolayer Surfaces

Dodecanethiol (DDT), hexadecanethiol (HDT) and ω-mercaptoundecanoic acid were purchased from Aldrich (Milwaukee, WI) and used as received. 1-(10-sulfhydryl-decyloxy)-benzene-3,5-dicarboxylic acid (IPA) was synthesised following the procedure described in [38]. The compound was obtained in a three step synthesis starting from a coupling reaction of 1,10-dibromodecane and diethyl 5-hydroxyisophthalate. The bromine group in the resulting diethyl 5-(10-thioacetyl-decyloxy)-isophthalate was substituted with a thioacetate group. The resulting compound was then treated in a potassium hydroxide/ethanol (KOH/EtOH) solution to obtain the final compound.

Films of Ag(I) + IPA (IAG) were prepared by transferring the monolayer of IPA to a 5 mM solution of silver (I) nitrate ($AgNO_3$) in acetonitrile. Ag(I) complexation of the surface was obtained after 3 h.

4-(10-sulfhydryl-decyloxy)-pyridine (PDT) was synthesised from 1,10-dibromodecane and 4-hydroxypyridine. The resulting 4-(10-bromo)-decyloxy-pyridine was converted to the final compound in one step according to the trimethylsilythioxy-dehalogenation reaction reported by Fox [23]. (1-mercaptoundec-11-yl)tri(ethylene glycol) (TEG) was synthesised according to literature procedures [31].

Gold slides were purchased from Evaporated Metal Films (EMF, Ithaca, NY). The slides have dimensions of 25 mm x 75 mm x 1 mm of float glass with cut edges and are coated with 5 nm of chromium or titanium followed by 100 nm of gold. The substrates were cut to suit experimental requirements. The slides were immersed in acid piranha solution (70% sulfuric acid / 30% hydrogen peroxide) at 90 °C for $10 - 15$ min to remove surface impurities. The slides were rinsed with water and ethanol, and dried with a stream of nitrogen. Slides were

Table 6.3.1: Chemical names, abbreviations and molecular weights (where appropriate) for all experimental surfaces.

Sample	**Abbreviation**	**Molecular Weight** ($g \cdot mol^{-1}$)
Bovine Serum Albumin	BSA	50 - 80 kDa
Dodecanethiol	DDT	201.4
Hexadecanethiol (10 mM)	HDT10	257.5
Hexadecanethiol (20 mM)	HDT20	257.5
1-(10-sulfhydryl-decyloxy)-benzene-3,5-dicarboxylic acid	IPA	353.5
Ag(I)-IPA	IAG	459.3
4-(10-sulfhydryl-decyloxy)-pyridine	PDT	266.4
Poly-L-Lysine (Stock solution)	PLL1	50 - 300 kDa
Poly-L-Lysine (10X dilution)	PLL10	50 - 300 kDa
Poly-L-Lysine (100X dilution)	PLL100	50 - 300 kDa
(1-mercaptoundec-11-yl)-tri(ethylene glycol)	TEG	333.5

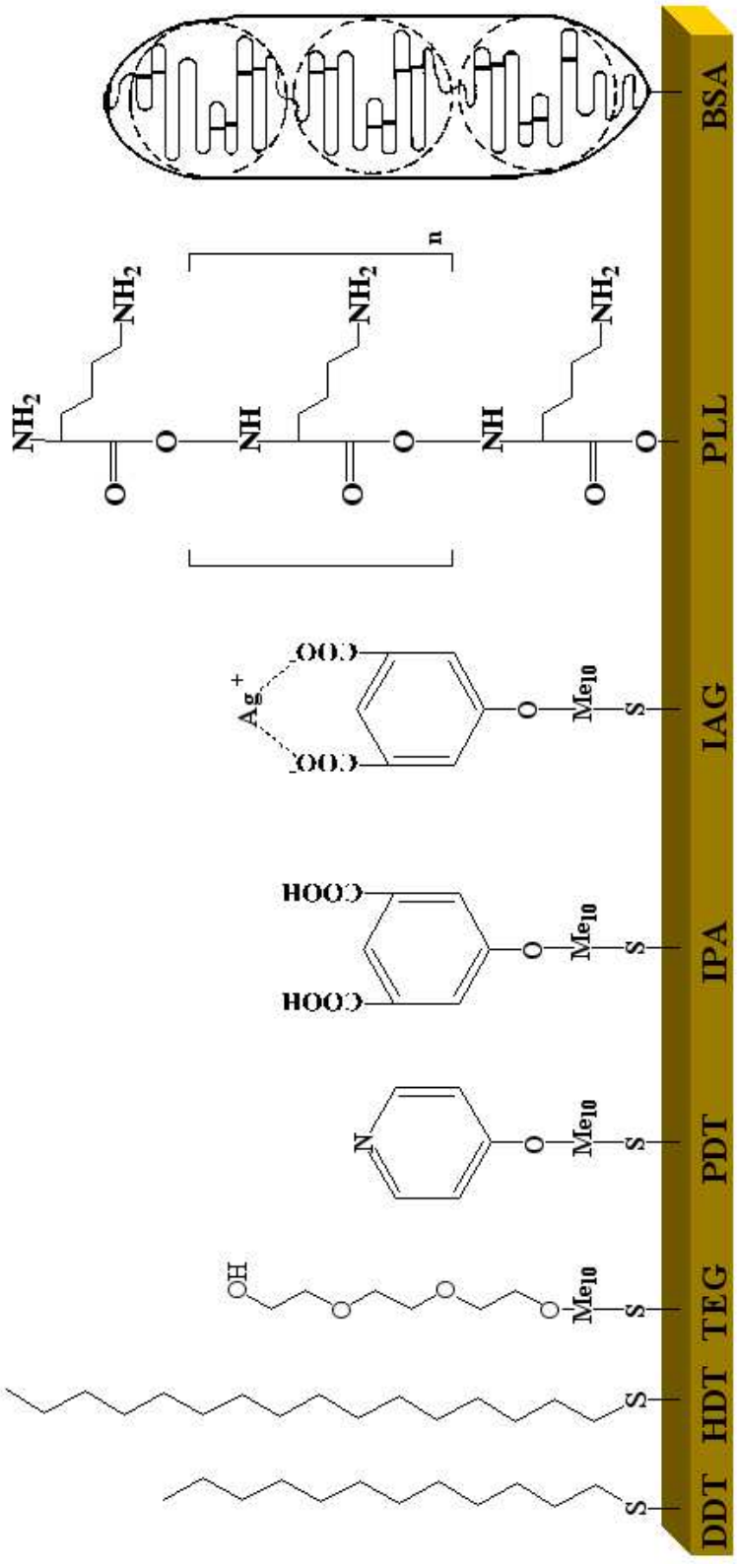

Figure 6.3.1: Schematic representation of the substrates examined. All species were bound to gold by thiol linkages, with the exception of PLL and BSA, and confluence of the layers was determined by contact angle and ellipsometric measurements (Table 6.4.2). PLL and BSA were deposited gravitationally onto the gold substrate, and, although layer homogeneity was not expected, water contact angles were measured for both surfaces. Ellipsometry was not performed on these surfaces, as the surfaces were assumed to be nonisotropic.

used immediately after cleaning to avoid surface contamination.

Monolayers of all alkanethiols were prepared by immersing the clean gold slides in a $1-2$ mM ethanol solution of the desired compound for at least 24 h. The films were rinsed with ethanol and dried with nitrogen before characterisation or experimentation.

6.3.2 Preparation of Randomly Deposited Surfaces

Compounds such as poly-L-lysine (PLL, MW $= 50-300$ kDa; Sigma-Aldrich) and bovine serum albumin (BSA, MW $= 50-80$ kDa; Sigma) are included in this section. PLL solutions were prepared at stock concentration (PLL1; 0.01 w/v%), and also at 10X dilution (PLL10; 0.001 w/v%) and 100X dilution (PLL100; 0.0001 w/v%) in 100 mM MES buffer. BSA (Sigma) was prepared at a concentration of 10 $\mathrm{mg \cdot mL^{-1}}$ in distilled, deionized water. All solutions were mixed at ambient temperature for $5-6$ h. After mixing, 10 mL of each solution was pipetted onto a gold-coated glass coupon, which had been soaked for 10 min in a 4:1 solution of sulfuric acid/hydrogen peroxide (H_2SO_4/H_2O_2) to remove surface contaminants. Slides were agitated at 0.81xg for 8 h to promote homogeneous deposition.

6.3.3 Self-Assembled Monolayer Characterisation

Water contact angles on each substrate were measured with a Rame-Hart Model 100-00 Goniometer (Mountain Lakes, NJ). Drops of water (2 μL) were deposited with a micropipette and the sessile drop contact angle was measured in triplicate. The average of three measurements is considered the contact angle for the surface, and the standard deviation of the measurements is reported.

Ellipsometric measurements were obtained with a Manual Photoelectric Rudolf 439L633P ellipsometer (Rudolph Instruments, Fairfield NJ). The measurements were taken at a 70° angle of incidence using a HeNe laser light (principal wavelength = 632.8 nm). The calculated thickness values for each film are the average of values obtained from three different samples. Measurements on each sample were taken at three different locations separated by at least 5 mm. The measurements were taken with the sample exposed to air and within $5-10$ min after taking the sample from solution and washing it with ethanol to remove physisorbed compounds. For thickness measurements of SAMs on gold, a bare gold substrate was used

to determine the optical constants of gold, specifically n, the refractive index, and k, the extinction index. Results were compared to values previously reported in the literature (n = 0.2 and k = 3.3) [30]. Based on the work of Folkers [18], values of n = 1.47 and k = 0 were assumed. Film thicknesses were calculated according to the model described in [18].

6.3.4 Microbial Growth and Storage

Clinical isolate samples of *Staphylococcus epidermidis* were kindly provided by Dr. Stephen Heard (University of Massachusetts Medical School, Worcester, MA). Cultures were maintained on Tryptic Soy Agar (40 $g \cdot L^{-1}$; Sigma) plates, and were re-pitched every 14 d. Prior to experimentation, cells were grown in Tryptic Soy Broth (30 $g \cdot L^{-1}$; Sigma) at 37 °C until mid-exponential growth phase (optical density at 600 nm $[O.D._{600}] = 0.9 \pm 0.05$). For cell probe experiments, 10 mL of cell suspension was transferred to a centrifuge tube and pelleted at a relative centrifugal force of 1360xg for 10 minutes (Centrific Centrifuge, Fischer) at 25°. The supernatant was then eluted, and the pellet resuspended in 4 mL of 100 mM 2-(N-Morpholino)ethanesulfonic acid (MES) buffer. Force curves were recorded with bare and HDT-coated tips as additional controls for force measurements.

6.3.5 Cell Probe Functionalisation

Atomic force microscope probes (CSC38 (B); Mikromasch, Portland, Oregon, USA) were functionalised with *S. epidermidis* according to [16]. Briefly, a custom triaxial micromanipulator was used to immerse the tip of the cantilever in a solution of 20 mM hexadecanethiol in ethanol. The cantilever was removed from the solution and allowed to dry for 5 min, and then immersed in a suspension of *S. epidermidis*, concentrated to an approximate cell density of $1x10^{11}$ cells $\cdot$ mL^{-1}. After an immersion time of 5 min, the cantilever was removed from suspension and allowed to dry for an additional 5 min to remove excess moisture. Cell attachment and orientation were verified by scanning electron microscopy (SEM), as well as by *in situ* force curve measurements on glass control substrata.

6.3.6 AFM Experiments

Each substrate was examined using an atomic force microscope (Dimension 3100 AFM with Nanoscope IIIa controller, Digital Instruments, Santa Barbara, CA). The AFM was calibrated according to manufacturer's specifications [24], as well as using the methods described in [8, 17, 39] to characterise the probe spring constant and piezoactuator travel distance.

Topographical images of each substrate were captured in contact mode at 25 μm^2 and 1 μm^2 scan areas with image resolution of 256x256 pixels using a bare silicon probe (CSC38 (B), Mikromasch, Portland, OR). Five images were captured for each sample at both scan sizes. Five control force cycles were captured at each 1 μm^2 area, at a scan rate of 1 Hz, nominal ramp size of 1000 nm and data resolution of 512 samples per curve.

Force cycles using the bacteria-functionalised probes were captured in contact mode using identical software parameters. The AFM was engaged in force mode to avoid raster-scanning of the surface, which may re-orient or dislodge the immobilised cell. Five cycles were captured for each of ten areas on each sample and analysed according to [15].

6.3.7 Force Cycle Analysis

For each sample, the location and magnitude of each of pull-off event was recorded, and processed separately to generate histogram data of percent normalised frequency against either the pull-off distance or force. This latter analysis is of interest, as it allows for direct comparison of the strength of the interactions as compared to the surface chemistry. Histograms for control and functionalised probe experiments are plotted simultaneously to demonstrate affinity differences between the bare silicon and cell probes. Each histogram data set was analysed in SigmaStat® v. 2.03 (Systat, Richmond, CA) using the Kruskal-Wallis One Way Analysis of Variance (ANOVA) on Ranks to determine statistical significance. Further, a multiple comparison test against a control group (Dunnetts' method) was performed on each set, compared to the SS data, to isolate differences between control and cell probe data.

6.3.8 Topographical Image Analysis

Root mean square roughness (R_q) calculations were performed for each sample using the AFM software (Nanoscope® v. 4.43r8, Digital Instruments) [24, 25]. The average and standard deviation of calculations for five images at each scan size was reported.

6.3.9 Theoretical Tensile Strength Modeling

Each topographical image was mapped at a variety of observational scales using SFrax™ (Surfract, Worcester, MA), following the theory developed by Brown *et al.* [6, 37], and described in Section 1.3.5. Briefly, patterning the image at some observational scale provides a total area, which is normalised to the projected surface area of the original image. SFrax™, by default, calculates the relative area at some five hundred scales. In a plot of relative area against scale, nonlinear features indicate scales at which the probe does not "see" surface texture. Conversely, linear features indicate surfaces which appear complex.

Plots of relative area against adhesive strength (defined, in this case, as the mean pull-off force of fifty AFM retraction curves for each substrate) are then generated for each observational scale, whereupon a linear regression is applied to the data. The regression coefficient, R^2, is recorded and plotted against observational scale for all measurements, yielding what is termed a Siegmann plot. Very high values of R^2 indicate observational scales at which the surface texture has significant influence over the adhesive strength. According to the Discrete Bonding Model (Section 1.3.5), the presence of a local maximum identifies the fundamental adhesive scale, which describes a necessary geometric characteristic of the surface without which adhesion cannot take place.

6.4 Results

6.4.1 Force Cycle Analysis

Cantilever spring constant values fell within the range of 0.036 ± 0.009 N $\cdot$ m^{-1}. Calibration of the piezoactuator correction factor yielded a value of 0.997 nm $\cdot$ nm^{-1}, indicating that the actual piezoactuator travel distance is less than that reported by the AFM software.

Example retraction curves for all substrates are shown in Figure 6.4.1. Adhesive force magnitudes range from 15 nN for TEG to 25 pN for IPA. Given the wide range of adhesion force magnitudes, the figure is shown in three parts to highlight the retraction profiles for all substrates. Force magnitudes of 50 pN or lower fall below the instrument noise level, and therefore do not represent an interaction that may be decoupled from the noise produced by the microscope equipment.

All retraction curves were analysed as described above, and the results are presented in histogram form in Figure 6.4.2. TEG and DDT display the most visible differences between the bacterial probe experiments and their associated controls. However, statistical analysis of the retraction data using the Kruskal-Wallis One Way ANOVA on Ranks shows statistically significant differences ($P < 0.001$) between all control/cell probe experiments. This indicates that the differences are greater than would be expected by chance or experimental error. Further, multiple comparison tests between the bacterial probe and control experiments demonstrate that there is a statistically significant difference ($P < 0.05$) between each control and cell probe pairing.

6.4.2 SAM Characterisation Results

Contact angle and ellipsometry results for all surfaces may be seen in Table 6.4.2. Results show that all species are hydrophobic to varying degrees. Specifically, Au, IPA, PLL100/10/1, and TEG, having $\theta_w = 30 - 60^o$ are moderately hydrophobic. IAG, PDT, and SS are hydrophobic ($\theta_w = 70 - 100^o$). BSA, DDT, and HDT10/20 are highly hydrophobic, having $\theta_w > 100^o$

Ellipsometry results show film thicknesses on the order of 1 nm, demonstrating that these molecules form monolayers on the gold substrate. The low standard deviation amongst

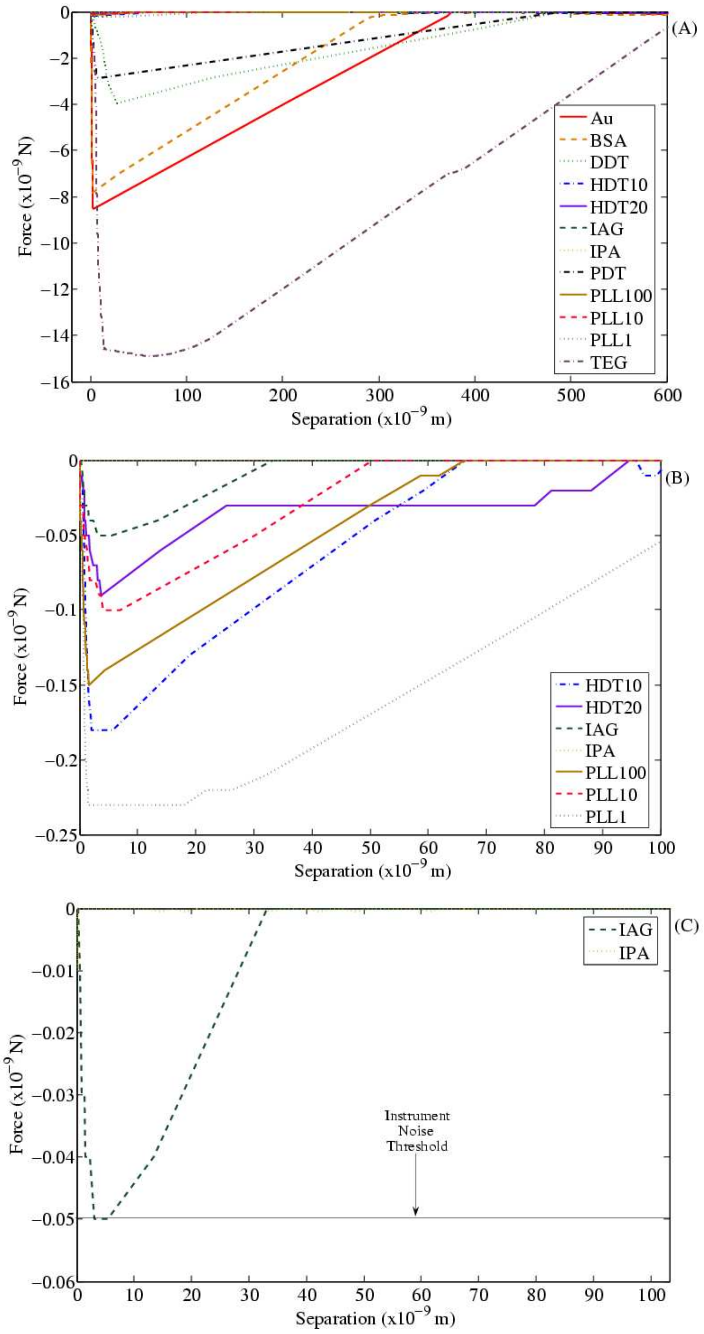

Figure 6.4.1: Example retraction curves for all substrates using a bacterial probe. (A)-(C) show the weaker forces, indicating which substrates have the lowest adhesion force magnitude. IPA and IAG appear at or below the instrument noise threshold, indicating that these surfaces interact more weakly than we are able to resolve with this instrument.

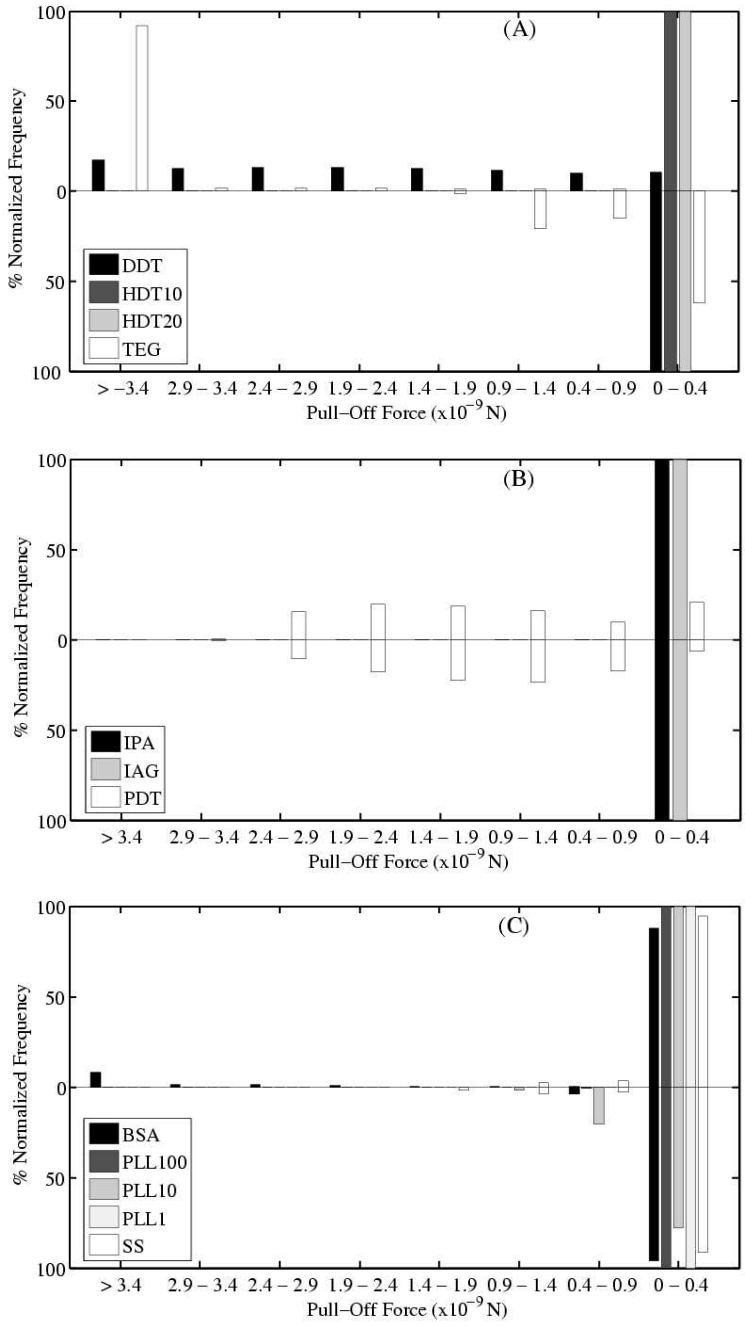

Figure 6.4.2: Pull-off force histograms for all chemical species, discretised into "Aliphatic," "Aromatic," and "Randomly-deposited" groups. Comparison of all groups according to the One Way ANOVA show a statistically significant difference between sampled populations ($P < 0.001$). Also, multiple comparison testing between control and bacterial probe experiments demonstrate statistically significant differences ($P < 0.05$) between the two sets of experiments.

Table 6.4.2: Experimental results of water contact angle, ellipsometric film thickness, root mean square roughness, and mean pull-off force for all experimental surfaces.

Sample	**Water Contact**[1] **Angle (°)**	**Film Thickness**[2] (nm)	$R_{q,25}$[3] nm	$R_{q,1}$[4] nm	Mean Pull-Off Force[5] nN
Au	76 ± 2	–[6]	1.68 ± 0.487	1.58 ± 0.879	11.6 ± 1.68
BSA	109 ± 3	–[7]	1.40 ± 0.849	1.25 ± 0.263	7.9 ± 1.40
DDT	105 ± 2	1.0 ± 0.2	1.11 ± 0.080	1.07 ± 0.660	4.7 ± 1.11
HDT10	114 ± 3	1.3 ± 0.2	0.70 ± 0.140	0.31 ± 0.060	0.2 ± 0.70
HDT20	108 ± 2	1.3 ± 0.2	0.10 ± 0.003	0.10 ± 0.020	0.1 ± 0.10
IPA	52 ± 3	1.2 ± 0.3	0.09 ± 0.010	0.09 ± 0.001	0.2 ± 0.09
IAG	74 ± 3	1.5 ± 0.3	1.24 ± 0.390	0.79 ± 0.170	0.2 ± 1.24
PDT	90 ± 3	1.3 ± 0.3	0.85 ± 0.080	0.47 ± 0.100	3.2 ± 0.85
PLL1	34 ± 3	–[7]	0.18 ± 0.120	0.17 ± 0.070	0.3 ± 2.17
PLL10	47 ± 3	–[7]	2.34 ± 0.290	1.02 ± 0.090	0.3 ± 2.34
PLL100	59 ± 3	–[7]	2.17 ± 0.630	1.12 ± 0.390	0.2 ± 0.79
SS	87 ± 2	–[6]	3.49 ± 0.750	1.26 ± 0.250	0.3 ± 0.01
TEG	55 ± 4	2.6 ± 0.3	0.79 ± 0.080	0.44 ± 0.090	18.0 ± 0.79

[1] Water contact angle; $N_D = 9$.

[2] Ellipsometric film thickness; $N_D = 9$.

[3] Root mean square roughness, Projected area = 25 μm^2; $N_D = 5$.

[4] Root mean square roughness, Projected area = 1 μm^2; $N_D = 5$.

[5] Mean pull-off force; $N_D = 50$.

[6] Film thicknesses were not measured for Au and SS, as both served as control surfaces for the subsequent experimentation.

[7] Film thicknesses for BSA and PLL were not calculated, as ellipsometry requires optical homogeneity, isotropism and negligible interactions between molecules. Since these molecules occur in a distribution of molecular weights, and can have significant intermolecular hydrogen bonding, ellipsometric results would not accurately represent these surfaces.

repeated measurements show that the layer is confluent across the surface. Measurements were not performed on the randomly deposited substrates, as we expect highly variable and non-reproducible results between multiple samples.

6.4.3 Topographical Image Analysis

Representative topographical images of all surfaces are shown in Figure 6.4.3. All images shown are 25 μm^2 in area, with 256x256 pixels per image. The maximum vertical scale on each image is 10 nm, with the exception of PLL10 and PLL1 (15 nm) and BSA (30 nm). Values of R_q for both areas are presented in Table 6.4.2.

6.4.4 Correlations to Adhesive Strength

Plots of R_q versus mean pull-off force are shown in Figure 6.4.4, with data sets discretised into the three physicochemical "families" described previously. Values were calculated for both 25 μm^2 and 1 μm^2 topographical images. Linear regression coefficients are also presented for each grouping and projected image area.

Plots of water contact angle versus mean pull-off force are shown in Figure 6.4.5, with data sets discretised into the three physicochemical "families" described previously. Linear regression coefficients are also presented for each grouping.

6.4.5 Theoretical Tensile Strength Modeling

Example relative area versus observational scale plots for all species are shown in Figure 6.4.6 for 25 μm^2 images, and Figure 6.4.7 for the 1 μm^2 images.

For several scales, plots of mean pull-off force against scale were generated (data not shown), and the correlation coefficients plotted against observational scale. The two scales are superimposed in Figure 6.4.8.

For the large scale analysis, a maximum value of $R^2 = 0.035$ is obtained at a scale of 2x10^{-4} μm^2. At the small scale, a local maximum of $R^2 = 0.125$ occurred at 3x10^{-6} μm^2, with a second global maximum of $R^2 = 0.25$ at 3x10^{-1} μm^2.

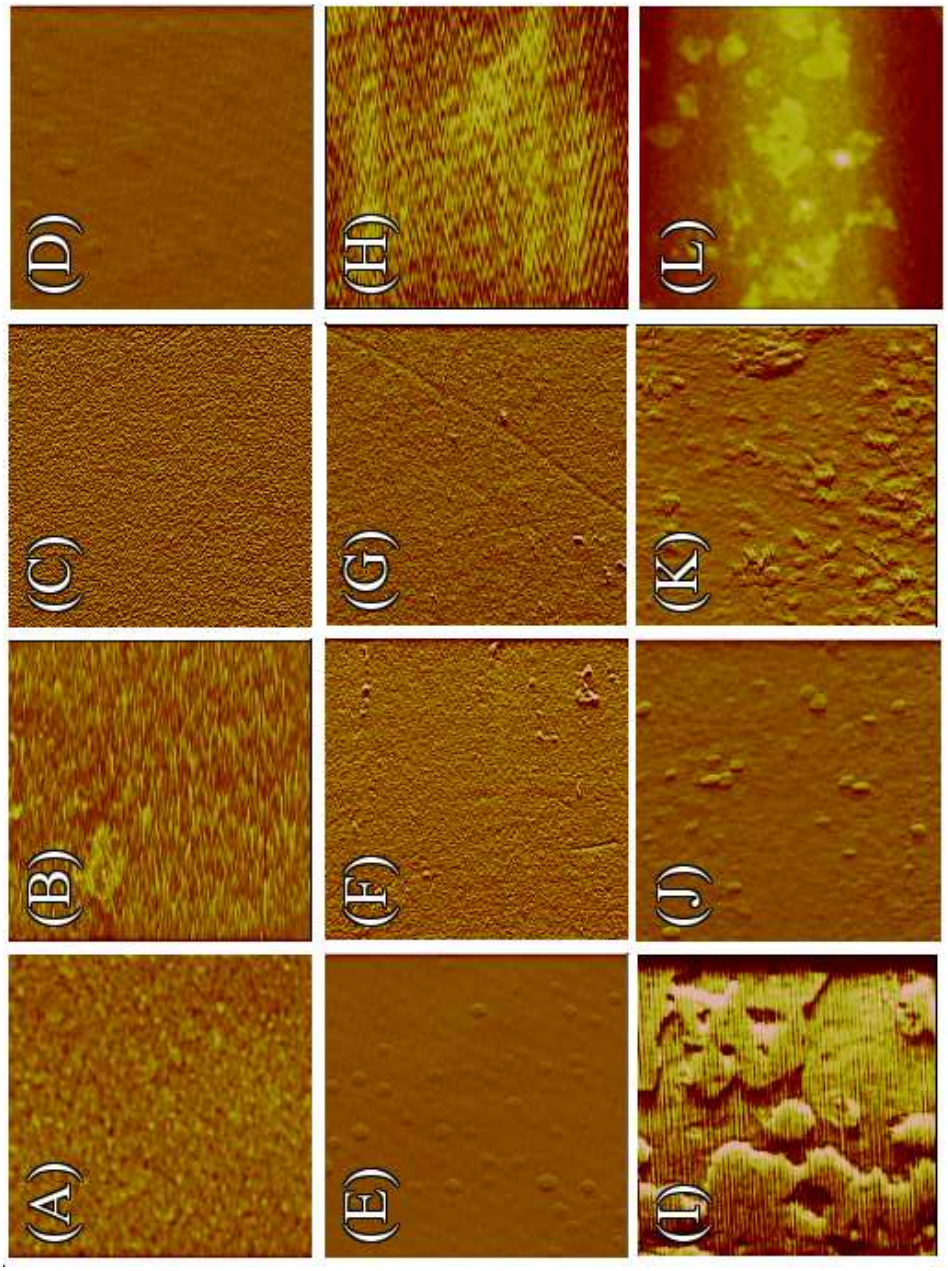

Figure 6.4.3: AFM topographies of all substrates. (A) Bare gold, (B) BSA, (C) DDT, (D) HDT10, (E) HDT20, (F) IAG, (G) IPA, (H) PDT, (I) PLL100, (J) PLL10, (K) PLL1, (L) TEG. All images are 25 μm^2 in scan area with 256x256 pixels per image.

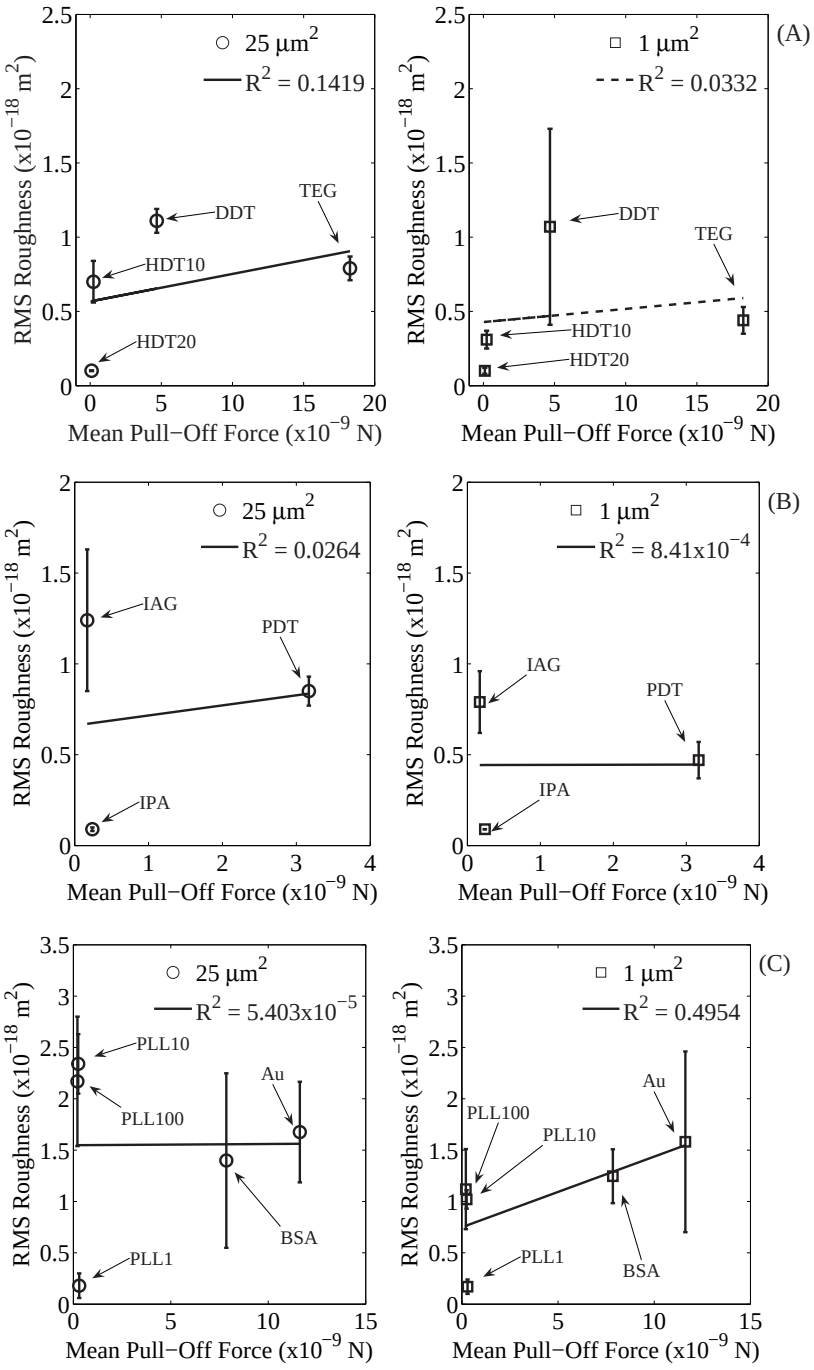

Figure 6.4.4: Plots of R_q versus mean pull-off force for aliphatic (A), aromatic (B) and randomly-deposited (C) species.

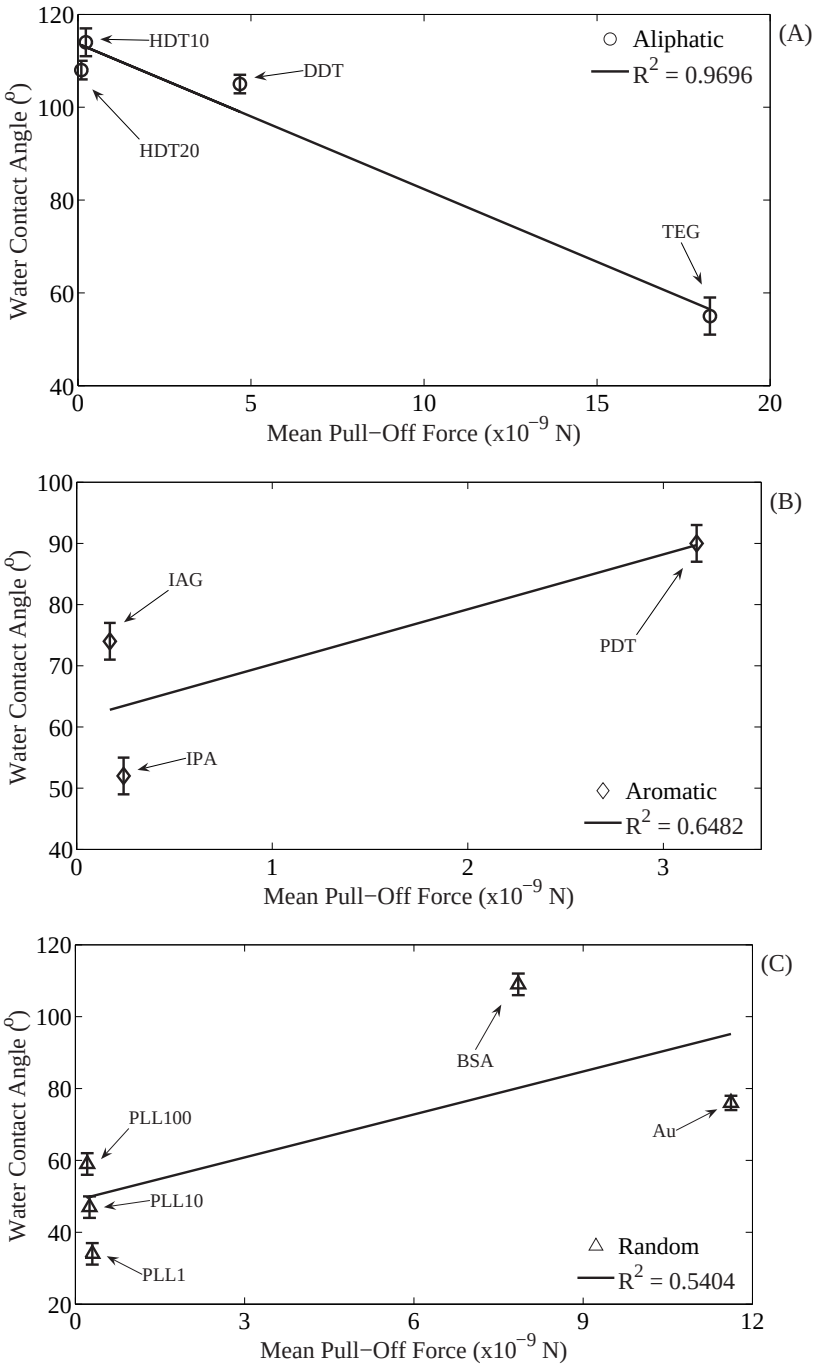

Figure 6.4.5: Plots of water contact angle versus mean pull-off force for aliphatic (A), aromatic (B) and randomly-deposited (C) species.

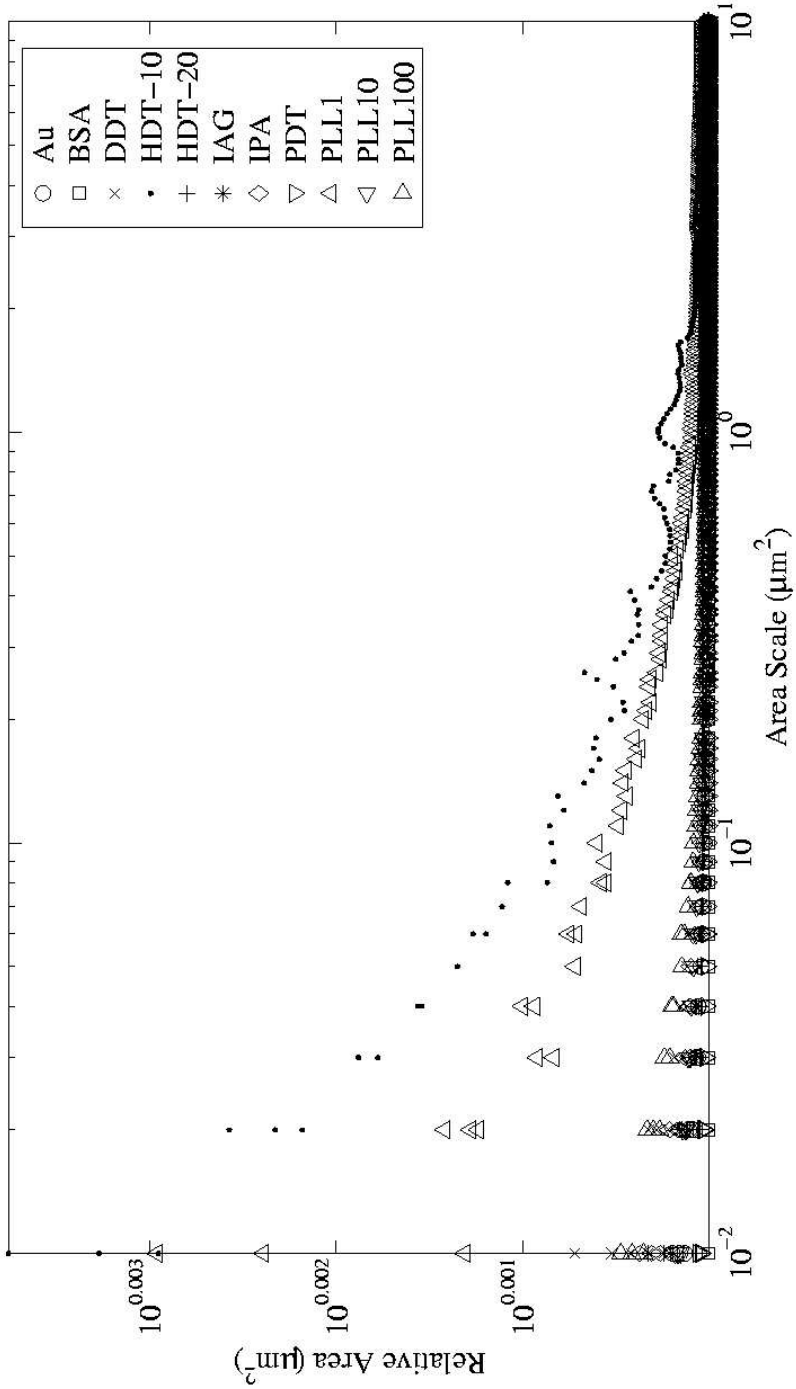

Figure 6.4.6: Relative area versus observational scale for 25 μm^2 images.

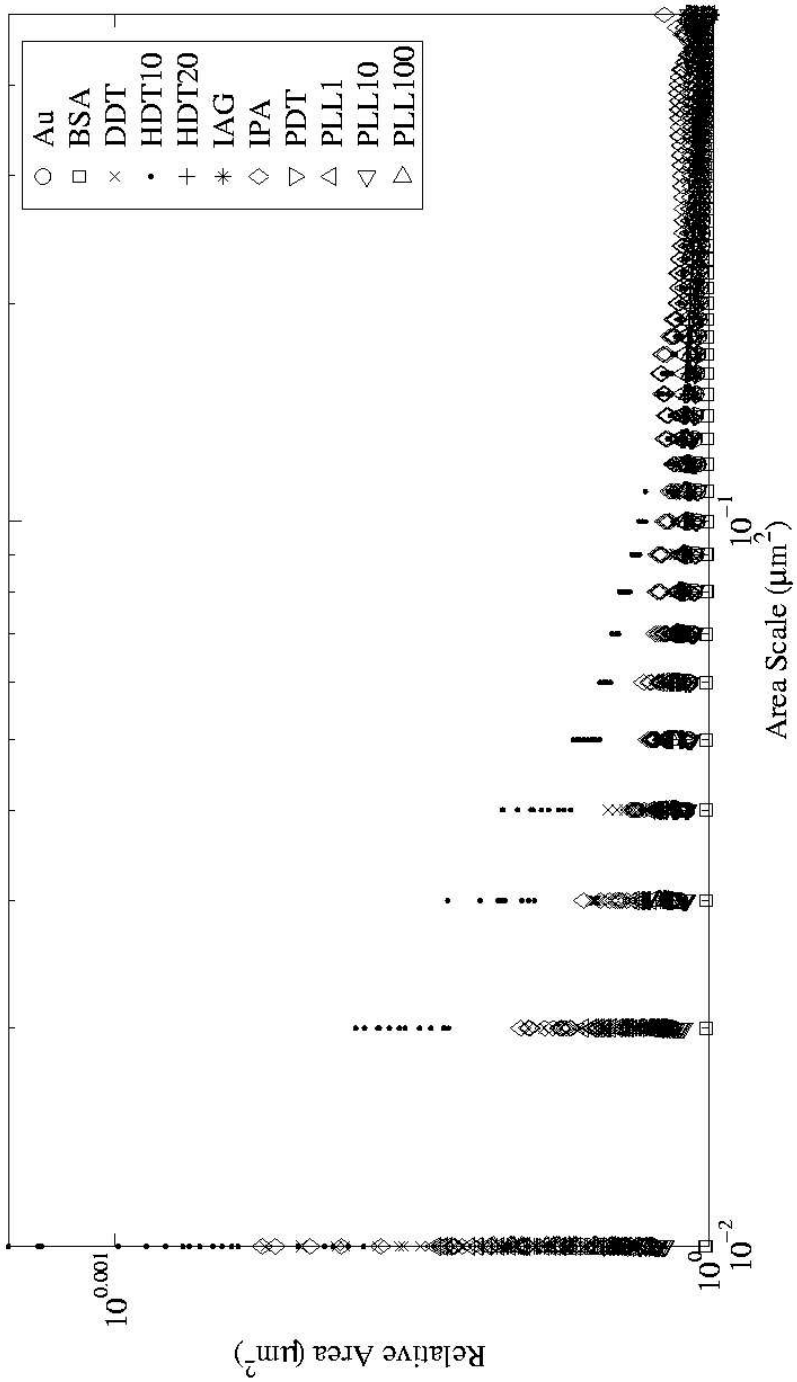

Figure 6.4.7: Relative area versus observational scale for 1 μm^2 images.

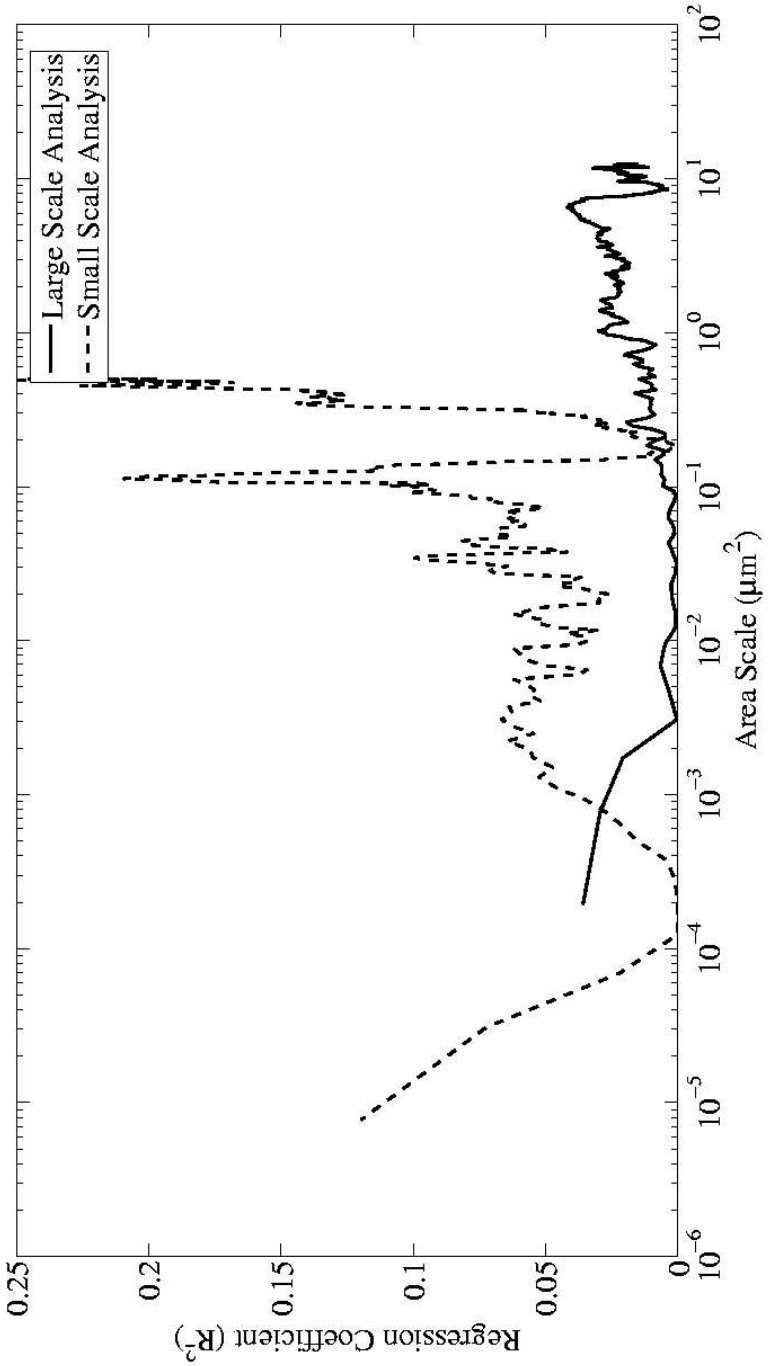

Figure 6.4.8: Siegmann plot showing regression coefficients versus observational scale for both projected areas.

6.5 Discussion

6.5.1 Applications of Conventional Correlation Parameters

Surface Roughness Correlation

Correlations between R_q and mean adhesive strength were poor, with significant weight placed on one or two data points in the regression. This may be explained by the fact that, although the surfaces were chemically unique, producing a range of adhesive strength spanning 18 nN, the calculated surface roughness varied by only 4.2 nm amongst all samples. Regressions plotted in the left column of Figure 6.4.4 show very weak relationships between the surface texture and adhesive strength ($R^2 \ll 20\%$). In order to better characterise the systems according to this parameter, it would be necessary to fill in the large gaps in data, particularly in the case of the Aliphatic grouping, where > 10 nN lies between the point describing DDT and that describing TEG.

These calculations also show scale dependence, in that changes in the projected area of the topographical image produce changes in the values of surface roughness. As the scan size is decreased from 25 μm^2 to 1 μm^2, the calculated values of R_q decrease in a disproportionate manner. While values for HDT20 and IPA remain essentially the same, values for all other substrates decrease by as little as 3.6% for DDT, and as much as 64% for SS. In comparing the two columns of Figure 6.4.4, we see the strongest correlation for the Aliphatic compounds at the larger resolution ($R^2 = 0.1419$), and the weakest for the Randomly Deposited compounds ($R^2 = 5.403x10^{-5}$). At the smaller resolution, the strongest correlation exists for the Randomly Deposited substrates ($R^2 = 0.4954$), and the weakest for the Aromatic surfaces ($R^2 = 8.41x10^{-4}$). Were the expression for R_q independent of the projected area of the image, the relationships amongst the various data groupings should remain the same.

These differences are due, in large part, to the resolution of the image, or, more fundamentally, the area represented by a single pixel in each image. At the larger resolution, one pixel has dimensions of 381.5 nm^2, while at the smaller resolution, the same pixel represents a projected area of 15.86 nm^2. This is a change of 95.8% in the surface area assigned to a single data point. As was described in the formulation for R_q in Equation 2.2, the value

of R_q is dependent upon the average height of the image, as well as the number of data points within the image. However, no corrections exist within this analytical expression to characterise the actual area described by each data point, meaning that each point has equal weight, regardless of the physical dimensions of that point. As such, if a researcher desired to compare the same surface at different area scales, the R_q parameter does not provide a valid correlation amongst the disparate data groupings.

Surface Wettability Correlation

As was the case for surface roughness, the correlation between water contact angle and adhesive strength is weak. While wettability can explain the variations in mean pull-off force to correlation coefficients of $R^2 > 0.50$, the regressions are often heavily weighted to the location of a single data point. For example, in Figure 6.4.5(A) and (B), the points representing TEG and PDT, respectively, highly influence the profile of the regression. Were those points absent, the fit would be significantly different. In fact, removing these outlying points, we see that the resulting regression would have slopes of infinity and close to zero, respectively. Such profiles, regardless of the value of the correlation coefficient, indicate no meaningful relationship between the parameters described by the data sets.

Similarly for Figure 6.4.5(C), were only the three points describing PLL considered, the linear regression would again have a slope approaching infinity, and that no meaningful correlation exists between wettability and adhesive strength. This may be explained by the non-confluent layers of PLL evident in AFM topographical images. In Figure 6.4.3(I-K), we see very uneven surface coverage by the PLL molecules, including features which may represent the tertiary structure of single poly-amino acids. This species exists in a range of molecular weights and spatial conformations, it is unlikely that any meaningful correlations may be established between the adhesive tensile strength and surface characterisation parameters.

Considering the procedure of measuring the contact angle itself, we again see a dependence upon the scale of the measurement. As was described in the Materials and Methods section, the angle was measured after 2 μL of water was placed atop each substrate sample. This represents a spherical volume having diameter 160 μm. As the contact angle increases,

the droplet radius also increases, and with it the total area of the water droplet in contact with the substrate. As such, each contact angle is measured at a different coverage area, and, therefore, represents the superposed interactions of widely different numbers of molecules. For the self-assembled monolayer surfaces, in which molecules are positioned approximately at the lattice points of the gold substrate, this describes an extremely large difference in the number of molecules leading to a contact angle of 10°, as opposed to the number of interactions giving a contact angle of 80°. Since the molecules making up each SAM are chemically unique, intermolecular forces will not be constant across a given area, inducing further differences in the interpretation of the contact angles of, for example, a straight-chain Aliphatic compound and a large, highly functionalised Aromatic compound. Should a researcher desire to compare a population of data taken on surfaces that possess significant chemical differences, the water contact angle measurement alone is not sufficient to fully characterise the surface properties of the substrate.

Summary

The above analyses show that the parameters most commonly used to characterise surfaces have very limited applicability in predicting the adhesive strength of a clinically relevant microbe to a surface. Most surprising amongst these results were those for TEG, which as a representation of poly(ethylene glycol), showed the highest adhesive strength. This material is extremely common in medical device manufacture [27, 28, 35], and is lauded for its biocompatibility, biostability, and resistance to microbial colonisation. The results described herein, however, contradict those findings. This may be explained by differences in adhesion geometry, in that previous research (*op. cit.*) could represent an interaction between the planktonic microbe and the chemically inactive ethylene glycol chain (*viz.*, the $-(CH_2-CH_2-O)-$ subunits), while our research demonstrates an interaction between the microbe and a reactive terminal hydroxyl group present as a result of incomplete polymerisation of the ethylene glycol monomer.

6.5.2 Application of the Discrete Bonding Model

Based on the *a priori* assumption that the texture of the surface will, to some extent, influence its adhesive characteristics, the Discrete Bonding Model was employed. By tiling the surface according to fractal theory, an accurate representation of the original surface is generated which is independent of the projected area of the original, and is, to some extent, decoupled from the image resolution. While providing clear theoretical benefits over the scale-sensitive roughness and water contact angle measurements, correlations still proved very weak in predicting the magnitude of the adhesive strength. As seen in the above characterisation techniques, regressions are highly dependent upon single points

The model has been applied, with excellent results, to characterise the surfaces of dinosaur skin imprints [3], chocolate cross-sections [32] and anthropological tooth samples [36]. In each case, however, these disparate applications required additional optimisation to accurately represent the surfaces. In the case of the anthropological samples (*op. cit.*), the teeth had been worn down over the course of thousands of years, yielding artificially smooth sample measurements. However, Brown *et al.* were able to improve the correlation by defining an importance coefficient, C_i, according to:

$$C_i = R_i^2 \frac{m_i}{m_{max}} \tag{6.1}$$

where R_i^2 is a single regression coefficient in the population, m_i is the slope of the regression associated with each R_i^2 value, and m_{max} is the maximum absolute slope of the entire population. Using C_i in lieu of R^2 for the Siegmann plot analysis amplified the data, allowing for significantly better correlations. Similar optimisation is likely necessary in the application of the model to microbial adhesion.

6.5.3 Criteria for Further Analysis

In addition to optimising the Discrete Bonding Model to better characterise the surface textures of this system, several other aspects of the project require additional analysis. For example, it is not yet clear if the population of images analysed ($N_D = 5$) is truly representative of the sample surface. Additional data would only serve to strengthen the

correlation in future analyses. Further, the wide variations in surface chemistry may lead to complications in interpreting the data as a whole. It would be beneficial to examine a simpler group of substrates, for example a series of alkanethiols differing only in the number of methylene groups in the chain, to truly determine the correlation parameters for adhesive strength, independent of the chemistry of the terminal group.

Additionally, more precise measurements of the adhesive strength may be necessary. While the value of the cantilever spring constant is acceptable, this value represents only a single aspect of an extremely complex interaction. Following the force balance methodology shown in Figure 5.1 of [9], it is possible to model the system during a pull-off event according to a series of springs, providing plastic and elastic resistance to linear displacement, and dashpots, which damp the velocity response of the spring as it returns to its equilibrium position, acting in series. This is theoretically similar to a door closer, where a spring provides the force necessary to close the door, and the dashpot slows the door so it does not slam.

In the system of a microbial cell tethered to an AFM tip, which serves to probe a SAM bound to a substrate material, the force balance during a pull-off event may be discretised into six individual contributions. This is shown diagramatically in Figure 6.5.1. At (A), we see the force of the cantilever acting on the tip; at (B), the force of the tip on the 1-hexadecanethiol tether; at (C), the force of the tether on the microbial cell wall; at (D), the force of the cell wall on an exopolymer; at (E), the force of the exopolymer on a SAM molecule; and, at (F), the force of the SAM molecule on the substrate. While complex in and of itself, this is a significant simplification of the system, as the tethers, exopolymers and SAM molecules are unlikely to interact on either individual or linear bases. Further, the internal structures of the cell wall, including the cytosol, cytoskeleton, organelles, and vacuole space, have been ignored. However, to obtain a true sense of the interaction force whilst using a cell probe, each of these contributions should be precisely characterised to determine their role in the total interaction.

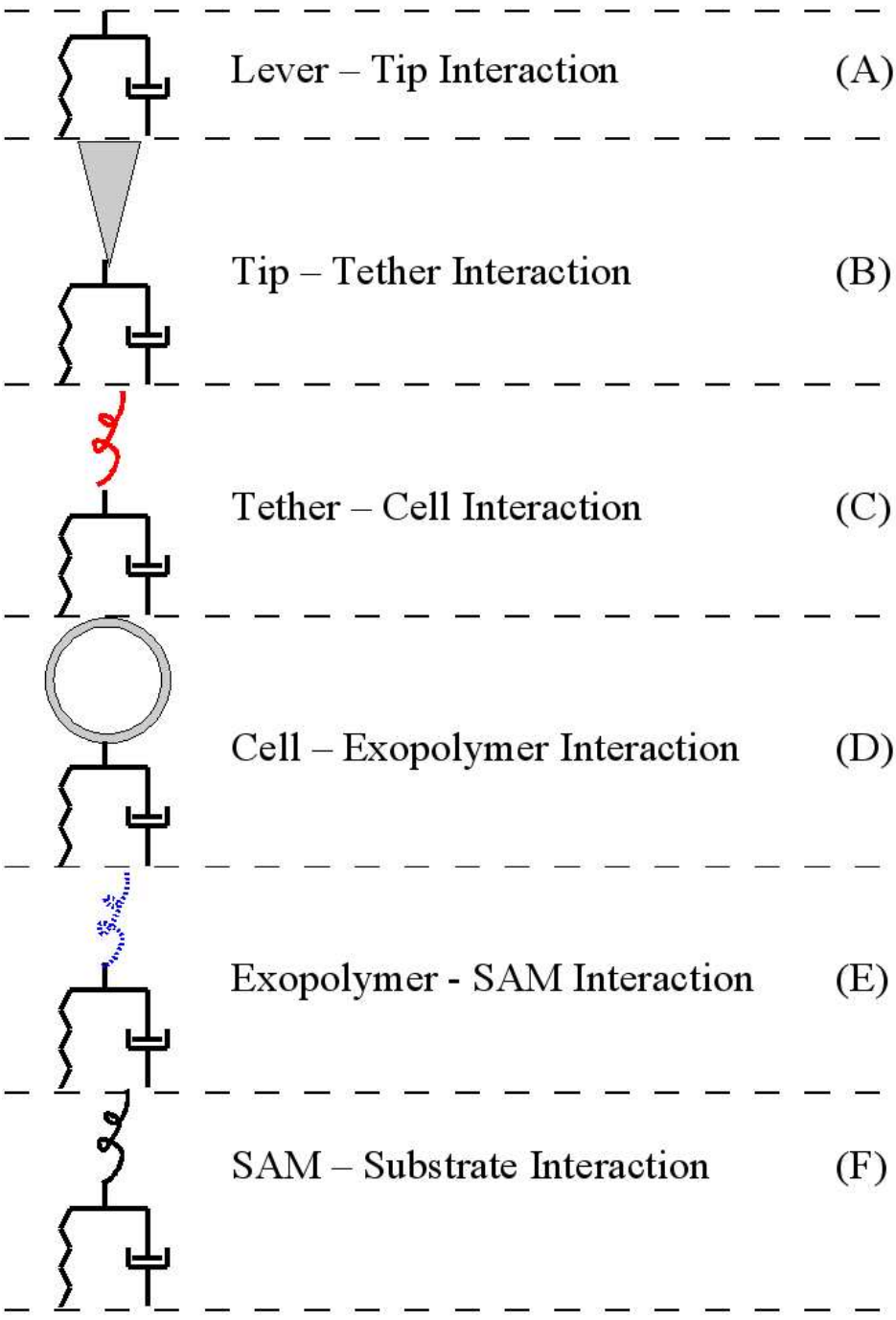

Figure 6.5.1: Diagramatic balance of all forces superposed while probing a SAM with a cell probe. (A) Cantilever - tip interaction; (B) Tip - tether interaction; (C) Tether - cell wall interaction; (D) Cell wall - exopolymer interaction; (E) Exopolymer - SAM interaction; (F) SAM - substrate interaction. This force balance illustrates the true complexity of the system under examination, and identifies possible points of error which may affect the quality of the adhesive force correlations.

6.6 Conclusions

In the context of microbial infections of medical devices, the two main topics to be considered are the adhesive properties of the microbe, followed by those of the device materials. Correlations amongst the adhesive strength of *Staphylococcus epidermidis* to a variety of surfaces to common methods of surface characterisation (*viz.*, surface wettability and root mean square surface roughness) were highly variable. For relatively simple aliphatic chains, water contact angle was an excellent predictor of adhesive strength. As the physicochemical complexity of the molecules increased, however, the correlation to surface wettability decreased significantly. For all materials, surface roughness had little to no influence over the adhesive characteristics. Application of a novel fractal-mapping technique shows promising preliminary results in better explaining the textural components necessary to promote or prevent microbial colonisation. This technique, however, requires additional analysis before any definitive conclusions may be reached.

6.7 Bibliography

[1] Y. H. An and R. J. Friedman. Concise review of mechanisms of bacterial adhesion to biomaterial surfaces. Journal of Biomedical Materials Research, 43:338–348, 1998.

[2] C. R. Arciola, D. Campoccia, S. Gamberini, M. E. Donati, and L. Montanaro. Presence of fibrinogen-binding adhesin gene in *Staphylococcus epidermidis* isolates from central venous catheter-associated and orthopaedic implant-associated infections. Biomaterials, 25:4825–4829, 2004.

[3] K. Articus, C. A. Brown, and K. P. Wilhelm. Scale-sensitive fractal analysis using the patchwork method for the assessment of skin roughness. Skin Research and Technology, 7:164–167, 2001.

[4] C. M. L. Bollen, W. Papaioanno, J. van Eldere, E. Schepers, M. Quirynen, and D. van Steenberghe. The influence of abutment surface roughness on plaque accumulation and peri-implant mucositis. Clinical Oral Implants Research, 7:201–211, 1996.

[5] R. Bos, H. C. van der Mei, and H. J. Busscher. Physico-chemistry of initial microbial adhesive interaction - its mechanisms and methods for study. FEMS Microbiology Reviews, 23:179–230, 1999.

[6] C. A. Brown. Scale-area analysis and roughness: a method for understanding the topographic component of adhesive strength. In K. M. Liechti, editor, Seventeenth Annual Meeting and the Symposium on Particle Adhesion, pages 5–7, Orlando, FL, February, 1994. The Adhesion Society.

[7] C. A. Brown and S. Siegmann. Fundamental scales of adhesion and area-scale fractal analysis. International Journal of Machine Tools and Manufacture, 41:1927–1933, 2001.

[8] N. A. Burnham, X. Chen, C. S. Hodges, G. A. Matei, E. J. Thoreson, C. J. Roberts, M. C. Davies, and S. J. B. Tendler. Comparison of calibration methods for atomic-force microscopy cantilevers. Nanotechnology, 14:1–6, 2003.

[9] N. A. Burnham and A. J. Kulik. Surface Forces and Adhesion. In B. Bhushan, editor, Handbook of Micro/Nano Tribology, pages 247–271. CRC Press, Boca Raton, 2nd edition, 1999.

[10] H. J. Busscher, H. Bialkowska-Hobrzanska, G. Reid, M. van der Kuijl-Booij, and H. C. van der Mei. Physicochemical characteristics of two pairs of coagulase-negative staphylococcal isolates with different plasmid profiles. Colloids and Surfaces B: Biointerfaces, 2:73–82, 1994.

[11] H.-J. Butt, M. Kappl, H. Mueller, R. Paiteri, W. Meyer, and J. Ruhe. Steric forces measured with the atomic force microscope at various temperatures. Langmuir, 15:2559–2565, 1999.

[12] L. Correa and D. Pittet. Problems and solutions in hospital-acquired bacteræmia. Journal of Hospital Infection, 46:89–95, 2000.

[13] J. W. Costerton, Z. Lewandowski, D. E. Caldwell, D. R. Korber, and H. M. Lappin-Scott. Microbial biofilms. Annual Reviews in Microbiology, 49:711–745, 1995.

[14] B. V. Derjaguin and L. Landau. Theory of the stability of strongly charged lyophobic sols and the adhesion of strongly charged particles in solutions of electrolytes. Acta Physicochimica (URSS), 14:633–662, 1941.

[15] R. J. Emerson. Microbial Adhesion to Medical Implant Materials: An Atomic Force Microscopy Study. Master's Thesis, Biological Interaction Forces Lab, Department of Chemical Engineering, Worcester Polytechnic Institute, 2004.

[16] R. J. Emerson and T. A. Camesano. A nanoscale investigation of pathogenic microbial adhesion to a biomaterial. Applied and Environmental Microbiology, 70(10):6012–6022, 2004.

[17] R. J. Emerson and T. A. Camesano. On the importance of precise calibration techniques for an atomic force microscope. Ultramicroscopy, 106(4-5):413–422, 2006.

[18] J. P. Folkers, P. E. Laibinis, and G. M. Whitesides. Self-assembled monolayers of alkanethiols on gold: Comparisons of monolayers containing mixtures of short- and

long-chain constituents with CH_3 and CH_2OH terminal groups. Langmuir, 8:1330–1341, 1992.

[19] A. G. Gristina. Biomaterial-centered infection: Microbial adhesion versus tissue integration. Science, 237:1588–95, 1987.

[20] N. J. Hallab, K. J. Bundy, K. O'Connor, R. L. Moses, and J. J. Jacobs. Evaluation of metallic and polymeric biomaterial surface energy and surface roughness characteristics for directed cell adhesion. Tissue Engineering, 7:55–71, 2001.

[21] S. O. Heard. Catheter-related infection: Diagnosis, prevention and treatment. Annals of the Academy of Medicine Singapore, 30:419–429, 2001.

[22] A. H. Hogt, J. Dankert, J. A. de Vries, and J. Feijen. Adhesion of coagulase-negative staphylococci to biomaterials. Journal of General Microbiology, 129:1959–1968, 1983.

[23] J. Hu and M. A. Fox. A convenient trimethylsilylthioxy-dehalogenation reaction for the preparation of functionalized thiols. Journal of Organic Chemistry, 64:4959–4961, 1999.

[24] Digital Instruments. Dimension 3100 Manual Ver. 4.43b. Technical report, Veeco Metrology Group, 1997.

[25] Digital Instruments. Scanning Probe Microscopy Training Notebook. Technical report, Veeco Metrology Group, 1998.

[26] N. Khardori and M. Yassien. Biofilms in device-related infection. Journal of Industrial Microbiology, 15:141–147, 1995.

[27] P. Kingshott, J. Wei, D. Bagge-Ravn, N. Gadegaard, and L. Gram. Covalent attachment of poly(ethylene glycol) to surfaces, critical for reducing bacterial adhesion. Langmuir, 19:6912–6921, 2003.

[28] H. J. Lee, K. D. Park, H. D. Park, W. K. Lee, D. K. Han, S. H. Kim, and Y. H. Kim. Platelet and bacterial repellence on sulfonated poly(ethylene glycol)-acrylate copolymer surfaces. Colloids and Surfaces B: Biointerfaces, 18:355–370, 2000.

[29] E. W. McAllister, L. C. Carey, P. G. Brady, R. Heller, and S. G. Kovacs. The role of polymeric surface smoothness of biliary stents in bacterial adhesion, biofilm deposition, and stent occlusion. Gastrointestinal Endoscopy, 39:422–425, 1993.

[30] M. A. Ordal, L. L. Long, R. J. Bell, S. E. Bell, R. R. Bell, R. W. Alexander Jr., and C. A. Ward. Optical properties of the metals aluminum, cobalt, copper, gold, iron, lead, nickel, palladium, platinum, silver, titanium and tungsten in the infrared and far infrared. Applied Optics, 22:1099–1119, 1983.

[31] C. Pale-Grosdemange, E. S. Simon, K. L. Prime, and G. M. Whitesides. Formation of self-assembled monolayers by chemisorption of derivatives of oligo(ethylene glycol) of structure $HS(CH_2)_{11}(OCH_2CH_2)_mOH$ on gold. Journal of the American Chemical Society, 113:12–20, 1991.

[32] F. Pedreschi, J. M. Aguilera, and C. A. Brown. Characterization of the surface properties of chocolate using scale-sensitive fractal analysis. International Journal of Food Properties, 5(3):523–535, 2002.

[33] M. Quirynen and C. M. Bollen. The influence of surface roughness and surface-free energy on supra- and subgingival plaque formation in man. Journal of Clinical Periodontology, 22(1):1–14, 1995.

[34] M. Quirynen, H. C. van der Mei, C. M. L. Bollen, Schotte A., Marechal M., Doornbusch G. I., Naert I., Busscher H. J., and van Steenberghe D. An *in vivo* study of the influence of the surface roughness of implants on the microbiology of supra- and subgingival plaque. Journal of Dental Research, 72:1304–1309, 1993.

[35] A. Razatos, Y.-L. Ong, F. Boulay, D. L. Elbert, J. A. Hubbell, M. M. Sharma, and G. Georgiou. Force measurements between bacteria and poly(ethylene glycol)-coated surfaces. Langmuir, 16:9155–9158, 2000.

[36] R. S. Scott, P. S. Ungar, T. S. Bergstrom, C. A. Brown, F. E. Grine, M. F. Teaford, and A. Walker. Dental microwear texture analysis within-species diet variability in fossil hominins. Nature, 436(4):693–695, 2005.

[37] S. Siegmann and C. A. Brown. Surface texture correlations with tensile adhesive strength of thermally sprayed coatings using area-scale fractal analysis. In E. Lugschneider and P.A. Kammer, editors, United Thermal Spray Conference - Proceedings DVS Verlag, Düsseldorf, Germany, 1999.

[38] E. R. Soto, J. C. MacDonald, C. G. F. Cooper, and W. G. McGimpsey. A non-covalent strategy for the assembly of supramolecular photocurrent-generating systems. Journal of the American Chemical Society, 125:2838–2839, 2003.

[39] E. J. Thoreson and N. A. Burnham. Standard-deviation minimization for calibrating the radii of spheres attached to AFM cantilevers. Review of Scientific Instruments, 75:1359–1362, 2004.

[40] V. Vadillo-Rodriguez, H. J. Busscher, W. Norde, J. de Vries, and H. C. van der Mei. On relations between microscopic and macroscopic physicochemical properties of bacterial cell surfaces: An AFM study on *Streptococcus mitis* strains. Langmuir, 19:2372–2377, 2003.

[41] C. J. van Oss. Interfacial Forces in Aqueous Media. Marcel Dekker, Inc., New York, NY, 1994.

[42] E. J. Verwey and J. T. G. Overbeek. Theory of the Stability of Lyophobic Colloids. Elsevier, Amsterdam, 1948.

[43] W. W. Wilson, M. M. Wade, C. Holman, and R. F. Champlin. Status of methods for assessing bacterial cell surface charge properties based on zeta potential measurements. Journal of Microbiological Methods, 43:153–164, 2001.

CHAPTER 7

Identification of the Point of Zero Separation in Microbial AFM Force Cycles

7.1 Abstract

Microbial adhesion to surfaces is mediated by the polymeric structures protruding from the cell wall into the bulk phase, often leading to biofilm-related infections of medical implant devices and biofouling of industrial equipment. The chemical, physical and mechanical properties of these external polymers have often been characterised through the acquisition and analysis of force-separation curves using atomic force microscopy (AFM). In the case of purely repulsive interactions on approach, however, analysis of these data has been hindered by the lack of a well-defined point of zero separation in the system. Many previous analyses have defined the point of zero separation as the external surface of the cell wall, and assumed the constant compliance region of the approach curve is representative of that

point. Data sets defined according to this methodology may be further processed using a steric model describing interactions arising from the compression of the polymer brush, allowing for the deduction of such parameters as the equilibrium length of the polymer brush and the two-dimensional grafting density of the polymers at the cell wall. In this work, we show that the constant compliance region is not representative of the microbial cell wall and that the mesh density (a three-dimensional parameter) is a more appropriate parameter for characterising the energy within the polymer brush. Further, we introduce a mathematical analysis technique by which the point of zero separation may be accurately quantified. For the specific case of *Pseudomonas aeruginosa*, a common biomedical and environmental isolate, evidence suggests the presence of two distinct polymer layers within the brush, having equilibrium thicknesses of 160 ± 8 nm and 1700 ± 400 nm and respective mesh densities of 0.19 ± 0.01 nm^{-3} and (7 ± 2) x 10^{-5} nm^{-3}. Using this technique, it is now possible to accurately quantify the point of zero separation in microbial AFM force-separation curves.

7.2 Introduction

Since its introduction in 1986, the atomic force microscope (AFM) [6] has shown exceptional applicability and adaptability to a wide range of experimental systems. While specifically designed for applications in the semiconductor and electronics industries, the AFM has also seen extensive use in the fields of biotechnology and microbiology. Several examples of these applications include: the measurement of atomic bond rupture-forces between organosilane monolayers [31]; the study of the physicochemical properties of microbial surface topographies [15]; characterisation of lectin-carbohydrate interactions at the nanometer scale [27]; measurement of interaction forces between complementary DNA strands [19]; and characterisation of bacterial-biomaterial interactions via mechanically or chemically modified probes [23–25].

The mechanical behaviour of the AFM has also been rigorously studied, most especially for its capability of measuring local mechanical properties (*viz.*, elastic modulus, hardness) as derived from force or deflection curves [1, 8, 18, 26]. In these latter cases, an omnipresent feature of the collected data has been an attraction in the approaching portion of the force cycle. After baselining the data, this appears as a region of negative force. Such data sets have been rigorously studied to determine the physical interpretation of this point, several theories of which are reviewed in [9]. From this work, it has been determined that the local minimum of the attractive event, which represents the point at which all force gradients acting on the cantilever sum to zero, is near to and commonly used to define the point of zero separation, *viz.*, the sample surface. This provides a very clear and precise reference point for downstream data processing.

In many microbiological and polymer systems, however, attractive events are not present [2, 20, 30]. This has been attributed to the steric forces exerted by the microbial polymer brush, normal to the substrate (*viz.*, a binding platform or the microbial cell wall), which screen the short-separation attractive events that allow for the straightforward processing of the data [10, 11]. These steric forces have been modeled mathematically, generating information regarding the equilibrium length and grafting density of the polymer brush [10, 11]. Their application, however, has been limited to describing data sets that have

already been completely processed.

Generally, three methodologies exist for the processing of approach curves lacking attractive minima. The first, employed by Dufrêne *et al.* [14,29], simply plots the force relative to the piezoactuator displacement, without defining the point of zero separation. This methodology is straightforward, but does not give any true sense of the magnitude of the polymer brush interactions relevant to microbial system.

The second, described by Ducker *et al.* [13], defines the point of zero separation by aligning the region of stiff contact of the approach curve to the vertical axis. This region describes the points within the measurement where cantilever deflection is equal to the displacement of the piezoactuator tube. For rigid samples, where sample indentation is negligible, the stiff contact region proceeds directly from the point of interaction. However, for soft samples where indentation may not be ignored, this procedure can significantly overestimate the value of force at zero separation. Conversely, in systems coated with a polymer brush, the point of zero separation may never be reached, leading to a very large underestimation of the force at zero separation.

Finally, Li and Logan [20] proposed a quantitative method of approach curve analysis. Briefly, the data in the approach curve are combined according to a four-term moving average. As described in their manuscript (*op. cit.*), plotting this "deflection gradient" against piezoactuator displacement reveals four phases, which describe, in order of increasing displacement: the non-interaction phase (far from the surface); the non-contact phase (interacting with, but not touching, the surface; includes electrostatic and steric interactions); the contact phase (touching and indenting the sample surface or probe); and the constant compliance phase (no sample indentation; deflection is due solely to piezoactuator displacement). This was the first model to attempt a mathematical treatment of repulsive approach curves, but does include several weaknesses.

Primarily, there is a loss of data resolution on averaging the data points, coupled with the justification of choosing four points for all systems. This choice is not explained in the manuscript, nor are the ramifications of choosing a larger or smaller number of data points for the analysis. The assumption of no sample indentation in the constant compliance (stiff contact) phase requires that the influence of the piezoactuator on the cantilever be subtracted

to make this phase vertical. This results in non-constant spacing between data points, with the greatest variability in those areas close to zero separation. Following from this, each point in the deflection gradient represents a different displacement magnitude. Additionally, significant noise artifacts exist in the region close to the sample surface, making an accurate determination of the point of zero separation difficult.

Returning to the steric model developed in [10], which was based on the work of Alexander [5] and de Gennes [12], it is possible to utilise a linearised version of their basic equation to define the point of zero separation. The polymer steric model is defined according to:

$$F(h) = 50 k_B T a_p L \Gamma^{\frac{3}{2}} \exp\left[-\frac{2\pi h}{L}\right] \tag{7.1}$$

where k_B is the Boltzmann constant, T is the absolute temperature, a_p is the radius of curvature of the probe, L is the equilibrium polymer brush length, and $\Gamma^{\frac{3}{2}}$ describes the volume density of polymers, as defined by the two-dimensional polymer grafting density at the point of zero separation. This last parameter has theoretical and practical limitations, and will be discussed in greater detail below.

This model was derived to account for both the increase in osmotic pressure within the polymer brush, and the increase in elastic energy of the brush as it is compressed by the probe. Butt's energy term, $k_B T \Gamma^{\frac{3}{2}}$, describes an energy per unit volume as deduced from the spacing of the polymers at their insertion point at the cell wall. Based on this definition, the steric model allows for interactions between adjacent polymers only, but precludes any inherent flexibility or meshing of the individual molecules. The fractional power of this quantity, while satisfying the dimensional requirements of the model, significantly limits the physical relevance of the parameter.

As such, we will make two modifications to the steric model: First, we will replace the quantity $\Gamma^{\frac{3}{2}}$ with Ξ, the mesh density of polymers in the brush, which is defined according to

$$\Xi \equiv \frac{1}{\xi^3} \tag{7.2}$$

where ξ is the mesh spacing, or the distance separating interacting polymers in the brush

at equilibrium conditions. This affords two theoretical benefits: Namely that Ξ does not require postulation regarding substrate properties, which cannot be reached by the probe, and allows the polymers to flex and interact with one another, and with themselves, as the brush is compressed.

Second, the model will be linearised by taking the natural logarithm of both sides of the equation. This will allow for straightforward identification of any region(s) of interest, as, in a semilogarithmic plane, the exponential term(s) will have a linear profile. This formulation will also allow for the amplification of relatively small interaction forces which may not be apparent in rectilinear coordinates.

Additionally, recorded data suggest the presence of a low-density outer polymer layer of relatively large thickness, and a shorter, high-density layer. The model will be formulated to represent the collected data, although no supporting evidence exists to verify the presence of this outer layer.

7.3 Materials and Methods

7.3.1 Microbial Growth and Storage

Lyophilized samples of *P. aeruginosa* (ATCC 10145) were acquired from the American Type Culture Collection (Manassas, VA, USA). *P. aeruginosa* was maintained on Tryptic Soy Agar (Sigma) plates, and grown in Tryptic Soy Broth (Sigma). All plates were recultured every 14 d. Cells were incubated for 12 h at 25 °C on a radially oriented tube-rotator (Glas-Col) in 25 mL vented tissue culture flasks (VWR) at approximately 75 RPM. Cells were then transferred to 50 mL of fresh liquid growth media and grown in an orbital shaker bath (Lab-Line) at 37 °C and relative centripetal force of 0.45 x g until late exponential growth phase ($[O.D._{600}] = 0.5 \pm 0.05$).

7.3.2 AFM Sample Preparation

Cell cultures were imaged with a Dimension 3100 atomic force microscope with Nanoscope® IIIa controller (Digital Instruments, Santa Barbara, CA) to establish cell morphology and record interaction forces with silicon cantilevers (CSC38(B), Mikromasch) with spring constants of 0.040 ± 0.001 N $\cdot$ m^{-1}, calculated according to [7,17]. Cantilevers were placed tips-up in the bottom half of clean Petri dishes and left under UV light for 5 min to remove any adsorbed water and/or hydrocarbons.

Prior to AFM analysis, cells were bound to cleaned glass slides [11]. In a Petri dish, 1 mL of hexadecanethiol was pipetted over each slide and placed in a laminar flow hood to dry for 10 min. While the slides dried, 30 mL of cell culture was divided between two centrifuge tubes and wrapped in Parafilm^{TM} to prevent leakage. Tubes were centrifuged at a relative centripetal force of 1390 x g for 15 minutes, after which time the supernatant was eluted and replaced with a like volume of 0.1 M 2-(N-Morpholino)ethanesulfonic acid (MES) buffer (Aldrich) at pH = 7.1. Tubes were vortexed to resuspend the cell pellets, and the contents were poured over the dry glass slides. The Petri dish was then covered and placed on a shaker table for 20 min to allow the cells to adhere.

After 20 min, the slides were placed on filter paper to remove excess liquid. Slides were affixed to the AFM stage using double-sided carbon tape, and the AFM was configured for

contact mode in liquid per the manufacturer's instructions. Upon locating and centering a cell in the capture field, five force cycles per cell were recorded for analysis.

7.3.3 Removal of Noise Artifacts

In the following, we will be attempting to analyse a series of extremely small signals. As such, instrument noise and interference artifacts will likely have a significant influence upon the profile of the data. Noise sources may arise from extraneous light from the laser diode spilling over the edges of the cantilever, which may reflect into the detector, light present in the experimental chamber, vibrational noise from the instrument or propagating through the AFM air table, mechanical instabilities in the cantilever, or thermal fluctuations within the experimental system.

To account for these influences, all data sets will be fitted with an offset sine wave prior to treatment with the modified steric model, according to:

$$F(h) = P_A sin\left(\frac{\pi}{P_B}h - P_C\right) + P_D \tag{7.3}$$

where P_A represents the amplitude of the interference, P_B is related to the period of the interference, P_C describes the phase offset, and P_D is a vertical offset. These four parameters are used to fit the quasi-horizontal portion of the approach curve at large separations, removing noise artifacts that may exist in this region.

7.3.4 Model Derivation

Collected data suggest the presence of two discrete polymer brushes of differing thicknesses and densities. Therefore, in this model, we will account for interactions between a bare AFM tip of paraboloid geometry interacting with a polymer brush having two distinct physical regions. This is shown schematically in Figure 7.3.1. In Figure 7.3.2, the two polymer regions described in Figure 7.3.1 are shown in the context of an AFM approach curve. Plotting the data in semilogarithmic coordinates, it is possible to see the two linear regions, denoted as "Polymer Region 1" and "Polymer Region 2," which represent the two distinct polymer brushes suggested by the raw AFM data. Additional regions within the approach curve

include:

Zero Interaction Region / Instrument Noise Level: At large separations, where the probe does not contact the substrate, instrument noise is the dominant contribution to the data set.

Polymer Region 2: At some point in the approach, the probe contacts the outer of the two polymer brushes, resulting in a vertical deflection of the cantilever and, therefore, a repulsive force.

Polymer Region 1 / Transition Point: At another point, the inner polymer brush begins to dominate the interaction profile, yielding an inflection at the Transition Point, followed by a slope of greater magnitude.

Constant Compliance: When the tip reaches a point within the brush where the tip-sample interaction is much more rigid than the cantilever, there is a linear relationship between force and separation, as the surface cannot be indented, and cantilever deflection is identical to piezoactuator displacement to within the detection limits of the instrument.

Tip "Rolling": As the tip loading force is further increased as the piezoactuator displaces, a "rolling" artifact is displayed, as the cantilever bends due to in-plane forces acting on the tip. This arises from the non-zero angle of repose of the cantilever.

Photodiode Saturation: Finally, when the deflection of the cantilever reaches the upper limit of the detectable range, the photodetector is saturated, yielding a horizontal force-separation (or deflection-displacement) response.

In this case, the model is formulated in terms of two limit functions, one of which describes the region where the brush has thickness of L_1 and mesh spacing of ξ_1, and the other describes the brush having thickness and mesh spacing L_2 and ξ_2, respectively.

Assuming the AFM probe has a paraboloid profile, we may express its differential area as:

$$dA_t = 2\pi a_p d\eta \tag{7.4}$$

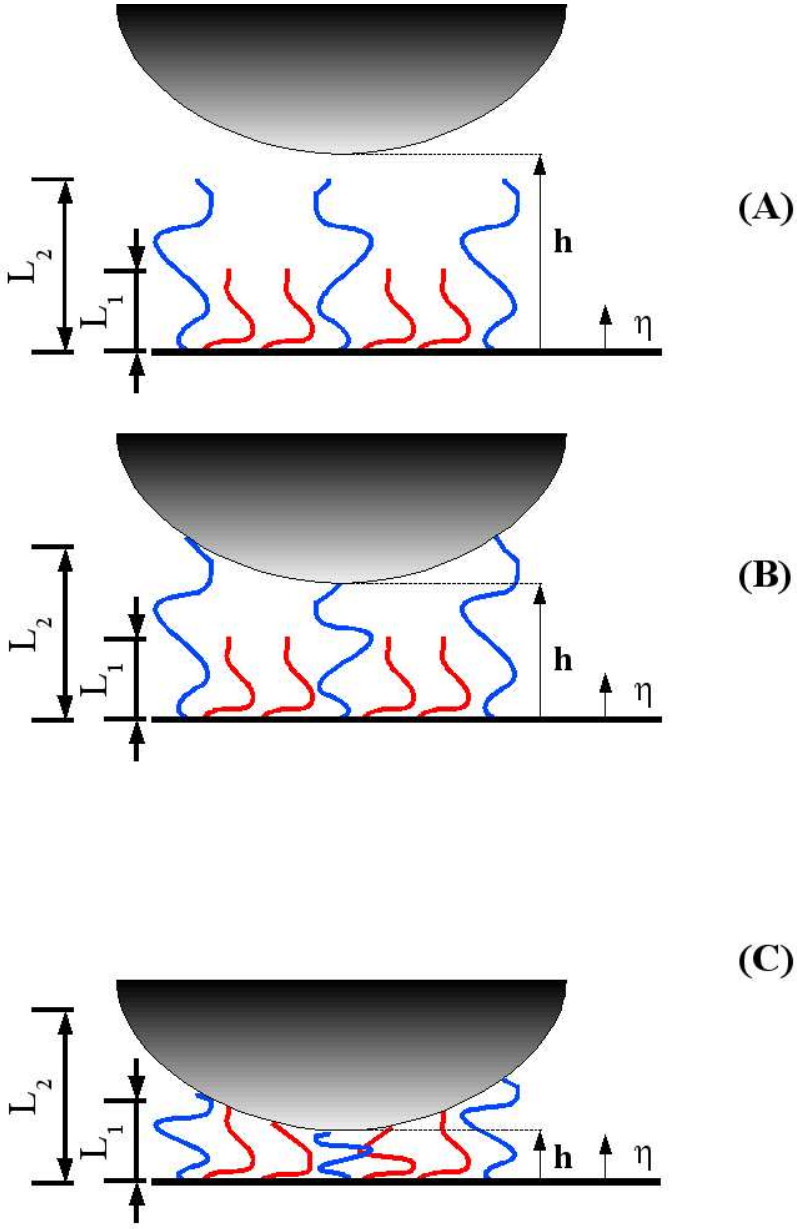

Figure 7.3.1: Schematic of a bare AFM tip interacting with a brush having two distinct regions. At (A), the tip does not interact with either region, allowing for the determination of a zero of force. At (B), the tip begins to compress the outer region, having equilibrium thickness of L_2 and mesh spacing ξ_2. At (C), the tip compresses the inner region, having equilibrium thickness of L_1 and mesh spacing ξ_1. Within this second region, cantilever deflection is dominated by the polymers of length L_1, and the contribution of polymers of length L_2 to the deflection profile is a constant, as described in the model derivation.

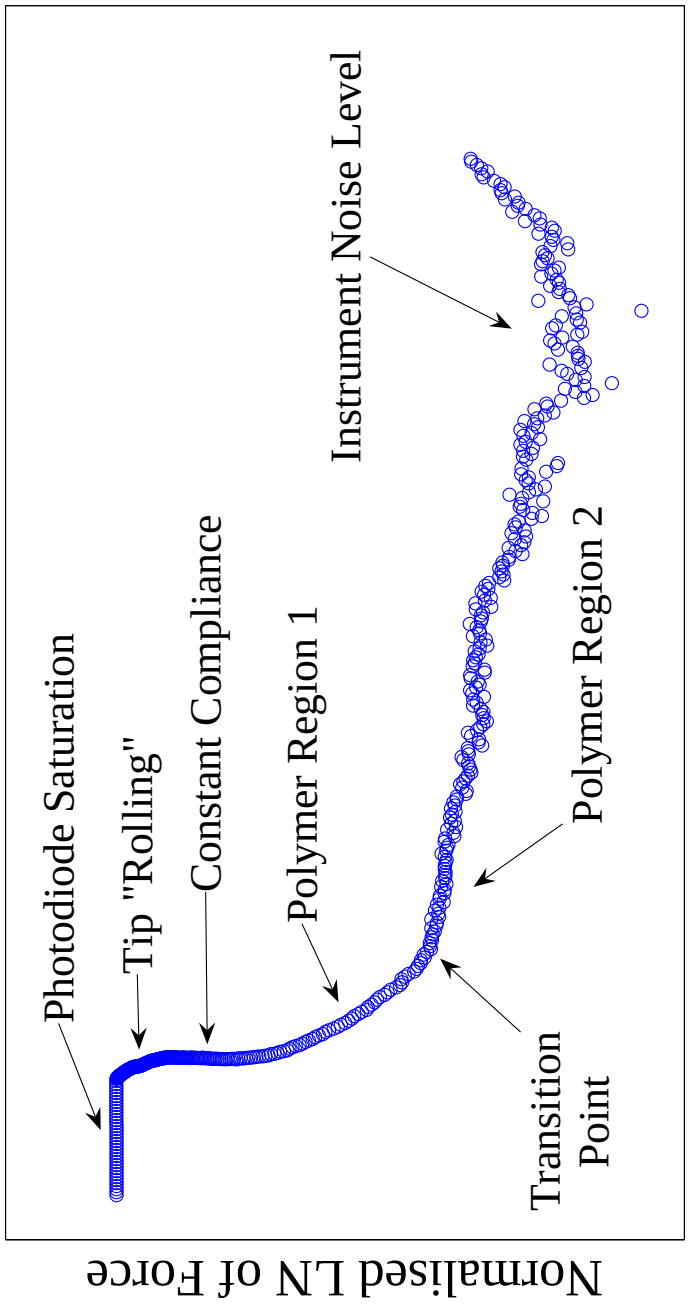

Figure 7.3.2: AFM approach curve displaying the origins of the interaction forces. The regions attributable to interactions with the microbial polymer brush(es) will appear as linear segments in semilogarithmic coordinates.

where dA_t is the differential area in contact with the brush, a_p is the radius of curvature of the probe, and $d\eta$ is the differential separation coordinate.

Beginning with de Gennes' expression for the energy per volume of the polymer brush in the region dominated by L_2 interactions, and integrating across the region from $h \rightarrow L_2$,

$$\frac{\text{energy}}{\text{volume}} = 100\frac{k_BT}{\xi_2^3}\exp\left[-\frac{2\pi}{L_2}\eta\right] \tag{7.5}$$

$$F(h) = 100\frac{k_BT}{\xi_2^3}\int_h^{L_2}\exp\left[-\frac{2\pi}{L_2}\eta\right]dA_t \tag{7.6}$$

where $F(h)$ defines the force at separation h, and all other quantities are defined as above.

Substituting in the definition of dA_t and integrating,

$$F(h)\big|_{L_1\leq h\leq L_2} = 100\frac{k_BT}{\xi_2^3}a_pL_2\left[\exp\left[-\frac{2\pi}{L_2}h\right] - \exp\left[-2\pi\right]\right] \tag{7.7}$$

This second exponential term is of negligible magnitude ($\exp(-2\pi) \approx 0.002$), and will be ignored, leaving the limit function for the thicker polymer brush as:

$$F(h)\big|_{L_1\leq h\leq L_2} = 100\frac{k_BT}{\xi_2^3}a_pL_2\ \exp\left[-\frac{2\pi}{L_2}h\right] \tag{7.8}$$

Similarly for the shorter-brush limit,

$$F(h)\big|_{0\leq h\leq L_1} = 100\frac{k_BT}{\xi_1^3}a_pL_1\ \exp\left[-\frac{2\pi}{L_1}h\right] \tag{7.9}$$

For convenience, the pre-exponential factors of Equations 7.8 and 7.9 are defined according to,

$$F_{L_1}(0) \equiv 100\frac{k_BT}{\xi_1^3}a_pL_1 \tag{7.10}$$

$$F_{L_2}(0) \equiv 100\frac{k_BT}{\xi_2^3}a_pL_2 \tag{7.11}$$

yielding the following:

$$F(h)\big|_{0\leq h\leq L_1} = F_{L_1}(0)\ \exp\left[-\frac{2\pi}{L_1}h\right] \tag{7.12}$$

$$F(h)\big|_{L_1\leq h\leq L_2} = F_{L_2}(0)\ \exp\left[-\frac{2\pi}{L_2}h\right] \tag{7.13}$$

Since the signals to be analysed are very small, Equations 7.12 and 7.13 are linearised by taking the natural logarithm, according to:

$$\ln\left[F(h)\big|_{0\leq h\leq L_1}\right] = \ln\left[F_{L_1}(0)\right] - \frac{2\pi}{L_1}h \quad \Rightarrow \ln\left[\frac{F(h)\big|_{0\leq h\leq L_1}}{F_{L_1}(0)}\right] = -\frac{2\pi}{L_1}h \tag{7.14}$$

$$\ln\left[F(h)\big|_{L_1\leq h\leq L_2}\right] = \ln\left[F_{L_2}(0)\right] - \frac{2\pi}{L_2}h \quad \Rightarrow \ln\left[\frac{F(h)\big|_{L_1\leq h\leq L_2}}{F_{L_2}(0)}\right] = -\frac{2\pi}{L_2}h \tag{7.15}$$

Now, by plotting the natural logarithm of the force against the separation coordinate, the length of each polymer brush may be calculated from slope of the linear segments in the plot.

Continuity at the Layer Boundary

For the above formulation to be valid, there must be continuity at the boundary $h = L_1$. Substituting this value into Equations 7.14 and 7.15 and rearranging,

$$F\left(L_1\right)\big|_{0\leq h\leq L_1} = F_{L_1}(0)\ \exp\left[-2\pi\right] \tag{7.16}$$

$$F\left(L_1\right)\big|_{L_1\leq h\leq L_2} = F_{L_2}(0)\ \exp\left[-2\pi\frac{L_1}{L_2}\right] \tag{7.17}$$

Equating these expressions and solving for $F_{L_2}(0)$,

$$F_{L_2}(0) = F_{L_1}(0)\exp\left[-2\pi\left(1-\frac{L_1}{L_2}\right)\right] \tag{7.18}$$

We know that the functions described in Equations 7.16 and 7.17 will intersect at the boundary, $h = L_1$. Substituting this value into Equation 7.16, we see that, in a plot of $\ln\left[\frac{F(h)}{F_{L_1}(0)}\right]$ versus h, this intersection will occur at -2π.

7.3.5 Solution Algorithm

Custom Matlab® scripts were written to automate the data analysis procedure, and to apply the model described above. The algorithm followed by these scripts allows for the transformation of the data set into semilogarithmic coordinates, followed by calculation of the two slopes described by Equations 7.14 and 7.15, by linear least-squares regression of the two limit regions. Data are then offset such that the intersection of the two limit functions rests at $(L_1, \ -2\pi)$ in the semilogarithmic plane.

The values of ξ_1 and ξ_2 are calculated from linear least-squares regression of the offset data, such that the y-intercepts of the regression functions represent the natural logarithm of $F_{L_1}(0)$ and $F_{L_2}(0)$. These force values proceed directly into the values of the mesh spacing, according to Equations 7.10 and 7.11.

7.3.6 Statistical Uncertainty Analysis

Statistical significance of the calculated results was determined using SigmaStat® v. 2.03 (Systat, Richmond, CA) using the Kruskal-Wallis One Way Analysis of Variance (ANOVA) on Ranks. Data will be analysed according to three forms: 1) Multiple calculations using the same data set, 2) multiple data sets recorded from a single cell (same location), and 3) individual data sets from multiple cells. Results were considered statistically significant if the probability coefficient, P, had a value ≤ 0.001.

7.4 Results

7.4.1 Raw AFM Data Sets

An example data set of a force-displacement curve taken on *P. aeruginosa* may be seen in Figure 7.4.1. As described previously, the approach curve does not display any attractive interactions to be used in defining the point of zero separation. The corrected data set, which has been processed to display the data as a function of tip-sample separation, is shown in Figure 7.4.2. The inset of this figure identifies a noise artifact at large displacement values, which must be characterised and subtracted before further data analysis.

7.4.2 Removal of Noise Artifacts

A plot of a typical noise profile may be seen in Figure 7.4.3. Choosing a point within the interference pattern, the data are fitted via least squares regression to Equation 7.3. Regression results are then subtracted from the original data set, leaving a filtered set for additional processing.

7.4.3 Model Fit Results

As can be seen in Figure 7.4.4, the large-separation interaction displayed by taking the natural logarithm of the raw data set (Figure 7.4.2) may be attributed to optical interference. While significant noise does still exist at separations > 600 nm, the two linear regions corresponding to the model developed in the previous section are evident. Plots of the two limit functions describing these regions are shown in Figure 7.4.5, with the intersection of the two functions resting at $(L_1,\ -2\pi)$. This intersection defines the point of zero separation for the system, assuming that the microbial cell wall is not deformed by the forces induced upon it by the AFM probe.

Results from the model fit may be seen in Table 7.4.1.

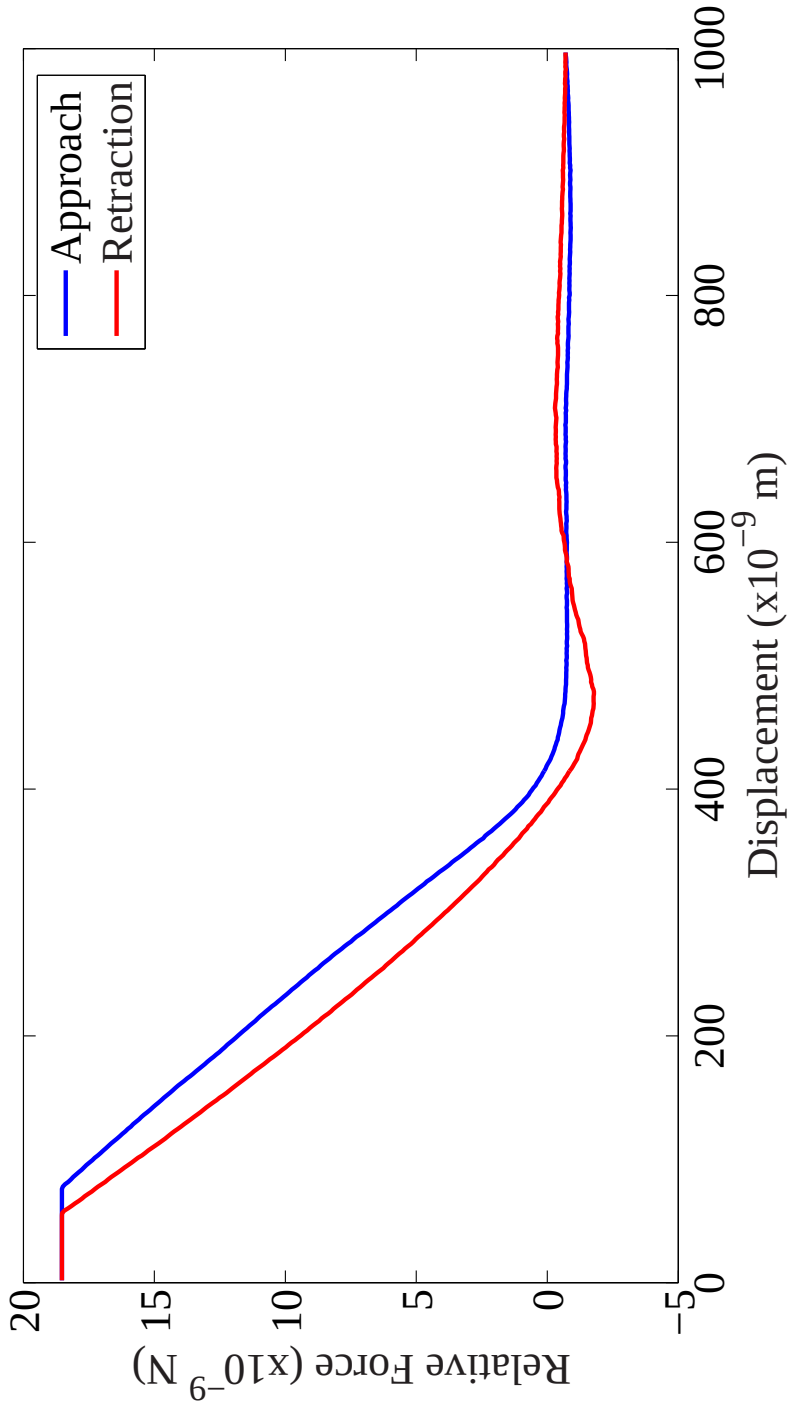

Figure 7.4.1: Example force cycle for *Pseudomonas aeruginosa*. As described previously, the approach curve, which is normally used to define the point of zero separation, does not exhibit any attractive behaviour.

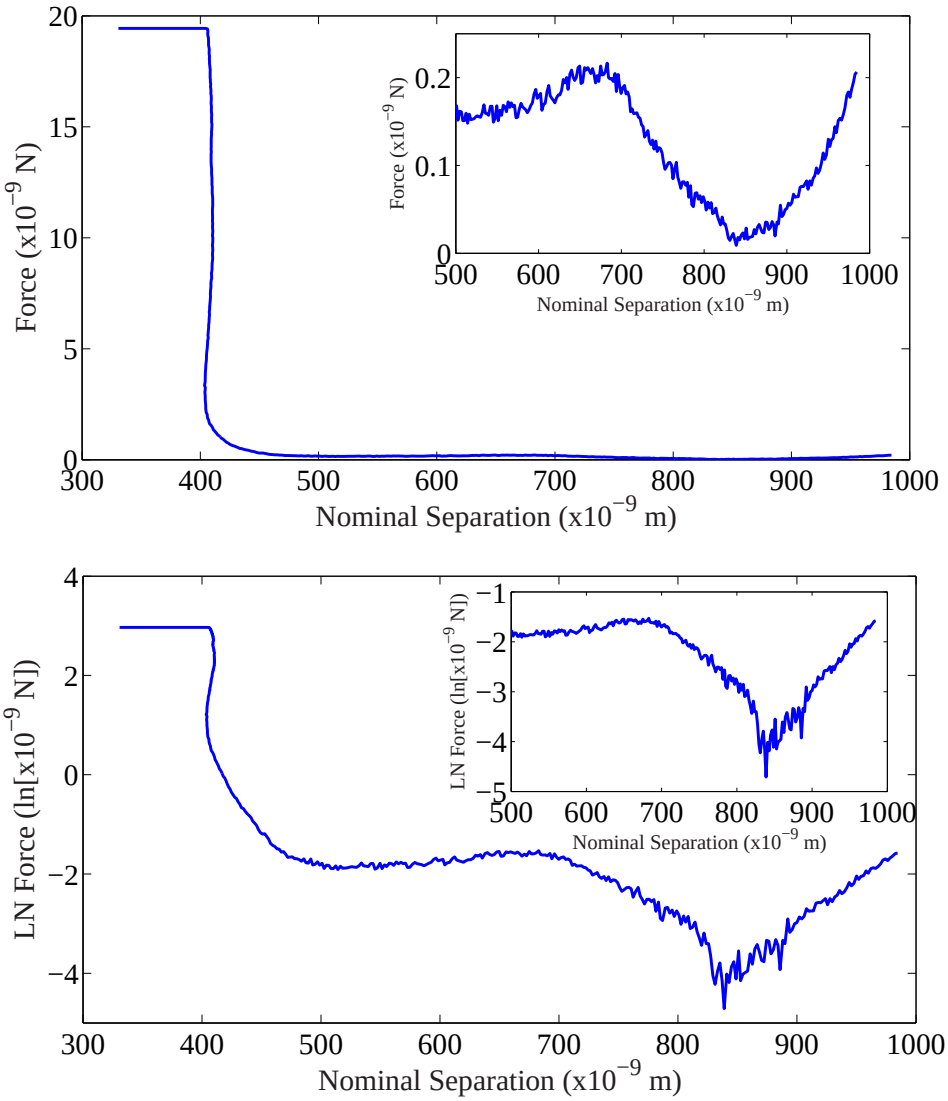

Figure 7.4.2: Example approach curve for *Pseudomonas aeruginosa* in rectilinear and semilogarithmic coordinates. The inset figure in the upper plot shows a periodic interference pattern existing at very small force magnitude ($<$ 0.25 nN). A "knee" exists at $\approx 700 - 850$ nm, which may describe a long-range interaction. The data must first be filtered to remove optical interference artifacts, however, before attempting to analyse this region.

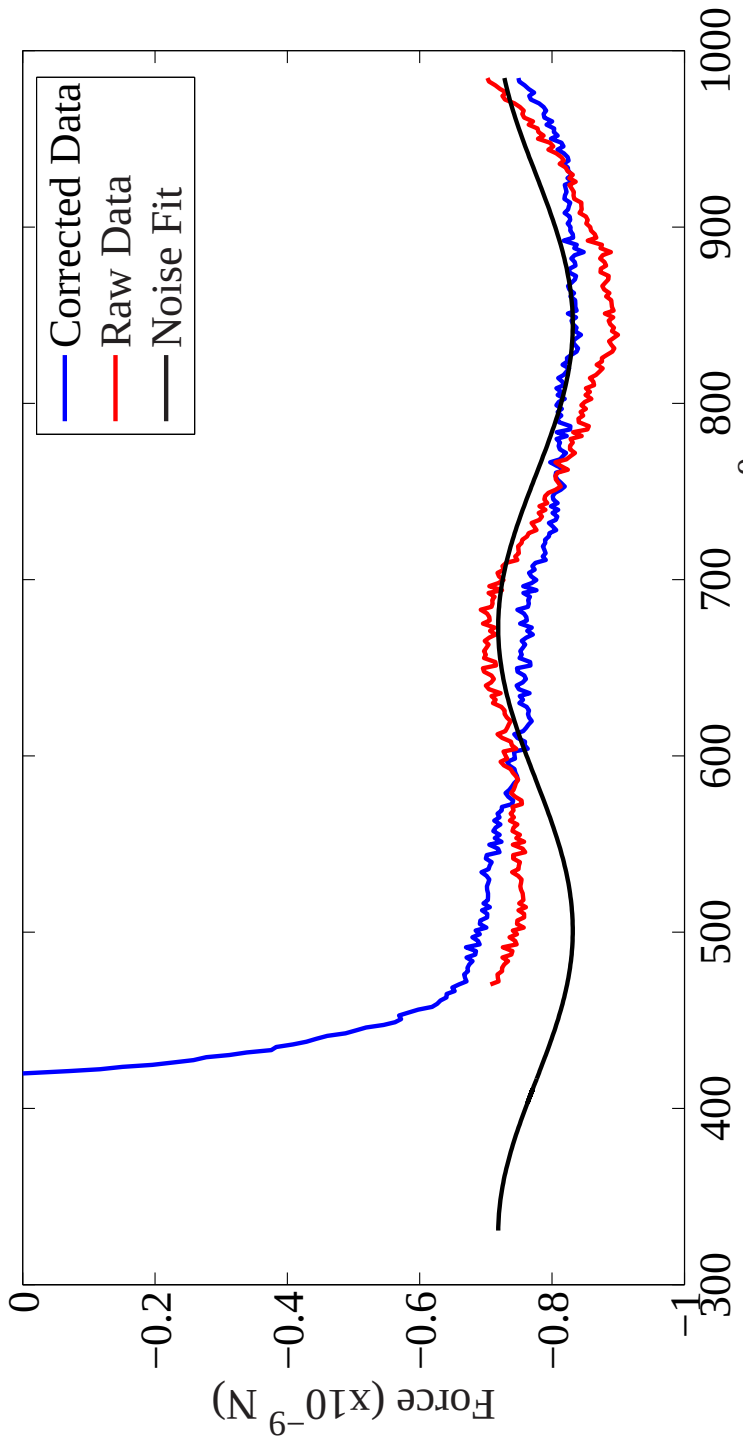

Figure 7.4.3: Example interference filtration according to Equation 7.3. Data (red) are fitted with the equation (black), results of which are subtracted from the raw data set, leaving a filtered force profile (blue).

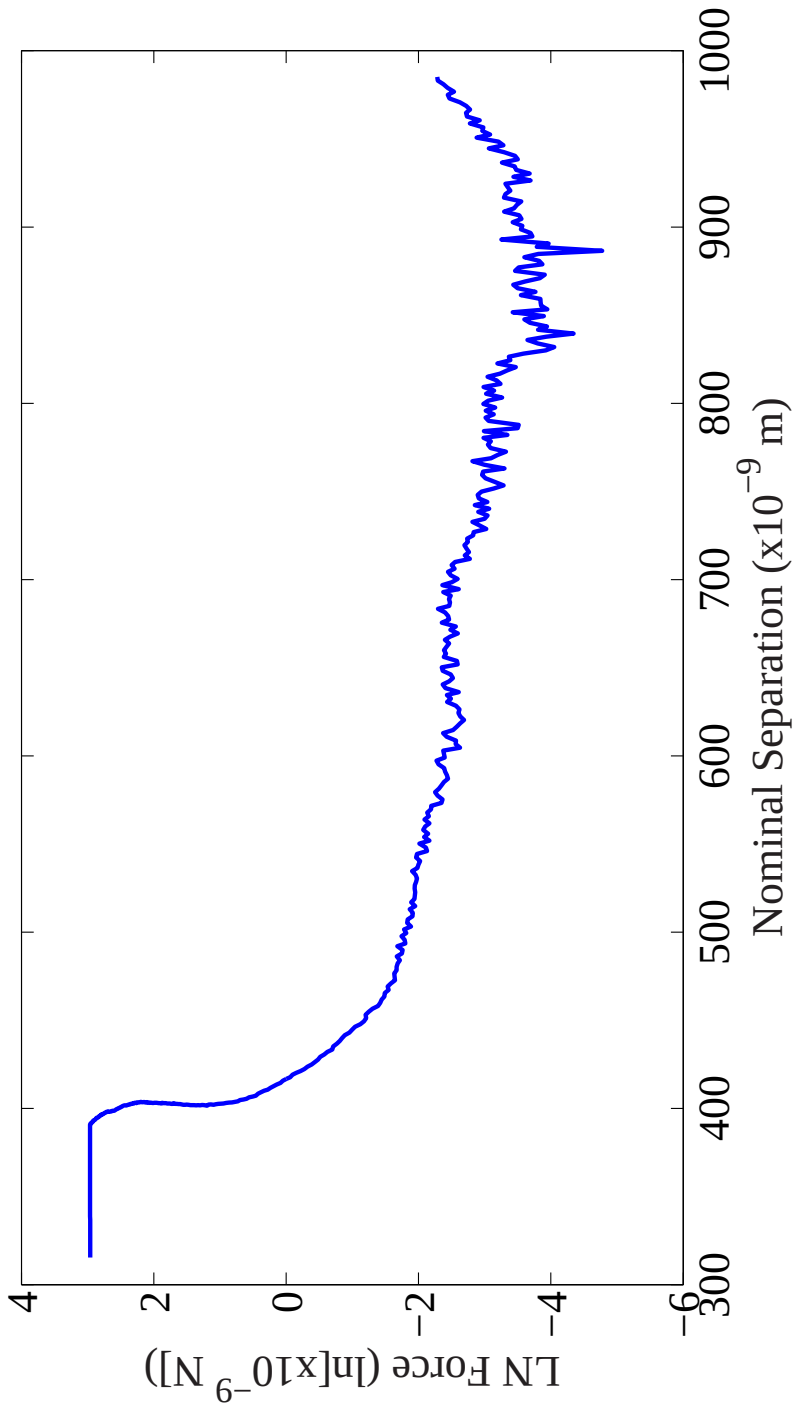

Figure 7.4.4: Example filtered data set in semilogarithmic coordinates. The "knee" region shown in the lower inset of Figure 7.4.2 is now absent after the removal of optical interference artifacts. Two unique linear regions are now evident prior to the constant compliance region. These regions are used in subsequent analysis to identify the point of zero separation.

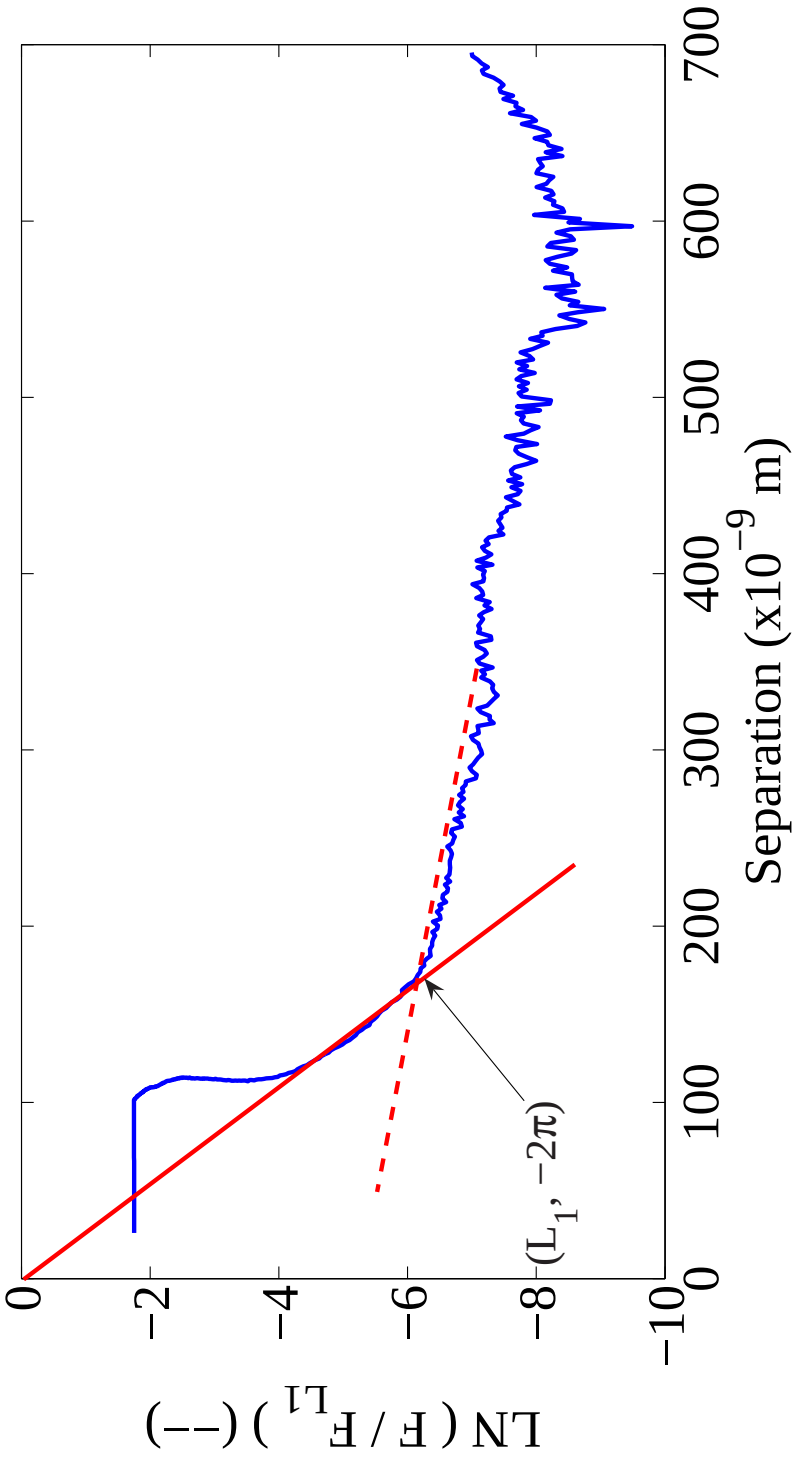

Figure 7.4.5: Example fit using the linearised steric model. Data have been offset such that the intersection of the two limit function rests at $(L_1, -2\pi)$. This intersection defines the point of zero separation for the system, assuming that the cell wall is not indented by the AFM probe.

7.4.4 Statistical Uncertainty Analysis

For the three forms analysed according to the One-Way ANOVA, no single form showed statistical significance. Specifically, for the case of repeated calculations using the same data set ($N = 10$), the probability measurement resulted in $P = 1.000$. For the case of multiple measurements on the same cell ($N = 10$), $P = 0.988$. And, for the case of individual measurements on multiple cells ($N = 15$), $P = 1.000$. This indicates that the differences between the calculated values in all cases could not be isolated from random sampling variability.

Table 7.4.1: Model results for the force within each limit regime, equilibrium polymer thicknesses, mesh spacing and mesh densities applied to multiple *P. aeruginosa* force cycles.

		Mean[1]	Standard Deviation	% Variation[2]
$F_{L_1}(0)$	(nN)	120	5	4.0%
$F_{L_2}(0)$	(nN)	0.40	0.07	20%
L_1	(nm)	160	8	5.0%
L_2	(nm)	1700	400	20%
ξ_1	(nm)	1.80	0.04	2.0%
Ξ_1	(nm^{-3})	0.19	0.01	6.0%
ξ_2	(nm)	30	3	13%
Ξ_2	(nm^{-3})	$7x10^{-5}$	$2x10^{-5}$	35%

[1] Values shown are calculated as the mean and deviation of model parameters from $N = 15$ force cycles.

[2] Percent variation is defined as the ratio of the standard deviation to the mean.

7.5 Discussion

7.5.1 Implications of the Model

As was seen in Figures 7.4.4 and 7.4.5, the data arising from a purely repulsive approach curve produces two linear regions, separated by an inflection point, after filtering out an oscillatory noise pattern and converting into semilogarithmic coordinates. This profile suggests the presence and influence of two unique polymer brushes on the approach interaction. Application of the model derived in previous sections, which was based upon the established derivations of Alexander [5] and de Gennes [12], allows for the calculation of the thickness and mesh density of two unique polymer brushes through simple mathematical treatment of AFM data sets. Further, the model allows for the identification of the point of zero separation, defined as the microbial cell wall, according to the calculated polymer brush thickness.

The change of parameters to the mesh density, $\frac{1}{\xi^3}$, from Butt's $\Gamma^{\frac{3}{2}}$ [10], represents a theoretical extension of the original derivation. Specifically, $\frac{1}{\xi^3}$ describes interactions within the brush without the restriction that interpolymer interactions are controlled solely by their spacing at their grafting points. This distinction allows polymers to interact both with adjacent chains and within the same chain (*i.e.*, to fold). Further, the parameter $\frac{1}{\xi^3}$ is a three-dimensional quantity, where Γ is based in two dimensions. Thus, the non-physical fractional power of Γ is avoided by employing a parameter which has physical significance within the region measurable by the instrumentation (*i.e.*, the AFM).

7.5.2 Parameter Results

Results corresponding to the region dominated by a brush having thickness L_1 and mesh spacing ξ_1 correlate well to the results of others. Similar lengths have been reported by Matias *et al.* [22], who employed transmission electron microscopy (TEM) to cryogenically-fixed sections of *Escherichia coli* and *P. aeruginosa*, measuring the thickness of the exopolymer brush with excellent accuracy and precision. However, the harsh chemical treatments necessary prior to the use of TEM, as well as the disruptive mechanical processes involved in sectioning a microbial cell, leave a margin of doubt as to whether the reported values (*op.*

cit.) and those obtained herein correlate well as a result of adequate measurement, or simple coincidence.

Results obtained for the brush having thickness L_2 and mesh spacing ξ_2 are much larger than expected for *P. aeruginosa*. Similar values have not been reported, and could not be verified by AFM topographical imaging of the bacterial cells. Data in this region, however, occur very close to the instrument noise level. It is therefore possible that the calculations in this region do not, in fact, represent physical polymers. Instead, this region may describe long-range physicochemical interactions within the bulk phase of the system, specifically in terms of electrostatic interactions between ions in solution and ions within the microbial polymer brush.

7.5.3 Data Presentation and Interpretation

In the construction of this model, the common display of force-separation curves in rectilinear coordinates has been altered, and the conventions used within this document should be briefly discussed. First, data are presented as the natural logarithm of force, normalised to the force at zero separation, versus separation distance. These coordinate axes were chosen to amplify the very small signals present in purely repulsive approach curves. Further, semilogarithmic coordinates allow for a more straightforward identification of various regions within the force cycle (*i.e.*, Figure 7.3.2).

Data describing the constant compliance region of the approach curve are reported as existing within the microbial polymer brush, and do not represent the microbial cell wall, as has been assumed by others [3,4,11,16,21,28]. Constant compliance is described as the region in which the deflection is due solely to piezoactuator displacement. This means that the substrate is more rigid than the cantilever, such that the tip does not significantly indent or deform the sample surface within this region. While this definition may be used to define the point of zero separation for a rigid, bare sample, the assumption is inappropriate for brushed surfaces. Specifically, since the response of the steric interaction increases exponentially with decreasing separation distance, it is unlikely that the cantilever is sufficiently stiff to completely compress the brush. Therefore, assuming that the microbial cell wall is not deformed by the probe, the region of constant compliance must occur at some distance away

from the point of zero separation on the positive Separation axis. It is possible that this point represents the maximum compressible thickness (or the minimum absolute thickness) of the polymer brush, although there is no evidence currently available to qualify this conclusion.

Next, the value of photodiode saturation is presented with a negative value. This may be attributed to two additional features of the data presentation, being that the data are normalised to the force at zero separation, as calculated from the small-separation limit function, and that the data are presented in semilogarithmic coordinates. Since all force magnitudes will be less than the force at zero separation, leading to a fractional value of the ratio $F(h)/F_{L_1}(0)$, the natural logarithm of which will be a negative number. Deconvolution of the saturation force, according to Figure 7.4.5, yields a saturation force of $\approx +20$ nN.

The magnitudes of the force at zero separation for the inner and outer brushes, $F_{L_1}(0)$ and $F_{L_2}(0)$ vary significantly from those seen in the open literature [3, 4, 11, 16, 28]. Also, the equilibrium polymer brush thicknesses in these reports are much different from those predicted by this model. While values of the force at zero separation of $\approx 2 - 10$ nN and equilibrium polymer brush thicknesses of $\approx 25 - 1000$ nm have been reported, it must be recognised that the data in the previous analyses were fitted with the original steric model after the coordinate system had been applied. In all cases, the point of zero separation was defined by the constant compliance region, and associated with the location of the microbial cell wall. Since we have shown that the constant compliance region occurs within the polymer brush, instead of at the cell wall, these discrepancies were expected. Specifically for the case of $F_{L_1}(0)$, a very large force magnitude is reasonable. This parameter may be interpreted as the force required to reach zero separation, without indenting the cell wall. While this value is two orders of magnitude larger than those reported previously, this very high force is consistent with the corollary that one cannot actually reach the point of zero separation of a brushed surface.

Further, we have extended the steric model of Butt *et al.* [10] to allow for the identification of the point of zero separation. In past research [3, 4, 11, 16, 21, 28], the original steric model has been used in the reverse manner, such that a coordinate system had already been applied to the recorded data, and the model was used to extract the polymer brush length and grafting density from the data. The reliability of this analysis technique rests upon the

assumptions inherent in the algorithm used to define the point of zero separation, as well as the assumption that this algorithm is compatible with the steric model. By utilising the mathematical model to define the point of zero separation, the identities of the assumptions inherent in both steps become more clear, and the theoretical foundations upon which the model is based are applied directly to the data. Therefore, the compatibility and reliability of this methodology are believed to be significantly higher than the previous cases.

7.6 Conclusions

In this work, we have shown that the constant compliance region in purely repulsive AFM approach curves falls within the microbial exopolymer brush, and does not represent the point of zero separation between the probe and cell wall. We have further demonstrated that the three-dimensional mesh density is a more appropriate parameter, as compared to the two-dimensional grafting density at the cell wall, for characterising the energy within the brush. Through straightforward mathematical analysis of the system, we have shown that the equilibrium polymer brush thickness, the polymer mesh density, and the point of zero separation for purely repulsive AFM approach curves may be simultaneously quantified, removing the need for separate processing steps. Utilising this mathematical method, it is now possible to consistently define the point of zero separation between the AFM probe and substrate as the cell wall, even though that location cannot actually be reached by the probe.

7.7 Bibliography

[1] E. A-Hassan, W. F. Heinz, M. D. Antonik, N. P. D'Costa, S. Nageswaran, C. A. Schoenenberger, and J. H. Hoh. Relative microelastic mapping of living cells by atomic force microscopy. Biophysical Journal, 74:1564–1578, 1998.

[2] N. I. Abu-Lail. The Effect of Biopolymer Properties on Bacterial Adhesion: An Atomic Force Microscopy (AFM) Study. Doctoral Dissertation, Biological Interaction Forces Lab, Department of Chemical Engineering, Worcester Polytechnic Institute, 2003.

[3] N. I. Abu-Lail and T. A. Camesano. Role of ionic strength on the relationship of biopolymer conformation, DLVO contributions and steric interactions to bioadhesion of *Pseudomonas putida* KT2442. Biomacromolecules, 4:1000–1012, 2003.

[4] N. I. Abu-Lail and T. A. Camesano. Role of lipopolysaccharides in the adhesion, retention and transport of *Escherichia coli* JM109. Environmental Science and Technology, 37:2173–2183, 2003.

[5] S. Alexander. Adsorption of chain molecules with a polar head: A scaling description. Journal de Physique (Paris), 38(8):983–987, 1977.

[6] G. Binnig, C. F. Quate, and C. Gerber. Atomic force microscope. Physical Review Letters, 56(9):930–933, 1986.

[7] N. A. Burnham, X. Chen, C. S. Hodges, G. A. Matei, E. J. Thoreson, C. J. Roberts, M. C. Davies, and S. J. B. Tendler. Comparison of calibration methods for atomic-force microscopy cantilevers. Nanotechnology, 14:1–6, 2003.

[8] N. A. Burnham and R. J. Colton. Measuring the nanomechanical properties and surface forces of materials using an atomic force microscope. Journal of Vacuum Science and Technology, 7:2906–2913, 1989.

[9] N. A. Burnham and A. J. Kulik. Surface Forces and Adhesion. In B. Bhushan, editor, Handbook of Micro/Nano Tribology, pages 247–271. CRC Press, Boca Raton, 2nd edition, 1999.

[10] H.-J. Butt, M. Kappl, H. Mueller, R. Paiteri, W. Meyer, and J. Ruhe. Steric forces measured with the atomic force microscope at various temperatures. Langmuir, 15:2559–2565, 1999.

[11] T. A. Camesano and B. E. Logan. Probing bacterial electrosteric interactions using atomic force microscopy. Environmental Science and Technology, 34:3354–3362, 2000.

[12] P. G. de Gennes. Polymers at an interface: A simplified view. Advances in Colloid and Interface Science, 27:189–209, 1987.

[13] W. A. Ducker and T. J. Senden. Measurement of forces in liquids using a force microscope. Langmuir, 8:1831–1836, 1992.

[14] Y. F. Dufrêne. Atomic force microscopy, a powerful tool in microbiology. Journal of Bacteriology, 184(19):5205–5213, 2002.

[15] Y. F. Dufrêne, C. J. P. Boonaert, H. C. van der Mei, H. J. Busscher, and P. G. Rouxhet. Probing molecular interactions and mechanical properties of microbial cell surfaces by atomic force microscopy. Ultramicroscopy, 86:113–120, 2001.

[16] R. J. Emerson and T. A. Camesano. A nanoscale investigation of pathogenic microbial adhesion to a biomaterial. Applied and Environmental Microbiology, 70(10):6012–6022, 2004.

[17] R. J. Emerson and T. A. Camesano. On the importance of precise calibration techniques for an atomic force microscope. Ultramicroscopy, 106(4-5):413–422, 2006.

[18] U. Landman, W. D. Luedtke, N. A. Burnham, and R. J. Colton. Atomistic mechanisms and dynamics of adhesion, nanoindentation and fracture. Science, 248:454–461, 27 April 1990.

[19] G. U. Lee, L. A. Chrisey, and R. J. Colton. Direct measurement of the forces between complementary strands of DNA. Science, 266(5186):771–773, 1994.

[20] X. Li and B. E. Logan. Analysis of bacterial adhesion using a gradient force analysis and colloid probe atomic force microscopy. Langmuir, 20(20):8817–8822, 2004.

[21] Y. Liu, M. Black, L. Caron, and T. Camesano. Role of cranberry juice on molecular-scale surface characteristics and adhesion behavior of *Escherichia coli*. Biotechnology and Bioengineering, 93(2):297–305, 2006.

[22] V. R. F. Matias, A. Al-Amoudi, J. Dubochet, and T. J. Beveridge. Cryo-transmission electron microscopy of frozen-hydrated sections of *Escherichia coli* and *Pseudomonas aeruginosa*. Journal of Bacteriology, 185:6112–6118, 2003.

[23] Y.-L. Ong, A. Razatos, G. Georgiou, and M. M. Sharma. Adhesion forces between *E. coli* bacteria and biomaterial surfaces. Langmuir, 15:2719–2725, 1999.

[24] A. Razatos, Y.-L. Ong, F. Boulay, D. L. Elbert, J. A. Hubbell, M. M. Sharma, and G. Georgiou. Force measurements between bacteria and poly(ethylene glycol)-coated surfaces. Langmuir, 16:9155–9158, 2000.

[25] A. Razatos, Y.-L. Ong, M. M. Sharma, and G. Georgiou. Evaluating the interaction of bacteria with biomaterials using atomic force microscopy. Journal of Biomaterial Science: Polymer Edition, 9(12):1361–1373, 1998.

[26] U. D. Schwarz. A generalized analytical model for the elastic deformation of an adhesive contact between a sphere and a flat surface. Journal of Colloid and Interface Sciences, 261:99–106, 2003.

[27] A. Touhami, B. Hoffmann, A. Vasella, F. A. Denis, and Y. F. Dufrêne. Probing specific lectin-carbohydrate interactions using atomic force microscopy imaging and force measurements. Langmuir, 19(5):1745–1751, 2003.

[28] V. Vadillo-Rodriguez, H. J. Busscher, W. Norde, J. de Vries, and H. C. van der Mei. On relations between microscopic and macroscopic physicochemical properties of bacterial cell surfaces: An AFM study on *Streptococcus mitis* strains. Langmuir, 19:2372–2377, 2003.

[29] B. C. van der Aa and Y. F. Dufrêne. *In situ* characterization of bacterial extracellular polymeric substance by AFM. Colloids and Surfaces B: Biointerfaces, 23:173–182, 2002.

[30] S. B. Velegol and B. E. Logan. Contributions of bacterial surface polymers, electrostatics and cell elasticity to the shape of AFM force curves. Langmuir, 18:5256–5262, 2002.

[31] L. A. Wenzler, G. L. Moyes, G. N. Raikar, R. L. Hansen, J. M. Harris, and T. P. Beebe Jr. Measurements of single-molecule bond-rupture forces between self-assembled monolayers of organosilanes with the atomic force microscope. Langmuir, 13:3761–3768, 1997.

CHAPTER 8

Possibilities for Future Studies

8.1 Abstract

This section describes several possible topics which, while interesting and relevant to the fundamental problem of microbial adhesion to medical implant materials, have not yet been addressed. Items will be presented in brief, in order to allow the researcher freedom in defining the details of the experimentation ... which is the most gratifying part of any experimentation.

8.2 Determination of the Cellular Spring Constant

During AFM retraction events, it is common to see strong adhesive peaks, which indicate the adhesive strength of one or more polymeric structures on the cell surface. Applying Hooke's Law to the cantilever deflection data, we are able to generate a value of force. However, in converting from deflection to force, we are only applying the spring constant of the cantilever, as calculated by the thermal noise method described in Chapter 4. As shown in Figure 6.5.1, however, the overall adhesive event is a superposition of several different spring constants acting in series. The contribution of the spring constant of the cantilever, while significant, may not be the only significant value present for the system. As such, the strength of each must be either precisely and accurately measured, or shown to be insignificant through rigorous empirical and theoretical validation. This system is exceptionally complex, but solution of the problem is necessary to obtain reliable values of adhesive strength using a cellular probe.

8.3 Emulation of *In Vivo* Systems for Biomedical Applications

The work presented in this document has focused significantly on the use of a model system, the tip-mounted cellular probe. This has proven a versatile tool in many situations, and will, hopefully, continue to be used. To date, however, the systems to which the tool has been applied have also been models. It is therefore proposed that experimentation directed at describing the *in vivo* adhesive properties of microbes be initiated. This includes modulation of temperature to a homeostatic value of 37 °C, as well as the use of fluids better representing the physiological environment. This may include different buffering agents, or, ideally, whole human serum. Fundamentally, the best way to solve an *in vitro* problem is to make it as similar as possible to the *in vivo* problem under investigation.

8.4 Antimicrobial Activity of SAM-Functionalised Substrates

In Chapter 6, we studied the relative adhesive affinity of *Staphylococcus epidermidis* to a variety of chemically-modified surfaces. Results showed that substrates functionalised with moderately hydrophobic compounds, most especially IPA and IAG, had the lowest adhesive strength to a *S. epidermidis* cell probe, falling at or below the noise level of the instrument. Even with a very low adhesive strength, however, conditions likely exist (*viz.*, stagnant fluid, impinging flow, microbial collisions, etc...) which would allow a few cells to attach to the surface. After this attachment step, the infection has begun. It is therefore of interest to explore the viability characteristics of microbes after they have attached to these substrates. Studies may include optimisation of the microbial deposition method (*viz.*, gravitational settling or variable flow characteristics and orientations), and description of the number of viable cells remaining after variable and protracted time periods.

CHAPTER 9

Research Summary

Throughout this body of research, we have sought to better understand the mechanisms by which bacteria and fungi adhere to surfaces, with particular emphasis on mitigating the significant problem of adhesion-initiated infections of medical implant devices. In Chapter 2 and [2], we proved the feasibility of attaching a single, metabolically active microbe to the tip of an AFM probe, which might be used to characterise the relative affinity of the microbe to an implant material surface, and also showed that an established biofilm infection increases promotes subsequent microbial attachment. Chapter 4 and [3] demonstrated the importance of thoroughly understanding the behaviour of one's instrument to achieve reproducible and credible results. Chapter 6 began an investigation of the influence of the substrate texture and surface chemistry on the strength of adhesion, with initial results demonstrating that the surface texture, in many cases, plays a more significant role than surface chemistry in the initial adhesive event. And, in Chapter 7, we propose a method by which the surface of a microbe might be quantitatively located and described for steric-dominated interactions, which are common in microbial systems.

Collaborative work in Chapter 3 and [1] explored a microbial antigenic mechanism, in the form of a polymer shell. Using AFM and several other analysis techniques, it was shown

that the shell is not confluent, but instead contains pores which allow for normal metabolic activity, but which prevent the transport of antimicrobial compounds across the cell wall. Additional collaboration, described in Chapter 5, showed that microbial adhesion to a protein layer is significantly influenced by the orientation of the protein molecules within that layer. As this conditioning layer is often deposited immediately following device implantation, and is capable of altering the substrate to be more attractive to microbial colonisation, the influence of the host's own body must be considered in the design of biomedical implant materials.

This research has not definitively characterised or eliminated the problem of microbial adhesion to medical implant devices. It has, however, provided a number of tools and techniques by which the problem might be further investigated, and has also demonstrated the importance of examining this problem from the point of view of the microbe itself. In the future, this information may be used in similar or widely different ways to continue the study of biomedical implant infections.

9.1 Bibliography

[1] H. C. Eisenman, J. D. Nosanchuk, J. B. W. Webber, R. J. Emerson, T. A. Camesano, and A. Casadevall. Microstructure of the cell wall-associated melanin in the human pathogenic fungus *Cryptococus neoformans*. Biochemistry, 44(10):3683–3693, 2005.

[2] R. J. Emerson and T. A. Camesano. A nanoscale investigation of pathogenic microbial adhesion to a biomaterial. Applied and Environmental Microbiology, 70(10):6012–6022, 2004.

[3] R. J. Emerson and T. A. Camesano. On the importance of precise calibration techniques for an atomic force microscope. Ultramicroscopy, 106(4-5):413–422, 2006.

CHAPTER 10

Appendices

A AFM Data Analysis - Scripts and Functions

Following are a series of Matlab® scripts and functions which were generated to calculate cantilever spring constants and automate the procedure for processing force curve data. The algorithm of the script may be seen in Figure A.1.

Noise spectra serve as the first input, which are used to calculate the spring constant of the cantilever, assuming the spectrum in the Fourier domain is a linear superposition of inverse frequency noise, white noise, and cantilever kinetic resonance (modeled as a simple harmonic oscillator). Raw deflection curves are then input, which are converted first to relative force against scanner displacement, then to absolute force against separation.

The method by which these latter quantities are calculated depend upon the characteristics of the force profile, *viz.*, whether or not there is attraction in the approach portion of the force cycle. If so, the minimum of the attraction is aligned to the vertical axis. If not, a new model describing steric interactions between a bare AFM tip and a polymer-coated surface is applied, which filters the data to remove optical noise artifacts, and then calculates the equilibrium polymer brush thickness according to the model derived in Chapter 7. In both

cases, the constant compliance regions of the retraction curves are aligned to those of the approach curves, satisfying the assumption of thermodynamic equilibrium inherent in the use of Hooke's Law.

Additional functionality allows the user to "check" the segments used in defining the constant compliance and zero force limits, and also collects information regarding pull-off events in the retraction curves. This latter may then be processed to produce histograms of normalised frequency of occurrence against pull-off force or distance.

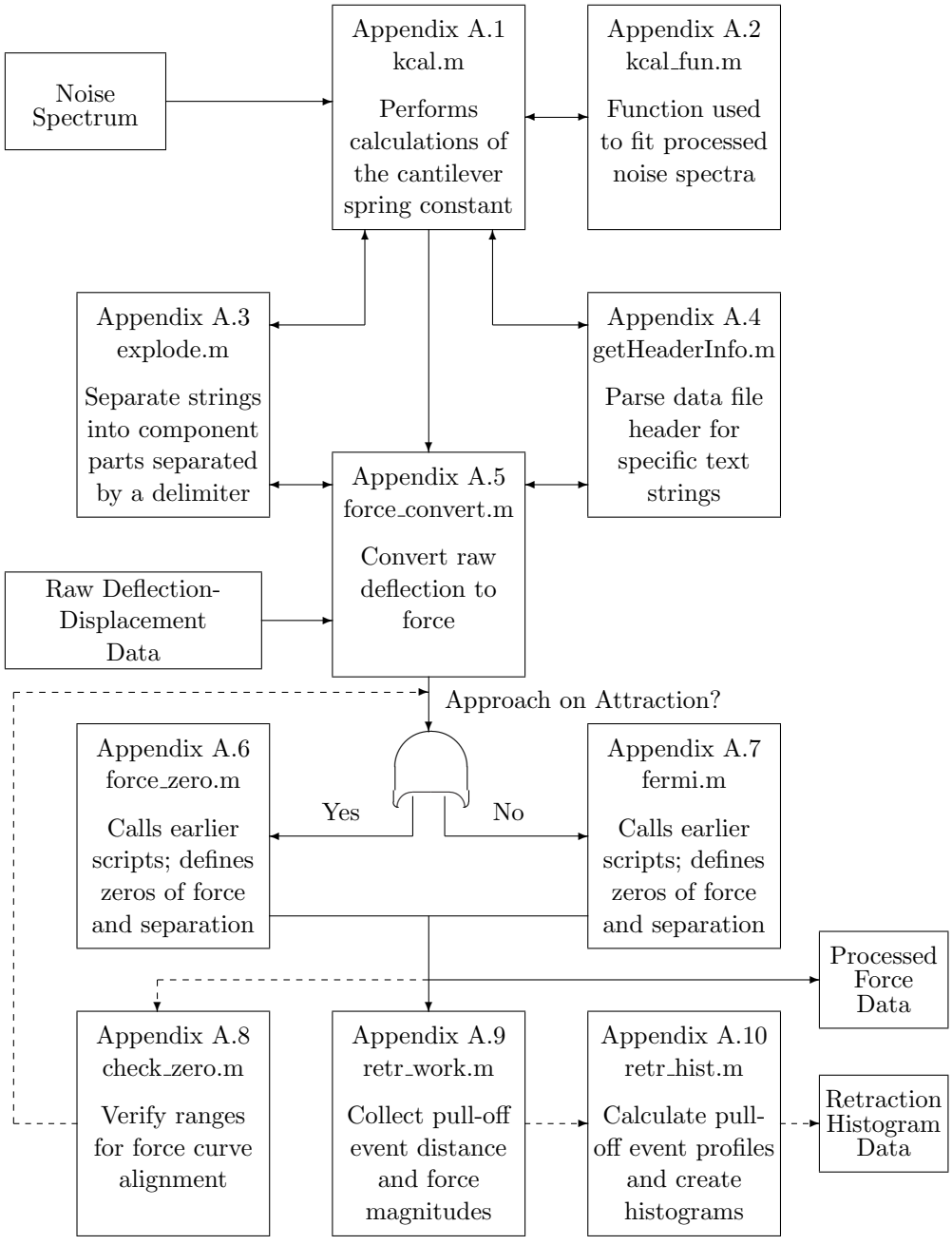

Figure A.1: Spring constant and force curve processing algorithm. Dashed lines represent optional functionality of the data analysis suite.

A.1 kcal.m

`kcal` reads the noise spectra recorded with the AFM, parses the header, processes the data used by `kcal_fun` for the nonlinear least squares regression, and returns the value of the cantilever spring constant. This function also returns the minimised 2-norm residual of the regression. The returned value of k_c may then be used in `force_convert` to process raw LSB data and output force. `kcal` was written with the assistance of Erik Thoreson and Torbjorn Bergstrom.

```
% Open the noise spectrum image, and record the file name and
% location for later exporting.
[fname,pathname]=uigetfiles;

% Open the data file for reading
fid = fopen([pathname, fname],'r');

% Read the header of the data file into memory.
i=1;
fheader(i,1)=cellstr(fgetl(fid));
 while ~strcmp(char(fheader(i,1)),'"\*File list end')
     i=i+1;
     fheader(i,1)=cellstr(fgetl(fid));
 end

% Locate strings containing Sens. Deflection and Z scale.
SensDefl_string=char(getHeaderInfo( ...
    fheader,'"\@Sens. Deflection: V',':','string'));
Zscale_string=char(getHeaderInfo( ...
    fheader,'"\@2:Z scale: V [Sens. Deflection]',')','string'));

% Split SensDefl and Zscal strings into component parts,
```

```
% separated by spaces.
SensDefl_string=explode(SensDefl_string,' ');
Zscale_string=explode(Zscale_string,' ');

% Define the constants used in the calculations, where:
% c(1) = Sens. Deflection (nm/V)
% c(2) = Z Scale (Hard Value)  (V/LSB)
% c(3) = Boltzmann Constant (J/K)
% c(4) = Absolute temperature (K)
% c(5) = Frequency resolution (Hz)
% c(6) = alpha_1, first vibrational mode of cantilever (dim)
c = [str2num(SensDefl_string{3}) ; str2num(Zscale_string{2})/65536; ...
    1.3807E-23 ; 298.15 ; 122 ; 1.8751^4];

% Define the first numerical point in the data set as the
% length of the header + 1. The data files contain an
% escape character between the header and the data, which
% would be difficult to import. Therefore, we skip it.
j = length(fheader) + 1;

% Close the data file so we can read in the data using dlmread.
fclose(fid);

% Read in comma-delimited numerical data. If another delimiter
% is desired, change the character between the two vertical
% quotes.
fdata = dlmread([pathname,fname],' ',j,0);

% Conversion to V. Transpose the array to allow the FFT
% function to work.
```

```
V = (fdata.*c(2))';

% Calculate the columnwise FFT of the voltage data. This
% is actually the FFT of each row of the raw data, since
% we transposed the array. 'fft' will only work on
% columns of data.
for i = 1:length(V)
    volts_fft(:,i) = fft(V(:,i));
end

% Calculate the complex conjugate roots of the FFT'd
% voltage data. The product of the FFT'd and conjugate
% data sets will give the square magnitude of the voltage
% in the Fourier domain, which is required later in the script.
for i = 1:length(volts_fft)
    volts_conj(:,i) = conj(volts_fft(:,i));
end

% Calculate the square voltage in the Fourier domain by
% the product of the FFT'd voltage and its complex conjugate
% pairs, divided by the square of the number of data points
% in each column.
for i = 1:length(volts_fft)
    for j = 1:length(volts_conj)
        sq_volts_fft(i,j) = (volts_fft(i,j) * volts_conj(i,j))/...
            (length(volts_fft))^2;
    end
end

% Calculate the mean square voltage matrix.
```

```
for i = 1:length(sq_volts_fft);
    msv(i) = sum(sq_volts_fft(i,:))/512;
end

% Define frequency scale from the total bandwidth of
% the instrument. Partition bandwidth into the same number of
% points as the msv vector.
for i = 1:length(msv);
    frequency(i,1) = i*122;
end

% Conversion of mean square voltage to mean square amplitude
% via Eqn. 10 in the above reference. The pre-factor includes
% diode wavelength, wavelengths from the interferometric portion
% of the Z step calibration procedure, and the angle of repose
% of the cantilever in the holder.
msa = (1/0.932423206).*(c(1)^2).*msv;

% Plot the mean square amplitude versus frequency graph.
fig1 = figure;
plot(frequency,msa,'.')

% Change to data cursor mode.
datacursormode on
dcm_obj = datacursormode(fig1);
set(dcm_obj,'DisplayStyle','window')

h = helpdlg('Define maximum of inverse frequency noise','1/f Noise');
uiwait(h);
w = waitforbuttonpress;
```

```
inv_f(1,:)=struct2array(getCursorInfo(dcm_obj));

% Activate zoom mode to locate the resonant peak.
zoom on
h = helpdlg('Zoom to the FIRST resonant peak, then click OK',...
'Zoom');
uiwait(h);

% Change to data cursor mode.
datacursormode on
dcm_obj = datacursormode(fig1);
set(dcm_obj,'DisplayStyle','window')

h = helpdlg('Define the white noise floor','White Noise');
uiwait(h);
w = waitforbuttonpress;
white(1,:)=struct2array(getCursorInfo(dcm_obj));

% Record the point associated with the maximum of the resonant
% peak and close the plot.
h = helpdlg('Click on the maximum point of the resonant peak',...
'Peak');
uiwait(h);
w = waitforbuttonpress;

% Definitions in the resonant peak array:
% res_pt(1,1) = Internal handle of the plot
% res_pt(1,2) = Frequency of the resonant peak (X-value)
% res_pt(1,3) = Amplitude at kinetic resonance (Y-value)
% res_pt(1,4) = Plane of the array (Z-value; equals 1 if 2-D array)
```

```
% res_pt(1,5) = Index of the selected data point
res_pt(1,:)=struct2array(getCursorInfo(dcm_obj));
close(fig1);

% Truncate the frequency series such that only the 50 points on
% either side of the resonant frequency are included.
frequency(res_pt(1,5)+50:length(frequency)) = [];
frequency(1:res_pt(1,5)-51) = [];

% Truncate the msa series such that only the 50 points on
% either side of the resonant frequency are included.
msa(:,res_pt(1,5)+50:length(msa)) = [];
msa(:,1:res_pt(1,5)-51) = [];



% Initial guesses for the 5 fitting parameters of the equation.
% Peak amplitude (xvk) and peak resonant frequency (vk) are set
% by each data set, and should change the least of all parameters.
% The value for white noise is set to a fraction of that
% calculated above since we do not actually reach the white noise
% floor within our frequency range.
a0 = [inv_f(1,3) white(1,3) res_pt(1,3)-white(1,3) 30 res_pt(1,2)];

% Define upper and lower boundaries for the fitting parameters.
%a_min = [0.001*a0(1,1) a0(1,2)-5E-6 0.999*a0(1,3) 0.1*a0(1,4) a0(1,5)-.1];
%a_max = [100*a0(1,1) a0(1,2)+5E-6 1.001*a0(1,3) 1.1*a0(1,4) a0(1,5)+.1];

% Define tolerance for the least squares curve fit.
options = optimset('TolFun',1E-9);
```

```
% Least squares curve fit to the nonlinear function, returning fitted
% values for the 5 fitting parameters, as well as the minimised squared
% 2-norm residual of the fit.
[a, resnorm] = lsqcurvefit(@kcal_fun,a0,frequency,msa);

% The Spring Constant, N/m.
kc = (12*c(3)*c(4)*a(1,4)*c(5)) / (c(6)*pi*res_pt(1,2)*res_pt(1,3)) * 1E17
```

A.2 kcal_fun.m

The `kcal_fun` function fits the processed square amplitude and frequency data to the non-linear equation shown in [1]. The fitting parameter values are used in `kcal` to calculate the cantilever spring constant. `kcal_fun` was written with the assistance of Erik Thoreson and Nguyen Huynh.

```
function F = kcal_fun(a,frequency)


x=frequency(:,1);


% Fitting Parameter Definitions
% a(1) = 1/f noise (A) [nm^2/s]
% a(2) = White noise floor (B) [nm^2]
% a(3) = Peak amplitude <x^2(nu_k)> [nm^2]
% a(4) = Quality factor (Q) [dimensionless]
% a(5) = nu_k (peak resonant frequency) [Hz]


for k=1:length(x);
     A_1(k) = a(1)/x(k);
     A_2 = a(3)/((a(4))^2);
     A_3(k) = (1 - (x(k)/a(5))^2)^2 ;
     A_4(k) = (x(k)/(a(4)*a(5)))^2;
     F(k) = A_1(k) + a(2) + (A_2 / (A_3(k) + A_4(k)));
end
```

A.3 explode.m

This Matlab® function courtesy of Sara Silva, obtained through The Mathworks Central File Exchange (`http://www.mathworks.com/matlabcentral/fileexchange/`). Since the `getHeaderInfo` function returns `char` strings after parsing the file header, we use the `explode` function to separate the non-numeric portions of the `char` strings into separate array elements, using whitespace as a delimiter. One element of the resulting array will be a numeric value of Sens. Deflection or Z scale. The element number is predictable, and can be separated into a new variable for use in subsequent operations.

```
function [split,numpieces]=explode(string,delimiters)
%EXPLODE    Splits string into pieces.
%   EXPLODE(STRING,DELIMITERS) returns a cell array with the
% pieces of STRING found between any of the characters in
% DELIMITERS.
%   [SPLIT,NUMPIECES] = EXPLODE(STRING,DELIMITERS) also returns
% the number of pieces found in STRING.
%
%   Input arguments:
%      STRING - the string to split (string)
%      DELIMITERS - the delimiter characters (string)
%   Output arguments:
%      SPLIT - the split string (cell array), each cell is a
% piece
%      NUMPIECES - the number of pieces found (integer)
%
%   Example:
%      STRING = 'ab_c,d,e fgh'
%      DELIMITERS = '_,'
%      [SPLIT,NUMPIECES] = EXPLODE(STRING,DELIMITERS)
```

```
%      SPLIT = 'ab'    'c'    'd'    'e fgh'
%      NUMPIECES = 4
%
%   See also IMPLODE, STRTOK
%
%   Created: Sara Silva (sara@itqb.unl.pt) - 2002.04.30

if isempty(string) % empty string, return empty and 0 pieces
   split{1}='';
   numpieces=0;

elseif isempty(delimiters) % no delimiters, return whole
                           % string in 1 piece
   split{1}=string;
   numpieces=1;

else % non-empty string and delimiters, the correct case

   remainder=string;
   i=0;

while ~isempty(remainder)
   [piece,remainder]=strtok(remainder,delimiters);
   i=i+1;
   split{i}=piece;
end
   numpieces=i;

end
```

A.4 getHeaderInfo.m

`getHeaderInfo` is used by the `kcal` function and `force_convert` script to parse the file headers for conversion of raw LSB data to cantilever deflection. `getHeaderInfo` was written by Torbjorn Bergstrom.

```
function rstring=getHeaderInfo(imHeader,token,delimiter,returntype)


if nargin < 4
    returnString=0;
else
    returnString=1;
end


offset=strmatch(token,imHeader);
temps=imHeader(offset);
[temp,rstring]=strtok(temps,delimiter);
if returnString
    return
end
test=1;
rstring=char(rstring);
rstring =rstring(2:length(rstring));


rstring=sscanf(rstring,'%g',1);
return
```

A.5 force_convert.m

The `force_convert` script uses the `kcal` function to convert raw LSB data from the Nanoscope® software to force and separation data. These data may be further processed (*e.g.,* in Microsoft Excel® or Matlab®) to subtract the influence of the cantilever while in contact with the surface and to set the coordinate system. `force_convert` was written with the assistance of Torbjorn Bergstrom.

```
function [sep_points,force_appr,force_retr,kc,pathname,fname] =...
    force_convert(pathname,filename)

% Call the kcal script to calculate the cantilever spring constant.
kc = kcal;

if nargin < 1
    [fname,pathname]=uigetfiles;
end

% Open the data file for reading
fid = fopen([pathname, fname],'r');

% Read the header of the data file into memory.
i=1;
force_header(i,1)=cellstr(fgetl(fid));
 while ~strcmp(char(force_header(i,1)),'"\*File list end');
     i=i+1;
     force_header(i,1)=cellstr(fgetl(fid));
 end

% Locate strings containing Sens. Deflection and Z scale.
SensDefl_force=char(getHeaderInfo( ...
```

```
    force_header,'"\@Sens. Deflection: V',':','string'));
Zscale_force=char(getHeaderInfo( ...
    force_header,'"\@4:Z scale: V [Sens. Deflection]',')','string'));
SensZscan_force=char(getHeaderInfo( ...
    force_header,'"\@Sens. Zscan: V',':','string'));
ramp_force=char(getHeaderInfo( ...
    force_header,'"\@4:Ramp size: V [Sens. Zscan]',')','string'));

% Since 2 deflection curves captured, need to separate out the
% appropriate Z scale conversion factor.
Zscale_force = Zscale_force(1,:);
ramp_force = ramp_force(1,:);

% Split SensDefl and Zscale strings into component parts,
% separated by spaces.
SensDefl_force=explode(SensDefl_force,' ');
Zscale_force=explode(Zscale_force,' ');
SensZscan_force = explode(SensZscan_force,' ');
ramp_force=explode(ramp_force,' ');

% Now convert the conversion factors from strings to numbers
SensDefl_force = str2double(SensDefl_force{3});
Zscale_force = str2double(Zscale_force{2});
SensZscan_force = str2double(SensZscan_force{3});
ramp_force = str2double(ramp_force{2});

% Z_Cal_Factor is the piezoactuator correction factor, as
% calculated from interferometric measurements from the
% microscope as compared to the actual piezoactuator
% displacement, as reported by the AFM software.
```

```
Z_Cal_Factor = 1.08518;

% Calculate the true ramp size (separation) as the product
% of the software-defined ramp size and the piezoactuator
% correction factor.
ramp_size = round(SensZscan_force * ramp_force * Z_Cal_Factor);
Sensitivity = (SensDefl_force * Zscale_force)/65536;

j = length(force_header)+1;
fclose(fid);
raw_data = dlmread([pathname,fname],',',j,0);

% Separates approach and retraction curves (deflection channel only)
curve_length = length(raw_data)/4;
defl_appr = raw_data(2*curve_length+1:3*curve_length);
defl_retr = raw_data(3*curve_length+1:4*curve_length);

for k = 1:curve_length;
    force_appr(k) = kc*Sensitivity*defl_appr(k);
    force_retr(k) = kc*Sensitivity*defl_retr(k);
end

% Define steps for separation axis.
for l = 1:curve_length
    sep_points(l) = l*(ramp_size/curve_length);
end
sep_points = sep_points';
```

A.6 force_zero.m

`force_zero` calls all functions as shown in Figure A.1. Using each of these functions, this script completely processes a force curve, including removal of the cantilever deflection contribution during stiff contact, baselining both approach and retraction curves at large separations, calculation of the point of zero separation (based on the first negative point in the retraction curve), and aligning the constant compliance regimes of the two curves. This version includes a user interface by which the user chooses linear segments from the unadjusted approach and retraction curves to describe the constant compliance and zero interaction regions of both curves. Retraction peaks (as described in `retr_work` and `retr_hist`) are collected via a function call to `retr_work`, which increment with the analysis of multiple curves during a single session.

```
% Ask the user if they'd like to use the help instructions.
button = questdlg('Would you like the help dialogues turned on?','Help?',...
    'Yes','No','Yes');

% Get rid of extraneous variables from previous runs.
clear *appr* *retr* i j k l *points*

% Execute @force_convert and import the converted force and separation
% data, the cantilever spring constant, and the pathname and filename
% of the processed force curve. These last two items may be used in
% exporting the data after processing.
[sep_points,force_appr,force_retr,kc,pathname,fname] = force_convert;

% Define individual separation arrays for approach and retraction.
sep_appr = sep_points;
sep_retr = sep_points;

% Force data come in as row vectors, and are transposed into columns here.
```

```
force_appr = force_appr';
force_retr = force_retr';

% Define an index array corresponding to the number of data points
% in the separation and force arrays.
i = (1:length(sep_points))';

% Plot the unmodified approach curve.
fig1 = figure;
plot(sep_appr,force_appr)

% Turn on the data cursor to allow user to select points.
datacursormode on
dcm_obj = datacursormode(fig1);
set(dcm_obj,'DisplayStyle','window')

% Step 1: Constant compliance in the approach curve.
if button(1,1) == 'Y';
    h = helpdlg(...
        'Click the two points describing the constant
        compliance region for the approach curve','Step 1');
    uiwait(h);
end

% Record points for approach curve constant compliance.
w = waitforbuttonpress;
cc_appr(1,:)=struct2array(getCursorInfo(dcm_obj));
w = waitforbuttonpress;
cc_appr(2,:)=struct2array(getCursorInfo(dcm_obj));
```

```
% Step 2: Zero interaction in the approach curve.
if button(1,1) == 'Y';
h = helpdlg('Click the two points describing the zero
interaction region for the approach curve','Step 2');
uiwait(h);
end

% Record points for approach curve zero interaction.
w = waitforbuttonpress;
zi_appr(1,:)=struct2array(getCursorInfo(dcm_obj));
w = waitforbuttonpress;
zi_appr(2,:)=struct2array(getCursorInfo(dcm_obj));
close(fig1)

% Plot unmodified retraction curve.
fig2 = figure;
plot(sep_retr,force_retr)

% Turn on the data cursor to allow user to select points.
datacursormode on
dcm_obj = datacursormode(fig2);
set(dcm_obj,'DisplayStyle','window')

% Step 3: Constant compliance in the retraction curve.
if button(1,1) == 'Y';
h = helpdlg('Click the two points describing the constant
compliance region for the retraction curve','Step 3');
uiwait(h);
end
```

```
% Record points for retraction curve constant compliance.
w = waitforbuttonpress;
cc_retr(1,:)=struct2array(getCursorInfo(dcm_obj));
w = waitforbuttonpress;
cc_retr(2,:)=struct2array(getCursorInfo(dcm_obj));

% Step 4: Zero interaction in the retraction curve.
if button(1,1) == 'Y';
h = helpdlg('Click the two points describing the zero
interaction region for the retraction curve','Step 4');
uiwait(h);
end

% Record points for retraction curve zero interaction.
w = waitforbuttonpress;
zi_retr(1,:)=struct2array(getCursorInfo(dcm_obj));
w = waitforbuttonpress;
zi_retr(2,:)=struct2array(getCursorInfo(dcm_obj));
close(fig2)

% Correct the constant compliance regime of the approach curve such that it
% is vertical.
m_appr = polyfit(sep_appr(cc_appr(1,5):cc_appr(2,5)),...
        force_appr(cc_appr(1,5):cc_appr(2,5)),1);
k = 2000;

while (m_appr(1,1) <= 0);
    k = k - 1;
    sep_appr(i) = sep_points(i) + (force_appr(i)/kc)*(1-k/100);
    m_appr = polyfit(sep_appr(cc_appr(1,5):cc_appr(2,5)),...
```

```
        force_appr(cc_appr(1,5):cc_appr(2,5)),1);
    if k <= -2000
        break
    end
end

% Correct the constant compliance regime of the retraction curve such that
% it is vertical.
m_retr = polyfit(sep_retr(cc_retr(1,5):cc_retr(2,5)),...
        force_retr(cc_retr(1,5):cc_retr(2,5)),1);
j = 2000;
while (m_retr(1,1) <= 0);
    j = j - 1;
    sep_retr(i) = sep_points(i) + (force_retr(i)/kc)*(1-j/100);
    m_retr = polyfit(sep_retr(cc_retr(1,5):cc_retr(2,5)),...
        force_retr(cc_retr(1,5):cc_retr(2,5)),1);
   if j <= -2000
       break
   end
end

% Calculate the vertical offsets for each curve based on the average
% distance from the X-axis of the previously-defined zero interaction
% region.
force_offset_appr = mean(force_appr(zi_appr(1,5):zi_appr(2,5)));
force_offset_retr = mean(force_retr(zi_retr(1,5):zi_retr(2,5)));

% Shift both curves to the X-axis using the offsets calculated above.
for i = 1:length(force_appr)
    force_appr(i) = force_appr(i) - force_offset_appr;
```

```
    force_retr(i) = force_retr(i) - force_offset_retr;
end

% Locate the first negative point in the retraction curve,
% which will used in defining the point of zero separation.
retr_zero = find(force_retr < 0);

% Sort separation data in ascending order.
sep_appr(:,1) = sort(sep_appr);
sep_retr(:,1) = sort(sep_retr);

% Translate the retraction curve such that the first negative point is
% aligned to the origin of the plane.
retr_offset = sep_retr(retr_zero(1,1));
for i = 1:length(sep_retr)
    sep_retr(i) = sep_retr(i) - retr_offset;
end

% Align the constant compliance region of the approach curve
% to that of the retraction curve.
for l = 1:length(sep_points);
    sep_appr(l) = sep_appr(l) - (sep_appr(l) - sep_retr(l));
end

% Run the retraction work script to record pull-off distance and force from
% the retraction curves.
retr_work
```

A.7 force_zero_repl.m

The `force_zero_repl` function is functionally analogous to `force_zero`, but is designed to operate on data sets which do not exhibit attraction on approach. Data at large separations are first filtered to remove optical interference, using an expression of the form $f(x) = a * sin[(x - b)/c] + d$, where a represents the amplitude, b the phase, c the period and d the vertical offset of the interference pattern. Instead of using the minimum of the approach curve as the reference point for defining the point of zero separation, `fermi` applies the Fermi-Dirac statistical distribution to the data set, mathematically determining this point, as well as identifying the equilibrium polymer brush thickness, polymer spacing, and the force at zero separation. Following the derivation for microbial exopolymers from Chapter 7, data are treated to determine the location of a surface that cannot be directly contacted with the AFM probe.

```
% Ask the user if they'd like to use the help instructions.
button = questdlg('Would you like the help dialogues turned on?',...
    'Help?','Yes','No','Yes');

% Get rid of extraneous variables from previous runs.
clear *appr* *retr* i j k l *points*

% Execute @force_convert and import the converted force and separation
% data, the cantilever spring constant, and the pathname and filename
% of the processed force curve. These last two items may be used in
% exporting the data after processing.
[sep_points,force_appr,force_retr,kc,pathname,fname] = force_convert;

% Define individual separation arrays for approach and retraction.
sep_appr = sep_points;
sep_retr = sep_points;
```

```
% Force data come in as row vectors, and are transposed into columns here.
force_appr = force_appr';
force_retr = force_retr';

% Define an index array corresponding to the number of data points
% in the separation and force arrays.
j = (1:length(sep_points))';

% Plot the approach curve.
fig1 = figure;
plot(sep_appr,force_appr)

% Turn on the data cursor to allow user to select points.
datacursormode on
dcm_obj = datacursormode(fig1);
set(dcm_obj,'DisplayStyle','window')

if button(1,1) == 'Y';
    h = helpdlg(...
        'Define the constant compliance region for the approach curve',...
        'Step 1');
    uiwait(h);
end

w = waitforbuttonpress;
cc_appr(1,:)=struct2array(getCursorInfo(dcm_obj));
w = waitforbuttonpress;
cc_appr(2,:)=struct2array(getCursorInfo(dcm_obj));

% Optical interference at large separation.
```

```
if button(1,1) == 'Y';
    datacursormode on
    h = helpdlg('Starting point of interference.',...
        'Step N');
    uiwait(h);
end

% Record points for approach curve constant compliance.
w = waitforbuttonpress;
noise_appr(1,:)=struct2array(getCursorInfo(dcm_obj));

close(fig1)

% Correct the constant compliance regime of the approach curve such that it
% is vertical.
m_appr = polyfit(sep_appr(cc_appr(1,5):cc_appr(2,5)),...
        force_appr(cc_appr(1,5):cc_appr(2,5)),1);
k = 2000;
while (m_appr(1,1) <= 0);
    k = k - 1;
    sep_appr(j,1) = sep_points(j,1) + (force_appr(j,1)/kc)*(1-k/100);
    m_appr = polyfit(sep_appr(cc_appr(1,5):cc_appr(2,5)),...
        force_appr(cc_appr(1,5):cc_appr(2,5)),1);

    if k <= -2000
        break
    end
end

% Subtract out an offset sine wave, attributable to laser spillover
```

```
% interference at large separations. Make a backup of the data, just in
% case.
far_1(:,1) = sep_appr(noise_appr(1,5):length(sep_appr),1);
far_1(:,2) = force_appr(noise_appr(1,5):length(force_appr),1);

a0 = [ 5 450 45 10 ];

[a,resnorm] = lsqcurvefit(@noise_sine_mod,a0,far_1(:,1),far_1(:,2)');

noise_fit(:,1) = noise_sine_mod(a,sep_appr(:,1));

for i = 1:length(noise_fit)
    force_appr(i,1) = force_appr(i,1) - noise_fit(i,1) + a(1,4);
end

% If Matlab takes the LN of a negative number, the output is imaginary.
% This correction moves all force data into Quadrant I, avoiding this
% issue. A further correction of 1% is added to the minimum value, since
% LN(0) is undefined.
F_correction = 1.01*abs(min(force_appr));

for i = 1:length(force_appr);
    force_appr(i,1) = force_appr(i,1) + F_correction;
end

% Convert force values to LN(force);
for i = 1:length(force_appr);
        log_force_appr(i,1) = log(force_appr(i,1));
end
```

```
% Create the ln(F) vs separation chart, and allow zooming to the area of
% interest. Then switch into data cursor mode to select points.
fig2 = figure;
plot(sep_appr,log_force_appr)
zoom on
h = helpdlg('Press OK when you have completed the zoom procedure',...
    'Zooming');
uiwait(h);
datacursormode on
dcm_obj = datacursormode(fig2);
set(dcm_obj,'DisplayStyle','window')

% Define the short-polymer region.
if button(1,1) == 'Y';
    h = helpdlg(...
        'Define the small-separation range.','Small Separation');
    uiwait(h);
end

% Record points for short polymers.
w = waitforbuttonpress;
fd_small(1,:)=struct2array(getCursorInfo(dcm_obj));
w = waitforbuttonpress;
fd_small(2,:)=struct2array(getCursorInfo(dcm_obj));

% Define the long-polymer region.
if button(1,1) == 'Y';
    h = helpdlg(...
        'Define the large-separation range.','Large Separation');
    uiwait(h);
```

```
end

% Record points for long polymers.
w = waitforbuttonpress;
fd_large(1,:)=struct2array(getCursorInfo(dcm_obj));
w = waitforbuttonpress;
fd_large(2,:)=struct2array(getCursorInfo(dcm_obj));

close(fig2)

% Calculate the slope and y-axis intercept of the two regions.
m_fd_small_1 = polyfit(sep_appr(fd_small(1,5):fd_small(2,5)),...
    log_force_appr(fd_small(1,5):fd_small(2,5)),1);
m_fd_large_1 = polyfit(sep_appr(fd_large(1,5):fd_large(2,5)),...
    log_force_appr(fd_large(1,5):fd_large(2,5)),1);

% Find the point of intersection of these two functions.
z_intersection = (m_fd_large_1(1,2) - m_fd_small_1(1,2)) /...
    (m_fd_small_1(1,1) - m_fd_large_1(1,1));
F_intersection = m_fd_small_1(1,1) * z_intersection + m_fd_small_1(1,2);

% Calculate the lengths of the short and long polymers.
L1 = -2*pi/m_fd_small_1(1,1);
L2 = -2*pi/m_fd_large_1(1,1);

% Calculate the z and F offsets based on the intersection point.
z_offset = L1 - z_intersection;
F_offset = 2*pi + F_intersection;

% Apply offset to separation data.
```

```
for i = 1:length(sep_appr);
    sep_appr_corr(i,1) = sep_appr(i,1) + z_offset;
    log_force_appr_corr(i,1) = log_force_appr(i,1) - F_offset;
end

% Run another polynomial fit on the two regions to determine the force at
% zero separation.
m_fd_small_2 = polyfit(sep_appr_corr(fd_small(1,5):fd_small(2,5)),...
    log_force_appr_corr(fd_small(1,5):fd_small(2,5)),1);
m_fd_large_2 = polyfit(sep_appr_corr(fd_large(1,5):fd_large(2,5)),...
    log_force_appr_corr(fd_large(1,5):fd_large(2,5)),1);

F_L1_0 = F_offset - log(F_correction);
F_L2_0 = F_L1_0 + 2*pi*L1/L2 - 2*pi;

% Calculate the two mesh densities.
xi_1 = (exp(F_L1_0) / (100 * 1.3807E-23 * 298.15 * 1E-8 * L1))^(-1/3) *...
    1E9;
xi_2 = (exp(F_L2_0) / (100 * 1.3807E-23 * 298.15 * 1E-8 * L2))^(-1/3) * ...
    1E9;

% Generate the plot of ln(F) against separation
fig4 = figure('Color',[1 1 1]);
annot = {
    cat(2,'F_{L1} = ',num2str(exp(F_L1_0)),' nN') ;...
    cat(2,'F_{L2} = ',num2str(exp(F_L2_0)),' nN') ;...
    cat(2,'L1 = ',num2str(L1),' nm') ;...
    cat(2,'L2 = ',num2str(L2),' nm') ;...
    cat(2,'\xi_{L1} = ',num2str(xi_1,4),' nm') ;...
    cat(2,'\xi_{L2} = ',num2str(xi_2,3),' nm') };
```

```
axes1 = axes(...
  'FontName','Times',...
  'FontSize',24,...
  'Parent',fig4);
xlabel(axes1,'Separation (x10^{-9} m)');
ylabel(axes1,'ln ( F / F_{L1} ) (--)');
box(axes1,'on');
hold(axes1,'all');

plot(sep_appr_corr,log_force_appr_corr)

annotation1 = annotation(...
  fig1,'textbox',...
  'Position',[0.6888 0.7337 0.2125 0.1855],...
  'LineStyle','none',...
  'FitHeightToText','off',...
  'FontName','times',...
  'FontSize',24,...
  'String',annot);
```

A.8 check_zero.m

`check_zero` allows the user to evaluate the proper ranges for the polynomial fits of the constant compliance and zero interaction regimes of force curves. Based on the ranges found in `force_zero`, `check_zero` plots the approach and retraction curves on two charts with the ranges used for fitting overlaid in red (constant compliance) and green (zero interaction). If the range overlaps into an interaction (*viz.*, an area that is not linear), the user can adjust the ranges in `force_zero` to one more suitable to the individual data sets.

```
% Open force_zero.m for reading.
fid = fopen('force_zero.m','r');

% Read first 100 lines of fid into memory.
for i=1:100;
    data1(i,1)=cellstr(fgetl(fid));
end

% Parse force_zero.m to get the various fitting scenarios from the script.
appr_small_sep=char(getHeaderInfo( ...
     data1,'m_appr = polyfit','s','string'));
appr_large_sep=char(getHeaderInfo( ...
     data1,'    polyfit(sep_appr','s','string'));
retr_small_sep=char(getHeaderInfo( ...
     data1,'m_retr = polyfit','s','string'));
retr_large_sep=char(getHeaderInfo( ...
     data1,'    polyfit(sep_retr','s','string'));

% Separate the results from above with comma delimiter to return strings of
% the ranges used in the polynomial fit.
appr_small_sep = explode(appr_small_sep,',');
appr_large_sep = explode(appr_large_sep,',');
```

```
retr_small_sep = explode(retr_small_sep,',');
retr_large_sep = explode(retr_large_sep,',');

% Define ranges for the fit of the constant compliance region.
appr1(:,1) = eval(appr_small_sep{1});
appr1(:,2) = eval(appr_small_sep{2});
retr1(:,1) = eval(retr_small_sep{1});
retr1(:,2) = eval(retr_small_sep{2});

% Define ranges for fit of the zero interaction region
appr2(:,1) = eval(appr_large_sep{1});
appr2(:,2) = eval(appr_large_sep{2});
retr2(:,1) = eval(retr_large_sep{1});
retr2(:,2) = eval(retr_large_sep{2});

% Create figure
figure1 = figure('Color',[1 1 1]);

% Create Approach axis
axes1 = axes('OuterPosition',[0 0.5 1 0.5],'Parent',figure1);
xlabel(axes1,'Separation (nm)');
ylabel(axes1,'Force (nN)');
box(axes1,'on');
hold(axes1,'all');

% Approach Data
plot1 = plot(sep_appr,force_appr,'Color',[0 0 1],'Parent',axes1);

% Rigid contact
plot2 = plot(appr1(:,1),appr1(:,2),'Color',[1 0 0],'Parent',axes1);
```

```
% Zero interaction
plot3 = plot(appr2(:,1),appr2(:,2),'Color',[0 1 0],'Parent',axes1);

% Create Retraction axis
axes2 = axes('OuterPosition',[0 0 1 0.5],'Parent',figure1);
xlabel(axes2,'Separation (nm)');
ylabel(axes2,'Force (nN)');
box(axes2,'on');
hold(axes2,'all');

% Retraction Data
plot4 = plot(sep_retr,force_retr,'Parent',axes2);

% Rigid contact
plot5 = plot(retr1(:,1),retr1(:,2),'Color',[1 0 0],'Parent',axes2);

% Zero interaction
plot6 = plot(retr2(:,1),retr2(:,2),'Color',[0 1 0],'Parent',axes2);

% Approach
annotation1 = annotation(...
  figure1,'textbox',...
  'Position',[0.668 0.8333 0.2031 0.08854],...
  'LineStyle','none',...
  'FitHeightToText','off',...
  'FontSize',20,...
  'String',{'Approach'});

% Retraction
```

```
annotation2 = annotation(...
  figure1,'textbox',...
  'Position',[0.6504 0.3264 0.2231 0.08854],...
  'LineStyle','none',...
  'FitHeightToText','off',...
  'FontSize',20,...
  'String',{'Retraction'});


fclose(fid);
```

A.9 retr_work.m

`retr_work` runs at the end of each instance of `force_zero`, and records all pull-off distances and force magnitudes for each retraction curve analysed. A pull-off event is defined as any point immediately preceded by a segment with a negative slope, immediately followed by a segment with a positive slope, existing at a separation greater than zero, and having a magnitude of less than 1 nN. These events are further processed by `retr_hist` to generate histograms of normalised frequency against pull-off force and distance.

```
% Determine if the variable 'sep_col' exists. This variable determines the
% column in which the pull-off distance peaks are recorded. If the variable
% exists, it is stepped by 2 to keep pull-off distance in the odd columns.
% If the variable does not exist, it is created with a value of 1,
% corresponding to column 1 of the array.
if exist('sep_col') == 1;
    sep_col = sep_col + 2;
else
    sep_col = 1;
end

% Create the variable 'force_col', which will be one column to the right of
% sep_col for each retraction curve processed.
force_col = sep_col + 1;

% Determine if the variable 'peaks', which contains the actual pull-off
% distance and force values, exists. If it does, then no changes are made.
% If it does not, a 10x1 zero array is created.
if exist('peaks') == 1;
    peaks = peaks;
else
    peaks = zeros(10,1);
```

```
end

% Determines if the variable 'points' exists. Since multiple peaks may be
% found in further processing, it is necessary to clear this variable, if
% it exists, to prevent double-counting peaks.
if exist('points') == 1;
    clear points
end

% Find all points in the curve which are located at 1) Separations greater
% than zero and 2) Forces less than 1. Since some data sets may not have a
% negative point directly before the adhesive peak, we must choose some
% point as a reference for further processing.
i = 0;
for j = 1:length(sep_retr);
    if (sep_retr(j,1) > 0 & force_retr(j,1) < 1)
        i = i + 1;
        retr(i,1) = sep_retr(j,1);
        retr(i,2) = force_retr(j,1);
    end
end

% Defining peaks according to two criteria: 1) That the point must be
% preceded by a segment having a slope less than zero and 2) That the point
% must be followed by a segment having a slope greater than zero. Discrete
% data may not be processed to find the relative maxima/minima of the
% profile (viz, where the first derivative is equal to zero). However, this
% method would also identify local maxima in the data set, which would
% require further downstream processing. This method eliminates those
% relative maxima from the processing procedure.
```

```
i = 0;
for j = 3:length(retr);
        i = i + 1;
    if ((retr(j-1,2) - retr(j-2,2)) / (retr(j-1,1) - retr(j-2,1)) < 0 &...
(retr(j,2) - retr(j-2,2)) / (retr(j,1) - retr(j-2,1)) > 0);
    end
        points(i,1) = retr(j-1,1);
        points(i,2) = retr(j-1,2);
end

% Record the pull-off distance and force in the variable peaks, defined as
% any points that have a negative value of force and a separation of more
% than 2 nm.
i = 0;
for j = 1:length(points);
    if (points(j,2) < 0 & points(j,1) > 2);
        i = i + 1;
        peaks(i,sep_col) = points(j,1);
        peaks(i,force_col) = points(j,2);
    end
end
```

A.10 retr_hist.m

`retr_hist` takes the recorded pull-off data from `retr_work` and further processes it to result in histograms of pull-off force magnitude and pull-off distance. Events are defined as those points coming from `retr_work` having distance magnitudes less than 250 nm and magnitudes greater than 50 pN. Data are normalised to the total number of peaks, and the output charts are in terms of % frequency against distance/force. A default of 10 bins are used in the generation of the histogram data.

```
% Determine the dimensions of the 'peaks' array, taken from retr_work.
size_peaks = size(peaks);

% Define a retractive peak as an event occurring at less than 200 nm
% separation distance, with magnitude greater than 50 pN. Assemble
% points meeting these criteria into the 'hist_data' array.
i = 0;
for j = 1:length(peaks(:,1))
    for k = 1:2:size_peaks(1,2)-1;
        if (peaks(j,k) <= 200 & peaks(j,k+1) <= -0.05 & peaks(j,k) ~= 0)
            i = i + 1;
            hist_data(i,1) = peaks(j,k);
            hist_data(i,2) = peaks(j,k+1);
        end
    end
end

% Sort the histogram data in ascending order.
sort(hist_data(:,:));

% Define the values of the bins based on the maximum values of force and
% distance. The number 10 may be modified in the following 3 lines to
```

```
% accomodate more bins.
for i = 1:20;
    dist_bins(i,1) = i * 10;
    force_bins(i,1) = i * min(hist_data(:,2))/10;
end

% Generate the mathematical histogram of the pull-off data based on the
% number of bins defined above.
dist_bins(:,2) = hist(hist_data(:,1),20);
force_bins(:,2) = hist(hist_data(:,2),20);

% Count the number of peaks, to be used to normalize the data into %
% frequency.
num_peaks = sum(dist_bins(:,2));

% Normalize the pull-off data to the total number of peaks identified.
for i = 1:length(dist_bins(:,1));
    dist_bins(i,2) = dist_bins(i,2) / num_peaks * 100;
    force_bins(i,2) = force_bins(i,2) / num_peaks * 100;
end

% Create bar charts of % frequency against pull-off force and distance.
figure1 = figure('Color',[1 1 1],'Name','Retraction Curve Analysis');
axes1 = axes('OuterPosition',[0 0.4985 1 0.5015],'Parent',figure1);
xlabel(axes1,'Pull-Off Distance (nm)');
ylabel(axes1,'Normalised Frequency (%)');
hold(axes1,'all');
axes2 = axes('OuterPosition',[0 0 1 0.4985],'Parent',figure1);
xlabel(axes2,'Pull-Off Force (nN)');
ylabel(axes2,'Normalised Frequency (%)');
```

```
hold(axes2,'all');

bar(dist_bins(:,1),dist_bins(:,2),'Parent',axes1);
bar(force_bins(:,1),force_bins(:,2),'Parent',axes2);

bars(:,1) = dist_bins(:,1);
bars(:,2) = dist_bins(:,2);
bars(:,3) = force_bins(:,1);
bars(:,4) = force_bins(:,2);
colname = {'Dist','Freq','Force','Freq'};

save('hist','hist_data','dist_bins','force_bins');
```

A.11 noise_sine.m

The `noise_sine` function is used by `fermi` to filter periodic interference at large separations from AFM force cycles. The filtration expression has the form $f(x) = log(a * sin[(x-b)/c] + d)$, where a represents the amplitude, b the phase, c the period and d the vertical offset of the interference pattern.

```
function F = noise_sine_mod(a,sep_appr);


x=sep_appr(:,1)


for k = 1:length(x)
    F(k) = log(a(1)*sin((x(k) - a(2))/a(3)) + a(4));
end
```

B Abbreviations

Abbreviation	Definition
% w/v	Percent, weight per volume basis
AFM	Atomic Force Microscope / Microscopy
ANOVA	Analysis of variance
Anti-C	Monoclonal antibody specific to the C-terminus of a peptide
Anti-Cb	Biotinylated monoclonal antibody specific to the C-terminus of a peptide
Anti-N	Monoclonal antibody specific to the N-terminus of a peptide
Anti-Nb	Biotinylated monoclonal antibody specific to the N-terminus of a peptide
APTES	Aminopropyltriethoxysilane
ASME	American Society of Mechanical Engineers
ATCC	American Type Culture Collection
Au	Gold
BSA	Bovine Serum Albumin
CLSM	Confocal laser scanning microscopy
DBM	Discrete Bonding Model
ddH_2O	Distilled, deionized water
DDT	Dodecanethiol
DLVO	Derjaguin-Landau-Verwey-Overbeek theory of colloid stability; accounts for London-van der Waals dispersion and electrostatic interactions
DNA	Deoxyribonucleic acid
DNP-S	Manufacturer's term describing a TappingMode^{TM} silicon nitride AFM

Continued on next page...

Abbreviation	Definition
	cantilever with a gold back-coating
ELISA	Enzyme-linked immunosorbent assay
EMF	Electromagnetic field
EPS	Extracellular polysaccharide or exopolysaccharide
FN	Fibronectin
FN-BR	Fibronectin binding receptor
GAS	Group A *Streptococci*
GBS	Group B *Streptococci*
HDT	1-hexadecanethiol; postscripts of 10 and 20 represent the molar concentration of HDT in ethanol
i-FN	Immobilised fibronectin
IAG	Ag(I)-IPA
IBM	International Business Machines Corporation
I.D.	Inner diameter
IgG	Immunoglobulin G
IPA	1-(10-sulfhydryl-decyloxy)-benzene-3,5-dicarboxylic acid
I.S.	Ionic strength
ISO	International Organization for Standardization
KH_2PO_4	Potassium phosphate (monobasic)
KCl	Potassium chloride
L-dopa	L-3,4-dihydroxyphenylalanine
LPS	Lipopolysaccharides
Mab	Monoclonal antibody
MES	2-N-Morpholinoethanesulfonic Acid

Continued on next page...

Abbreviation	Definition
NaCl	Sodium chloride
Na_2HPO_4	Sodium phosphate (dibasic)
NMR	Nuclear magnetic resonance
$O.D._{600}$	Optical density at 600 nm
PBS	Phosphate buffered saline
PBST	PBS with 0.05% Tween20
PI	Proportional-integral feedback system; control system commonly used in AFMs
PDMS	Poly(dimethyl siloxane)
PDT	4-(10-sulfhydryl-decyloxy)-pyridine
PET	Polyethylene
PETE	Polyethylene terephthalate
PLL	Poly-L-lysine; postscripts of 1, 10 and 100 denote stock, 10X dilution and 100X dilution, respectively
PMMA	Poly(methyl methacrylate)
PP	Polypropylene
PTFE	Poly(tetrafluoro ethylene)
PU	Polyurethane
RFV	Relative fluorescent units
RMS	Root mean square
RPM	Revolutions per minute
s-FN	Soluble fibronectin
SA	*Staphylococcus aureus*
SAM	Self-assembled monolayer
SD	Standard deviation

Continued on next page...

Abbreviation	Definition
SDS-PAGE	Sodium dodecyl sulfate polyacrylamide gel electrophoresis
SE	*Staphylococcus epidermidis*
SEM	Scanning electron microscopy
SPIP	The Scanning Probe Image Processor; Image Metrology, Denmark
spp.	Indicating multiple species or multiple strains of the same species
SS	Stainless steel
STM	Scanning tunneling microscope
TEG	(1-mercaptoundec-11-yl)-tri(ethylene glycol)
TEM	Transmission electron microscopy
TESPA	TappingMode^{TM} etched silicon probe with aluminum back-coating
TSB	Tryptic soy broth
UV	Ultraviolet light, corresponding to wavelengths of $330 - 380$ nm
XDLVO	Extended Derjaguin-Landau-Verwey-Overbeek theory of colloid stability; includes the classical DLVO theory, as well as a term describing Lewis acid-base interactions
XPS	X-ray photoelectron spectroscopy

C Symbols

Symbol	Definition	Dimensions
a_m	Radius of a microbial cell	m
a_p	Radius of curvature of a spherical AFM probe or elastic indenter	m
$a_{p,eff}$	Effective probe radius of curvature, used in the steric models	m
A	Hamaker constant	J
A_k	Constant describing inverse frequency noise	$\mathrm{Hz} \cdot \mathrm{nm}^2$
A_0	Measured optical density of microbial culture at time = 0	—
A_m	Measured optical density of microbial culture at t > 0	—
A_p	Nominal area over which an adhesive interaction occurs	m^2
A_s	Minimum area required for an adhesive interaction to occur	m^2
A_t	Area of a paraboloid AFM tip	m
A_{ts}	Total surface area evaluated at the scale of a single adhesive event	m^2
B_k	Constant describing white noise	nm^2
c	y-coordinate of the focus of a parabola	m
C	Constant describing the strength of an adhesive event at zero relative area	$\mathrm{N} \cdot \mathrm{m}^{-2}$
C_i	Coefficient of importance; A linear regression coefficient weighted to the normalised slope of a population of regressions	–
d	Spacing coefficient of a diffraction grating	$\# \cdot \mathrm{mm}^{-1}$

Continued on next page...

Symbol	Definition	Dimensions
D	Distance between the focus and each point on a parabola	m
δD	Minimised standard deviation of D for each point in a parabola	m
e	Unit charge of an electron	C
E_E	Electrostatic interaction energy contribution	k_BT
E_T	Total interaction energy due to DLVO forces	k_BT
E_V	London-van der Waals interaction energy contribution	k_BT
f_{FD}	Fermi-Dirac distribution function, in terms of tip-sample separation	—
F	Force	N
F_c	Point identified with the focus of a parabola	m
F_E	Force due to electrostatic DLVO interactions	N
f_{St}	Force per unit area due to steric interactions	$\mathrm{N \cdot m^{-2}}$
F_{St}	Force due to steric interactions	N
F_V	Force due to London-van der Waals interactions	N
h	Separation distance	nm
h_c	x-coordinate of the vertex of a parabola	m
H	Distance between diffraction grating and screen	m
k	Cantilever spring constant	$\mathrm{N \cdot m^{-1}}$
k_B	Boltzmann constant	$\mathrm{J \cdot K^{-1}}$
k_c	Horizontal coordinate of the center of a circle with radius R	m
K_m	Debye-Hückel parameter	$\mathrm{m^{-1}}$

Continued on next page...

Symbol	Definition	Dimensions
l_0	Minimum separation distance between two bodies in contact	m
L	Equilibrium polymer brush length; subscripts 1 and 2 indicate effects of multiple brushes in a single interaction	m
L_{FD}	Equilibrium polymer brush thickness from the modified steric equation; describing the distance at which the probability of contacting a polymer is equation to 0.5	m
ΔL	Constant from the Fermi-Dirac statistical distribution; describes the width of the transition region	m
m	Integer multiple of the wavelength of the AFM laser diode, λ_L	—
m_i	Slope of a linear regression; subscript i represents one of several measurements	$\mathrm{N \cdot m^{-2}}$
m_{max}	Maximum slope of the population m_i	$\mathrm{N \cdot m^{-2}}$
m_s	Fraction of total sites available for bonding; varies between 0 and 1	—
M	Total number of points within an area	—
n	Bulk concentration of ions in solution	$\mathrm{mol \cdot L^{-1}}$
$n_{i,\infty}$	Number concentration of ions in solution	$\mathrm{mol \cdot L^{-1}}$
N	Density of charged groups within the polymer brush	$\mathrm{m^{-3}}$
N_A	Avogadro's number	$\mathrm{\# \cdot mol^{-1}}$
N_D	Number of experimental data sets	—
N_{int}	Integer number of interference wavelengths	—
N_{Re}	Fluid Reynolds' number	—

Continued on next page...

Symbol	Definition	Dimensions
N_t	Number of discrete adhesive events with strength S_s	—
P	Measure of probability	—
P_A	Parameter describing the amplitude of an oscillatory interference pattern	N
P_B	Parameter describing the phase offset of an oscillatory interference pattern	m
P_C	Parameter describing the period of an oscillatory interference pattern	m
P_D	Parameter describing the vertical offset of an oscillatory interference pattern	N
Q	Quality factor of an AFM cantilever; described as the ratio of maximum energy stored in the cantilever to the amount dissipated per cycle	—
R	Radius of curvature of an AFM probe	m
R^2	Least squares regression coefficient; subscript i represents one measurement within a population	—
R_a	Average roughness	m
R_q	Root-Mean-Square roughness	m
s_s	Differential strength of an adhesive interaction	$\mathrm{N \cdot m^{-2}}$
S_s	Minimum, finite strength of an adhesive interaction	$\mathrm{N \cdot m^{-2}}$
S_t	Total measurable tensile strength of an interaction	$\mathrm{N \cdot m^{-2}}$
t	Time	h
T	Absolute temperature	K

Continued on next page...

Symbol	Definition	Dimensions
x	Cantilever deflection	m
$\langle x^2(\nu_k)\rangle$	Mean square amplitude at kinetic resonance	nm^2
x_c	Fast-scan direction data used in radius of curvature calculation	m
y	Distance between diffracted laser spots	m
z	Bulk valence of an ionic species	—
Δz	Cantilever displacement, used in calculation of ΔZ_m	m
z_c	Height data used in radius of curvature calculation	m
z_i	Valence of each ionic species in solution	—
Z	Valence of ions within a microbial polymer brush	—
Z_{Ave}	Average height of a given area	m
Z_i	Height of a given area	m
ΔZ_m	Machine-recorded displacement, as determined from interferometric measurements	m
$\Delta Z_m / \Delta V_m$	Sensitivity; conversion factor between AFM photodiode voltage and piezoactuator displacement	$nm \cdot V^{-1}$
ΔZ_p	Displacement predicted by geometric measurements, as determined from AFM laser diode wavelength and cantilever angle of repose	m

D Greek Symbols

Symbol	Definition	Dimensions
α_i	Constant describing the resonant mode of an AFM cantilever; the subscript "1" refers to the fundamental resonant mode	—
γ_L	Total free energy of liquid	$\mathrm{mJ} \cdot \mathrm{m}^{-2}$
γ_i^{LW}	Apolar (Lifshitz-van der Waals) component of the surface free energy	$\mathrm{mJ} \cdot \mathrm{m}^{-2}$
γ_i^+	Electron-accepting component of the polar (Acid-Base) surface free energy	$\mathrm{mJ} \cdot \mathrm{m}^{-2}$
γ_i^-	Electron-donating component of the polar surface free energy	mJcdot m^{-2}
Γ	Polymer grafting density; subscripts 1 and 2 indicate effects of multiple polymer brushes in an interaction	m^{-2}
δ	Indentation depth	m
$\Delta\nu$	Frequency resolution of an atomic force microscope	Hz
ε_0	Dielectric permittivity of a vacuum	$\mathrm{C}^2 \cdot \mathrm{J}^{-1} \cdot \mathrm{m}^{-1}$
ε_R	Relative dielectric permittivity of water	—
ζ_{Smol}	Zeta potential as calculated from the Smoluchowski equation	V
η	Separation coordinate used to formulate the differential area of a paraboloid AFM tip	m
θ_I	Angle used in calculation of the laser diode wavelength	rad
θ_L	Contact angle under liquid L	$^\circ$

Continued on next page...

Symbol	Definition	Dimensions
θ_R	Angle of repose of the AFM cantilever in its holder	rad
θ_W	Water contact angle	rad
κ	Debye screening length	m^{-1}
λ	Softness parameter	m^{-1}
λ_c	Collective decay length of a retarded van der Waals interaction	nm
λ_L	Wavelength of the AFM laser diode	m
μ	Microbial growth rate	h^{-1}
μ_E	Electrophoretic mobility	$\mathrm{m}^2 \cdot [\mathrm{V}^{-1} \cdot \mathrm{s}^{-1}]$
μ_f	Fluid viscosity	$\mathrm{kg} \cdot [\mathrm{m}^{-1} \cdot \mathrm{s}^{-1}]$
ν_k	Kinetic resonant frequency of an AFM cantilever	Hz
ξ	Polymer mesh spacing	m
Ξ	Polymer mesh density, corresponding to $\frac{1}{\xi^3}$	m^{-3}
φ_m	Reduced microbial surface potential	—
φ_p	Reduced probe surface potential	—
ψ_m	Microbial surface potential	V
ψ_p	Probe surface potential	V
Ψ_0	Surface zeta potential	V
Ψ_{Don}	Donnan potential of polymer layer	V

E Bibliography

[1] N. A. Burnham, X. Chen, C. S. Hodges, G. A. Matei, E. J. Thoreson, C. J. Roberts, M. C. Davies, and S. J. B. Tendler. Comparison of calibration methods for atomic-force microscopy cantilevers. Nanotechnology, 14:1–6, 2003.